

TASK I STAGE FINAL REPORT

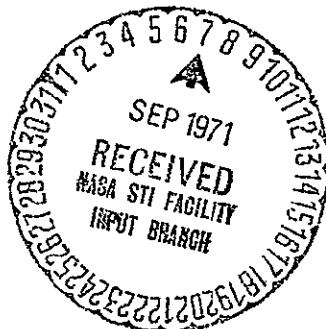
**VOLUME I**

**EVALUATION OF RANGE AND DISTORTION TOLERANCE  
FOR HIGH MACH NUMBER TRANSONIC FAN STAGES**

By

C.C. Koch, K.R. Bilwakesh, and V.L. Doyle

GENERAL ELECTRIC COMPANY  
Aircraft Engine Group  
Cincinnati, Ohio 45215



Prepared For

NATIONAL AERONAUTICS AND SPACE ADMINISTRATION

August, 1971

NASA Lewis Research Center  
Contract NAS3-11157  
Charles H. Voit Project Manager

1971-33201

(ACCESSION NUMBER) 1971-33201	(HRU) G-3	(CODE) 2	(CATEGORY) 2
(PAGES) 100			
(NASA CR OR TMX OR AD NUMBER) CR-72806			

FACILITY FORM 602

1 Report No. NASA CR-72806	2. Government Accession No.	3. Recipient's Catalog No.	
4. Title and Subtitle "EVALUATION OF RANGE AND DISTORTION TOLERANCE FOR HIGH MACH NUMBER TRANSONIC FAN STAGES," TASK I STAGE FINAL REPORT, VOLUME I.		5 Report Date August 1971	
		6. Performing Organization Code	
7. Author(s) C.G. Koch, K.R. Bilwakesh, and V.L. Doyle		8. Performing Organization Report No. - GE R71 AEG-133	
		10. Work Unit No.	
9. Performing Organization Name and Address General Electric Company Aircraft Engine Group Cincinnati, Ohio 45215		11. Contract or Grant No. NAS3-11157	
12. Sponsoring Agency Name and Address National Aeronautics and Space Administration Washington, D.C. 20546		13. Type of Report and Period Covered Contractor Report	
		14. Sponsoring Agency Code	
15. Supplementary Notes Project Manager, Charles H. Voit, Fluid System Components Division NASA-Lewis Research Center Cleveland, Ohio 45433			
16. Abstract  This report documents the performance and discusses the results of testing a single-stage 1400 ft/sec tip speed transonic compressor. Objectives of the program were to investigate efficiency, weight flow range, and tolerance to distorted inlet airflows. Tests were conducted with undistorted inlet flow and with both radial and circumferential inlet flow distortions. With undistorted inlet flow, the stage demonstrated a peak adiabatic efficiency at 100% design speed of 0.852 at a total-pressure ratio of 1.624 and an inlet corrected weight flow of 217.2 lb/sec. Stall margin of over 20% was obtained at the above operating condition. Radial and circumferential inlet flow distortions caused substantial reductions in unstalled weight flow range and efficiency.  Volume I of this report contains a description of test apparatus and procedure, presentation and analysis of the experimental results, and graphical presentations of the data. Volume II (NASA CR-72964) contains tabulations of the computer output of the data reduction programs. Overall performance data are listed for all undistorted and distorted inlet flow tests; blade element data are listed for both undistorted and radial distortion tests; and, vector diagram data are listed for tests with circumferential inlet flow distortion.			
17. Key Words (Suggested by Author(s)) Transonic Fan Distortion Tolerance Compressor		18. Distribution Statement Unclassified - Unlimited	
19. Security Classif. (of this report) Unclassified	20. Security Classif. (of this page) Unclassified	21. No. of Pages 205	22. Price* \$3.00

\* For sale by the National Technical Information Service, Springfield, Virginia 22151

## TABLE OF CONTENTS

<u>Section</u>	<u>Page</u>
<u><b>VOLUME I</b></u>	
I. SUMMARY	1
II. INTRODUCTION	2
III. APPARATUS AND PROCEDURE	3
1. Test Compressor Stage	3
2. Inlet Distortion Equipment	4
3. Test Facility	4
4. Instrumentation	5
a. Undistorted Inlet Test Instrumentation	5
b. Radial Distortion Test Instrumentation	5
c. Circumferential Distortion Test Instrumentation	6
d. Stall Test Instrumentation	6
5. Data Reduction Methods	6
a. Overall Performance Data Program	7
b. Blade Element Data Program	8
c. Circumferential Distortion Data Program	9
6. Test Procedure	10
a. Shakedown Testing with Undistorted Inlet Flow	10
b. Undistorted Inlet Performance Testing	11
c. Undistorted Inlet Testing with Inlet Duct	11
d. Radial Distortion Testing	12
e. Circumferential Distortion Testing	12
IV. RESULTS AND DISCUSSION	13
1. Undistorted Inlet Performance	13
a. Overall Performance Data	13
b. Blade Element Data	13
c. Efficiency Loss Due to Part-Span Shroud	14
d. Comparison of the Performance of the Rotor Operated in the Task I Stage with Its Performance in an Isolated Rotor Configuration (Rotor 1B)	15
e. Effect of the Long Inlet Duct Used for Distortion Testing on the Compressor Performance	19
f. Investigation of Stator Setting Angle Effects	19
2. Performance with Tip Radial Inlet Flow Distortion	20
a. Overall Performance Data	20
b. Blade Element and Vector Diagram Data	21
c. Analysis of Stall Limits with Radial Distortion	22

TABLE OF CONTENTS (Concluded)

<u>Section</u>	<u>Page</u>
<u>VOLUME I (Concluded)</u>	
3. Performance with Circumferential Inlet Flow Distortion	22
a. Overall Performance Data	22
b. Flow Survey Data	23
c. Analysis of Performance with Circumferential Distortion	24
V. CONCLUSIONS	28
REFERENCES	29
APPENDIX A - SYMBOLS	31
TABLES	35
FIGURES	49
<u>VOLUME II</u>	
APPENDIX A - SYMBOLS	1
APPENDIX B - DUPLICATE LISTING OF TABLE VII, OVERALL PERFORMANCE DATA	7
APPENDIX C - SYMBOLIC LISTING OF ROTOR AND STATOR BLADE ELEMENT DATA	15
APPENDIX D - TABULATIONS OF BLADE ELEMENT DATA FOR UNDISTORTED INLET TESTING	19
APPENDIX E - TABULATIONS OF BLADE ELEMENT DATA FOR RADIAL INLET DISTORTION TESTING	81
APPENDIX F - TABULATIONS OF FLOW SURVEY DATA FOR CIRCUMFERENTIAL INLET DISTORTION TESTING	89
DISTRIBUTION LIST	117

## LIST OF TABLES

<u>Table</u>	<u>Page</u>
I. Summary of Task I Stage and Blade Row Design Parameters.	35
II. Cascade Projection Data for Rotor 1B.	36
III. Stator Cascade Projection Data.	37
IV. Summary of Instrumentation Used for Task I Stage Testing.	38
V. Summary of Blade Element Data Reduction Constants.	39
a) Rotor	39
b) Stator	40
VI. Symbolic Listing of Blade Element Data.	41
a) Rotor	41
b) Stator	42
VII. Listing of Overall Performance Data.	43
a) Shakedown Test with Undistorted Inlet	43
b) Undistorted Inlet Performance Test	44
c) Undistorted Inlet Test with Long Inlet Duct	46
d) Radial Inlet Distortion Test	47
e) Circumferential Inlet Distortion Test	48

## LIST OF ILLUSTRATIONS

<u>Figure</u>		<u>Page</u>
1. Task I Stage Flowpath.		49
2. Partial View of Rotor 1B.		50
3. Photographs of a Variable-Stagger Stator Vane.		51
4(a). Stator Vane Inspection Results for Tip Section.		52
4(b). Stator Vane Inspection Results for Pitchline Section.		53
4(c). Stator Vane Inspection Results for Hub Section.		54
5. Photographs of Inlet Distortion Screens.		55
a) Radial Distortion Screen		55
b) Circumferential Distortion Screen		56
6. Schematic Diagram of House Compressor Test Facility.		57
7. Meridional View Showing Instrumentation Locations.		58
8. Circumferential Development Showing Instrumentation Locations.		59
9. Photographs of Instrumentation.		60
a) Fixed Discharge Total Pressure-Total Temperature Wake Rake Located at Plane 2.2		60
b) Sensing Element of Angle-Seeking Static-Pressure Wedge Traverse Probe		60
c) Sensing Element of Cobra Traverse Probe		60
d) Fixed Inlet Distortion Total-Pressure Rake at Plane 0.18		61
e) Sensing Element of Four-Parameter Combination Traverse Probe		61
f) Sensing Element of Shielded Hot-Wire Anemometer Traverse Probe		61

LIST OF ILLUSTRATIONS (Continued)

<u>Figure</u>		<u>Page</u>
10.	Relationship Between Flow Function and Meridional Mach No. Used for Transferring Traverse Measurements to Blade Edges.	62
11.	Stage Performance Map with Undistorted Inlet Flow.	63
12.	Rotor Performance Map with Undistorted Inlet Flow.	64
13(a).	Rotor Blade Element Data with Undistorted Inlet Flow, at 5% Immersion from Tip.	65
13(b).	Rotor Blade Element Data with Undistorted Inlet Flow, at 10% Immersion from Tip.	67
13(c).	Rotor Blade Element Data with Undistorted Inlet Flow, at 30% Immersion from Tip.	69
13(d).	Rotor Blade Element Data with Undistorted Inlet Flow, at 50% Immersion from Tip.	71
13(e).	Rotor Blade Element Data with Undistorted Inlet Flow, at 70% Immersion from Tip.	73
13(f).	Rotor Blade Element Data with Undistorted Inlet Flow, at 90% Immersion from Tip.	75
13(g).	Rotor Blade Element Data with Undistorted Inlet Flow, at 95% Immersion from Tip.	77
14(a).	Stator Blade Element Data with Undistorted Inlet Flow, at 5% Immersion from Tip.	79
14(b).	Stator Blade Element Data with Undistorted Inlet Flow, at 10% Immersion from Tip.	81
14(c).	Stator Blade Element Data with Undistorted Inlet Flow, at 30% Immersion from Tip.	83
14(d).	Stator Blade Element Data with Undistorted Inlet Flow, at 50% Immersion from Tip.	85
14(e).	Stator Blade Element Data with Undistorted Inlet Flow, at 70% Immersion from Tip.	87

LIST OF ILLUSTRATIONS (Continued)

<u>Figure</u>		<u>Page</u>
14(f).	Stator Blade Element Data with Undistorted Inlet Flow, at 90% Immersion from Tip.	89
14(g).	Stator Blade Element Data with Undistorted Inlet Flow, at 95% Immersion from Tip.	91
15.	Continuous Traverse Data at Rotor Exit Plane 1.51 at 100% Speed with Undistorted Inlet Flow for Readings 55 (Max. Flow), 56 (Near Peak Efficiency), and 58 (Near Stall).	93
16(a).	Radial Profiles of Adiabatic Efficiency at 100% Speed Obtained in the Task I Stage and Rotor 1B Tests, Near Peak Efficiency.	94
16(b).	Radial Profiles of Adiabatic Efficiency at 100% Speed Obtained in the Task I Stage and Rotor 1B Tests, Near Stall.	95
16(c).	Radial Profiles of Adiabatic Efficiency at 100% Speed Obtained in the Task I Stage and Rotor 1B Tests, Maximum Flow.	96
17(a).	Stator Exit Total-Pressure Wake Profiles at 100% Speed with Undistorted Inlet Flow, Near Peak Efficiency, Reading 27.	97
17(b).	Stator Exit Total-Pressure Wake Profiles at 100% Speed with Undistorted Inlet Flow, Near Stall, Reading 64.	99
18(a).	Comparison of Radial Profiles of Rotor Total-Pressure Ratio at 100% Speed, Near Peak Efficiency, Obtained from Fixed and Traversing Instruments.	101
18(b).	Comparison of Radial Profiles of Rotor Total-Temperature Ratio at 100% Speed Near Peak Efficiency Obtained from Fixed and Traversing Instruments.	102
18(c).	Comparison of Radial Profiles of Rotor Adiabatic Efficiency at 100% Speed Near Peak Efficiency Obtained from Fixed and Traversing Instruments.	103
19(a)	Stator Exit Total-Temperature Wake Profiles at 100% Speed with Undistorted Inlet Flow, Near Peak Efficiency, Reading 27.	104

LIST OF ILLUSTRATIONS (Continued)

<u>Figure</u>	<u>Page</u>
19(b). Stator Exit Total-Temperature Wake Profiles at 100% Speed with Undistorted Inlet Flow, Near Stall, Reading 64.	105
20. Radial Profiles of Rotor and Stator Loss Coefficients at 100% Speed Near Peak Efficiency.	106
21. Radial Profiles of Rotor and Stator Diffusion Factors at 100% Speed Near Peak Efficiency.	107
22(a). Radial Profiles of Rotor Axial Velocities at 100% Speed Near Peak Efficiency.	108
22(b). Radial Profiles of Stator Axial Velocities at 100% Speed Near Peak Efficiency.	109
23. Stator Exit Axial Velocity Profiles at 100% Speed.	110
24. Rotor Exit Axial Velocity Profiles at 100% Speed.	111
25(a). Variations of Rotor Performance Parameters with Weight Flow at 100% Speed; 90% Immersion from Tip.	112
25(b). Variations of Stator Performance Parameters with Weight Flow at 100% Speed; 90% Immersion from Tip.	117
25(c). Variations of Rotor Performance Parameters with Weight Flow at 100% Speed; 10% Immersion from Tip.	120
25(d). Variations of Stator Performance Parameters with Weight Flow at 100% Speed; 10% Immersion from Tip.	125
26. Stage Performance Map with Undistorted Inlet Flow and Long Inlet Duct.	128
27. Comparison of Inlet Casing Boundary Layer Profiles at 100% Speed, Undistorted Inlet Flow, Between Long Inlet Duct with Distortion Support Screen and Short Inlet Duct without Distortion Support Screen.	129
28. Variation of Weight Flow and Efficiency with Stator Setting Angle.	130
29. Stage Performance Map with Inlet Tip-Radial Distortion.	131

LIST OF ILLUSTRATIONS (Continued)

<u>Figure</u>		<u>Page</u>
30.	Rotor Performance Map with Inlet Tip-Radial Distortion.	132
31.	Variation of Inlet Distortion Parameter for Radial and Circumferential Distortion Tests.	133
32.	Radial Profiles of Fluid Conditions at 100% Speed Near Stall with Inlet Tip-Radial Distortion, Reading 82.	134
33(a).	Rotor Blade Element Data with Inlet Tip-Radial Distortion, at 5% Immersion from Tip.	137
33(b).	Rotor Blade Element Data with Inlet Tip-Radial Distortion, at 10% Immersion from Tip.	139
33(c).	Rotor Blade Element Data with Inlet Tip-Radial Distortion, at 30% Immersion from Tip.	141
33(d).	Rotor Blade Element Data with Inlet Tip-Radial Distortion, at 50% Immersion from Tip.	143
33(e).	Rotor Blade Element Data with Inlet Tip-Radial Distortion, at 70% Immersion from Tip.	145
33(f).	Rotor Blade Element Data with Inlet Tip-Radial Distortion, at 90% Immersion from Tip.	147
33(g).	Rotor Blade Element Data with Inlet Tip-Radial Distortion, at 95% Immersion from Tip.	149
34(a).	Stator Blade Element Data with Inlet Tip-Radial Distortion, at 5% Immersion from Tip.	151
34(b).	Stator Blade Element Data with Inlet Tip-Radial Distortion, at 10% Immersion from Tip.	153
34(c).	Stator Blade Element Data with Inlet Tip-Radial Distortion, at 30% Immersion from Tip.	155
34(d).	Stator Blade Element Data with Inlet Tip-Radial Distortion, at 50% Immersion from Tip.	157
34(e).	Stator Blade Element Data with Inlet Tip-Radial Distortion, at 70% Immersion from Tip.	159

LIST OF ILLUSTRATIONS (Continued)

<u>Figure</u>		<u>Page</u>
34(f).	Stator Blade Element Data with Inlet Tip-Radial Distortion, at 90% Immersion from Tip.	161
34(g).	Stator Blade Element Data with Inlet Tip-Radial Distortion, at 95% Immersion from Tip.	163
35(a).	Variation of Rotor Aerodynamic Loading Quantities with Throttle Setting at 100% Speed for Radial Distortion and Undistorted Inlet Flow, at 5% Immersion from Tip.	165
35(b).	Variation of Rotor Aerodynamic Loading Quantities with Throttle Setting at 100% Speed for Radial Distortion and Undistorted Inlet Flow, at 10% Immersion from Tip.	168
36(a).	Radial Variation of Rotor Diffusion Factor Near 100% Speed Stall for Radial Distortion and Undistorted Inlet Flow.	171
36(b).	Radial Variation of Rotor Static-Pressure-Rise Coefficient Near 100% Speed Stall for Radial Distortion and Undistorted Inlet Flow.	172
36(c).	Radial Variation of Rotor Total-Temperature Ratio Near 100% Speed Stall for Radial Distortion and Undistorted Inlet Flow.	173
37.	Stage Performance Map with Circumferential Inlet Flow Distortion.	174
38.	Rotor Performance Map with Circumferential Inlet Flow Distortion.	175
39(a).	Circumferential Variation of Flow Conditions at 100% Speed Near Stall with Circumferential Inlet Flow Distortion, Plane 0.95.	176
39(b).	Circumferential Variation of Flow Conditions at 100% Speed Near Stall with Circumferential Inlet Flow Distortion, Plane 1.51.	177
39(c).	Circumferential Variation of Flow Conditions at 100% Speed Near Stall with Circumferential Inlet Flow Distortion, Plane 2.20.	179
40(a).	Circumferential Variation of Flow Conditions at 100% Speed Maximum Weight Flow with Circumferential Inlet Flow Distortion, Plane 0.95.	181

LIST OF ILLUSTRATIONS (Concluded)

<u>Figure</u>		<u>Page</u>
40(b).	Circumferential Variation of Flow Conditions at 100% Speed Maximum Weight Flow with Circumferential Inlet Flow Distortion, Plane 1.51.	182
40(c).	Circumferential Variation of Flow Conditions at 100% Speed Maximum Weight Flow with Circumferential Inlet Flow Distortion, Plane 2.20.	184
41(a).	Rotor Blade Element Work Coefficient - Flow Coefficient Characteristics, Uncorrected for Inlet Swirl and Axial Velocity Change at 100% Speed; 10% Immersion from Tip.	186
41(b).	Rotor Blade Element Work Coefficient - Flow Coefficient Characteristics, Corrected for Inlet Swirl at 100% Speed; 10% Immersion from Tip.	187
41(c).	Rotor Blade Element Work Coefficient - Flow Coefficient Characteristics, Corrected for Inlet Swirl and Axial Velocity Change at 100% Speed; 10% Immersion from Tip.	188
42(a).	Rotor Blade Element Work Coefficient - Flow Coefficient Characteristics, Uncorrected for Inlet Swirl and Axial Velocity Change at 100% Speed; 50% Immersion from Tip.	189
42(b).	Rotor Blade Element Work Coefficient - Flow Coefficient Characteristics, Corrected for Inlet Swirl at 100% Speed; 50% Immersion from Tip.	190
42(c).	Rotor Blade Element Work Coefficient - Flow Coefficient Characteristics, Corrected for Inlet Swirl and Axial Velocity Change at 100% Speed; 50% Immersion from Tip.	191
43(a).	Rotor Blade Element Work Coefficient - Flow Coefficient Characteristics, Uncorrected for Inlet Swirl and Axial Velocity Change at 100% Speed; 90% Immersion from Tip.	192
43(b).	Rotor Blade Element Work Coefficient - Flow Coefficient Characteristics, Corrected for Inlet Swirl at 100% Speed; 90% Immersion from Tip.	193
43(c).	Rotor Blade Element Work Coefficient - Flow Coefficient Characteristics, Corrected for Inlet Swirl and Axial Velocity Change at 100% Speed; 90% Immersion from Tip.	194

## I. SUMMARY

The efficiency, weight flow range, and tolerance to distorted inlet air flows were evaluated for a single-stage, 1400 ft/sec tip speed transonic compressor under Task I of NASA Contract NAS3-11157. The Task I Stage was tested with undistorted inlet flow and with both radial and circumferential inlet distortions.

The 1400 ft/sec tip speed Rotor 1B used in the Task I Stage was tested previously as an isolated blade row under NASA Contract NAS3-7617. A set of stator vanes was designed under the present contract to match the rotor exit flow at design speed and return it to the axial direction at stator exit.

Results of the undistorted inlet overall performance tests at 100% design speed showed that the Task I Stage achieved a total-pressure ratio of 1.624 at a weight flow of 217.2 lbs/sec with an adiabatic efficiency of 0.852. Stall margin was over 0.20 at this operating point. Rotating stall limits were determined at 50, 70, 80, 90, 100, and 110% of design speed. Blade element data for rotor and stator blade rows were obtained at five operating conditions at each speed.

Peak rotor efficiency at 100% design speed was approximately 2 percentage points less in the Task I Stage tests than measured in previous Rotor 1B tests. Unstalled weight flow range at 100% speed increased, however. It was believed that the addition of stators close to the rotor trailing edge, plus a hub flowpath change made when adding the stators, increased rotor hub loading and decreased rotor tip loading and produced both the efficiency and the flow range differences.

Tip radial and circumferential inlet distortion tests were conducted at 70, 90, and 100% design speed. Stall points were determined at these speeds for both types of inlet distortion. Overall performance points were taken near stall, near peak efficiency, and at maximum flow for each speed. Blade element traverses with radial distortion were obtained at 100% speed at the above three operating conditions. Circumferential distortion screen rotation tests were conducted at three similar operating conditions at 100% speed. Substantial reductions in stall margin and efficiency were caused by inlet flow distortions. At design speed with radial distortion, for example, 5 percentage points in adiabatic efficiency were lost, and stalling weight flow increased from 186.5 lbs/sec to 208.5 lbs/sec. Design speed stalling weight flow with circumferential distortion increased to 197.5 lbs/sec, and peak stage efficiency was reduced by approximately 3 percentage points.

## II. INTRODUCTION

The need to reduce the size and weight of gas turbine engines for advanced military and commercial aircraft has led to the use of high-tip-speed fan and compressor stages, and thus, data on the aerodynamic performance of such stages at various operating conditions will be beneficial in future design and development efforts. This research program was initiated to obtain information on the efficiency, stall margin, and distortion tolerance of a representative high-tip-speed transonic compressor stage.

The 1400 ft/sec tip speed single-stage compressor, designated the Task I Stage, was tested with undistorted inlet flow and with both radial and circumferential inlet flow distortions. The results and analysis of these tests are reported herein. Major objectives of the Task I phase of this research program were: to determine the efficiency and unstalled weight flow range of the Task I Stage; to evaluate any effect the stator might have on the rotor performance; and, to obtain blade element data on both rotor and stator. Additional objectives were to determine the tolerance of the compressor stage to radially and circumferentially distorted inlet flows and to obtain extensive data on the structure of the distorted flow fields. The Task I Stage employed existing 1400 ft/sec tip speed Rotor 1B and a matching stator. The rotor had been tested previously as an isolated blade row and demonstrated excellent efficiency and weight flow range. It thus was selected as the basic component of a stage having a high performance potential and representative of current advanced engine compressors.

### III. APPARATUS AND PROCEDURE

#### 1. TEST COMPRESSOR STAGE

The basic design requirement for the Task I Stage was to provide a stator to match the flow conditions leaving Rotor 1B, a high-performance 1400 ft/sec tip speed rotor previously tested as an isolated blade row (Reference 1). The Task I Stage test vehicle employed much of the existing hardware from earlier Rotor 1B testing, including rotor blades and inlet ducting. New hardware included the stator vanes, stator hub region flowpath parts, and a special inlet section for distortion testing. The flowpath is shown in Figure 1, which also shows the original Rotor 1B test vehicle flowpath for comparison. Photographs of the rotor and a stator vane are shown in Figures 2 and 3.

Additional details of the Task I Stage design are given in Reference 2, and Table I is a summary of Task I Stage blade row design parameters and predicted performance. The rotor and stator were matched at a stage design condition of 219.4 lbs/sec weight flow at 100% corrected rotor speed. Predicted stage overall performance at this point was a total-pressure ratio of 1.617 with an adiabatic efficiency of 0.873. This stage design point corresponded to a Rotor 1B test point near peak efficiency at design speed. The rotor had 0.206 stall margin\*, a total-pressure ratio of 1.636, and an adiabatic efficiency of 0.8915 at this operating condition. Complete Rotor 1B test data are presented in Reference 1.

The design of Rotor 1B is described in Reference 3. This 1400 ft/sec tip speed rotor had an inlet hub:tip radius ratio of 0.5, a tip solidity of 1.3, and an aspect ratio of 2.5 with radially constant chord length. Design tip diffusion factor was 0.35, and design tip inlet relative Mach number was 1.43. The tip blade section shape was a multiple-circular-arc type. A part-span shroud was located at approximately 60% span from the hub; below the part-span shroud the blade section shapes were double-circular-arc type. Rotor cascade geometry is given in Table II. Rotor tip clearance at 100% speed was in the range from 0.030 inch to 0.037 inch, approximately the same as in previous Rotor 1B tests.

The stator vanes were designed to be compatible with the rotor exit absolute air angles measured in Rotor 1B test Reading 52 (Reference 1), the operating condition defined as the Task I Stage design point. The stator had double-circular-arc type vane sections at the outer part of the blade which blended into arbitrarily shaped hub sections designed especially for low suction surface Mach numbers. Stator hub solidity was 2.155, and the aspect ratio was

---

\* Stall margin =  $\left[ \left( \frac{P/P}{W\sqrt{\theta/\delta}} \right)_{\text{stall}} / \left( \frac{P/P}{W\sqrt{\theta/\delta}} \right)_{\text{operating point}} \right] - 1.0$

2.065 with radially nonconstant chord. Additional stator design details are given in Reference 2 and in Tables I and III of this report.

A comparison of stator vane hardware quality with the design intent is given in Figures 4(a), 4(b), and 4(c) for tip, pitchline, and hub vane sections, respectively. Average vane sections were determined from probograph inspections of five vanes selected at random. Agreement with design intent was generally good.

## 2. INLET DISTORTION EQUIPMENT

The Task I radial and circumferential inlet distortion screens were the same types used in the previous Rotor 1B distortion testing reported in Reference 1. The radial distortion screen for Task I covered the outer 40% of the annulus area, while the circumferential screen spanned 90° of the annulus from hub to tip. Both screens were made of 20 mesh, 0.016-inch-diameter wire, giving a screen solidity of 0.54. Photographs of the distortion screens are shown in Figure 5. The distortion parameter,  $(P_{max.} - P_{min.})/P_{max.}$ , for this screen material was estimated from previous test data to be 0.20 at the Task I Stage design weight flow and speed.

The support screen, which spanned the entire annulus, and to which the distortion screens were attached, was designed to be rotated 360° past the instrumentation for the circumferential inlet flow distortion testing. The support screen material was one-inch-square mesh with 0.093-inch-diameter wire and gave an open area of 83.4%. The support screen was designed to separate into halves to facilitate installation.

The distortion screens were located one rotor diameter forward of the rotor leading edge, and were mounted in a cylindrical section approximately one rotor diameter long which was inserted into the test vehicle only during distortion testing.

## 3. TEST FACILITY

Performance tests were conducted in General Electric's House Compressor Test Facility in Lynn, Massachusetts. The test compressor drew atmospheric air through two banks of filters. The first filter bank was intended to remove 22% of the particles larger than 3-5 microns (dust spot test), and the second filter bank was intended to remove 90-95% of the remaining particles down to the same size. The air then passed through a coarse-wire inlet screen, into the bellmouth and then through the test compressor. In the exit assembly, the compressor discharge flow was split into two concentric streams. The inner air stream was passed into an exit pipe containing a flow straightener and a venturi flow meter and then was exhausted to the atmosphere. The outer air stream passed through a slide cylindrical throttle valve into a collector. Two pipes, each of which contained a flow straightener and a venturi flow meter, then discharged the outer stream to the atmosphere. Power to drive the test compressor was provided by a high-pressure noncondensing steam turbine rated at 15,000 horsepower. A schematic layout of the test facility is shown in Figure 6.

#### 4. INSTRUMENTATION

A listing of major fixed and traverse instruments provided for each phase of the testing is given in Table IV. The locations of these instruments, and of the hub and casing static-pressure taps, are shown in the instrumentation schematics, Figures 7 and 8.

All traverse probes were calibrated for Mach number and pitch angle effects, and these calibrations were used in the data reduction calculations. Static wire calibrations for thermocouple sensors were properly accounted for. Fixed temperature and pressure rakes were calibrated for Mach number and yaw angle effects. These generally proved to be small enough to be neglected, except for the effect of Mach number on total-temperature recovery.

##### a. Undistorted Inlet Test Instrumentation

Overall performance measurements were obtained from fixed instrumentation at stage inlet and exit, located at seven radial positions corresponding to design streamlines passing through 5%, 10%, 30%, 50%, 70%, 90%, and 95% of the annulus height from the tip at the rotor exit, Plane 1.51. The inlet total pressure was obtained from six 7-element pitot-static rakes located in the bellmouth at Plane 0.01. The inlet total temperature was measured with 24 chromel-alumel thermocouples distributed over the face of the vehicle inlet screen. Stage exit conditions were measured at Plane 2.20 with seven 14-element total-pressure and total-temperature wake rakes. Figure 9(a) shows a picture of one of these rakes. Discharge static pressures were measured by eight hub and eight casing static taps at the exit plane.

For blade element data, the inlet total conditions were obtained in the same manner as for overall performance data. The static pressure at rotor inlet, Plane 0.95, was measured at each immersion with an angle-seeking static-pressure wedge traverse probe shown in Figure 9(b). At the rotor exit/stator inlet station, Plane 1.51, the total pressure, total temperature, and flow angle were obtained at each immersion from a cobra probe. Figure 9(c) shows the cobra probe's sensing head. One 8° wedge probe, similar to the probe shown in Figure 9(b) and designated T-4 in Figures 7 and 8, was used to measure static pressure at this location. Stator exit total temperatures and total pressures were obtained from the fixed wake rakes used to determine overall performance. Exit static pressures and absolute flow angles were measured at each immersion with an angle-seeking static-pressure wedge probe (T-11 in Figures 7 and 8).

##### b. Radial Distortion Test Instrumentation

The inlet total pressure used for overall performance with radial inlet flow distortion was based on measurements from two 7-element inlet distortion total-pressure rakes, shown in Figure 9(d), located downstream of the distortion screen at Plane 0.18. Inlet total temperature was obtained from the 24 thermocouples distributed over the vehicle inlet screen at Plane 0.01. The stage exit conditions for overall performance were measured by the same exit wake rakes used in undistorted inlet tests.

Blade element data with radial inlet flow distortion were determined using the same instrumentation as had been employed for the undistorted inlet tests, except that rotor inlet conditions for each immersion at Plane 0.95 were based on measurements of total pressure, total temperature, static pressure, and flow angle from a combination probe. Figure 9(e) shows a photograph of the combination probe sensing element.

#### c. Circumferential Distortion Test Instrumentation

Overall performance data with circumferential inlet distortion were obtained from measurements taken with the same fixed instrumentation as had been employed in the radial distortion tests.

Flow survey data were acquired at each blade row inlet and exit using four-parameter combination probes, designated T-3, T-8, and T-13 in Figures 7 and 8. Values of total pressure, total temperature, static pressure, and flow angle at three radial positions (corresponding to the 10%, 50%, and 90% of annulus height immersions) were obtained using these probes.

#### d. Stall Test Instrumentation

Three hot-wire anemometer probes at Plane 1.51, shown in Figure 9(f), were immersed during stall tests to the 10%, 50%, and 90% immersions to detect the initiation of stall and the radial extent of the rotating stall cells. For all other testing the hot-wire probes were removed from the airstream.

### 5. DATA REDUCTION METHODS

Three separate computer programs were used to reduce the test data. The Overall Performance Data Program computed average fluid properties at each measuring station from data measured by fixed instruments. It then calculated overall stage and rotor performance parameters such as total-pressure ratio and adiabatic efficiency. The Blade Element Data Program calculated vector diagram and blade element performance parameters for seven streamline sections of both the rotor and the stator. This program processed data measured by both fixed and traversing instruments. The above two computer programs were used primarily to reduce data obtained during undistorted inlet and radial inlet flow distortion testing. A special Circumferential Distortion Data Program was used to calculate vector diagram data at numerous circumferential, radial, and axial locations for circumferential inlet flow distortion testing. This data reduction computer program also calculated overall performance data from average fluid properties determined by mass averaging throughout the entire flow field. Input data for this program were obtained from both fixed and traverse instruments for 12 different circumferential positions of the distortion screen and at 5 immersions.

Several assumptions were made that were common to all three data reduction programs. First, it was assumed that the radial position and meridional slope angle of each stream surface on which data were recorded were fixed at the design value for all operating conditions. Second, all mass-averaging

calculations used to determine average total-temperature and total-pressure values were formulated in terms of enthalpy and entropy. Finally, the real gas properties of dry air were used in all thermodynamic calculations.

Additional information on data reduction methods appears in the following sections.

a. Overall Performance Data Program

Average stage inlet conditions with undistorted inlet flow were taken as the arithmetic average of the Plane 0.01 thermocouple and total-pressure pitot rake readings. With radial inlet flow distortion the average stage inlet total temperature was calculated as mentioned above, but inlet total pressure was radially mass averaged from readings of the two distortion rakes located at Plane 0.18 between the distortion screen and the rotor. The static pressure used in the mass-averaging procedure was determined at each of the seven instrument positions by a linear interpolation versus radius between arithmetically averaged hub and casing wall static pressure values. Total pressure at each radial position was taken as the arithmetic average of the values given by the two inlet distortion rakes. An approximate value of average inlet total pressure was also calculated by this program for the case of circumferential inlet flow distortion; at each radial instrument position, the pressure reading from the Plane 0.18 rake located in the 270° extent undistorted region was weighted three times as heavily as that from the rake located in the 90° extent distorted region when calculating the local average pressure. These were then mass averaged radially as in the case of radial inlet flow distortion. With either inlet distortion, Plane 0.18 flow angles were assumed to be zero degrees, or axial.

Average stage exit total pressure and total temperature were calculated from data measured by the Plane 2.20 wake rakes. Both radial and circumferential mass averaging were used to properly account for variations of measured properties across the stator spacing as well as radially. The static pressure required at each of the seven radial measurement positions was again obtained by linear interpolation between average wall static pressure values. In addition to overall fluid properties at Plane 2.20, the data reduction program also calculated average total temperature and total pressure at each radial position by mass averaging circumferentially across each wake rake. Flow angles at Plane 2.20 were assumed to equal zero degrees plus or minus any stator stagger adjustment. These methods of obtaining discharge conditions were believed to offer excellent accuracy for the axisymmetric flow fields expected with undistorted or radially distorted inlet conditions, but to be only approximate for circumferential distortion testing. In order to calculate more accurate total properties with circumferential distortion at each specific discharge wake rake radial and circumferential location, the static pressure associated with each particular wake rake was interpolated from readings of hub and casing wall static taps located at the same circumferential position as the wake rake.

Rotor exit total pressure at each of the seven radial measurement positions was taken as the arithmetic average of the three highest readings on each stage exit wake rake. Total temperature at each radial position was assumed equal to the stage exit value. Average total pressure at the rotor exit station was calculated by a radial mass-averaging procedure which used a weight flow fraction at each radial position calculated from stage exit properties and flow angles.

The average total temperatures and total pressures at the stage inlet, rotor exit, and stage exit measurement stations were used to calculate overall performance parameters for the stage as a whole and for the rotor as an isolated blade row. In addition, the Overall Performance Data Program computed average total-temperature and total-pressure values at each of the seven radial positions at each measuring station; these values were then used as input data to the other data reduction computer programs.

#### b. Blade Element Data Program

Blade element and vector diagram data were obtained for both rotor and stator during undistorted and radial distortion tests. Traverse probe measurements for undistorted inlet and radial distortion tests were obtained at seven immersions at the inlet and exit stations of each blade row. Circumferential uniformity was assumed for all such traverse data.

Rotor inlet static pressure and flow angle at Plane 0.95 were obtained at each immersion from an angle-seeking wedge probe for undistorted inlet testing. Immersion values of total pressure and total temperature at rotor inlet were assumed equal to compressor inlet values measured at Plane 0.01. With radial distortion, the rotor inlet total pressure, total temperature, static pressure, and flow angle were obtained at each immersion with a four-parameter combination probe. Total pressure, total temperature, and flow angle at rotor exit/stator inlet station, Plane 1.51, were obtained from cobra probe traverses, while the static pressure was obtained from 8° static-pressure wedge probe measurements for both undistorted and radial distortion tests. Stator exit total pressure and total temperature were obtained from fixed instrumentation as calculated by the Overall Performance Data Program. Static pressure and flow angle were measured with an angle-seeking static-pressure wedge probe.

When the thermodynamic properties were determined at seven radial positions at each measuring plane, they were transferred along streamlines to the leading and trailing edges of each blade row. As mentioned, the slopes, radii, and streamtube convergence along streamlines between measurement plane and blade edge were assumed to remain fixed at the design values for all flow conditions. The tangential velocity was obtained at the edges of the blades by applying the condition of constant moment of angular momentum along each streamline. The calculated meridional Mach number at the measurement plane was used to determine the meridional Mach number at the blade edge from the streamtube convergence relationship illustrated in Figure 10. This method was a good approximation when the radius change between the blade edge and the measurement plane was small. However, since there was appreciable swirl velocity at the rotor trailing

edge, any large radius changes would adversely affect the approximate results. Table V gives the constants used in these computations for both rotor and stator. With the measured total conditions assumed to be constant along the design streamlines, and the tangential velocities and meridional Mach numbers determined at blade edges in the above manner, the velocities, Mach numbers, and all vector diagram components were determined at the edges of each blade row.

Calculated blade element performance parameters included diffusion factor, static-pressure-rise coefficient, total-pressure-loss coefficient and loss parameter, adiabatic and polytropic efficiency, plus total-temperature and total-pressure ratios. Table VI gives a symbolic listing of these parameters.

Values of rotor and stator total-pressure-loss coefficient and loss parameter and of blade element efficiency were obtained by two different methods. Method 1, which was generally preferred, used the standard vector diagram data obtained from the traversing cobra probe at Plane 1.51 for Mach numbers and velocities. However, this method used the total pressure and total temperature at Plane 1.51 inferred from the fixed rakes at Plane 2.2. The total pressure at each immersion at Plane 1.51 was obtained as the arithmetic average of the three highest readings of total pressure from the corresponding stator exit wake rake. These values were calculated by the Overall Performance Data Program and were used as inputs to this blade element data calculation. Method 2 used the same vector diagram data as Method 1 but with the total pressure and total temperature measured by the traversing cobra probe at Plane 1.51. These stagnation properties measured at Plane 1.51 were taken to represent both rotor exit and stator inlet conditions.

#### c. Circumferential Distortion Data Program

With the nonaxisymmetric flow produced by circumferential inlet flow distortions special procedures were required in order to determine the circumferential variation of vector diagram parameters and to calculate overall performance from fluid properties that had been mass averaged circumferentially as well as radially. At certain operating conditions compressor speed and weight flow were maintained constant, and the distortion screen was rotated to 12 different circumferential positions. Both fixed and traverse instruments were read at each screen position, and the resulting data input to the Circumferential Distortion Data Program.

Stage exit total temperatures and total pressures, measured at Plane 2.20 by wake rakes, were obtained in the form of local mass-averaged values at 10, 30, 50, 70, and 90% immersions at each screen position from the Overall Performance Data Program. Stage exit static pressure and flow angle were measured by a four-parameter traverse probe at Plane 2.20 immersed to the 10, 50, and 90% immersions at each screen position. At Planes 0.95 and 1.51 (the stage inlet and rotor exit planes) total pressures, static pressures, and flow angles were measured at three immersions by four-parameter probes. Rotor exit total temperatures were also obtained from the Plane 1.51 four-parameter probe.

Input data were first corrected for variations in atmospheric conditions by applying temperature and pressure correction factors  $\theta$  and  $\delta$  as determined from the Plane 0.01 data listed in the output of the Overall Performance Data Program for the appropriate screen position. The stage corrected inlet temperature was then assumed constant, equal to  $518.688^\circ R$ . Radial interpolations versus radius were used with the data from the traverse probes to determine fluid properties at the 30% and 70% immersions where traverse data had not been recorded. The circumferential position of each instrument, and thus of each item of measured data, relative to the distortion screen centerline, was then determined. Finally, by linear interpolation versus circumferential position, a value of total temperature, total pressure, static pressure, and flow angle was deduced at 12 standard circumferential positions at each of the 5 radial positions at Planes 0.95, 1.51, and 2.20.

These four fluid conditions, plus the assumption of design streamline slope angle, were sufficient to calculate all vector diagram components at each of the standard points in the flow field. In addition to calculating vector diagram data, the Circumferential Distortion Data Program also used this extensive set of data to calculate an average value of total temperature and total pressure at each measuring station. These were obtained by a mass-averaging procedure which accounted for circumferential as well as radial variations. These average fluid properties were then used to calculate overall performance for the stage and for the rotor as an isolated blade row.

## 6. TEST PROCEDURE

### a. Shakedown Testing with Undistorted Inlet Flow

A shakedown test was conducted with undistorted inlet flow as the initial phase of the Task I Stage testing to demonstrate the mechanical integrity of blading and test vehicle, to check out instrumentation and data reduction procedures, and to determine safe limits of operation. The test procedure employed during the shakedown test was, in general, typical of the procedure followed during the undistorted inlet test phase of the program.

A primary consideration of the shakedown test was to establish the limits of stall-free operation over the range of speeds from 50% to 110% of design. First, the most-open safe throttle setting was determined at each speed. The throttle was then closed slowly until hot-wire anemometer and strain gage signals indicated the formation of rotating stall cells. The radial extent of the stall cells was established from the strength of the signals observed on the three hot-wire anemometer probes located at the rotor exit Plane 1.51 at the 10, 50, and 90% immersions. These probes were used only during stall testing and were removed from the airstream for all other readings. The discharge throttle valve setting and ICPAC\* system weight flow were recorded at

---

\*The ICPAC system (Instantaneous Compressor Performance Analysis Computer) is an analogue circuit which senses weight flow and pressure ratio, and which plots these quantities nearly instantaneously to provide an approximate on-line compressor performance man.

stall. The corrected inlet weight flow at stall was determined from a correlation of ICPAC flow with corrected nozzle flow for all throttle settings at each speed.

Overall performance readings were taken at points near stall, near peak efficiency, and at maximum flow for each speed. Various stator settings, from  $-8^\circ$  open to  $+11^\circ$  closed, were investigated to evaluate their effect on stage and rotor overall performance for the purpose of establishing the optimum stator setting to be used in the remaining Task I testing.

Blade element traverses were obtained at two throttle settings near peak efficiency at 100% speed during the shakedown test. Four traverse probes were immersed to seven radial positions each. The Plane 1.51 static-pressure wedge probe was manually set at the flow angle indicated by the nulled yaw position of the cobra probe at Plane 1.51. The other static-pressure wedge probes, located at Planes 0.95 and 2.20, were flow-angle seeking. An overall performance point was taken immediately before each blade element traverse at the same throttle setting with all probes removed from the airstream.

#### b. Undistorted Inlet Performance Testing

Shakedown test results were used to select the design stator setting for undistorted inlet flow testing. Operating procedures were very similar to those used in the shakedown test, but the emphasis of undistorted inlet testing was on obtaining blade element traverse data at a large number of operating conditions.

After accelerating to a particular speed at the open-throttle position and stabilizing, a blade element traverse reading and the associated overall performance reading were recorded. The discharge throttle valve was then closed to stall, to obtain a repeat check of the stall limit. A point near stall was then selected to obtain overall performance and blade element traverse data. Three additional operating conditions, equally spaced along the speed line between near-stall and open-throttle points, were selected at which to take data. With the completion of the five overall performance and blade element data readings at one speed, the vehicle was accelerated to the next higher speed along a constant throttle line at the maximum flow end of the speed line and the procedure repeated.

Three continuous traverses were conducted at 100% speed to more clearly define the effect of the part-span shroud wake on rotor exit conditions. The cobra probe located at Plane 1.51 was immersed to 36 closely spaced radial positions, and total pressure, total temperature, and flow angle measurements were obtained.

#### c. Undistorted Inlet Testing with Long Inlet Duct

An undistorted inlet test was also conducted to determine the effect of the long inlet duct that was later used for inlet distortion testing on baseline overall performance and stall limits. The long inlet duct was used with the distortion support screen installed but without a distortion screen in place for this test.

The support screen split line was set at  $120^{\circ}$  from top center to allow its wake to pass between the two inlet distortion total-pressure rakes located at  $30^{\circ}$  and  $195^{\circ}$  from top center. The compressor was stalled at 70%, 90%, and 100% speeds. Three overall performance readings were taken at previously tested operating conditions at each speed. A continuous traverse reading at the rotor inlet, Plane 0.95, was obtained at the near-stall point for each speed in order to gain information on stage inlet boundary layer thickness.

d. Radial Distortion Testing

Stall points with radial distortion were established at 70%, 90%, and 100% speeds. Overall performance readings were obtained at maximum flow near stall and an intermediate throttle setting at each speed. Three blade element traverses were taken with radial distortion at 100% speed in conjunction with the overall performance readings taken at that speed.

e. Circumferential Distortion Testing

The circumferential distortion tests were conducted at the same speeds (70%, 90%, and 100%) that were used for radial distortion. The stall limit was determined at each speed. Overall performance data were acquired at three operating conditions - maximum flow, near stall, and an intermediate flow setting at all three speeds.

Three screen rotation tests were conducted at 100% speed with 12 screen positions at each operating point. The circumferential distortion screen centerline was set at a nominal position of  $195^{\circ}$  for the initial reading with all traverse probes retracted. An overall performance reading was taken after stabilization, and then the traverse was conducted with data measured at each of three immersions while the probes were actuated inward. With the probes at their innermost location (90% immersion), the distortion screen was rotated  $30^{\circ}$  to the next position. Conditions were stabilized, and the probes retracted to their outermost (10% immersion) location while data were read at each immersion. An overall performance reading was taken when all probes were removed from the airstream. The screen was then rotated to the next position and the procedure repeated.

## IV. RESULTS AND DISCUSSION

### 1. UNDISTORTED INLET PERFORMANCE

Testing with undistorted inlet flow was conducted during the shakedown test, the undistorted inlet performance test, and during a special test utilizing the long inlet duct (normally used for distortion testing) without an inlet distortion screen installed. Presentation and discussion of the data from these tests appear in the following sections.

#### a. Overall Performance Data

Listings of measured overall performance parameters for the three undistorted inlet tests are given in Table VII(a) - (c). Table VII(a) presents the data obtained during the shakedown testing. One of the major objectives of the shakedown tests was to determine the effect of stator setting on weight flow and efficiency. The results obtained from the tests in which the stator setting angle was varied are discussed in Section IV-1.f. where it is shown that the design stator setting of zero degrees was found to be the best compromise between efficiency and stall margin considerations.

Overall performance data recorded during undistorted inlet performance testing are listed in Table VII(b). All data in this listing were obtained at the design stator setting. Performance maps are presented in Figures 11 and 12 for stage and rotor performance, respectively. The performance of Rotor 1B, as reported in Reference 1, is also shown in Figure 12 for comparison. The predicted stage performance at the stage design point, based on the earlier Rotor 1B test data, is shown in Figure 11. At the design stage pressure ratio at 100% speed, the achieved weight flow was within one percent of the design intent.

The compressor was stalled at least twice at all speeds except 110%; repeatability of the stalling weight-flow values was generally within 1.5 lb/sec (less than 1%). The stall lines shown on the performance maps, Figures 11 and 12, are based on the highest recorded stalling flow at each speed, and thus are conservative. Hot-wire anemometer signals indicated that the rotating stall cells initiated at the rotor tip at all speeds. At all speeds the velocity fluctuations associated with the rotating stall cells were largest at the tip and pitchline and were rather slight near the hub. An intermittent rotating stall was observed at 110% speed at the rotor tip.

#### b. Blade Element Data

Blade element data readings were obtained at five operating conditions at each speed. The readings at which blade element data were obtained are indicated in Table VII(b), which lists the measured overall performance parameters for each reading. Listings of calculated blade element performance quantities for the rotor and the stator blade rows are contained in Appendix D of Volume II (Reference 4). For each radial position a plot of deviation angle, diffusion

factor, total-pressure-loss coefficient, and total-pressure-loss parameter versus incidence angle was prepared containing data from all speeds tested. Figures 13(a)-(g) present these plots for the rotor, and Figures 14(a)-(g) contain similar plots for the stator. Data from Rotor 1B tests at 100% speed are shown in Figures 13(b)-(f) for comparison with the data obtained in the Task I Stage tests.

Stator design data for diffusion factor and deviation angle are shown in Figures 14(a)-(g) for reference. The stator was specifically designed for operating in the Task II stage, as described in Reference 2, but also was made compatible with the Task I Stage. The stator losses therefore were compared with design prediction for operation in the Task II Stage. The loss level generally was consistent with design prediction. The stator loading was also consistent with design intent, and the deviation angles at design speed generally were 1-2° lower than predicted by the design method. Performance of this stator in the Task II Stage is described in Reference 5.

For both the rotor and the stator blade element data, the reported values of loss coefficient, loss parameter, and blade element efficiency were based on total-pressure and total-temperature ratios determined from the discharge wake rakes (Method 1) rather than from the readings of the Plane 1.51 cobra traverse probe (Method 2). The Data Reduction Methods section of this report describes the details of the two data analysis methods. Data reported from Rotor 1B tests were obtained by a procedure similar to Method 1. Inspection of the Method 2 results showed that the traverse probe measurements of total-temperature ratio were higher than the energy input indicated by the vector diagram data and also were inconsistent with both Rotor 1B data and the discharge instrument readings. It was suspected that local throttling caused by the probe itself in the short axial space between rotor trailing edge and stator leading edge was responsible for the high measured temperatures.

### c. Efficiency Loss Due to Part-Span Shroud

The Plane 1.51 rotor exit cobra probe was traversed to 36 radial positions at open throttle, near peak efficiency, and near stall conditions at 100% speed with undistorted inlet flow. Radial profiles of total-pressure ratio, total-temperature ratio, and flow angle were obtained which showed the wall boundary layers and the part-span shroud wake in more detail than was possible from the 7-immersion blade element data traverses. Figure 15 presents plots of these radial profiles; the radial position of the part-span shroud is indicated on the plots. Radial profiles of rotor efficiency at 100% speed [shown in Figures 16(a)-(c) at near peak efficiency, maximum flow, and near-stall weight flow conditions, respectively] indicate substantial losses due to the part-span shroud. Mass-weighted values of rotor efficiency lost because of the shroud were determined from the traverse data plotted in Figure 16. The resulting values represent the total part-span shroud efficiency penalty. Generally, only some of the part-span shroud wake impinged on the fixed stator exit instruments, and thus only part of the total efficiency penalty was actually reflected in the calculated overall performance data. Therefore, the portion of the part-span shroud loss appearing in the overall performance data was

also calculated for both the Task I Stage and the Rotor 1B tests for comparison. The listing below compares total part-span shroud loss in rotor efficiency to the apparent loss as reflected in the overall performance data.

It can be seen that the efficiency levels calculated by the Overall Performance Data Program did not reflect all the shroud loss except at maximum flow, and thus were optimistic by several tenths of a point. Also seen from this comparison is that the shroud loss that did appear in the overall performance calculations was essentially the same for both Task I Stage and Rotor 1B tests at comparable conditions.

TASK I STAGE TESTS					ROTOR 1B TESTS					
Reading Number	Discharge Valve Setting	Weight Flow (Lbs/Sec)	Total Efficiency Loss Due to Shroud (%)	Apparent Efficiency Loss Due to Shroud, in Overall Performance Data (%)	Reading Number (Ref. 1)	Discharge Valve Setting	Weight Flow (Lbs/Sec)	Apparent Efficiency Loss Due to Shroud, in Overall Performance Data (%)	Operating Condition	
25	15	221.9	2.94	3.00	54	15	221.2	3.76	Max. Flow	
27	9	217.2	0.89	0.53	52	11	219.4	0.49	Near Peak Efficiency	
28	6	204.0	0.57	0.37	64	8	204.8	0.44	Near Stall	

d. Comparison of the Performance of the Rotor Operated in the Task I Stage with Its Performance in an Isolated Rotor Configuration (Rotor 1B)

One of the principal objectives of this program was to evaluate the influence of the stator on the performance of this rotor. Figure 12 presents the performance maps for the rotor when operated in the Task I Stage and when operated in an isolated rotor configuration, Rotor 1B. Weight-flow levels with open throttle, where the rotor cascade throat regions determine the flow induction, showed negligible change. Stalling flow at design speed was significantly lower (5%) compared to the isolated Rotor 1B configuration. However, this increased range in the Task I Stage configuration was accompanied by a reduction in the 100% speed peak adiabatic efficiency. Detailed investigation of the data, discussed below, indicated that these two phenomena might be interrelated.

A major area of concern in the analysis of Task I Stage performance with undistorted inlet flow was the reduction in 100% design speed rotor adiabatic efficiency compared to results from previous Rotor 1B tests. As indicated in the rotor performance map, Figure 12, the peak Task I design speed rotor efficiency of 0.880 was apparently reduced 1.8 percentage points below the Rotor 1B value of 0.898. An investigation therefore was made to determine the

validity of the data, to obtain a fully consistent comparison between rotor efficiency values, and to identify the reasons for the deterioration in performance. A careful examination of basic measured data was made for both Task I and earlier Rotor 1B tests to assure that the apparent loss in rotor efficiency was not due to an instrument or data editing problem. No indication of faulty instrument readings could be found in either set of measurements. Thus it was concluded that the measured data were valid, and therefore any discrepancies could only have arisen from differences in data reduction, data sampling methods, or from a real change in rotor efficiency.

An effort was made to determine if the use of 7 radial positions at which measurements were obtained (rather than 5 as in Rotor 1B tests), the different mass-averaging methods used, or other differences in data acquisition or processing could be the reason for the efficiency discrepancy. Task I Stage rotor efficiency was recalculated for 100% speed Readings 27, 29, and 30 using only the measured data at the 10%, 30%, 50%, 70%, and 90% immersions as in Rotor 1B tests and using data calculation methods consistent with those of the Rotor 1B test program, Reference 1. The recalculated Task I rotor adiabatic efficiency values averaged 0.5 percentage point higher than those calculated by the original Task I Stage methods. The conclusion drawn from this exercise was that the obvious differences in data sampling and calculation methods accounted for part, but not all, of the apparent reduction in rotor efficiency. A reduction of 1.3 points in rotor efficiency was still unexplained.

The more subtle question of data sampling was investigated. For the Task I Stage, rotor exit fluid properties at each immersion were actually determined from readings of the stator exit wake rakes. In the Rotor 1B tests, on the other hand, total temperature and total pressure were measured directly behind the rotor. The Task I data therefore were checked to see if anything such as excessively thick stator wakes or large wall boundary layer growth in the stator had caused an error in the efficiency calculations. No evidence of this was found. Plots of Task I stator total-pressure wakes are shown in Figure 17 for 100% speed operation near peak efficiency and near-stalling weight flow. For Reading 27, near peak efficiency, the stator wakes were distinct and did not fill the entire space between adjacent vanes. There was a region of free-stream total pressure at each immersion which could be identified as the rotor exit value. This was also the case near stalling weight flow, except possibly at 90% and 95% immersion, even though the stator wakes were noticeably thicker. In order to properly calculate rotor efficiency, it was not only necessary to identify the free-stream total pressure between stator wakes, but it also was necessary that this free-stream value properly represented the rotor exit condition. Radial profiles of rotor exit total pressure, total temperature, and rotor adiabatic efficiency are shown in Figure 18 at 100% speed near peak efficiency. Measurements obtained from a traverse probe at the rotor exit are compared to those from the stator exit wake rakes. Wall boundary layers at the rotor exit, Plane 1.51, are clearly shown by the traverse data. The absolute magnitudes of each quantity plotted differ, due to instrumentation accuracy, but generally excellent agreement in profile shape can be seen. There was no indication of large secondary flows or wall boundary

layer separations in the stator that could have reduced the free-stream total pressure and caused an erroneously low rotor efficiency to be calculated from the stator exit wake rake readings.

The possibility of errors in total temperature measurement caused by a wake sampling problem was investigated. Circumferential variations in total temperature measured by the stator exit wake rakes are shown in Figure 19 for 100% speed operation near peak efficiency and near stall. These variations are due to rotor wakes accumulating against the stator pressure surfaces, as explained in References 6 and 7. Since total temperature at each immersion was obtained for a circumferential mass average across a stator vane spacing, the temperature variations shown in Figure 19 were properly accounted for. Assuming that the total temperatures used to calculate the Rotor 1B data were valid (these were measured by rakes located in the unsteady flow field approximately two chord lengths downstream of the rotor), then it was concluded that total-temperature sampling difficulties were not responsible for the difference in rotor efficiency.

The part-span shroud losses at peak rotor efficiency condition for Task I configuration and Rotor 1B configuration were presented in the section on part-span shroud losses. It was shown in the previous section that part-span shroud loss appearing in the overall performance calculations for the two tests were essentially identical at this condition. Thus, none of the 1.3 percentage points difference in peak rotor efficiency was caused by differences in part-span shroud wake sampling.

Figure 16(a) contains comparisons between Task I and Rotor 1B adiabatic efficiency data obtained from both fixed instrument and traverse probe readings at 100% speed near peak efficiency. Figures 16(b) and 16(c) show traverse and fixed instrument data for Task I and fixed instrument data for Rotor 1B at 100% speed near stall and at maximum flow. It can be seen that good agreement exists in the outer part of the annulus between data obtained in the two test configurations. However, at the peak efficiency condition, Figure 16(a), both fixed instrument and traverse probe data show that the rotor efficiency near the hub was substantially less in the Task I configuration than in the Rotor 1B configuration. The same trend is seen also at the near-stall condition, Figure 16(b). However, at the open-throttle condition, Figure 16(c), there was good agreement between the two sets of fixed Task I and Rotor 1B instrument data at the hub as well as near the tip. At the peak efficiency operating condition, shown in Figure 16(a), the decrease in blade element efficiency at 70% and 90% immersions, when mass averaged as in a 5-immersion overall performance calculation, was sufficient to account for the 1.3 percentage point efficiency discrepancy indicated by a valid and consistent comparison of overall performance data.

Further evidence of reduced hub performance can be seen in Figures 20 through 22 in which radial profiles of rotor and stator total-pressure-loss coefficients, diffusion factors, and axial velocities at 100% design speed near the peak efficiency operating condition of the Task I Stage are compared to Rotor

1B test data or to stator design values. Near the hub the Task I Stage axial velocities were less than anticipated, and the aerodynamic loadings were somewhat larger than expected from Rotor 1B test data or design predictions. Stator losses at the 70% and 90% immersions were nearly equal to design intent, but rotor relative total-pressure-loss coefficients were substantially higher than Rotor 1B test data.

The increased aerodynamic loading at the hub of the rotor may be due to two factors. First, the curvature of the hub wall contour just aft of the rotor trailing edge was reduced when the stators were added to the Rotor 1B test vehicle to form the Task I Stage. A comparison of Task I Stage and Rotor 1B flowpaths is shown in Figure 1. The reduced hub curvature would not accelerate the hub flow as strongly and thus would tend to reduce the hub axial velocities. Second, the total pressure at the hub was less than that at the tip, and thus there was a low hub axial velocity at the stator exit station after all the swirl had been removed from the flow. The low stator hub exit axial velocity may have forced the flow to be redistributed in such a way as to reduce the rotor exit hub axial velocity below the level measured in Rotor 1B tests. The large increase in rotor hub losses, however, cannot be explained solely by the relatively moderate changes in rotor hub exit axial velocity. The rotor relative total-pressure-loss coefficient at the 90% immersion is larger in the Task I Stage than in the Rotor 1B test data when compared at the same incidence, at the same diffusion factor, at the same static-pressure-rise coefficient, or at the same axial velocity ratio. Thus it can only be speculated that slight changes in the flow caused by the change in flowpath and the addition of the stators near the rotor trailing edge induced a major change in the flow near the rotor hub, such that these blade elements had much different loss characteristics even under the same conditions. A large-scale secondary flow pattern in the rotor or a hub wall separation might be responsible, but neither of these can be identified from the available data.

An analysis of test results was also made in order to determine why the unstalled weight flow range at high speed was greater in the Task I Stage than in the Rotor 1B isolated rotor configuration, as shown in Figure 12. At 100% design speed, for example, the stalling weight flow was reduced from 197 lbs/sec to 187 lbs/sec. A displacement of the flow from the hub toward the tip that was produced by the flowpath changes, addition of stator vanes, and the deteriorated rotor hub performance is believed to have caused the improvement in stall limits, while at the same time causing the efficiency penalty discussed earlier.

The stator hub axial velocity experienced a large reduction as the compressor was throttled toward stall, as shown in Figure 23. Concurrently, the rotor hub axial velocities were reduced below Rotor 1B levels, as shown in Figure 24. Rotor tip axial velocity was increased above the Rotor 1B value at the same operating condition as the flow was shifted outward. Variations of rotor and stator axial velocities, aerodynamic loadings, loss coefficients, and total-temperature and total-pressure ratios with weight flow are shown in Figure 25 for the 10% and 90% immersions. Rotor 1B test data are given in this figure for comparison. The deterioration of the flow and general performance near the

hub as weight flow was reduced can be seen in these characteristics. At the tip, the characteristics shown in Figure 25(c) indicate that the flow shift to the tip increased the axial velocities, reduced the work input and the total-pressure losses, and in general resulted in lower aerodynamic loadings. This process apparently was sufficient to delay the onset of rotating stall at the rotor tip until considerably lower weight flows were reached than was possible in Rotor 1B testing at 100% speed.

e. Effect of the Long Inlet Duct Used for Distortion Testing on the Compressor Performance

An undistorted inlet test was conducted to determine the effect of the long inlet duct, inlet distortion instrumentation, and support screen used for inlet distortion testing on the baseline stall limits and efficiency of the compressor. Overall performance data recorded during this test are tabulated in Table VII(c). The test was run in poor weather conditions, which resulted in some ice accumulation on the support screen and inlet distortion total-pressure rakes. The performance data were recalculated after editing out those inlet total pressure measurements which seemed to have been affected by the ice. Inlet total-temperature measurements apparently were not affected. Table VII(c) contains the corrected data only.

The compressor stage performance is displayed on the performance map for this test, Figure 26. Task I Stage overall performance from undistorted inlet performance tests (with the short inlet ducting, Figure 11) is also shown for comparison in Figure 26. These results indicated that stage efficiency may have been reduced at lower speeds, but not at 100% speed. The stall limits at 70% and 90% speeds were unaffected, but at 100% speed rotating stall originated at 192 lbs/sec weight flow instead of 187 lbs/sec. The reduction in 100% speed unstalled weight flow range was greater than could be explained as being due to experimental accuracy or repeatability, but was not typical of all speeds, and thus was not considered as evidence of a major deterioration in stall limits.

The inlet casing boundary layer was surveyed near stalling weight flow at 100% speed using the four-parameter traverse probe located at Plane 0.95. The measured radial variation of total pressure is shown in Figure 27, compared to results of a similar survey made during Rotor 1B tests with the short inlet duct. The long inlet duct and the pressure of the distortion support screen caused only a slight increase in the inlet casing boundary layer thickness.

In general, the conclusions drawn from this brief test were that the long inlet ducting, the distortion support screen, and the use of distortion instrumentation had only small effects on compressor efficiency and stall limits.

f. Investigation of Stator Setting Angle Effects

Overall performance readings were recorded during the shakedown test, Table VII (a), at 100% design speed to determine the effect of stator setting on weight flow and adiabatic efficiency. A series of data points near peak efficiency, Readings 11 through 15 and Reading 19, was recorded with stator

stagger angles set as low as  $8^\circ$  less than design and up to  $11^\circ$  greater than design at a constant throttle valve setting. Weight flow appeared to be constant within data repeatability, except at the extreme ( $+11^\circ$ ) setting where high loss at negative incidence restricted the flow. Stage adiabatic efficiency varied by approximately two points over the range of stator settings investigated; peak efficiency of 0.855 was recorded in Reading 15 at a stator stagger  $8^\circ$  higher than design. Efficiency at design stator setting, Reading 13, was 0.836. The compressor was stalled at 100% speed with the stators set at  $-3^\circ$ ,  $0^\circ$ , and  $+8^\circ$ ; minimum stalling weight flow was obtained at the design stator setting,  $0^\circ$ . The variation of corrected weight flow and of rotor and stage adiabatic efficiencies with stator setting angle at a constant throttle valve setting is presented in Figure 28. The stalling weight flows at the stator settings of  $-3^\circ$ ,  $0^\circ$ , and  $+8^\circ$  are also shown in this figure.

Based on the results shown in Figure 28, and considering the scatter in the efficiency data, it was decided that the design stator setting gave the best compromise between stage efficiency and unstalled weight flow range. Thus the remainder of the test program was conducted with the stator set at the design stagger angle. Data obtained later in the program at design stator stagger gave stage efficiencies of over 0.85 (within one point of the maximum value shown in Figure 28, 0.855 at a setting angle of  $8^\circ$ ), verifying that selection of the design setting was an appropriate choice.

## 2. PERFORMANCE WITH TIP-RADIAL INLET FLOW DISTORTION

### a. Overall Performance Data

Performance data from tests with a radial inlet distortion pattern covering the outer 40% of the annulus area were obtained at 70%, 90%, and 100% of design corrected speed. Table VII(d) contains a listing of overall performance parameters for this test. The Task I Stage performance map with radial inlet flow distortion is shown in Figure 29. Performance of the stage with undistorted inlet flow is also given in this figure for comparison. The performance map for the Task I rotor with radial distortion is compared to the Task I rotor undistorted inlet performance and to the Rotor 1B performance with radial distortion in Figure 30.

Rotating stall was encountered at each speed. As in earlier Rotor 1B tests, hot-wire anemometer signals recorded at the inception of rotating stall indicated that the outer 50% of the rotor span was the stall-limiting blading. The Task I rotor stall line with radial inlet flow distortion was noticeably improved over that achieved in Rotor 1B tests, even though the distortion screens were made of the same material in each case. The improvement in stall limits may have been due to the addition of stators to form the Task I Stage. The stators are believed to be mainly responsible for the improved stall limits with undistorted inlet flow, and could have had a somewhat similar favorable effect with radial distortion. It could also have been possible that by locating the distortion screen approximately two feet farther forward, the severity of the inlet flow distortion may have been reduced enough to increase the

rotor stall limits. The variation of the distortion parameter,  $(P_{\max.} - P_{\min.})/P_{\max.}$ , with weight flow is shown in Figure 31 for the Task I Stage radial and circumferential distortion tests. It can be seen that the highest value of the distortion parameter reached in the radial distortion was approximately 0.18, which was noticeably less than the value of 0.20 reported in Reference 1 for the Rotor 1B test.

#### b. Blade Element and Vector Diagram Data

Listings of blade element and vector diagram data obtained at 100% speed with radial inlet flow distortion are given in Volume II, Appendix E (Reference 4) for both rotor and stator. Radial variations of measured fluid properties and calculated axial velocities are given in Figure 32 for operation at 100% speed near stall. The severity of the inlet distortion can be seen in the large deficiencies in inlet total pressure and inlet axial velocity near the tip. It can also be seen that the total-pressure distortion is fully attenuated, and in fact the total pressure is greater at the tip than at the hub at the stator exit.

Figure 32 also gives a comparison between wall static pressures from static taps and stream values obtained from traverse probes. Agreement is acceptable at the tip, but is poor at the hub at Planes 0.95 and 1.51 where the wall slopes were substantial. Although some amount of inaccuracy in the vector diagram data resulted from this measurement problem, the radial distortion data are internally consistent and allow valid comparisons to be made between various operating conditions in this test.

Values of total-pressure-loss parameter, loss coefficient, and deviation angle are plotted versus diffusion factor for each immersion in Figures 33 and 34 for rotor and stator, respectively. These figures compare data obtained with radial inlet flow distortion to 100% speed data obtained with undistorted inlet flow. Better agreement between undistorted inlet and radial distortion blade element data was obtained by plotting these data against diffusion factor rather than by plotting versus incidence angle. Rotor total-pressure-loss coefficient data calculated from both rotor exit traverse probe readings (Method 2) and from stator exit fixed instrument readings (Method 1) are shown in Figure 33. The agreement with the undistorted inlet data at the same diffusion factor is generally good in terms of the trend of the data and acceptable with respect to level. The rotor total-pressure-loss coefficients calculated from Plane 1.51 traverse probe readings generally gave the best agreement with undistorted inlet data, probably because these instruments were closest to the rotor and thus least affected by flow shifts that were inconsistent with the assumption of design streamline locations. Stator total-pressure-loss parameter and loss coefficient values shown in Figure 34 were calculated using only the readings from fixed discharge instruments (Method 1), and showed very good agreement with the undistorted inlet data. Deviation angles for both the rotor and the stator measured with radial inlet flow distortion also agreed very well with undistorted inlet data at the same diffusion factor.

### c. Analysis of Stall Limits with Radial Distortion

As mentioned above, rotating stall originated at the tip of the rotor during tip radial inlet flow distortion tests. The rotor tip was the stall limiting blading in undistorted inlet flow tests as well; and, therefore, an analysis was made to determine if the aerodynamic loading of the rotor tip at stall was dependent on the type of inlet flow. The variation of rotor total-temperature ratio, diffusion factor, and static-pressure-rise coefficient with discharge throttle valve setting are shown in Figure 35 for 5% and 10% immersions with both radial distortion and undistorted inlet flow. An attempt to extrapolate these values to stall has been made in the figure. It can be seen that with radial distortion the stalling tip work input was the same as with undistorted inlet flow, but diffusion factors and static-pressure-rise coefficients were slightly higher. The differences in stalling aerodynamic loading were not large, however, and it appears that for this compressor the maximum rotor tip loading did not depend upon the type of inlet flow regime.

Although the aerodynamic loading at the rotor tip was approximately the same with both radial distortion and undistorted inlet flow near stall, the conditions at other parts of the span were much less severe with radial distortion. The unloading of the rotor hub can be seen in Figure 36 which gives a comparison of radial profiles of rotor aerodynamic loading quantities near stall.

## 3. PERFORMANCE WITH CIRCUMFERENTIAL INLET FLOW DISTORTION

### a. Overall Performance Data

Overall performance was determined at 70%, 90%, and 100% speeds with circumferential inlet flow distortion. The pattern covered 90° of the circumference from hub to tip and had a value of the distortion parameter, as shown in Figure 31, equal to approximately 0.15 at design speed near stall. Stall limits were identified at each speed, and data were recorded near stalling weight flow, at maximum flow and at an intermediate flow. A listing of overall performance parameters for this test is given in Table VII(e).

Performance maps for the stage and for the rotor alone are shown in Figures 37 and 38, respectively. Task I Stage performance with undistorted inlet flow is shown in each figure for comparison, and Rotor 1B circumferential distortion performance is also shown in Figure 38. Rotating stall was encountered at each speed. Hot-wire anemometer signals recorded at the inception of rotating stall indicated that stalls originated in the outer 50% span of the rotor blades. A greater unstalled weight flow range was obtained during the Task I Stage circumferential distortion testing than in previous Rotor 1B tests, and no intermittent stall was observed as had been the case during Rotor 1B isolated blade row tests. The increased stall limits were believed to be due either to a favorable effect of the stator on rotor tip section distortion tolerance, on a lower level of distortion, or on less angularity in the flow, both of these latter due to placing the distortion screen farther ahead of the rotor.

Overall performance data were recorded for Readings 84 through 92, listed in Table VII(e), with the center of the distortion pattern placed at 195° from top center, aft looking forward, in order to be aligned with one of the inlet distortion total pressure rakes. Due to the limited sampling of data obtained during single readings taken with the distortion screen in this nominal position, the Overall Performance Data Program calculated somewhat inaccurate average values of fluid properties and overall performance parameters for circumferentially distorted flow. In order to obtain data more representative of actual flow conditions, overall performance and traverse data were obtained at 12 screen positions for each of three operating points as described in the Test Procedure section. The screen rotation test data were processed using the Circumferential Distortion Data Program to obtain circumferentially as well as radially mass-averaged stage inlet and exit total pressures and stage exit total temperatures. A correlation was then made between the average properties calculated in this manner and the corresponding properties obtained from single overall performance readings at the nominal distortion screen position. Results obtained using Readings 93-104, at a discharge valve setting of 9.6, were correlated with data from Readings 91 and 105 taken at the same discharge valve setting but with the screen at the nominal position. Similarly, results obtained using Readings 106-117 were correlated with data from Readings 90 and 118, and results obtained using Readings 119-130 were correlated with data from Readings 92 and 131. A set of average correction factors was obtained for stage pressure ratio and discharge total temperatures. These correction factors were then applied to Readings 84-89 for which no screen rotation tests were performed and new overall performance parameters were calculated. Data appearing in Table VII(e) have been adjusted in this manner. Both the original and adjusted efficiency and total-pressure ratio data are plotted in Figures 37 and 38. It can be seen that the adjusted efficiency data were much more realistic than the original values computed by the Overall Performance Data Program.

#### b. Flow Survey Data

Fluid properties and vector diagram data obtained during screen rotation tests at 100% speed are tabulated in Appendix F of Volume II (Reference 4). These data were calculated by the Circumferential Distortion Data Program described in the Data Reduction Methods section of this report. Plots of the circumferential variations of key measured and calculated quantities appear in Figures 39 and 40 for the near-stall and maximum-weight-flow conditions, respectively.

Hub and casing wall static pressures measured by wall static taps are presented along with the static pressure measured by the traverse probe at the rotor inlet, Plane 0.95, in Figures 39(a) and 40(a). It can be seen that the traverse measurements did not agree with the measurements of the wall static taps, particularly at the hub. The wall static pressure readings were believed to be the more accurate, but the vector diagram data were automatically calculated by the computer program using the stream static-pressure traverse readings. The rotor inlet vector diagram data are thus questionable in terms of absolute accuracy, but are internally consistent and should allow valid comparisons of the flow conditions at various circumferential positions to be made. Better

agreement was obtained between traverse static pressure and wall static pressure readings at the other measuring stations where probe inaccuracies due to wall slope were less likely to be encountered. Only the traverse static pressure data, which were used to calculate vector diagrams, were therefore plotted for the rotor exit and stator exit stations.

The circumferential plots shown in Figures 39 and 40 show that the compressor tip attenuated the inlet distortion at both operating conditions. At maximum weight flow, Figure 40, the distorted inlet region appeared as a total-pressure deficiency at the stator exit having a distortion parameter  $[(P_{\max.} - P_{\min.})/P_{\max.}]$  only 0.676 of that existing at the rotor inlet. Near stall, Figure 39, the tip distortion parameter at the stator exit was 0.768 of that at rotor inlet but, in this case, the inlet distortion appeared as a region of higher-than average total pressure at the compressor exit. The inlet distortion at the hub appeared in all cases as a region of low discharge total pressure; the discharge distortion parameter was 1.204 times the value at the inlet for maximum weight flow operation and was 1.402 times the inlet value near stall. The discharge hub axial velocity near stall was virtually stagnated in the distorted region at a circumferential position of 190°, Figure 39(c). The hub axial velocity at the rotor exit station, Figure 39(b), was not reduced so drastically, however, indicating that much of the hub distortion amplification was caused by separated flow in the stator.

### c. Analysis of Performance with Circumferential Distortion

The response of the compressor to the severe variations in inlet axial velocity and flow angle was very complex and showed large variations from hub to tip and from one throttle setting to another. An analysis therefore was performed following a stage characteristic approach, in order to condense the data and to reveal significant performance trends.

The procedure used was to compute a flow coefficient and a work coefficient, containing correction factors for the effects of inlet swirl and axial velocity change, at numerous circumferential positions at each radius. The resulting corrected characteristics were compared to blade element characteristics calculated from undistorted inlet data. The conventional flow coefficient.

$$\varphi = V_{z_1} / U_1$$

is related to the rotor inlet relative and absolute air angles by:

$$\tan \beta'_1 = \frac{1}{\varphi} - \tan \beta_1$$

The corrected flow coefficient,  $\varphi_0$ , is defined as that necessary to produce the actual  $\beta'_1$  if there were no inlet swirl rather than the actual, nonzero value of  $\beta_1$ . Therefore, with the corrected value of  $\beta_1$  equal to zero and with the value of  $B_1'$  held constant, the above equation gives:

$$\varphi_0 = \varphi / (1 - \varphi \tan \beta_1)$$

The conventional work coefficient defined below is related to the flow coefficient by the usual turbomachinery equation:

$$\Psi = g j c_p \Delta T / U_i^2 = \left( \frac{r_2}{r_1} \right)^2 - 1 + \varphi (\tan \beta'_1 - \frac{r_2}{r_1} \frac{V_{Z_2}}{V_{Z_1}} \tan \beta'_2)$$

The work coefficient corrected for inlet swirl,  $\Psi_o$ , is defined as that which would be obtained when operating at the corrected flow coefficient: that is, operation with zero inlet swirl but with the actual values of  $\beta'_1$ ,  $\beta'_2$ , and axial velocity ratio. Thus, if  $r_2/r_1 \approx 1$ , the above equation leads to:

$$\Psi_o = \Psi \frac{\varphi_o}{\varphi}$$

In a given high-speed compressor, if work input is changed by a change in inlet swirl, the axial velocity ratio will change because of compressibility. The turbomachinery equation given above shows that a change in axial velocity in itself produces a further change in work input. Thus, the work coefficient corrected for axial velocity is defined as that existing if  $V_{Z_2}/V_{Z_1} = 1.0$ , but at the actual values of  $\beta'_1$  and  $\beta'_2$ :

$$\Psi_{cor} = \left( \frac{r_2}{r_1} \right)^2 - 1 + \varphi (\tan \beta'_1 - \frac{r_2}{r_1} \tan \beta'_2)$$

or,

$$\Psi_{cor} = \Psi + \frac{r_2}{r_1} \varphi \tan \beta'_2 \left( \frac{V_{Z_2}}{V_{Z_1}} - 1 \right)$$

The inlet swirl correction can also be made to  $\Psi_{cor}$ , so that:

$$(\Psi_{cor})_o = \Psi_{cor} \frac{\varphi_o}{\varphi} = \frac{\varphi_o}{\varphi} \left[ \Psi + \frac{r_2}{r_1} \varphi \tan \beta'_2 \left( \frac{V_{Z_2}}{V_{Z_1}} - 1 \right) \right]$$

The Task I Stage circumferential distortion data were reduced to obtain values of the work coefficients and flow coefficients derived above. In order to associate a rotor exit total temperature with an inlet axial velocity and swirl angle, the circumferential displacement of fluid particles entering the rotor at various circumferential locations was estimated from the inlet and exit flow angles. The fluid particles were assumed to follow design stream-surfaces in the meridional plane.

Because poor static pressure traverse data were obtained at the rotor inlet station, the axial velocities shown in Figures 39 and 40 were inconsistent with undistorted inlet data. The axial velocities therefore were recalculated for this analysis using traverse static pressure profiles adjusted to be consistent with wall static pressure readings. This resulted in better agreement with undistorted inlet data. Rotor exit axial velocities based on static pressure traverse data, as shown in Figures 39 and 40, were of acceptable accuracy for use in calculating the corrected work coefficient data.

The values of  $\beta_2'$  were taken to be those obtained at 100% speed near the stage design point with undistorted inlet flow. These values were used to compute all the corrected work coefficient data for both circumferential distortion and undistorted inlet test points. This procedure reduced the methods reliance upon traverse data obtained at the rotor exit station, and was found to reduce scatter in the data. The radius ratio term in the work coefficient was evaluated based on streamline radii at the measuring stations at rotor inlet and exit.

Figures 41, 42 and 43 present corrected and uncorrected characteristics curves for tip, pitch, and hub blade elements, respectively. All data shown are for 100% speed operation, and both the maximum weight flow and the near stalling flow operating conditions are shown. Similar data for 100% speed operation with undistorted inlet flow are also shown for comparison. The circumferential locations at which the fluid element crossed the rotor inlet measuring plane are listed for each data point on these figures; these locations correspond to the circumferential positions at Plane 0.95 in Figures 39(a) and 40(a) at which the rotor inlet fluid properties can be found.

The characteristic data for the 10% immersion are shown in Figures 41(a) through 41(c). The uncorrected data, shown in Figure 41(a), show the large variations in operating conditions experienced by this blade element at various points around the circumference. Comparison of Figures 41(a) and 41(b) shows that the data in the latter figure, corrected for inlet swirl, have somewhat less scatter and agree somewhat more closely with undistorted inlet data. Tip data corrected for axial velocity ratio as well as inlet swirl are presented in Figure 41(c). This correction has further reduced the scatter in the data. The corrected tip element characteristic data with circumferential inlet flow distortion can be seen in Figure 41(c) to be consistent with the undistorted inlet flow data once the effects of inlet swirl and axial velocity ratio have been accounted for.

Similar sets of uncorrected and corrected characteristics curves are shown in Figures 42 and 43, for the 50% and 90% immersions. These figures show that at the pitch immersion, as at the tip, the correction factors were capable of collapsing the data into a band that could be identified as an average characteristic. The hub data, however, could not be collapsed into a tight enough band to identify an average curve. In general, it was demonstrated that the characteristic method employed was able to account for the effects of inlet swirl successfully, but that the axial velocity correction required more accurate data to be used successfully at all immersions.

The characteristics data for near-stall conditions indicate that operation was possible in the distorted region of the annulus at points on both the uncorrected and corrected characteristics that were not reached with undistorted inlet flow without encountering rotating stall. It is also significant that the corrected curves do not show any systematic evidence of local stalling and subsequent recovery along a hysteresis path. The eventual appearance of rotating stall is difficult to explain, since there was a large portion of the annulus in which incidence and loading levels never approached the undistorted inlet stalling values. Conventional aerodynamic loading or stalling incidence angle concepts do not appear to be able to predict these results. It can only be speculated that the ability of the blading to operate at incidence angles and loadings greater than the undistorted inlet limiting values may be due to the time-unsteady nature of the flow relative to the rotor. The rotor blades generally experienced these adverse conditions only in the region from  $160^\circ$  to  $260^\circ$ , which correspond to an exposure time of only 0.0023 second at design speed. Somewhat more time was spent by the rotor in the region from  $340^\circ$  to  $120^\circ$  where the loadings were very low. These times should be compared to the time of approximately 0.0006 second taken by a fluid particle to pass through the rotor.

## V. CONCLUSIONS

1. The Task I Stage demonstrated an acceptable performance level using a new stator following Rotor 1B.
2. A generally detrimental rotor-stator interaction at the hub was believed to be responsible for a decrease in rotor hub efficiency compared to results of previous isolated rotor tests. Another contributor to this may have been a reduction in rotor hub trailing edge flowpath curvature made when the stators were added.
3. The deterioration in stage hub performance shifted flow to the tip and reduced rotor tip aerodynamic loadings. The result was an increase in design speed stall margin through greater weight flow range. Large weight flow range due to weak hub flow is not uncommon in single-stage fans, but may not be usable in a multistage compressor because of the adverse effect produced upon succeeding stages.
4. Although severe reductions in stalling total-pressure ratio and in weight flow range were produced by a tip radial inlet flow distortion, the stall-limiting rotor tip aerodynamic loading compared well with undistorted inlet flow data. It was also determined that blade element data obtained both with radial inlet flow distortion and with undistorted inlet flow correlated reasonably well at the same speed and diffusion factor.
5. With circumferential inlet flow distortion, the nonuniform work input of the rotor tip section, caused by variations in inlet axial velocity and swirl, was shown to be consistent with undistorted inlet data on a blade element characteristic basis. The unstalled range of operation along the characteristic was much greater in the case of distorted inlet flow operation than with undistorted inlet flow.

#### REFERENCES

1. Seyler, D.R. and Gostelow, J.P.: Single Stage Experimental Evaluation of High Mach Number Compressor Rotor Blading, Part 2, Performance of Rotor 1B, NASA CR-54583, September 22, 1967.
2. Doyle, V.L. and Koch, C.C.: Evaluation of Range and Distortion Tolerance for High Mach Number Transonic Stages, Design Report NASA CR-72720, July 23, 1970.
3. Seyler, D.R. and Smith, L.H., Jr.: Single Stage Experimental Evaluation of High Mach Number Compressor Rotor Blading, Part 1, Design of Rotor Blading, NASA CR-54581, April 1, 1967.
4. Koch, C.C., Bilwakesh, K.R., and Doyle, V.L.: Evaluation of Range and Distortion Tolerance for High Mach Number Transonic Fan Stages, Task I Stage Final Report, Volume II, NASA CR-72964, August 1971.
5. Bilwakesh, K.R.: Evaluation of Range and Distortion Tolerance for High Mach Number Transonic Fan Stages, Task II Stage Data and Performance Report for Undistorted Inlet Flow Testing, NASA CR-72787, January 1971.
6. Kerrebrock, J.L. and Mikolajczak, A.A.: Intra-Stator Transport of Rotor Wakes and Its Effect on Compressor Performance, ASME, Paper No. 70-GT-39, 1970.
7. Sulam, D.H., Keenan, M.J., and Flynn, J.T.: Single Stage Evaluation Of Highly-Loaded High-Mach-Number Compressor Stages, II. Data and Performance - Multiple-Circular-Arc Rotor, NASA CR-72694, 1970.

## APPENDIX A

## SYMBOLS

Symbol	Description	Units
A	Annulus or streamtube area	in. <sup>2</sup>
a	Length along chord line to location of maximum displacement between camber line and chord line	in.
C	Chord length of cylindrical section	in.
$C_h$	Enthalpy - equivalent static-pressure-rise coefficient:	
$C_p$	$C_h = \frac{2gJ c_p t_1 \left[ \left( \frac{p_2}{p_1} \right)^{\frac{\gamma-1}{\gamma}} - 1 \right]}{V_1'^2} - (U_2^2 - U_1^2)$	---
$C_p$	Static-pressure-rise coefficient:	
$C_p$	$C_p = \frac{p_2 - p_1}{p_1' - p_1}$	---
$c_p$	Specific heat at constant pressure	Btu/lb-° R
D	Diffusion factor:	
$D_{rotor}$	$D_{rotor} = 1 - \frac{V_2}{V_1'} + \frac{r_2 V_{\theta 2} - r_1 V_{\theta 1}}{2 \bar{r} \sigma V_1'}$	---
$D_{stator}$	$D_{stator} = 1 - \frac{V_2}{V_1} + \frac{r_1 V_{\theta 1} - r_2 V_{\theta 2}}{2 \bar{r} \sigma V_1}$	---
g	Acceleration due to gravity	32.174 Ft/Sec <sup>2</sup>
i	Incidence angle, difference between flow angle and camber line angle at leading edge in cascade projection	Degrees
	$\alpha$ $\beta$ $\gamma$ $\delta$ $\psi$	

Symbol	Description	Units
$i_{SS}$	Suction surface incidence angle, difference between flow angle and leading edge suction surface	Degrees
J	Mechanical equivalent of heat	778.161 Ft-Lb/Btu
M	Mach number	---
N	Rotational speed	RPM
P	Total or stagnation pressure	PSIA
p	Static pressure	PSIA
r	Radius	In.
$\bar{r}$	Mean radius, average of streamline leading-trailing edge radii	In.
T	Total or stagnation temperature	$^{\circ}$ R
$\Delta T$	Total temperature rise	$^{\circ}$ R
t	Static temperature	$^{\circ}$ R
$t_e$	Airfoil edge thickness	In.
$t_m$	Airfoil maximum thickness	In.
U	Rotor speed	Ft/Sec
V	Air velocity	Ft/Sec
W	Weight flow	Lbs/Sec
Z	Displacement along compressor axis	In.
$\beta$	Flow angle, angle whose tangent is the ratio of tangential-to-axial velocity	Degrees
$\Delta\beta$	Air-turning angle, $\Delta\beta = \beta_1 - \beta_2$	Degrees
$\gamma^{\circ}$	Blade-chord angle (stagger), angle in cascade projection between blade chord and axial direction	Degrees
$\gamma$	Ratio of specific heats	---
$\delta^{\circ}$	Deviation angle, difference between flow angle and camber-line angle at trailing edge in cascade projection	Degrees

Symbol	Description	Units
$\delta$	Pressure correction, $\frac{P_{actual}}{14.696 \text{ PSIA}}$	---
$\epsilon^\circ$	Slope of meridional streamline	Degrees
$\theta$	Temperature correction, $\frac{T_{actual}}{518.7^\circ \text{ R}}$	---
$\theta^\circ$	Circumferential position from top center	Degrees
$\eta$	Efficiency	---
$\kappa^\circ$	Angle between tangent to blade meanline and the axial direction	Degrees
$\sigma$	Solidity, ratio of chord to spacing	---
$\Phi^\circ$	Camber angle, difference between angles in cascade projection of tangents to camber line at extremes of camber-line arc	Degrees
$\varphi$	Flow coefficient	---
$\psi$	Work coefficient	---
$\bar{w}$	Total-pressure-loss coefficient:	
Rotor, $\bar{w}'$	$\bar{w}' = \frac{P_{2'ad} - P_{2'}^i}{P_{1'}^i - P_1}$	---
Stator, $\bar{w}$	$\bar{w} = \frac{P_1 - P_2}{P_{1'}^i - P_1}$	---
$\frac{\bar{w} \cos \beta_2}{20}$	Total-pressure-loss parameter	---

#### Subscripts

ad	Adiabatic
an	Annulus
cor	Corrected to unity axial velocity ratio
d	Downstream measurement plane (Table V)

<u>Subscripts</u>	<u>Description</u>
e	Edge of blade (Figure 10)
h	Hub
id	Ideal
j	Immersion
m	Meridional direction
p	Polytropic
S	Measurement plane (Figure 10)
SS	Suction surface
t	Tip at Station 1.0
u	Upstream measurement plane (Table V)
z	Axial direction
$\theta$	Tangential direction
o	Corrected to zero inlet swirl
l	Leading edge
	Trailing edge
0.01, 0.18, 0.95, 1.51, 2.20	Measurement station designations (Figures 7 and 8)

#### Superscripts

- ' Relative to rotor
- \* Critical flow condition

Table I. Summary of Task I Stage and Blade Row Design Parameters.

Parameter	Task I Stage Design
Rotor inlet corrected tip speed, Ft/Sec	1400
Stage inlet corrected weight flow, Lbs/Sec	219.4
Stage total-pressure ratio	1.617
Stage adiabatic efficiency	0.873
Rotor inlet tip diameter, In.	36.5
Rotor inlet hub/tip radius ratio	0.5
Rotor inlet corrected weight flow per unit annulus area, Lb/Sec-Sq Ft	40.25
Rotor inlet tip relative Mach number	1.414
Rotor tip diffusion factor	0.382
Rotor total-pressure ratio	1.636
Rotor adiabatic efficiency	0.8915
Rotor tip solidity	1.3
Rotor aspect ratio	2.5
Number of rotor blades	44
Stator inlet hub absolute Mach number	0.684
Stator exit flow angle, Degrees	0
Stator hub diffusion factor	0.474
Stator total-pressure loss, percent stator inlet total pressure	1.17
Stator hub solidity	2.155
Stator aspect ratio	2.065
Number of stator vanes	46

Table II. Cascade Projection Data for Rotor 1B.

Streamline	$\frac{r_1}{r_t}$	$\kappa_1^\circ$	$\kappa_{SSL}^\circ - \kappa_1^\circ$	$\frac{t_{el}}{C}$
1	0.9955	61.88	2.46	0.0060
2	0.9586	60.06	2.91	0.0063
3	0.9202	58.47	3.41	0.0066
4	0.8807	56.94	4.03	0.0069
5	0.8388	55.37	4.75	0.0072
6	0.7947	53.81	5.47	0.0076
7	0.7473	52.00	5.98	0.0080
8	0.6963	50.48	6.51	0.0084
9	0.6404	49.06	7.02	0.0089
10	0.5768	47.52	7.54	0.0094
11	0.5000	45.31	8.02	0.0100
Streamline	$\frac{r_2}{r_t}$	$\kappa_2^\circ$	$\frac{t_m}{C}$	$\frac{t_{es}}{C}$
1	0.9804	54.93	0.0350	0.0058
2	0.9484	54.72	0.0387	0.0062
3	0.9135	53.53	0.0425	0.0065
4	0.8768	51.91	0.0467	0.0069
5	0.8385	49.69	0.0509	0.0072
6	0.7980	46.76	0.0554	0.0076
7	0.7547	42.26	0.0604	0.0080
8	0.7092	36.20	0.0658	0.0085
9	0.6507	28.35	0.0714	0.0090
10	0.6096	17.49	0.0778	0.0094
11	0.5557	2.86	0.0850	0.0010
Streamline	$\gamma^\circ$	$\frac{a}{C}$	$\sigma$	$\Phi^\circ$
1	60.77	0.731	1.3062	6.95
2	58.89	0.696	1.3534	5.34
3	57.07	0.658	1.4075	4.94
4	55.17	0.616	1.4685	5.03
5	52.94	0.562	1.5387	5.68
6	50.29	0.500	1.6204	7.05
7	47.13	0.500	1.7183	9.74
8	43.34	0.500	1.8363	14.28
9	38.71	0.500	1.9836	20.71
10	32.51	0.500	2.1754	30.03
11	24.09	0.500	2.4447	42.45

Table III. Stator Cascade Projection Data.

Number of vanes = 46

Design Parameter	Streamline									Units
	Tip SL 1	SL 2	SL 3	SL 4	SL 5	SL 6	SL 7	SL 8	Hub SL 9	
$\bar{r}$	17.836	17.443	17.103	15.642	14.228	12.855	11.489	11.134	10.831	Inches
$r_{1.6}$	17.836	17.432	17.083	15.586	14.132	12.706	11.263	10.882	10.553	Inches
$r_{2.0}$	17.836	17.454	17.123	15.697	14.325	13.005	11.715	11.386	11.109	Inches
C	3.650	3.633	3.606	3.493	3.396	3.299	3.222	3.199	3.184	Inches
$\sigma$	1.4983	1.5197	1.5438	1.6288	1.7386	1.8794	2.0536	2.1045	2.1557	---
$t_m/C$	0.0650	0.0640	0.0629	0.0588	0.0548	0.0507	0.0468	0.0458	0.0450	---
$t_e/t_m$	0.1231	0.1250	0.1272	0.1361	0.1460	0.1598	0.1709	0.1747	0.1778	---
$\kappa_1^\circ$	40.09	39.48	39.06	39.10	40.15	41.24	42.85	43.55	44.00	Degrees
$\kappa_2^\circ$	-13.11	-10.99	-10.21	-8.94	-8.80	-9.17	-10.41	-11.31	-12.54	Degrees
$\gamma^\circ$	13.46	14.21	14.24	14.58	15.76	16.99	18.89	19.43	19.62	Degrees
$\Phi^\circ$	53.20	50.57	49.27	48.04	48.95	50.41	53.26	54.86	56.54	Degrees

Table IV. Summary of Instrumentation Used for Task I Stage Testing.

Plane	Undistorted Inlet Testing	Radial Distortion Testing	Circumferential Distortion Testing
0.01, Vehicle Inlet	6 7-element P, p rakes	6 7-element P, p rakes	6 7-element P, p rakes
	24 T thermocouples	24 T thermocouples	24 T thermocouples
0.18, Stage Inlet	---	2 7-element P rakes	2 7-element P rakes
0.95, Rotor Inlet	1 p, $\beta$ wedge probe	1 P, T, p, $\beta$ combin- ation probe	1 P, T, p, $\beta$ combin- ation probe
1.51 Stator Inlet	1 P, T, $\beta$ cobra probe	1 P, T, $\beta$ cobra probe	1 P, T, p, $\beta$ combin- ation probe
	1 p wedge probe	1 p wedge probe	
	3 hot-wire probes	3 hot-wire probes	
2.20, Stage Exit	7 14-element P, T wake rakes	7 14-element P, T wake rakes	7 14-element P, T wake rakes
	1 p, $\beta$ wedge probe	1 p, $\beta$ wedge probe	1 P, T, p, $\beta$ combin- ation probe

Table V. Summary of Blade Element Data Reduction Constants.

(a) Rotor - Task I

Parameter	% Immersion	Plane 0.95	Edge 1	Edge 2	Plane 1.51
(No Blockage Included)	5	78.50			62.89
	10	119.70			99.21
	30	177.58			148.69
$A_j$	50	157.38			133.36
	70	145.51			111.59
	90	86.66			74.96
	95	49.60			36.54
$r_j$	0	18.323	18.164	17.885	17.838
	5	17.835	17.70	17.513	17.462
	10	17.420	17.310	17.137	17.081
	30	15.604	15.622	15.595	15.568
	50	13.977	13.916	14.034	14.056
	70	11.972	12.182	12.456	12.543
	90	9.910	10.257	10.895	11.030
	95	9.285	9.675	10.513	10.652
	100	8.737	9.125	10.129	10.287
$\epsilon_j$	0	-2.68	-9.0	-5.68	-2.28
	5	-2.15	-7.1	-5.1	-.78
	10	-1.88	-4.80	-4.60	-.99
	30	1.07	0.40	-1.50	-.56
	50	4.74	4.35	1.30	.98
	70	9.49	9.55	4.75	3.68
	90	15.78	16.30	10.10	7.82
	95	17.60	18.10	12.10	10.0
	100	19.59	19.46	14.95	13.42
$x_j^*(\alpha_{SSj}^*)$	0		61.88 (64.34)	54.93	
	5		60.60 (63.30)	54.80	
	10		59.61 (62.64)	54.42	
	30		56.01 (60.47)	50.68	
	50		52.56 (58.40)	43.79	
	70		49.71 (56.50)	32.15	
	90		47.11 (54.77)	14.29	
	95		46.13 (54.03)	8.00	
	100		45.31 (53.33)	2.86	

Radii are in inches

Areas are in square inches

Parameter	% Immersion	
$\frac{(w_j/w^*)_1}{(w_j/w^*)_u}$	5	1.0843
	10	1.0837
	30	1.0707
	50	1.0586
	70	1.0555
	90	1.0388
	95	1.0330
$\frac{(w_j/w^*)_2}{(w_j/w^*)_d}$	5	.9963
	10	.9932
	30	.9788
	50	.9762
	70	.9729
	90	.9747
	95	.9754
$\bar{r}_j$ (Used for Diffusion Factor)	5	17.640
	10	17.201
	30	15.613
	50	13.989
	70	12.355
	90	10.622
	95	10.065
$\sigma_j$ (Used for Diffusion Factor)	5	1.334
	10	1.369
	30	1.508
	50	1.684
	70	1.906
	90	2.217
	95	2.339

Table V. Summary of Blade Element Data Reduction Constants (Concluded).

## (b) Stator - Task I

Parameter	% Immersion	Plane 1.51	Edge 1	Edge 2	Plane 2.20
(No Blockage Included) $A_j$	5	62.89			58.73
	10	99.21			91.59
	30	148.69			134.20
	50	133.36			121.11
	70	111.59			108.78
	90	74.96			64.09
	95	36.54			29.08
	0	17.838	17.836	17.836	17.836
	5	17.462	17.450	17.463	17.478
	10	17.081	17.075	17.125	17.130
$r_j$	30	15.568	15.610	15.700	15.750
	50	14.056	14.175	14.363	14.420
	70	12.543	12.725	12.980	13.075
	90	11.030	11.300	11.720	11.775
	95	10.652	10.950	11.388	11.475
	100	10.287	10.625	11.100	11.168
	0	-.28	0	0	0
	5	-.78	.30	.28	.155
	10	-.99	.575	.60	.30
	30	-.56	2.18	1.65	.89
$c_j$	50	.98	4.50	2.70	1.325
	70	3.68	7.40	3.75	1.60
	90	7.82	10.30	4.50	1.28
	95	10.0	11.0	4.60	1.035
	100	13.42	11.38	4.70	.650
	0		40.09	-13.08	
	5		39.47	-11.13	
	10		39.11	-10.10	
	30		39.01	-8.87	
	50		39.80	-8.75	
(At nominal stator setting)	70		40.86	-9.10	
	90		42.22	-10.58	
	95		42.76	-12.36	
	100		43.32	-12.88	

Radius are in inches  
Areas are in square inches

Parameter	% Immersion	
$\frac{(w_j/w^*)_1}{(w_j/w^*)_u}$	5	1.0028
	10	1.0099
	30	1.0294
	50	1.0388
	70	1.0339
	90	1.0178
	95	1.0104
	0	.9842
	10	.9856
	30	.9884
$\frac{(w_j/w^*)_2}{(w_j/w^*)_d}$	50	.9879
	70	1.00
	90	1.028
	95	1.0356
	0	17.457
	10	17.100
	30	15.655
	50	14.269
	70	12.853
	90	11.510
$\bar{r}_j$ (used for Diffusion Factor)	95	11.169
	0	5
	5	1.523
	10	1.544
	30	1.631
	50	1.742
	70	1.880
	90	2.051
	95	2.098

TABLE VI SYMBOLIC LISTING OF BLADE ELEMENT DATA

ROTOR BLADE ROW - NASA TASK I											
		POINT NUMBER		BLADE ELEMENT PERFORMANCE RESULTS				DATE			
RADIAL POSITION		REL INLET FLOW ANG	ABS INLET FLOW ANG	CMRR LN LE ANGLE	INCID ANG MN CMRR LN	INCID ANG SUCT SURF	INLET ABS VELOCITY	INLET REL VELOCITY	INLET AX VELOCITY	INLET ABS TANG VEL	INLET REL TANG VEL
1											
2											
3											
4		$\beta_1'$	$\beta_1$	$\kappa_1^0$	$\iota$	$\iota_{ss}$	$v_1$	$v_1'$	$v_{z1}$	$v_{\theta 1}$	$v_{\theta 1}'$
5											
6											
7											
RADIAL POSITION		REL EXIT FLOW ANG	ABS EXIT FLOW ANG	CMRR LN TE ANGLE	REL DEV ANG TE	REL TURN ANGLE	EXIT ABS VELOCITY	EXIT REL VELOCITY	EXIT AX VELOCITY	EXIT ABS TANG VEL	EXIT REL TANG VEL
1											
2											
3		$\beta_2'$	$\beta_2$	$\kappa_2^0$	$\iota^0$	$\Delta\theta'$	$v_2$	$v_2'$	$v_{z2}$	$v_{\theta 2}$	$v_{\theta 2}'$
4											
5											
6											
7											
RADIAL POSITION		ROTOR SPD AT INLET	INLET ABS MACH NO	INLET REL MACH NO	AXIAL VEL RATIO	TRAV LOSS COEFFICIENT	TR TL PRESS LOSS PARAM	T ADIABATIC EFFICIENCY	POLYTROPIC EFFICIENCY	DIFFUSION FACTOR	CH1
1											
2											
3		$u_1$	$M_1$	$M_1'$	$\frac{v_{z2}}{v_{z1}}$	$\omega'$	$\frac{\omega' \cos \beta_2'}{2\sigma}$	$\eta_{ad}$	$\eta_p$	$D$	$C_h$
4											
5											
6											
7											
Method 2, Traverse Inst.											
RADIAL POSITION		ROTOR SPD AT EXIT	EXIT ABS MACH NO	EXIT REL MACH NO	SOLIDITY COEFFICIENT	LOSS	TOT PRESS LOSS PARAM	AUB EFFICIENCY	POLY MOMEN RISE/ MEAS RISE	STAT PRESS RISE COEFF	
1											
2											
3		$u_2$	$M_2$	$M_2'$	$\sigma$	$\omega'$	$\frac{\omega' \cos \beta_2'}{2\sigma}$	$\eta_{ad}$	$\eta_p$	$\frac{U_2 V_{\theta 2} - U_1 V_{\theta 1}}{J g c_p \Delta T}$	$C_p$
4											
5											
6											
7											
Method 1, Fixed & Traverse Instr.											
RADIAL POSITION		PERCENT IMMERSION	TRAV TOT PRESS RATIO	TRAV TOT TEMP RATIO	FIXED TOT PRESS RATIO	FIXED TOT TEMP RATIO	OVERALL PERFORMANCE SUMMARY				
1		5.0000					PERFORMANCE PARAMETERS				
2		10.0000	$\frac{P_{1.51}}{P_{0.95}}$	$\frac{T_{1.51}}{T_{0.95}}$	$\frac{P_{1.51}}{P_{0.95}}$	$\frac{T_{1.51}}{T_{0.95}}$	STAGE DATA ROTOR DATA ROTOR DATA				
3		30.0000					FIXED INST. FIXED INST. TRAV. INST.				
4		50.0000					Total Pressure Ratio = $P_{2.20}/P_{0.18}$				
5		70.0000					Adiabatic Efficiency = $\eta_{ad}$				
6		90.0000					Polytropic Efficiency = $\eta_p$				
7		95.0000					Percent Design Speed = $\sqrt{N/6}$				
							Cor. Nozzle Weight Flow = $W\sqrt{6/5}$				
							Discharge Valve Setting = Vane Schedule				
							= Stator				
							LE Check Flow/Noz. Flow =				
							Assumed LE Flow Coeff. =				
							TE Check Flow/Noz. Flow =				
							Assumed TE Flow Coeff. =				

TABLE VI SYMBOLIC LISTING OF BLADE ELEMENT DATA (Concluded)

42

STATOR BLADE ROW - NASA TASK I												
BLADE ELEMENT PERFORMANCE RESULTS												
POINT NUMBER READING NUMBER DATE												
RADIAL POSITION	REL INLET FLOW ANG	ABS INLET FLOW ANG	CMBR LN LE ANGLE	INCID ANG MN CMBR LN	INCID AVG SGT SURF	INLET ABS VELOCITY	INLET REL VELOCITY	INLET AX VELOCITY	INLET ABS TANG VEL	INLET REL TANG VEL		
1												
2												
3	*N/A	$\theta_1$	$\alpha_1^o$	1	N/A	$v_1$	N/A	$v_{z1}$	$v_{\theta 1}$	N/A		
4												
5												
6												
7												
RADIAL POSITION	REL EXIT FLOW ANG	ABS EXIT FLOW ANG	CMBR LN LE ANGLE	DEV ANG $\tau_B$	TURB ANGLE	EXIT ABS VELOCITY	EXIT REL VELOCITY	EXIT AX VELOCITY	EXIT ABS TANG VEL	EXIT REL TANG VEL		
1												
2												
3	N/A	$\theta_2$	$\alpha_2^o$	2	$\Delta\phi$	$v_2$	N/A	$v_{z2}$	$v_{\theta 2}$	N/A		
4												
5												
6												
7												
RADIAL POSITION	ROTOR SPD AT INLET	INLET ABS MACH NO	INLET REL MACH NO	AXIAL VEL RATIO					DIFFUSION FACTOR	CH1		
1												
2												
3												
4	N/A	$M_1$	N/A	$\frac{v_{z2}}{v_{z1}}$					D	$C_h$		
5												
6												
7												
RADIAL POSITION	ROTOR SPD AT EXIT	EXIT ABS MACH NO	EXIT REL MACH NO	SOLIDITY COEFFICIENT	LOSS	TOT PRES LOSS PARAM	ADB EFFICIENCY	POLY MOMEN RISE/ MEAS T RISE	STAT PRESS RISE COEFF			
1												
2												
3												
4	N/A	$M_2$	N/A	$\sigma$	$\bar{\omega}$	$\frac{\bar{\omega} \cos \theta_2}{2\sigma}$	N/A	$\eta_p$	N/A	$C_p$		
5												
6												
7												
RADIAL POSITION	PERCENT IMMERSION	TRAV TOT PRESS RATIO	TRAV TOT TEMP RATIO	FIXED TOT PRESS RATIO	FIXED TOT TEMP RATIO			OVERALL PERFORMANCE SUMMARY				
1	5.0000							PERFORMANCE PARAMETERS	STAGE DATA	STATOR DATA		
2	10.0000	$\frac{P_{2.2}}{P_{1.51}}$	$\frac{T_{2.2}}{T_{1.51}}$	$\frac{P_{2.2}}{P_{1.51}}$	$\frac{T_{2.2}}{T_{1.51}}$			FIXED INST.	FIXED INST.	TRAV. INST.		
3	30.0000							Total Pressure Ratio	$P_{2.20}/P_{0.18}$	$P_{2.20}/P_{1.51}$	$P_{2.20}/P_{1.51}$	
4	50.0000							Polytropic Efficiency	$\eta_p$	$\eta_p$	-----	
5	70.0000							Percent Design Speed	= N/A	Discharge Valve Setting		
6	90.0000							Cor. Nozzle Weight Flow	= $W_{vQ/8}$	Vane Schedule	= Stator	
7	95.0000							IE Check Flow/Noz. Flow	=	TE Check Flow/Noz. Flow	=	
								Assumed IE Flow Coeff.	=	Assumed TE Flow Coeff.	=	

\* Not Applicable: NA

Table VII. Listing of Overall Performance Data.

## (a) Shakedown Test With Undistorted Inlet

Reading Number	Percent Design Speed	Throttle Setting	Inlet Corrected Weight Flow (lbs/sec)	Stage		Rotor		Type Point*	Stator Setting (deg)
				Total Pressure Ratio	Adiabatic Efficiency	Total Pressure Ratio	Adiabatic Efficiency		
1	50.3	50	125.62	1.0786	0.7572	1.0910	0.8728	O.P.	0
2	50.0	50	125.20	1.0780	0.7297	1.0903	0.8417	O.P.	0
3	50.1	2	89.41	1.1376	0.7752	1.1426	0.8018	O.P.	0
4	70.1	50	172.11	1.1509	0.7148	1.1809	0.8491	O.P.	0
5	70.1	3	130.21	1.2820	0.7918	1.2918	0.8171	O.P.	0
6	90.1	30	205.73	1.2683	0.6795	1.3242	0.8078	O.P.	0
7	90.1	6	183.53	1.5319	0.8457	1.5510	0.8718	O.P.	0
8	100.2	25	221.12	1.3440	0.7135	1.3894	0.7976	O.P.	-3
9	100.1	15	220.61	1.4617	0.8148	1.4804	0.8438	O.P.	-3
10	100.0	15	219.52	1.4600	0.8100	1.4796	0.8400	B.E.	-3
11	100.0	9	216.48	1.6190	0.8391	1.6445	0.8674	B.E.	-3
12	100.1	9	216.51	1.6208	0.8322	1.6570	0.8731	O.P.	-8
13	100.2	9	217.29	1.6218	0.8363	1.6428	0.8602	O.P.	0
14	100.0	9	217.29	1.6262	0.8460	1.6463	0.8689	O.P.	+4
15	100.0	9	216.50	1.6428	0.8553	1.6617	0.8764	O.P.	+8
16	100.0	15	221.67	1.4601	0.7902	1.4826	0.8240	O.P.	0
17	99.8	6.15	204.95	1.7034	0.8427	1.7346	0.8737	O.P.	0
18	100.0	6.15	202.98	1.6932	0.8324	1.7359	0.8614	O.P.	-3
19	100.1	9	213.81	1.6547	0.8455	1.6810	0.8740	O.P.	+11
20	100.0	6.15	206.83	1.7194	0.8478	1.7397	0.8676	O.P.	+8
21	110.1	9	230.38	1.7088	0.8100	1.7359	0.8358	O.P.	0
22	90.1	9	196.74	1.4830	0.8680	1.4992	0.8933	O.P.	0
23	80.1	9	175.28	1.3567	0.8762	1.3688	0.9030	O.P.	0
24	80.1	3.5	149.79	1.3890	0.7952	1.4053	0.8248	O.P.	0

\*The following symbols indicate the type of data recorded:

OP - Overall Performance Data From Fixed Instruments

BE - Blade Element Traverse Data Plus Overall Performance

CT - Continuous Traverse Data Plus Overall Performance

SRT - Screen Rotation Test for Circumferential Distortion Traverse Data Plus Overall Performance

Table VII. Listing of Overall Performance Data (Continued).

## (b) Undistorted Inlet Performance Test

Reading Number	Percent Design Speed	Throttle Setting	Inlet Corrected Weight Flow (lbs/sec)	Stage		Rotor		Type Point*
				Total Pressure Ratio	Adiabatic Efficiency	Total Pressure Ratio	Adiabatic Efficiency	
25	100.0	15	221.89	1.4587	0.8111	1.4811	0.8457	B.E.
26	100.0	15	221.12	1.4589	0.7964	1.4814	0.8305	O.P.
27	100.0	9	217.17	1.6239	0.8518	1.6463	0.8776	B.E.
28	100.0	6	204.03	1.7037	0.8281	1.7377	0.8613	B.E.
29	100.1	7.5	212.65	1.6761	0.8504	1.7020	0.8776	B.E.
30	100.1	11	219.33	1.5630	0.8461	1.5805	0.8686	B.E.
31	90.2	15	204.39	1.3761	0.8212	1.3946	0.8574	B.E.
32	90.0	9	196.56	1.4863	0.8739	1.5001	0.8955	B.E.
33	90.0	7.5	192.81	1.5105	0.8706	1.5256	0.8928	B.E.
34	90.0	6	183.44	1.5269	0.8465	1.5457	0.8726	B.E.
35	90.1	30	205.36	1.2726	0.7030	1.3206	0.8153	B.E.
36	50.1	30	123.15	1.0861	0.8127	1.0958	0.9012	B.E.
37	50.1	30	123.20	1.0860	0.8095	1.0957	0.8983	O.P.
38	50.0	15	114.70	1.1073	0.8463	1.1129	0.8889	B.E.
39	50.0	11	109.34	1.1166	0.8796	1.1210	0.9115	B.E.
40	50.0	9	106.75	1.1213	0.8831	1.1251	0.9094	O.P.
41	50.1	6	100.80	1.1288	0.8504	1.1321	0.8712	B.E.
42	50.1	2	89.28	1.1369	0.8065	1.1416	0.8333	B.E.
43	70.1	30	169.98	1.1674	0.7937	1.1910	0.8989	B.E.
44	70.1	15	160.99	1.2193	0.8858	1.2311	0.9304	B.E.
45	70.0	9	151.55	1.2548	0.8909	1.2628	0.9166	B.E.
46	70.0	6	141.97	1.2712	0.8465	1.2788	0.8682	B.E.
47	70.1	3	128.91	1.2809	0.7950	1.2910	0.8212	B.E.
48	80.1	30	188.52	1.2131	0.7417	1.2442	0.8420	B.E.
49	80.1	15	185.71	1.2927	0.8507	1.3087	0.8930	B.E.
50	80.0	9	174.54	1.3534	0.8755	1.3642	0.8996	B.E.
51	80.1	6	162.43	1.3814	0.8468	1.3927	0.8691	B.E.
52	80.1	3.5	150.16	1.3864	0.7942	1.4026	0.8237	B.E.
53	90.1	11	199.43	1.4435	0.8666	1.4587	0.8927	O.P.
54	100.1	25	220.48	1.3419	0.6839	1.4000	0.7872	O.P.

\*The following symbols indicate the type of data recorded:

OP - Overall Performance Data From Fixed Instruments  
 BE - Blade Element Traverse Data Plus Overall Performance  
 CT - Continuous Traverse Data Plus Overall Performance  
 SRT - Screen Rotation Test for Circumferential Distortion Traverse Data Plus Overall Performance

Table VII. Listing of Overall Performance Data (Continued).

## (b) Undistorted Inlet Performance Test (Concluded)

Reading Number	Percent Design Speed	Throttle Setting	Inlet Corrected Weight Flow (lbs/sec)	Stage		Rotor		Type Point*
				Total Pressure Ratio	Adiabatic Efficiency	Total Pressure Ratio	Adiabatic Efficiency	
55	100.1	15	219.94	1.4643	0.8087	1.4860	0.8416	C.T.
56	100.1	9	216.33	1.6144	0.8474	1.6335	0.8698	C.T.
58	100.0	6	202.06	1.6934	0.8356	1.7279	0.8701	C.T.
59	50.0	4	96.17	1.1350	0.8271	1.1411	0.8625	O.P.
60	50.1	4	95.00	1.1331	0.8045	1.1364	0.8237	O.P.
61	70.0	3	129.66	1.2808	0.7886	1.2913	0.8155	O.P.
62	80.0	2.45	143.40	1.3852	0.7693	1.4057	0.8057	O.P.
63	90.1	5	176.81	1.5292	0.8140	1.5521	0.8443	O.P.
64	100.0	5.5	198.11	1.6968	0.8064	1.7370	0.8451	O.P.
65	110.2	9	230.47	1.7044	0.8073	1.7305	0.8322	O.P.
66	110.1	7	226.68	1.8307	0.8101	1.8738	0.8441	O.P.
67	109.9	9	229.89	1.7045	0.8079	1.7298	0.8320	B.E.
68	109.9	9	230.02	1.7049	0.8119	1.7304	0.8363	O.P.
69	110.3	6.75	225.55	1.8502	0.8030	1.9015	0.8421	B.E.
70	110.1	7.25	228.61	1.8148	0.8168	1.8554	0.8498	B.E.
71	110.0	8	228.43	1.7584	0.8155	1.7884	0.8420	B.E.
72	110.2	13	230.69	1.5656	0.7764	1.5920	0.8074	B.E.
73	50.0	15	114.97	1.1067	0.8471	1.1121	0.8887	O.P.
74	80.1	11	179.07	1.3353	0.8795	1.3468	0.9067	O.P.

\*The following symbols indicate the type of data recorded:

- OP - Overall Performance Data From Fixed Instruments
- BE - Blade Element Traverse Data Plus Overall Performance
- CT - Continuous Traverse Data Plus Overall Performance
- SRT - Screen Rotation Test for Circumferential Distortion Traverse Data Plus Overall Performance

Table VII. Listing of Overall Performance Data (Continued).

## (c) Undistorted Inlet Test with Long Inlet Duct

Reading Number	Percent Design Speed	Throttle Setting	Inlet Corrected Weight Flow (lbs/sec)	Stage		Rotor		Type Point*
				Total Pressure Ratio	Adiabatic Efficiency	Total Pressure Ratio	Adiabatic Efficiency	
132	70.0	30	168.95	1.184	0.8056	1.199	0.8750	O.P.
133	70.1	9	146.34	1.259	0.8229	1.268	0.8750	O.P.
134	70.1	3	126.37	1.275	0.7568	1.288	0.8018	C.T.
135	100.1	15	220.37	1.486	0.8294	1.506	0.8588	O.P.
136	100.1	9	214.61	1.633	0.8510	1.658	0.8846	O.P.
137	100.1	6.5	202.34	1.681	0.8333	1.722	0.8728	C.T.
138	90.0	30	204.18	1.290	0.7521	1.321	0.8376	O.P.
139	90.1	9	194.21	1.484	0.8554	1.500	0.8795	O.P.
140	90.1	5.5	177.75	1.525	0.8162	1.541	0.8432	C.T.

\*The following symbols indicate the type of data recorded:

- OP - Overall Performance Data From Fixed Instruments
- BE - Blade Element Traverse Data Plus Overall Performance
- CT - Continuous Traverse Data Plus Overall Performance
- SRT - Screen Rotation Test for Circumferential Distortion Traverse Data Plus Overall Performance

Table VII. Listing of Overall Performance Data (Continued).

## (d) Radial Inlet Distortion Test

Reading Number	Percent Design Speed	Throttle Setting	Inlet Corrected Weight Flow (lbs/sec)	Stage		Rotor		Type Point*
				Total Pressure Ratio	Adiabatic Efficiency	Total Pressure Ratio	Adiabatic Efficiency	
75	70.0	50	167.99	1.1878	0.7761	1.2078	0.8534	O.P.
76	70.0	10	148.40	1.2657	0.8385	1.2745	0.8639	O.P.
77	70.0	15	156.89	1.2440	0.8235	1.2546	0.8671	O.P.
78	90.1	50	202.87	1.2882	0.6989	1.3236	0.7769	O.P.
79	90.0	11	195.05	1.4623	0.8259	1.4777	0.8500	O.P.
80	90.0	15	198.33	1.4139	0.8130	1.4309	0.8424	O.P.
81	100.0	50	216.41	1.3359	0.6650	1.3803	0.7436	B.E.
82	100.0	10.5	212.58	1.5914	0.8003	1.6129	0.8251	B.E.
83	100.0	14	215.95	1.5168	0.7854	1.5377	0.8130	B.E.

\*The following symbols indicate the type of data recorded:

- OP - Overall Performance Data From Fixed Instruments
- BE - Blade Element Traverse Data Plus Overall Performance
- CT - Continuous Traverse Data Plus Overall Performance
- SRT - Screen Rotation Test for Circumferential Distortion Traverse Data Plus Overall Performance

Table VII. Listing of Overall Performance Data (Concluded).

## (e) Circumferential Inlet Distortion Test

Reading Number	Percent Design Speed	Throttle Setting	Inlet Corrected Weight Flow (lbs/sec)	Stage		Rotor		Type Point*	Dist. Screen And Position (deg. From TDC)
				Total Pressure Ratio	Adiabatic Efficiency	Total Pressure Ratio	Adiabatic Efficiency		
84	70	50	165.2	1.192	.746	1.214	.826	O.P.	195
85	70	5	130.8	1.285	.757	1.300	.793	O.P.	
86	70	10	146.6	1.269	.818	1.283	.857	O.P.	
87	90	50	204.4	1.319	.763	1.358	.848	O.P.	
88	90	7.5	179.0	1.501	.818	1.526	.853	O.P.	
89	90	11	192.1	1.469	.831	1.494	.870	O.P.	
90	100	50	220.1	1.390	.738	1.445	.829	O.P.	
91	100	9.6	204.6	1.604	.820	1.638	.858	O.P.	
92	100	13	213.5	1.556	.830	1.583	.865	O.P.	
93-104	100	9.6	205.3	1.602	.816	1.638	.853	SRT	195-165
105	100	9.6	205.8	1.602	.814	1.637	.854	O.P.	195
106-117	100	50	219.2	1.389	.736	1.447	.828	SRT	195-165
118	100	50	218.3	1.389	.736	1.448	.833	O.P.	195
119-130	100	13	211.9	1.555	.828	1.582	.862	SRT	195-165
131	100	13	212.3	1.555	.831	1.583	.867	O.P.	195

\*The following symbols indicate the type of data recorded:

- OP - Overall Performance Data From Fixed Instruments
- BE - Blade Element Traverse Data Plus Overall Performance
- CT - Continuous Traverse Data Plus Overall Performance
- SRT - Screen Rotation Test for Circumferential Distortion Traverse Data Plus Overall Performance

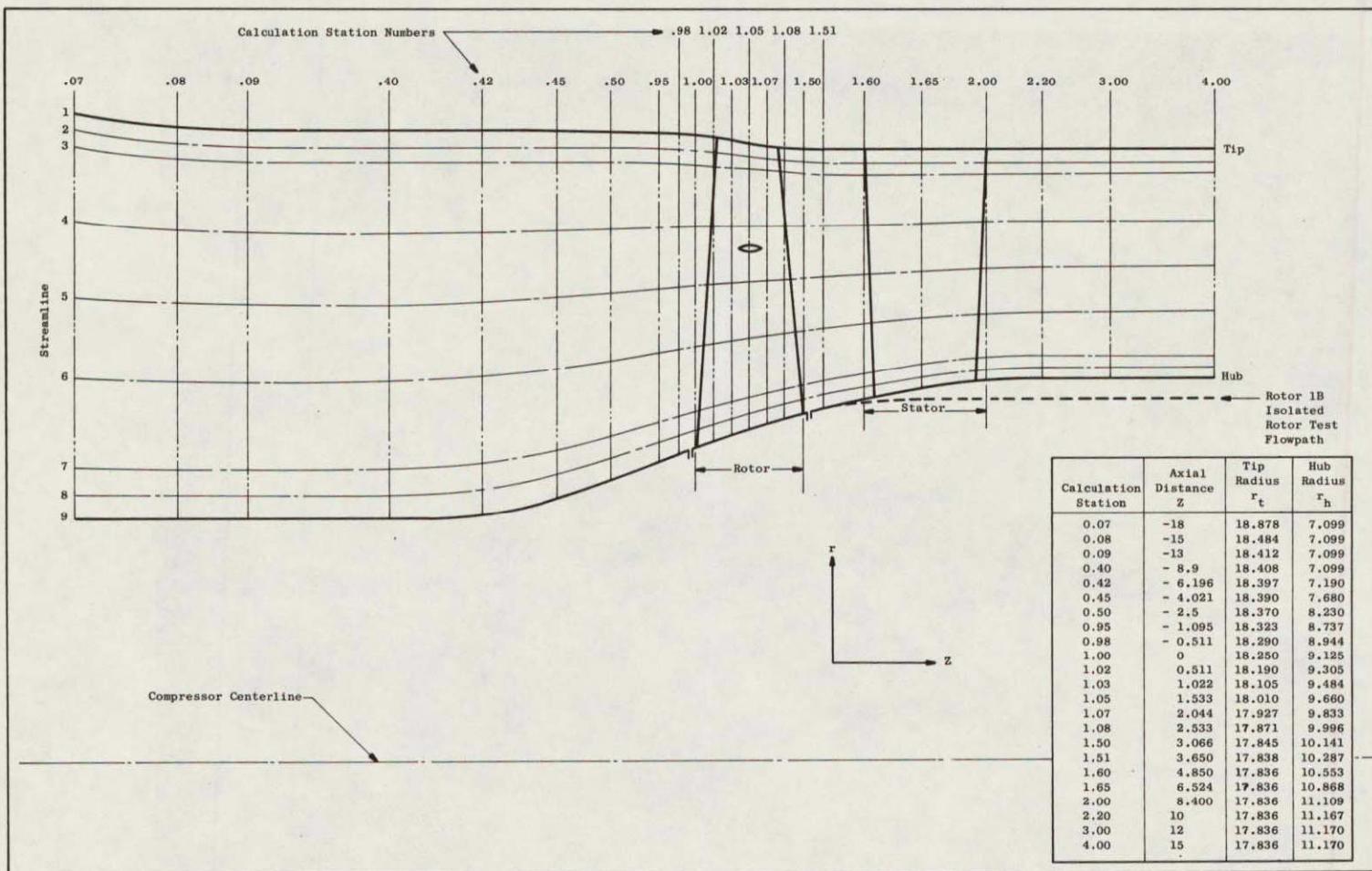


Figure 1. Task I Stage Flowpath.

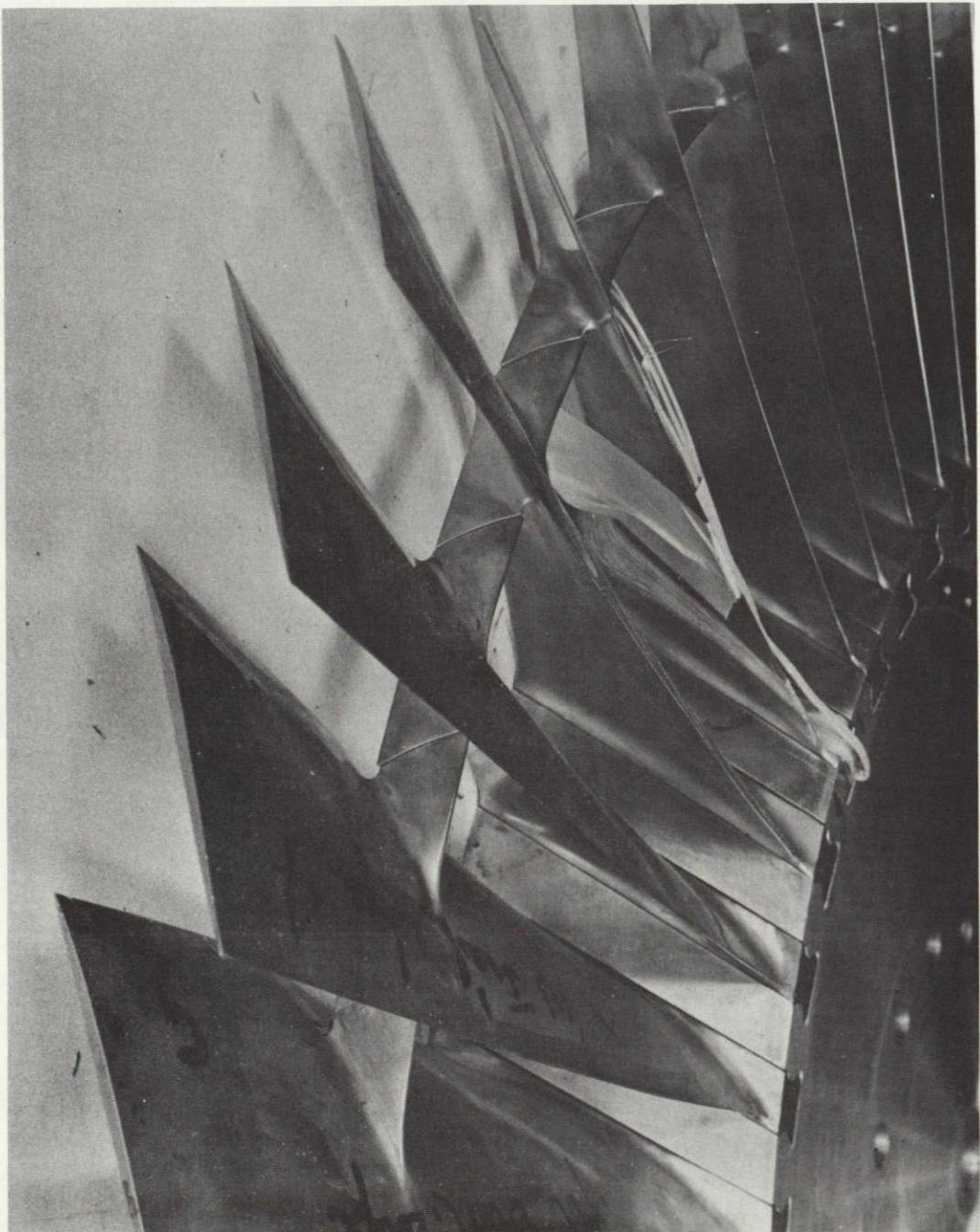


Figure 2. Partial View of Rotor 1B.

NOT REPRODUCIBLE

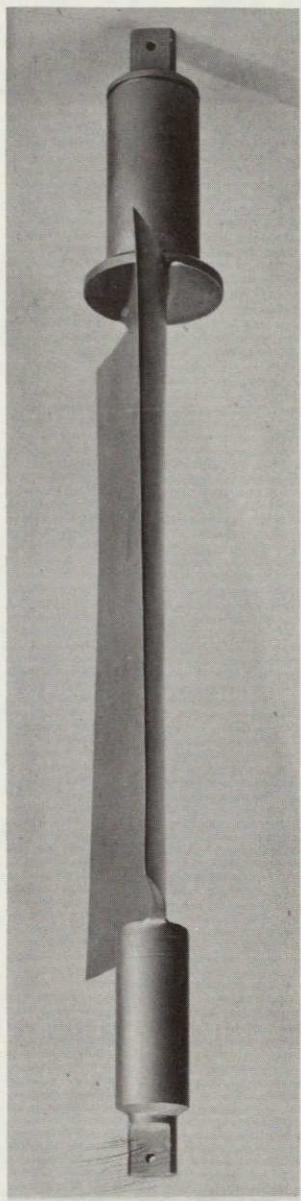
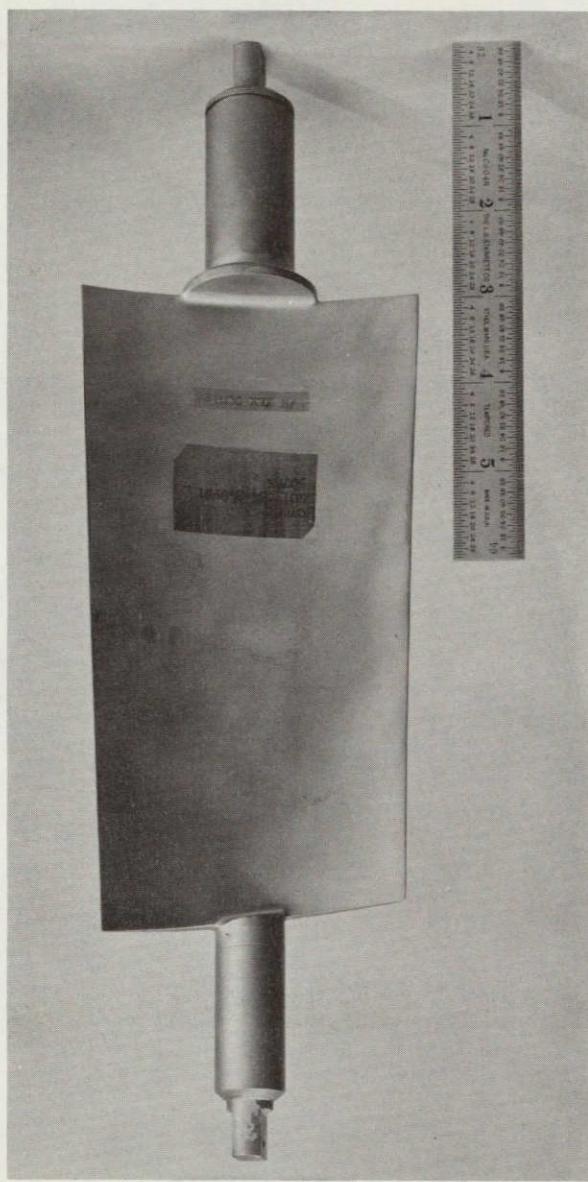


Figure 3. Photographs of a Variable-Stagger Stator Vane.

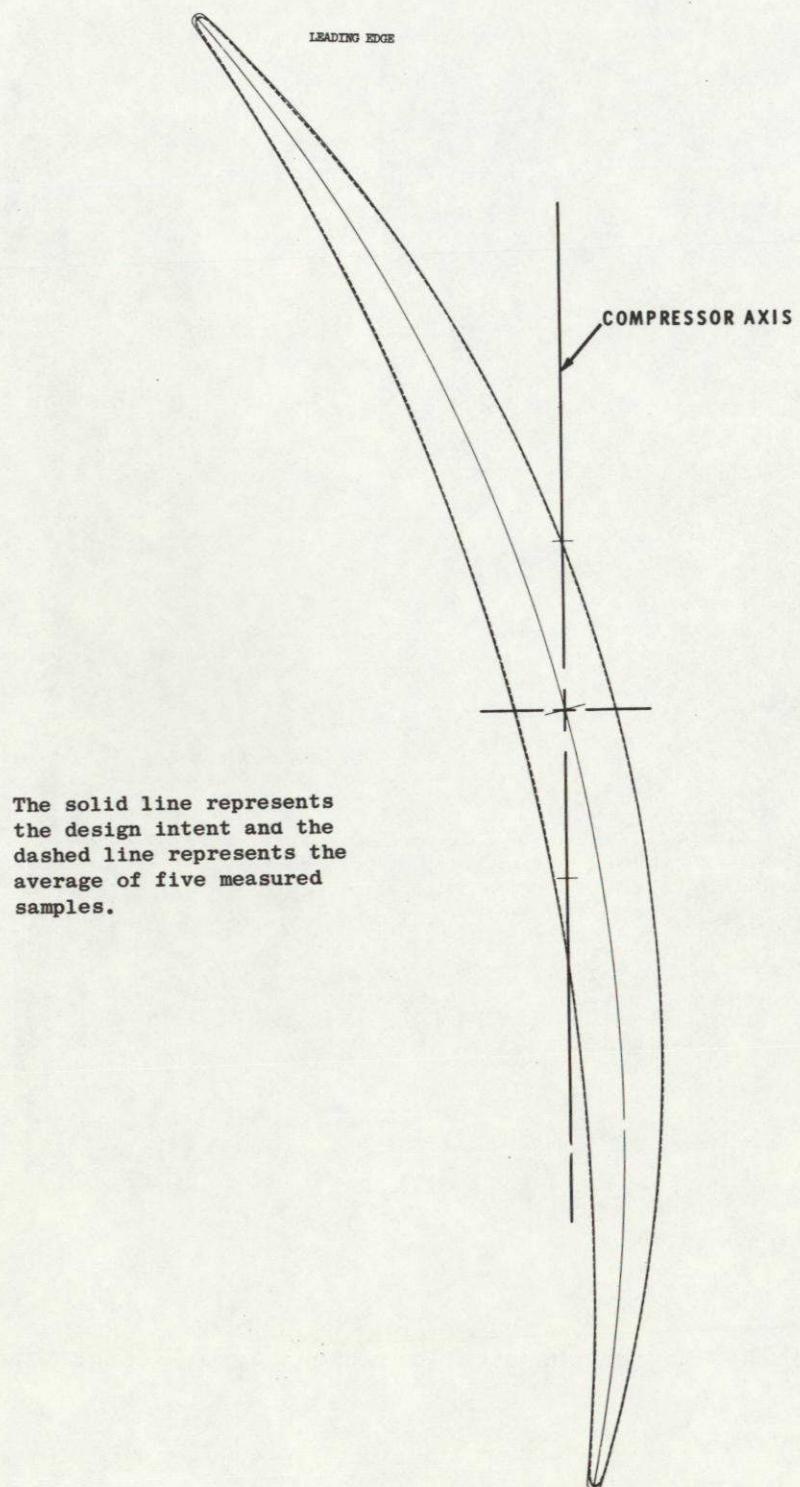


Figure 4 (a). Stator Vane Inspection Results for Tip Section.

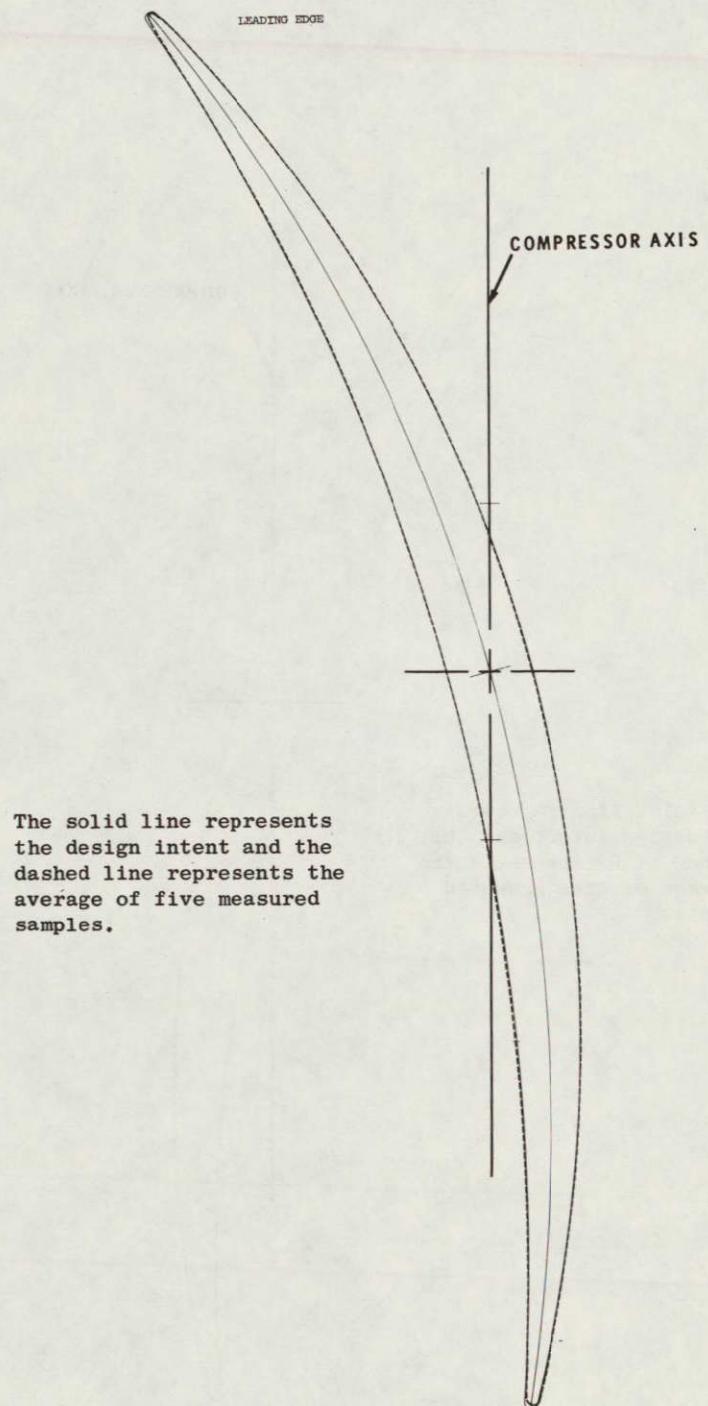


Figure 4 (b). Stator Vane Inspection Results for Pitchline Section.

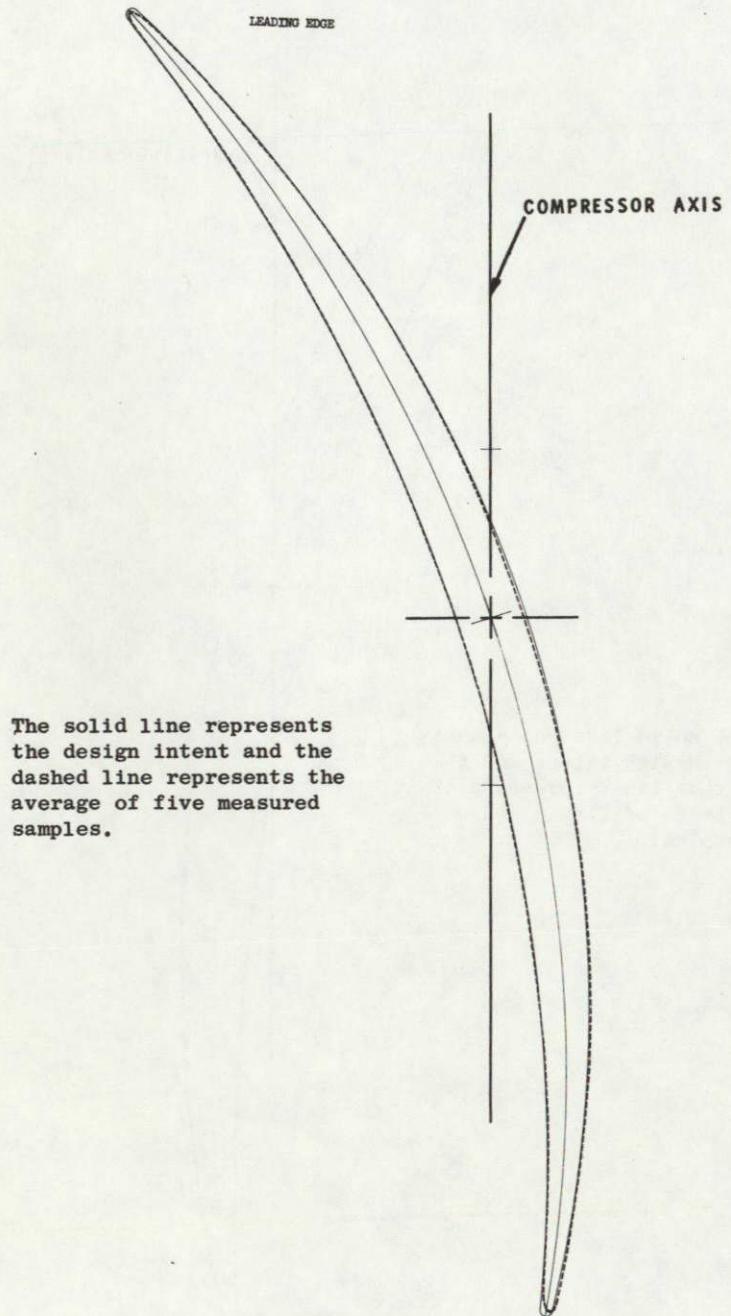
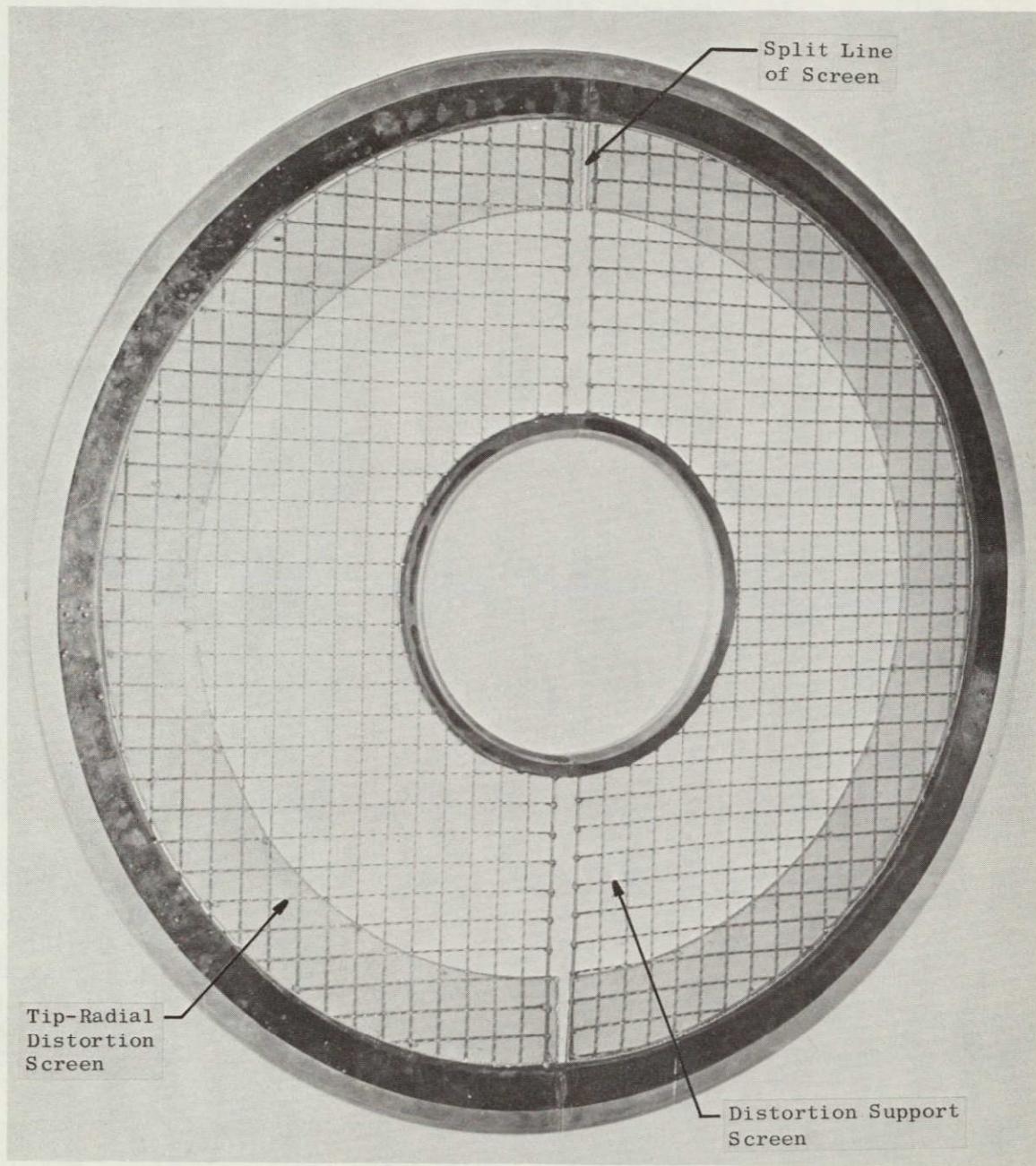
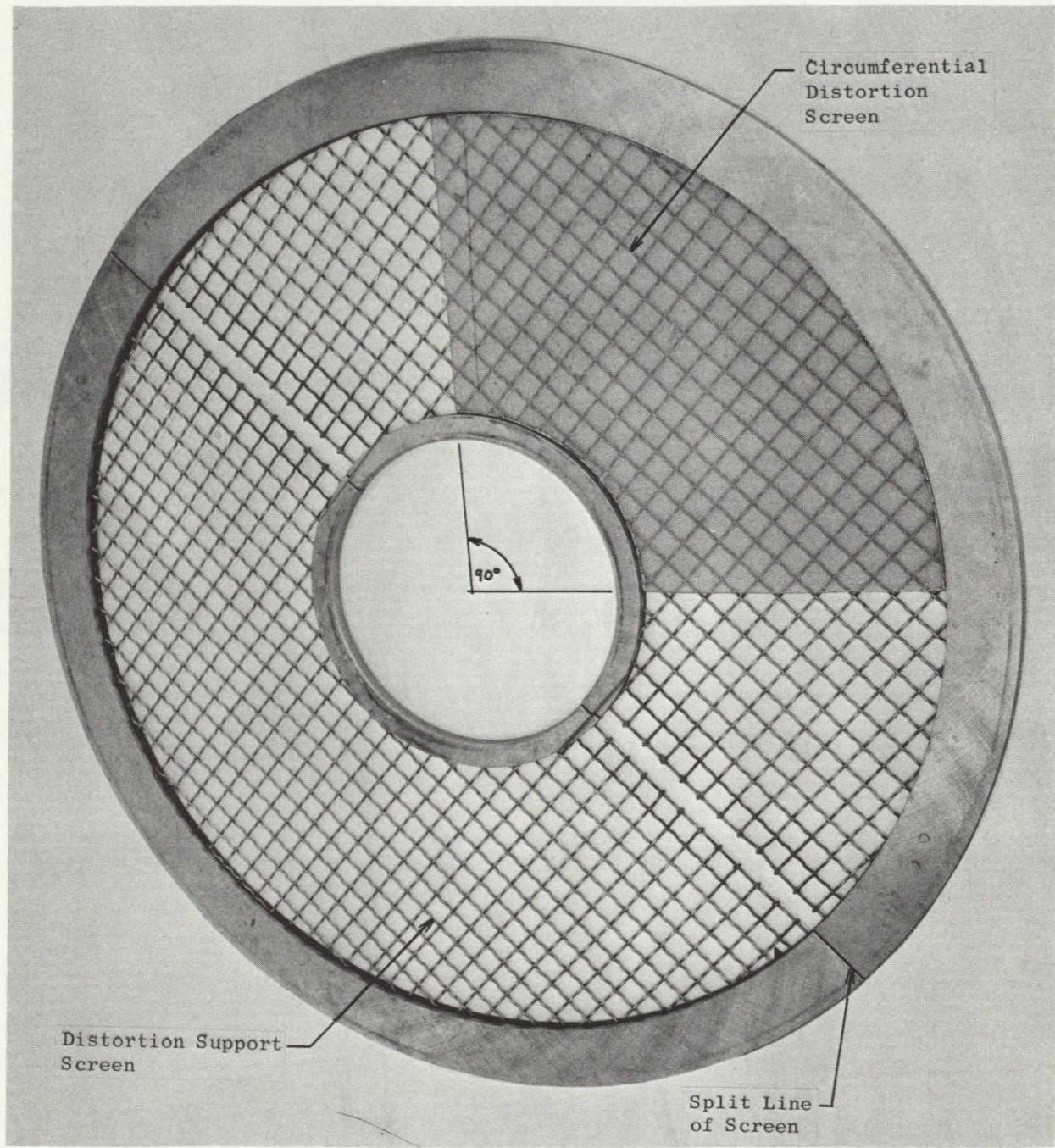


Figure 4 (c). Stator Vane Inspection Results for Hub Section.



(a) Radial Distortion Screen

Figure 5. Photographs of Inlet Distortion Screens.



(b) Circumferential Distortion Screen

Figure 5. Photographs of Inlet Distortion Screens (Concluded).

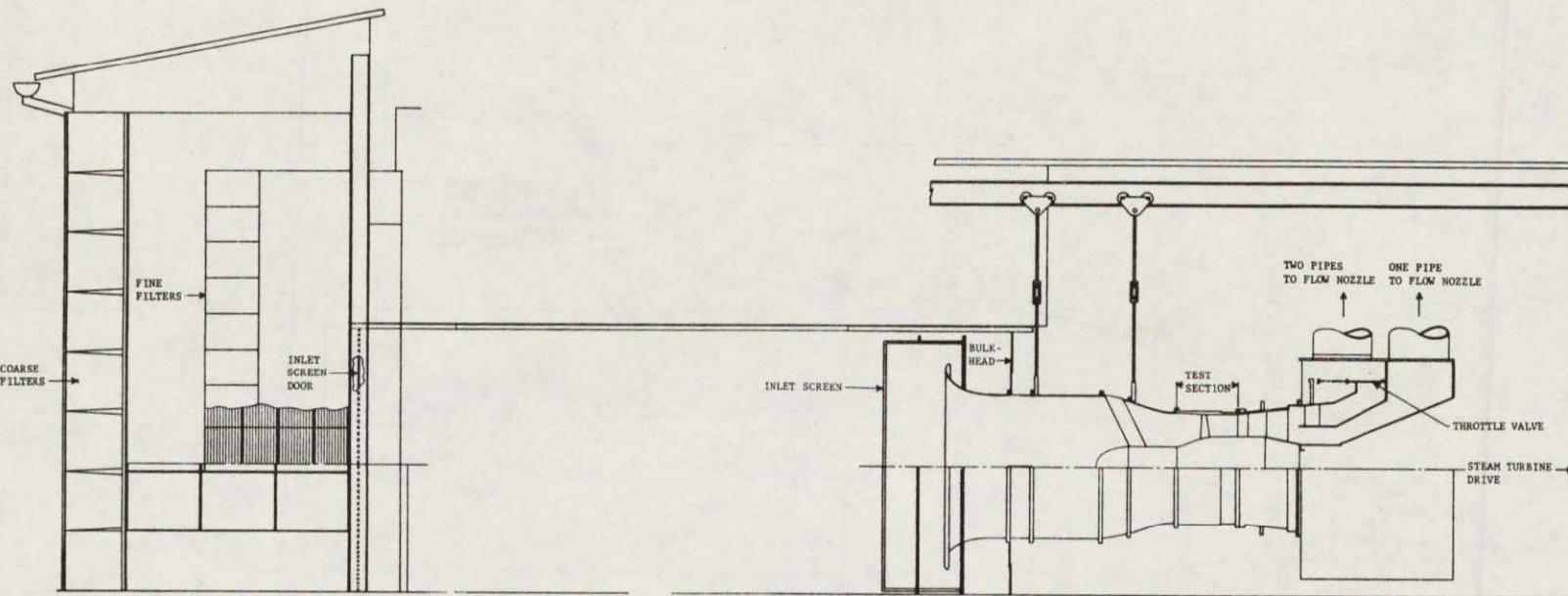


Figure 6. Schematic Diagram of House Compressor Test Facility.

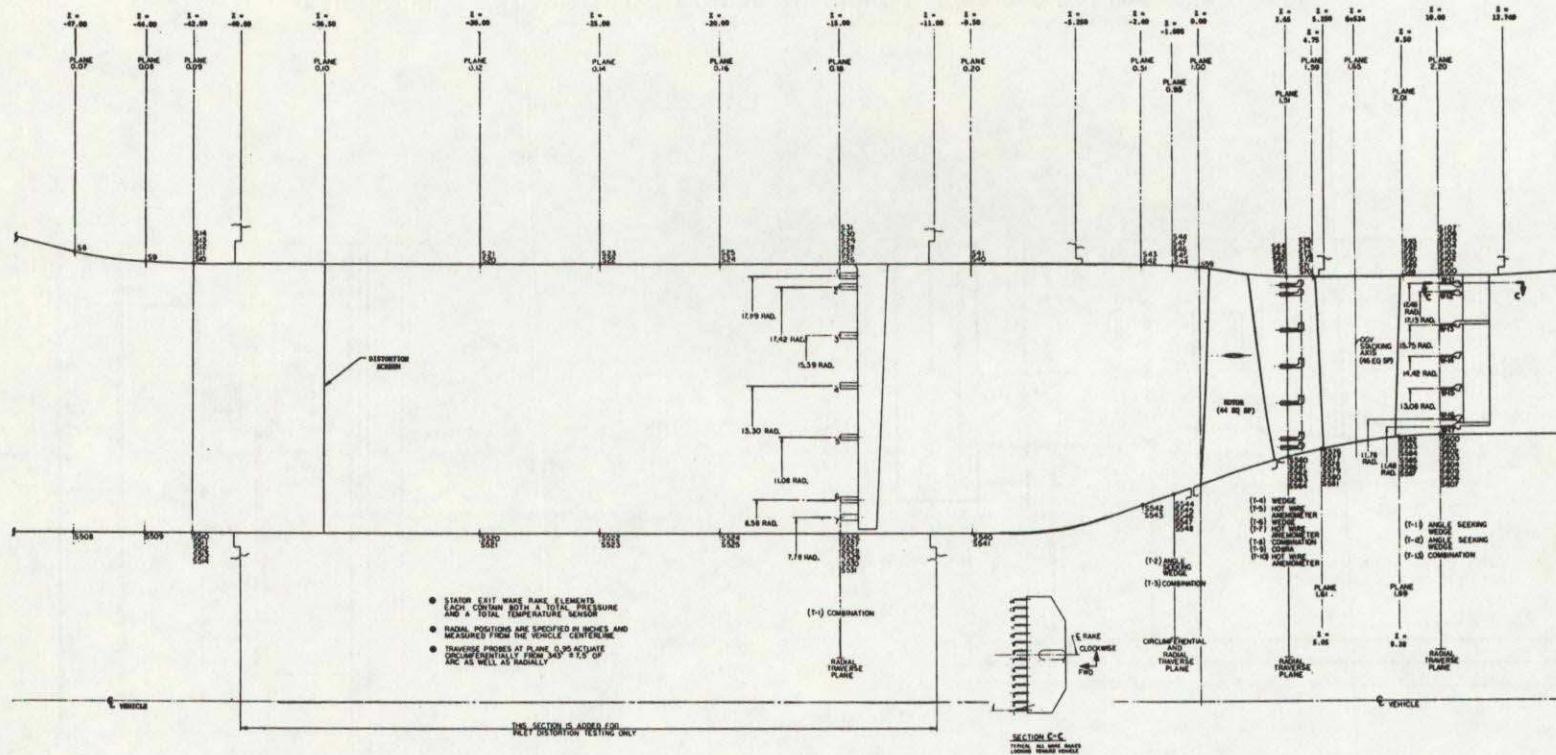
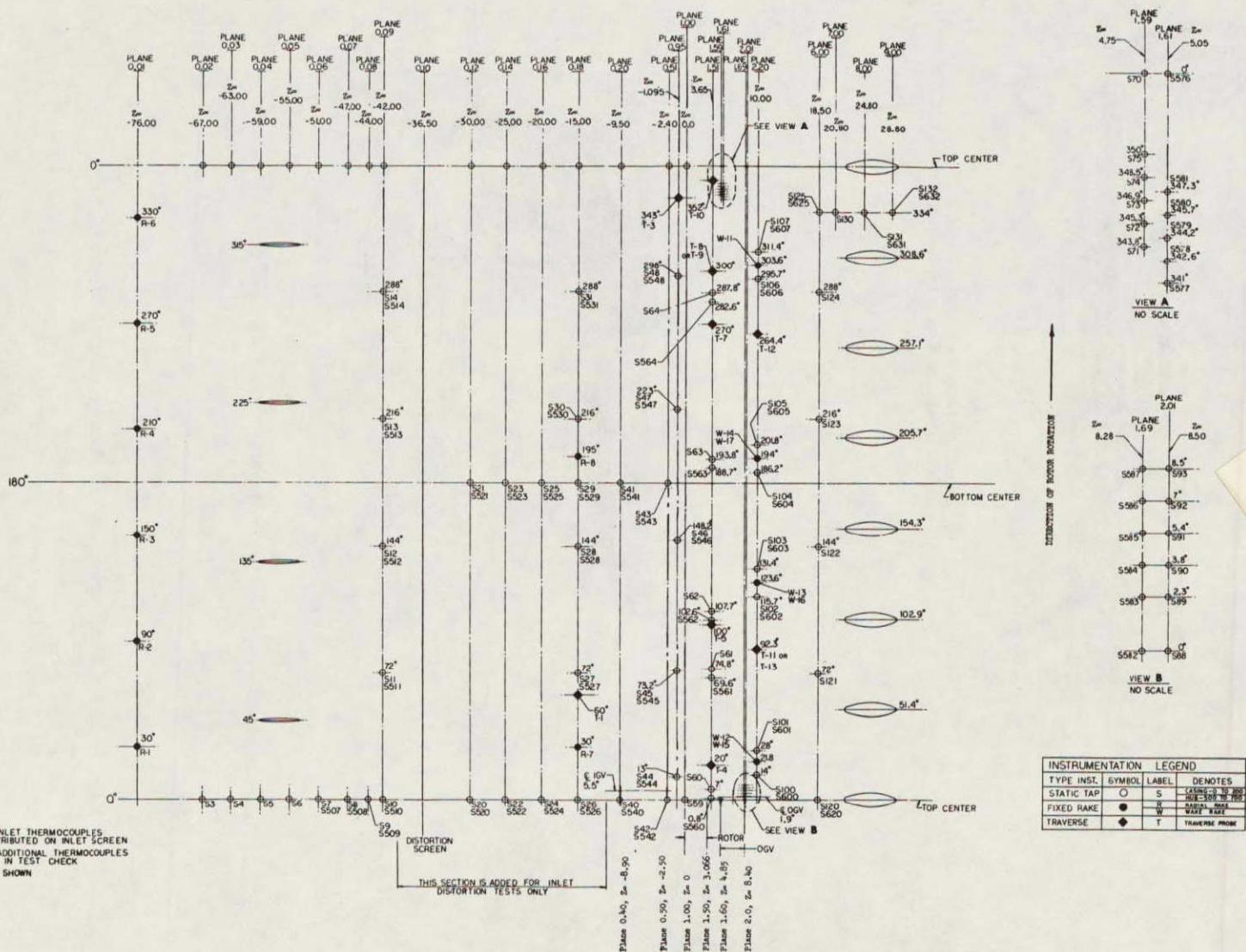
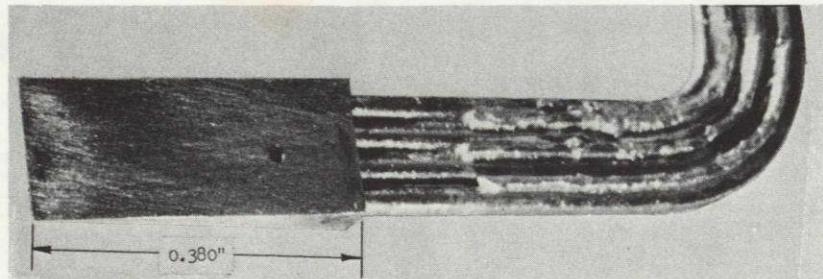


Figure 7. Meridional View Showing Instrumentation Locations.

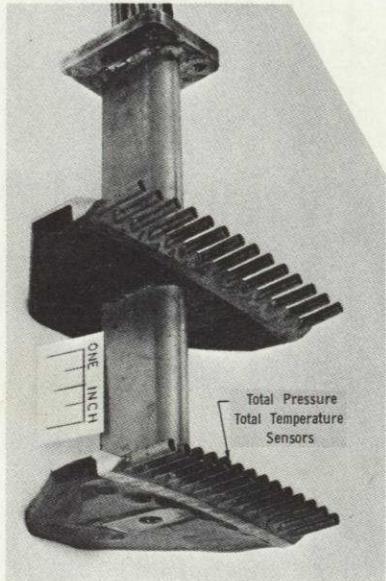


NOT REPRODUCIBLE

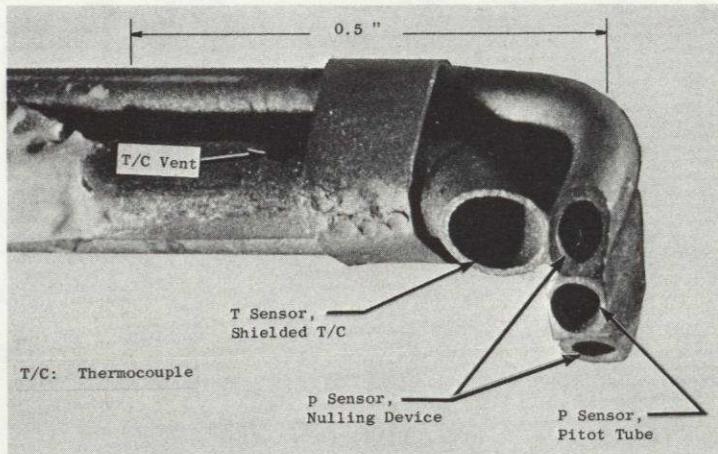
Figure 8. Circumferential Development Showing Instrumentation Locations.



(b) Sensing Element of Angle-Seeking  
Static-Pressure Wedge Traverse Probe

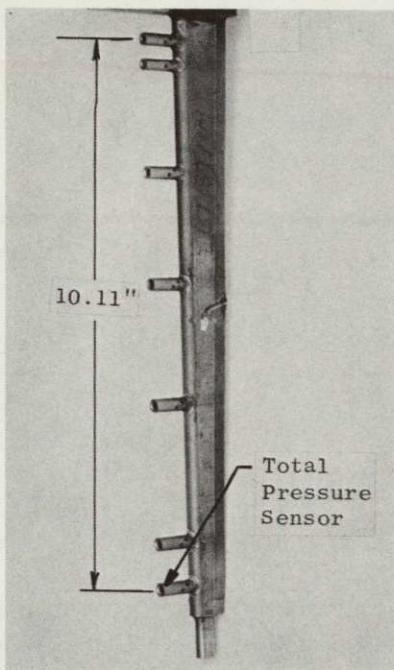


(a) Fixed Discharge Total Pres-  
sure - Total Temperature Wake  
Rake Located at Plane 2.2

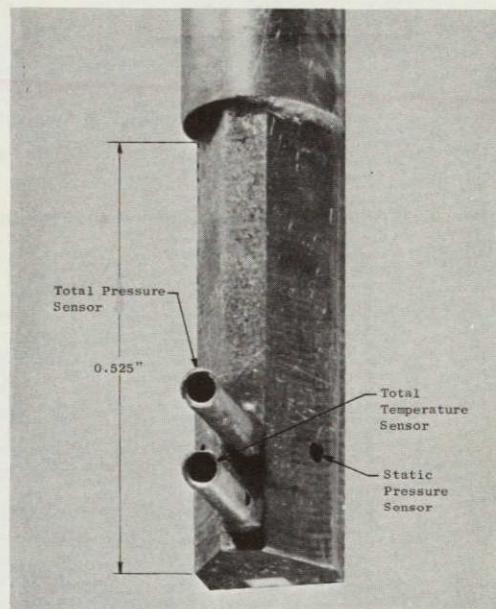


(c) Sensing Element of Cobra Traverse Probe

Figure 9. Photographs of Instrumentation.



(d) Fixed Inlet Distortion  
Total Pressure Rake at  
Plane 0.18



(e) Sensing Element of Four-Parameter  
Combination Traverse Probe

NOT REPRODUCIBLE



(f) Sensing Element of Shielded Hot-  
Wire Anemometer Traverse Probe

Figure 9. Photographs of Instrumentation (Concluded).

(Dashed lines with arrows and inset formulas indicate calculation sequence for sample case.)

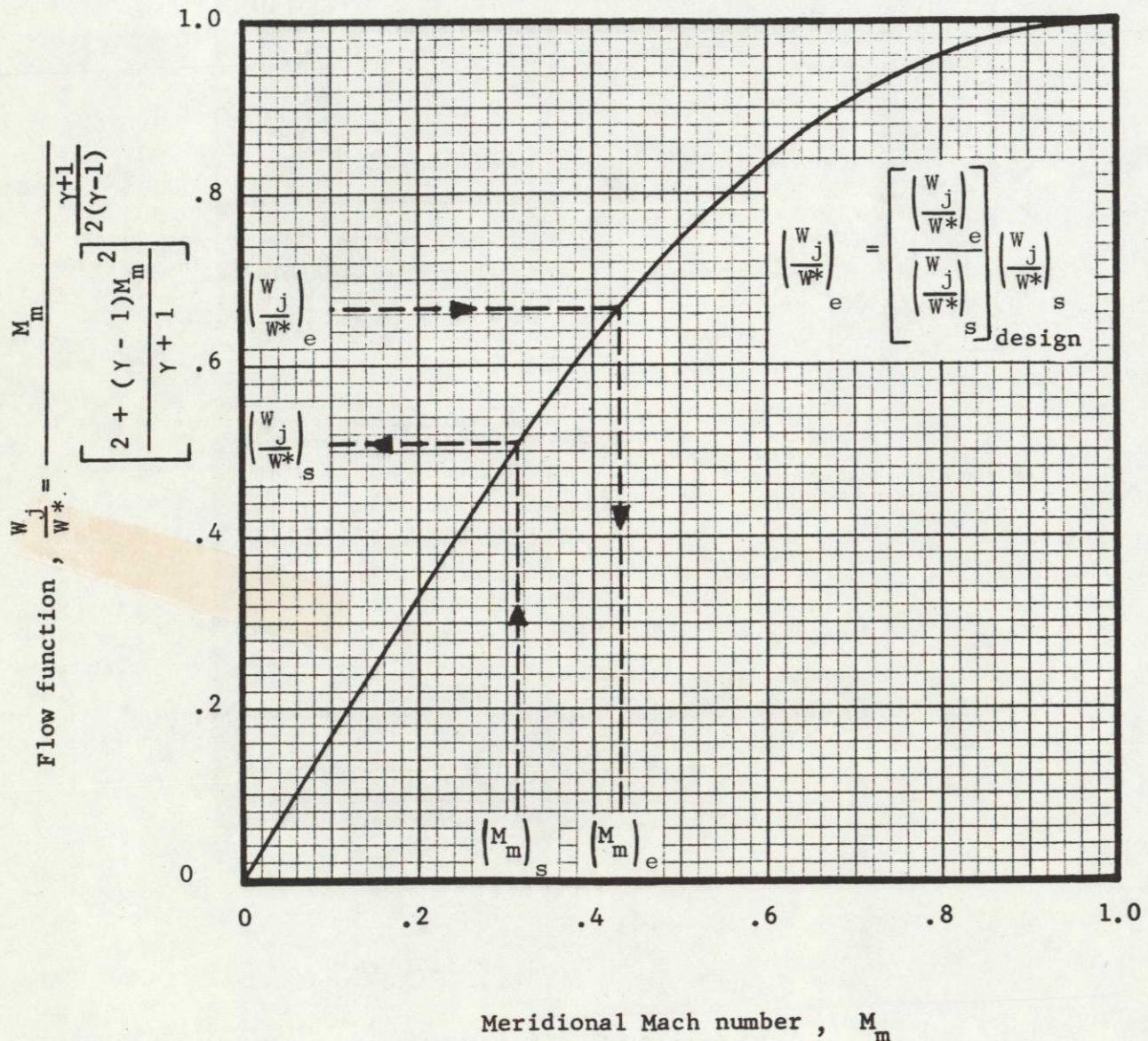


Figure 10. Relationship Between Flow Function and Meridional Mach No. Used for Transferring Traverse Measurements to Blade Edges.

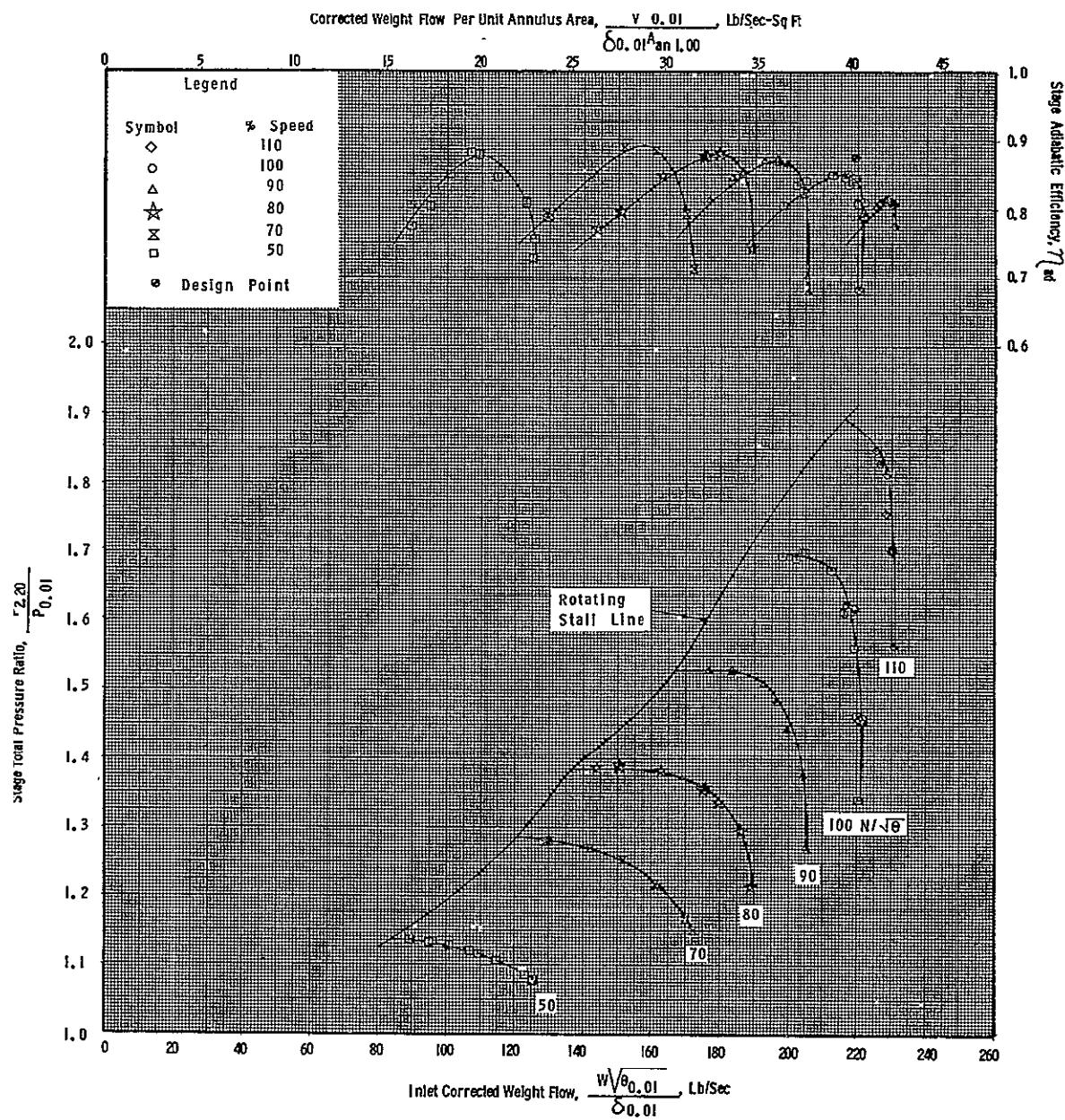


Figure 11. Stage Performance Map with Undistorted Inlet Flow.

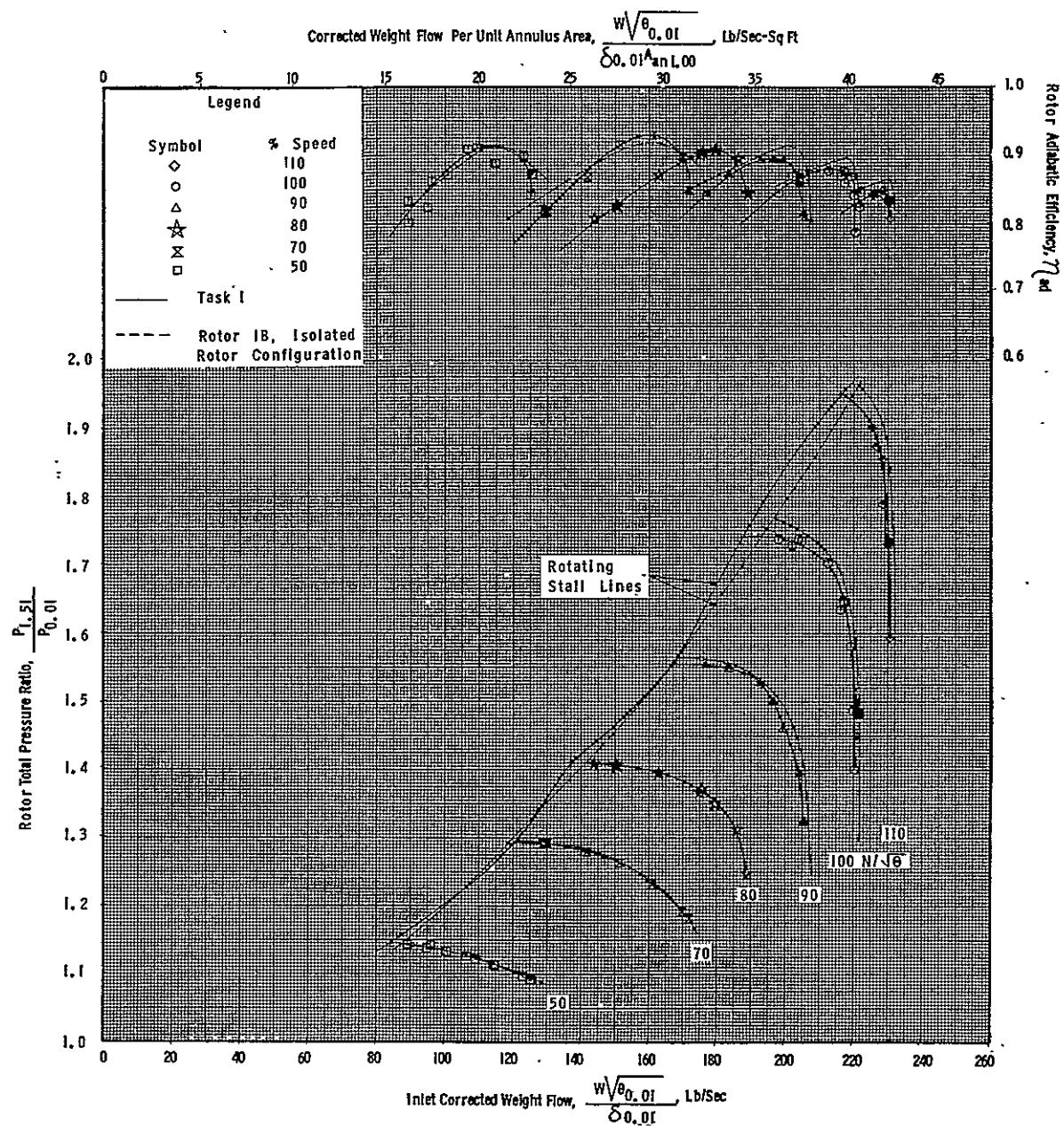


Figure 12. Rotor Performance Map with Undistorted Inlet Flow.

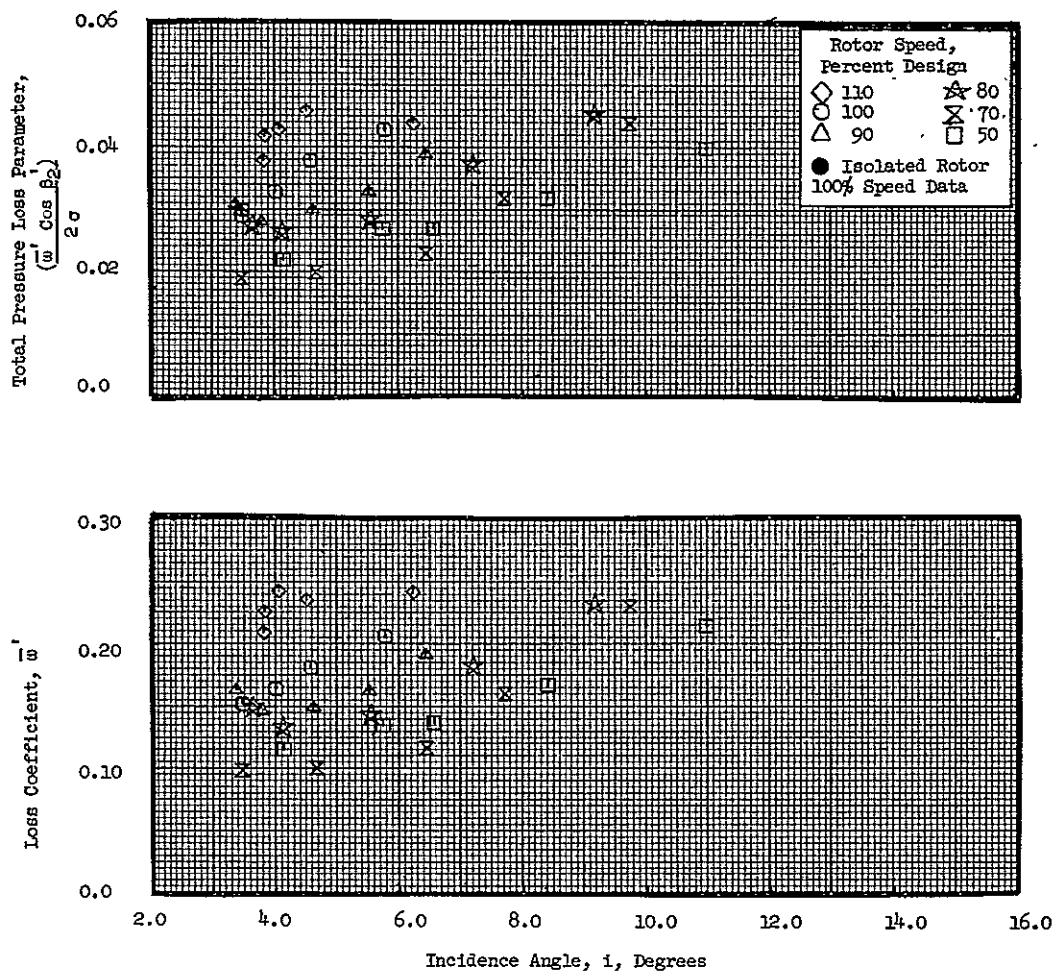


Figure 13 (a). Rotor Blade Element Data with Undistorted Inlet Flow, at 5% Immersion from Tip.

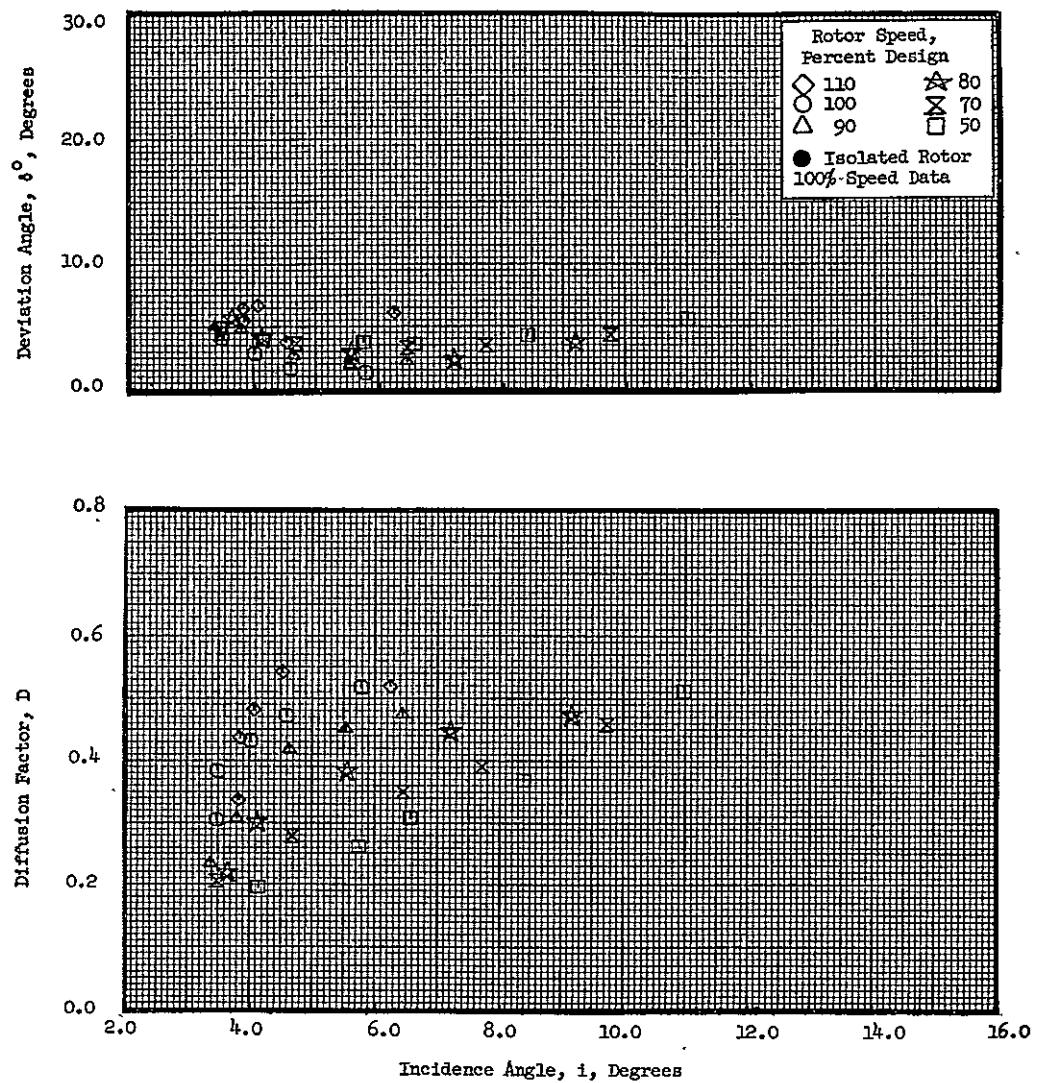


Figure 13 (a). Rotor Blade Element Data with Undistorted Inlet Flow, at 5% Immersion from Tip (Concluded).

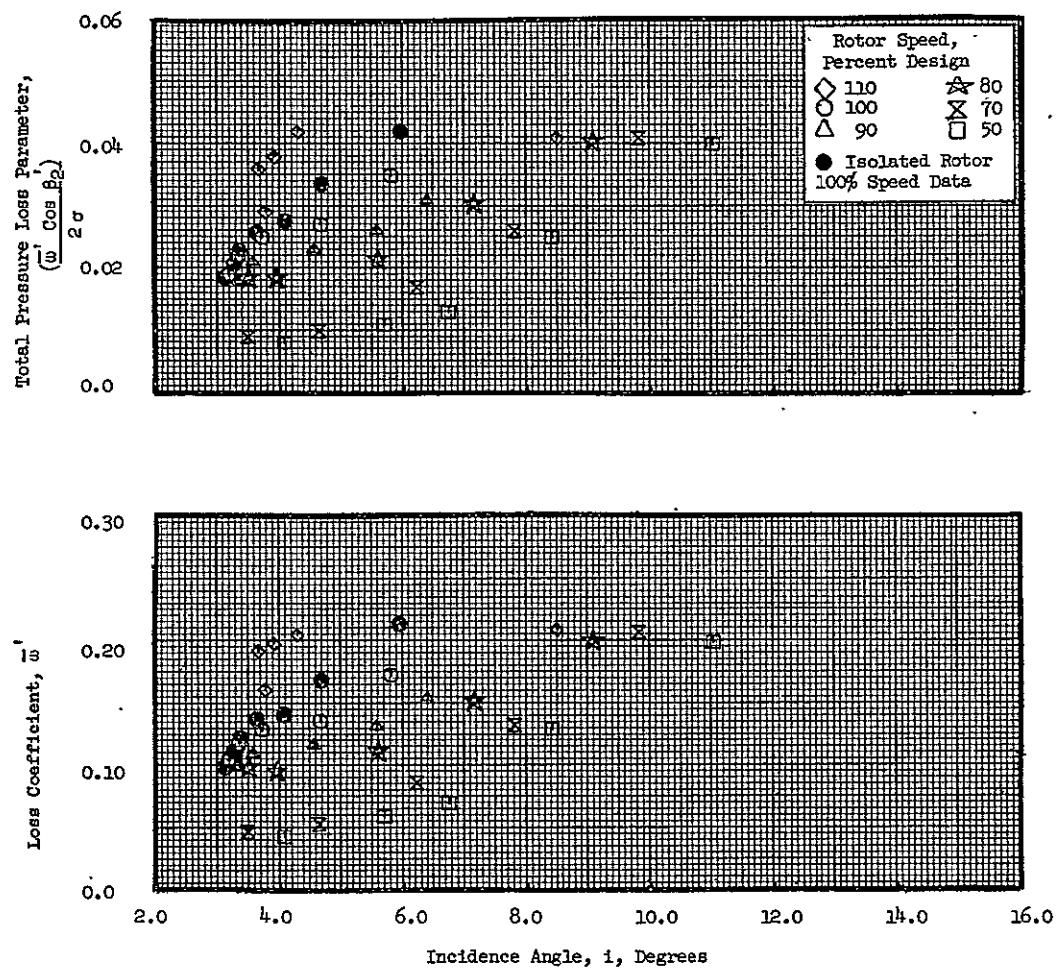


Figure 13 (b). Rotor Blade Element Data with Undistorted Inlet Flow, at 10% Immersion from Tip.

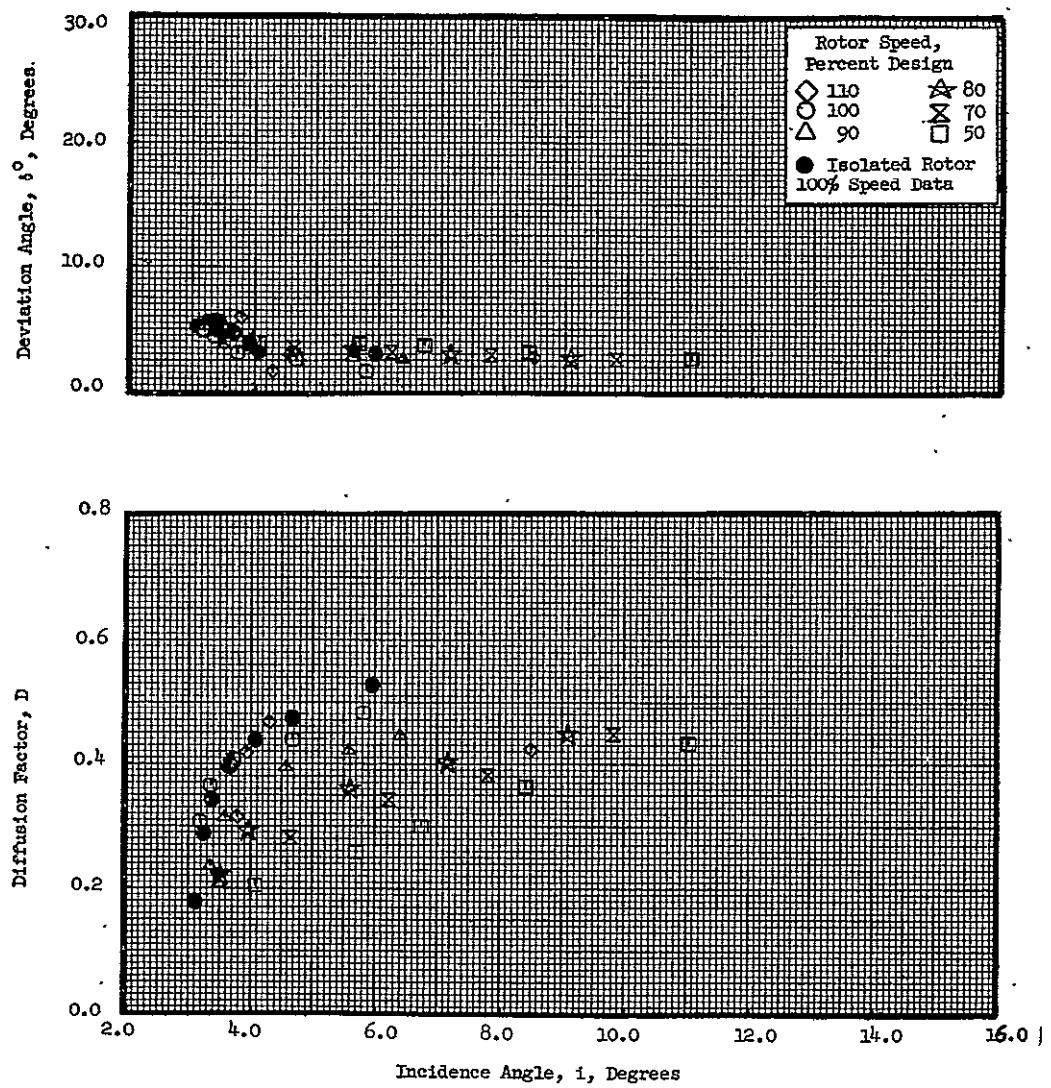


Figure 13 (b). Rotor Blade Element Data with Undistorted Inlet Flow, at 10% Immersion from Tip (Concluded).

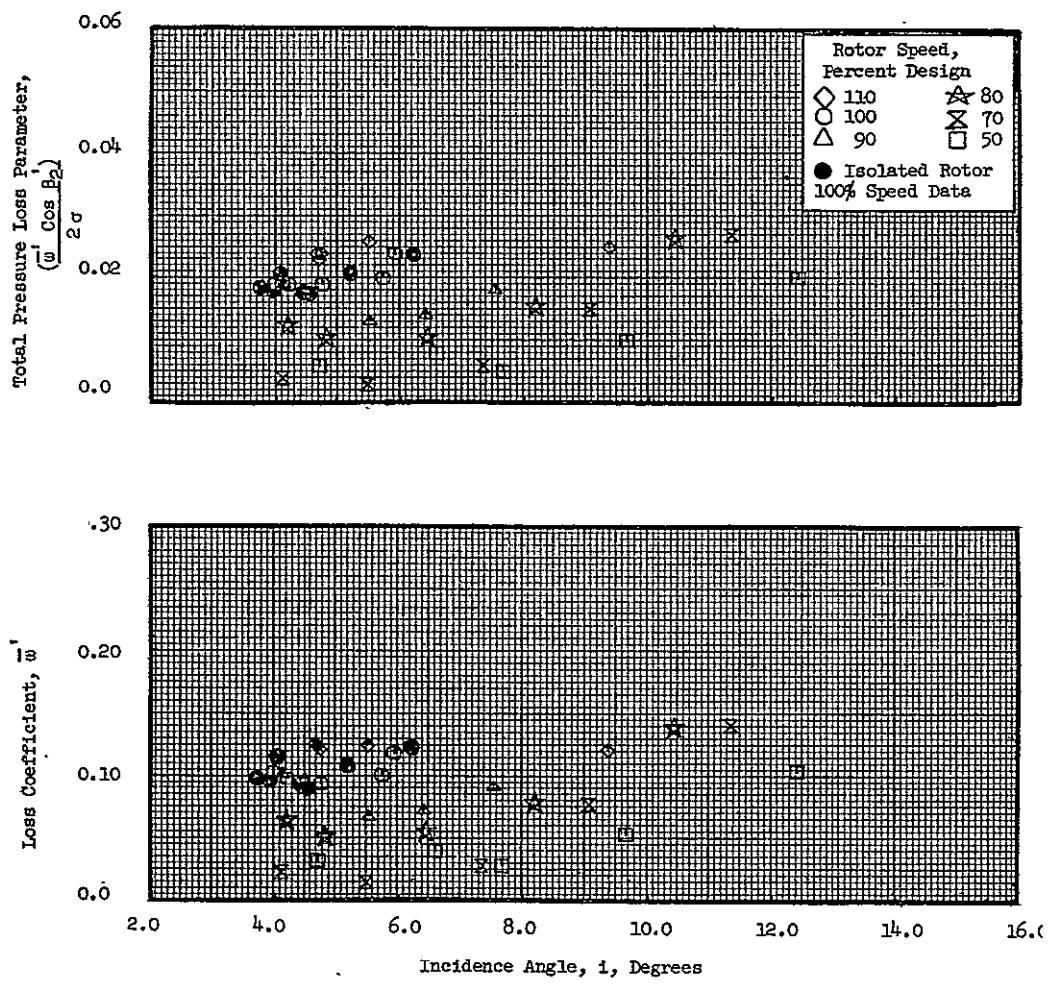


Figure 13 (c). Rotor Blade Element Data with Undistorted Inlet Flow, at 30% Immersion from Tip.

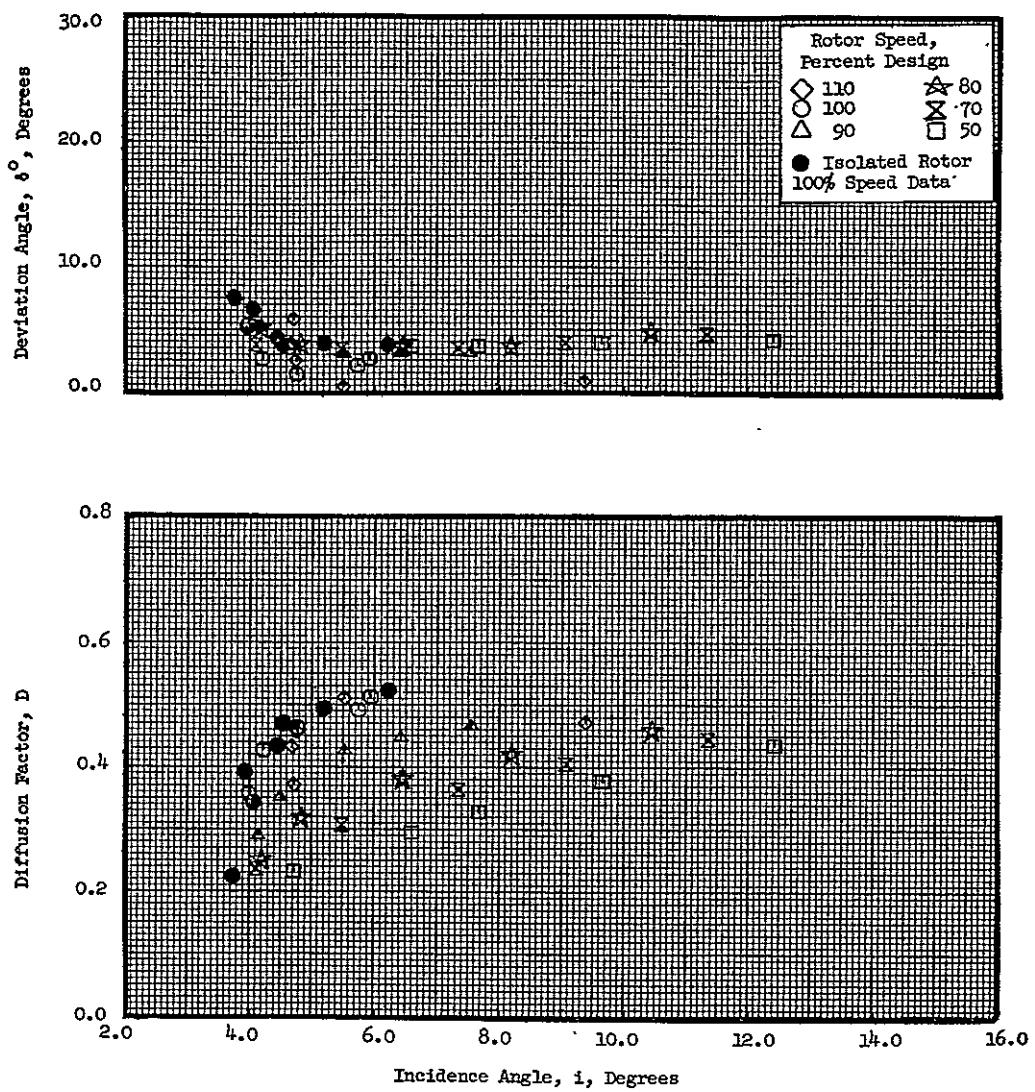


Figure 13 (c). Rotor Blade Element Data with Undistorted Inlet Flow, at 30% Immersion from Tip (Concluded).

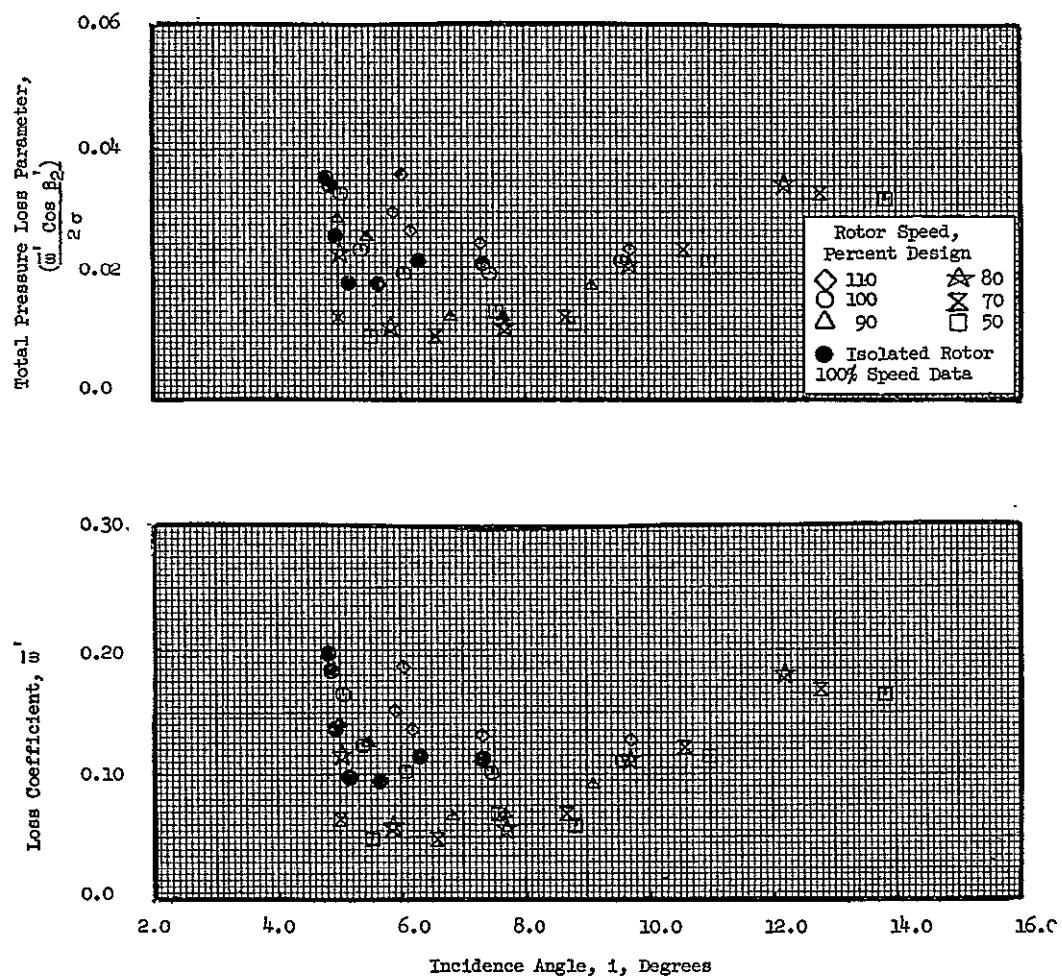


Figure 13 (d). Rotor Blade Element Data with Undistorted Inlet Flow, at 50% Immersion from Tip.

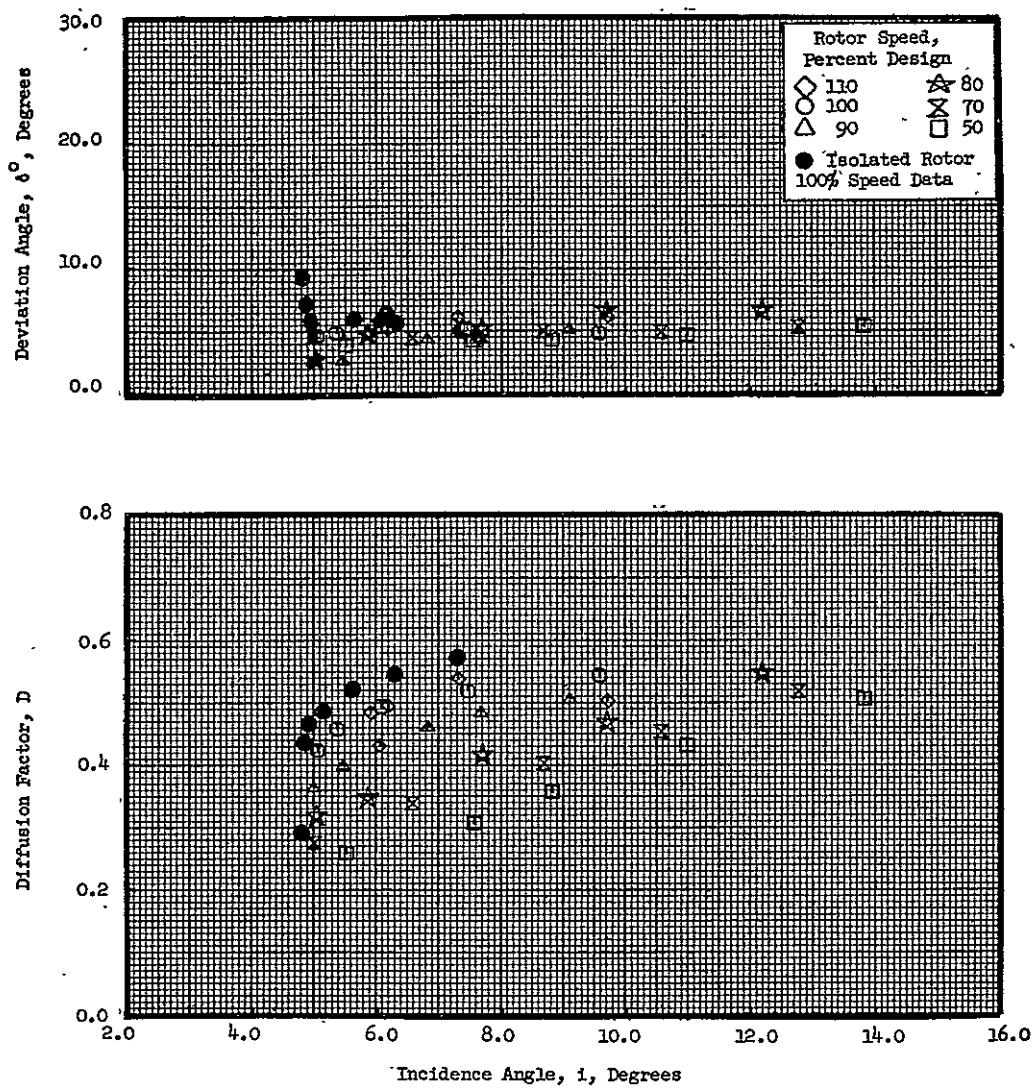


Figure 13 (d). Rotor Blade Element Data with Undistorted Inlet Flow, at 50% Immersion from Tip (Concluded).

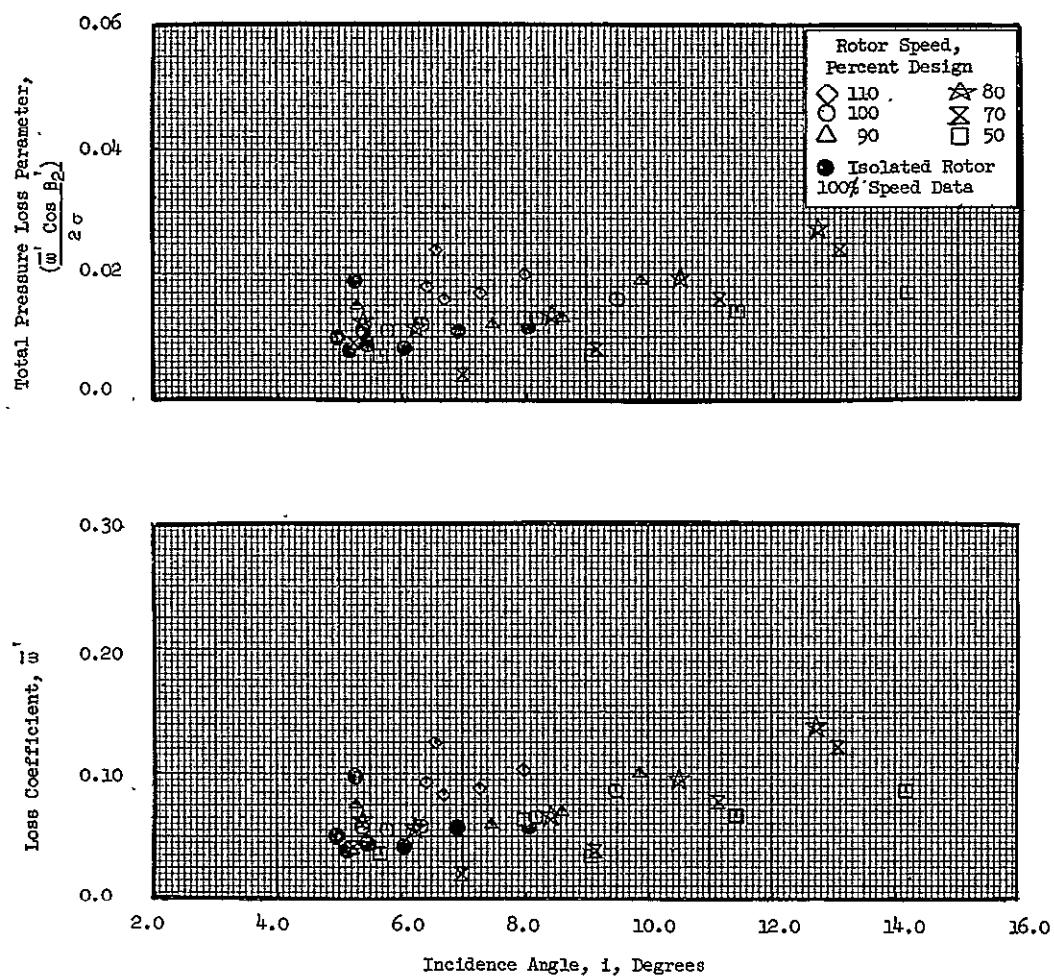


Figure 13 (e). Rotor Blade Element Data with Undistorted Inlet Flow, at 70% Immersion from Tip.

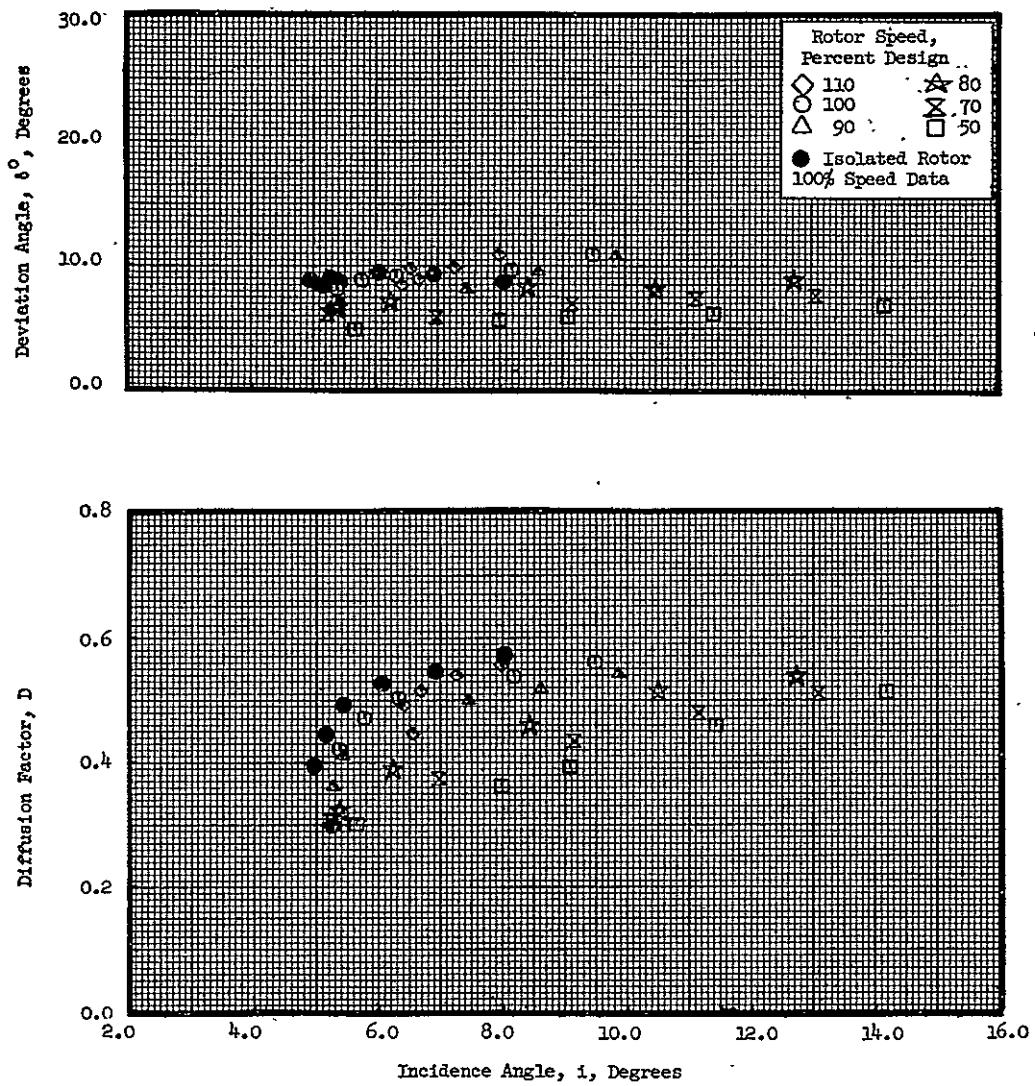


Figure 13 (e). Rotor Blade Element Data with Undistorted Inlet Flow, at 70% Immersion from Tip (Concluded).

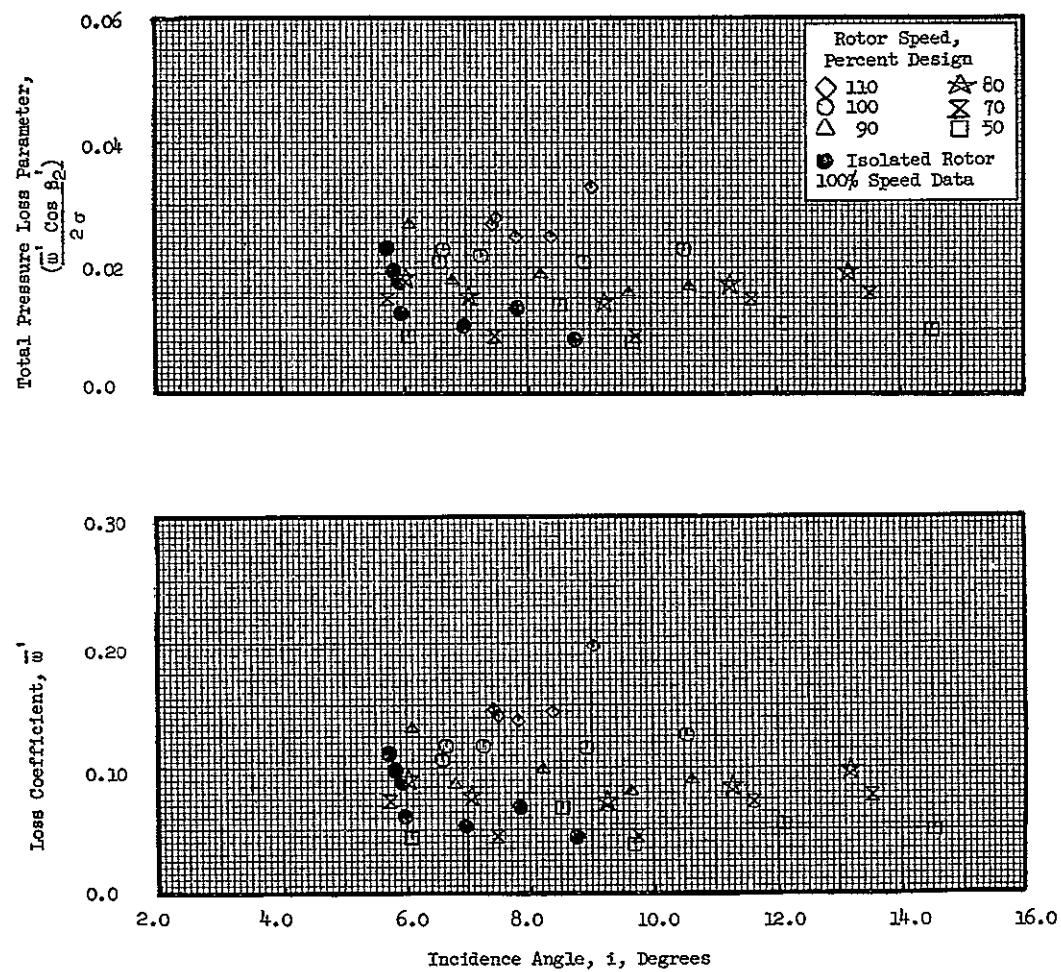


Figure 13 (f). Rotor Blade Element Data with Undistorted Inlet Flow, at 90% Immersion from Tip.

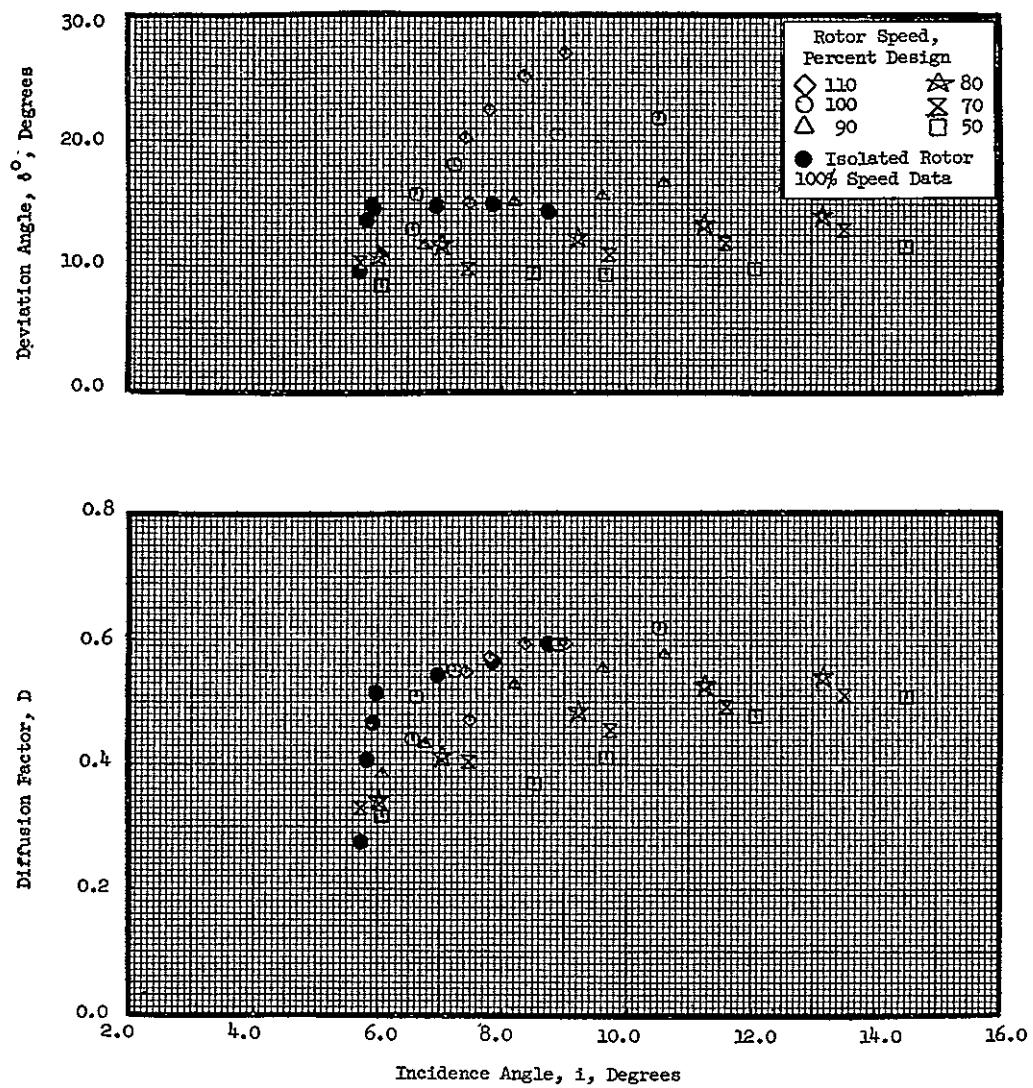


Figure 13 (f). Rotor Blade Element Data with Undistorted Inlet Flow, at 90% Immersion from Tip (Concluded).

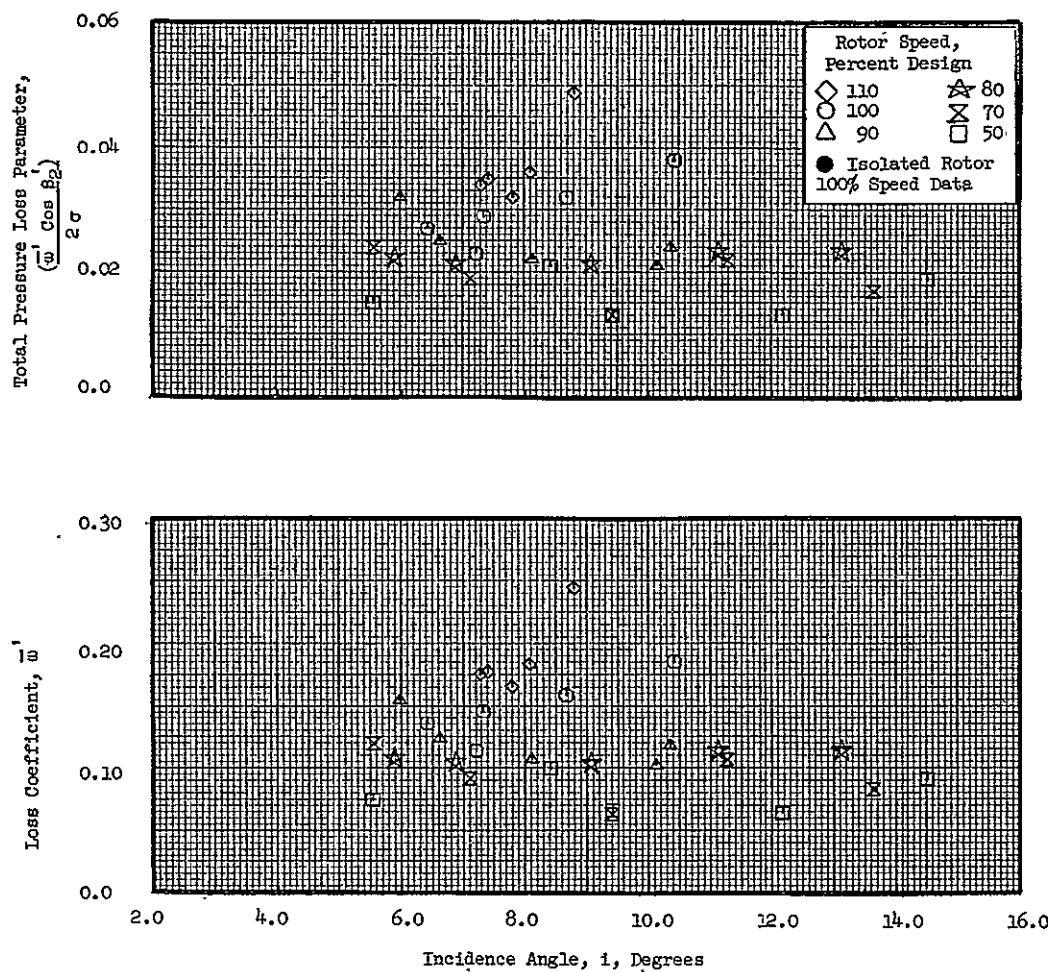


Figure 13 (g). Rotor Blade Element Data with Undistorted Inlet Flow, at 95% Immersion from Tip.

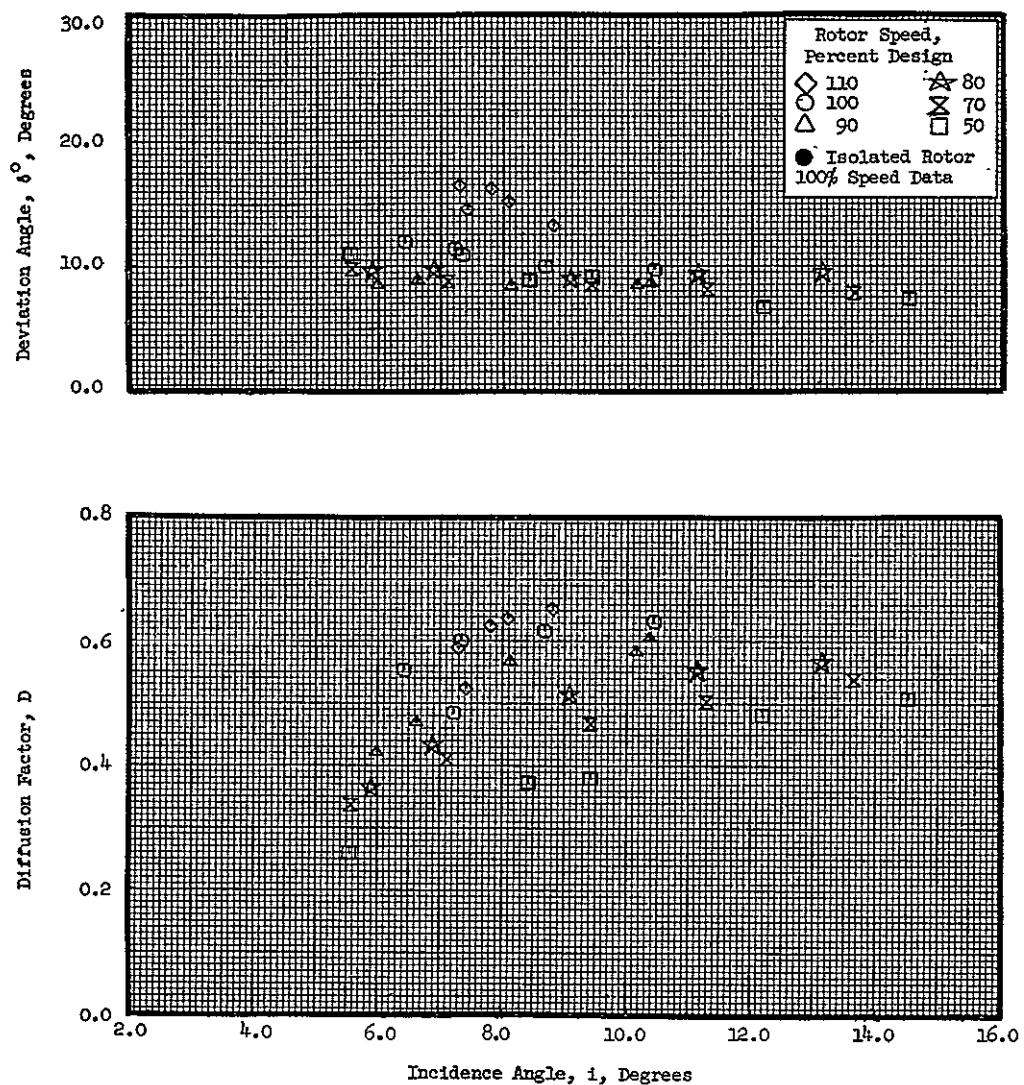


Figure 13 (g). Rotor Blade Element Data with Undistorted Inlet Flow, at 95% Immersion from Tip (Concluded).

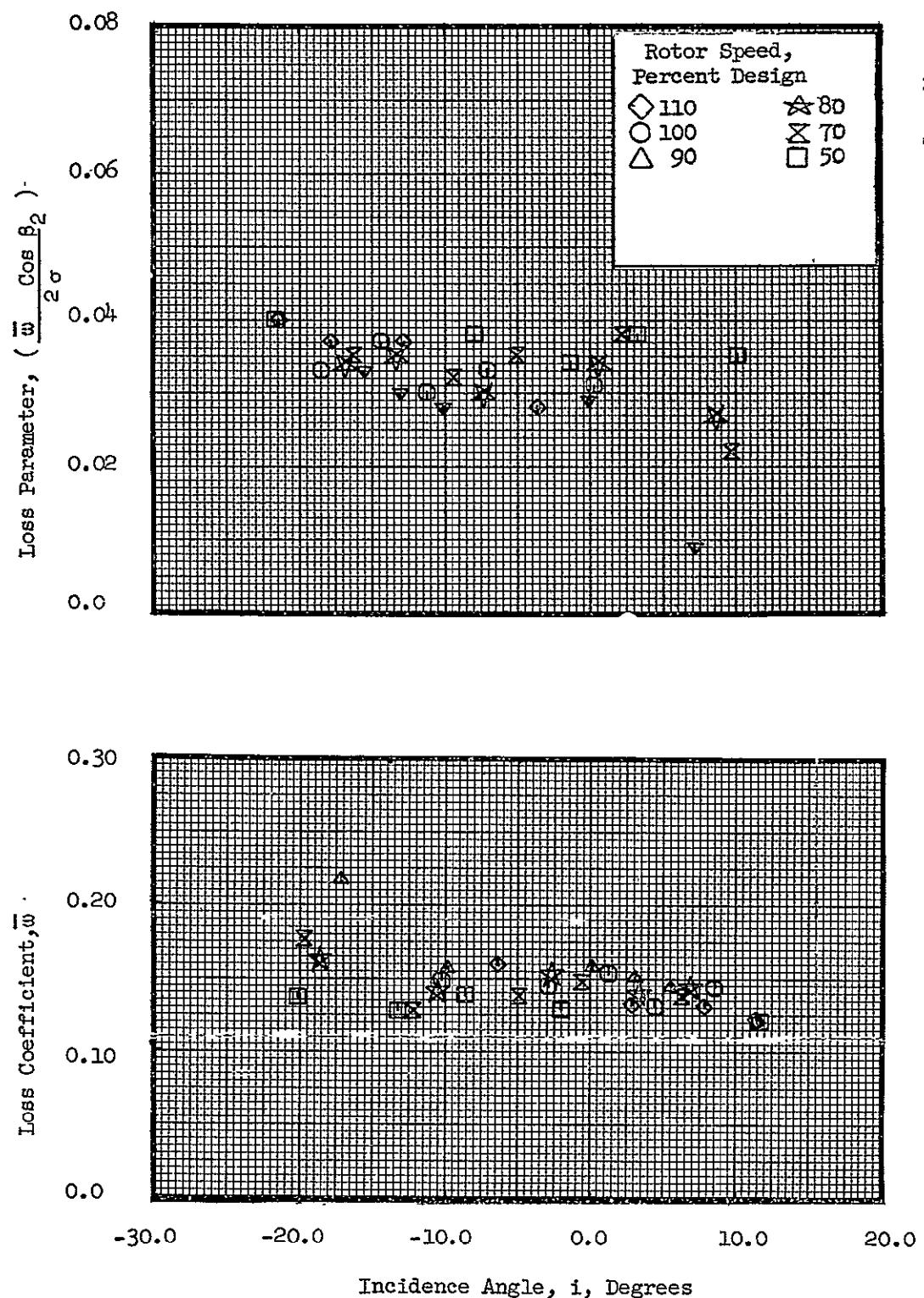


Figure 14 (a). Stator Blade Element Data with Undistorted Inlet Flow, at 5% Immersion from Tip.

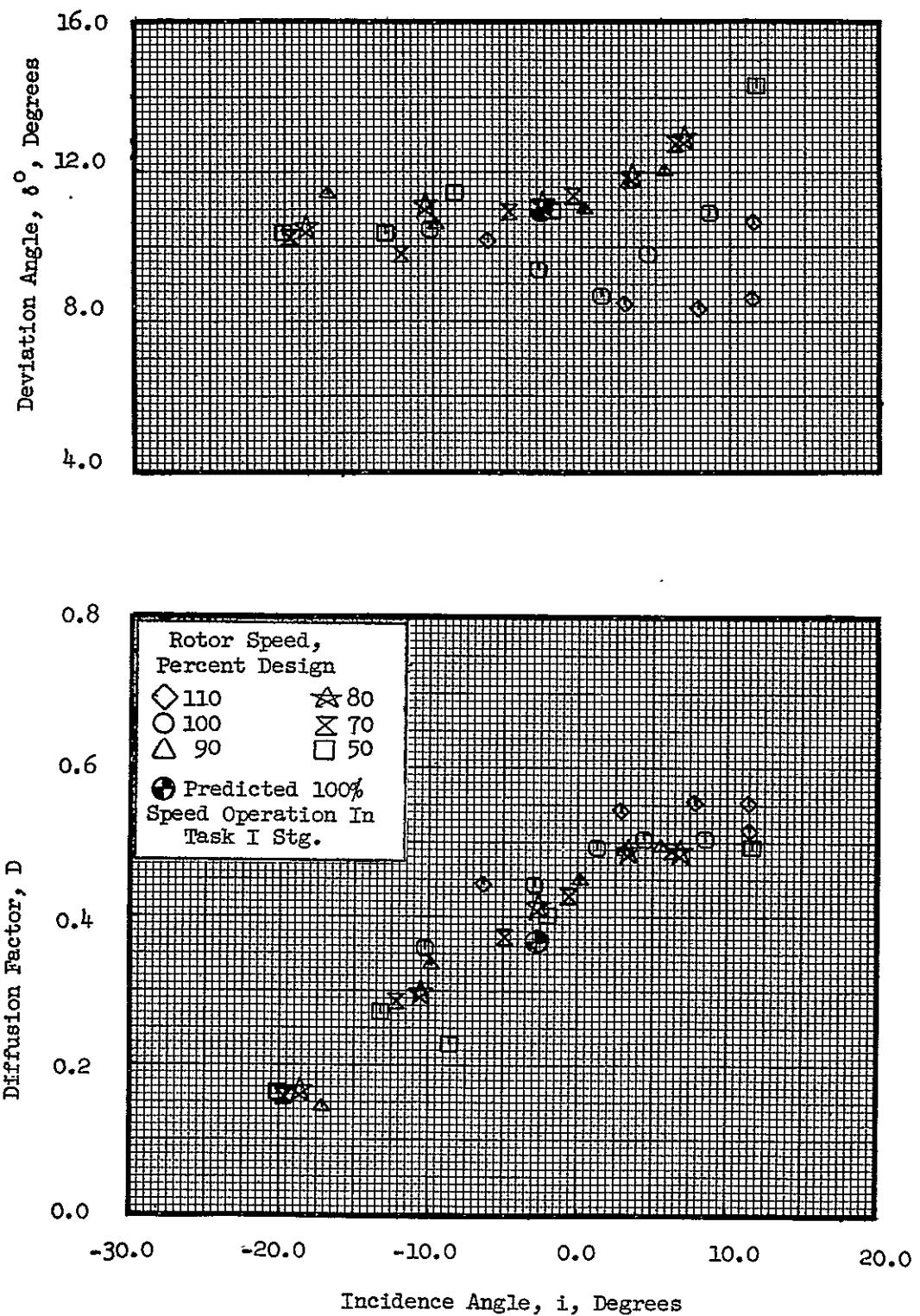


Figure 14 (a). Stator Blade Element Data with Undistorted Inlet Flow, at 5% Immersion from Tip (Concluded).

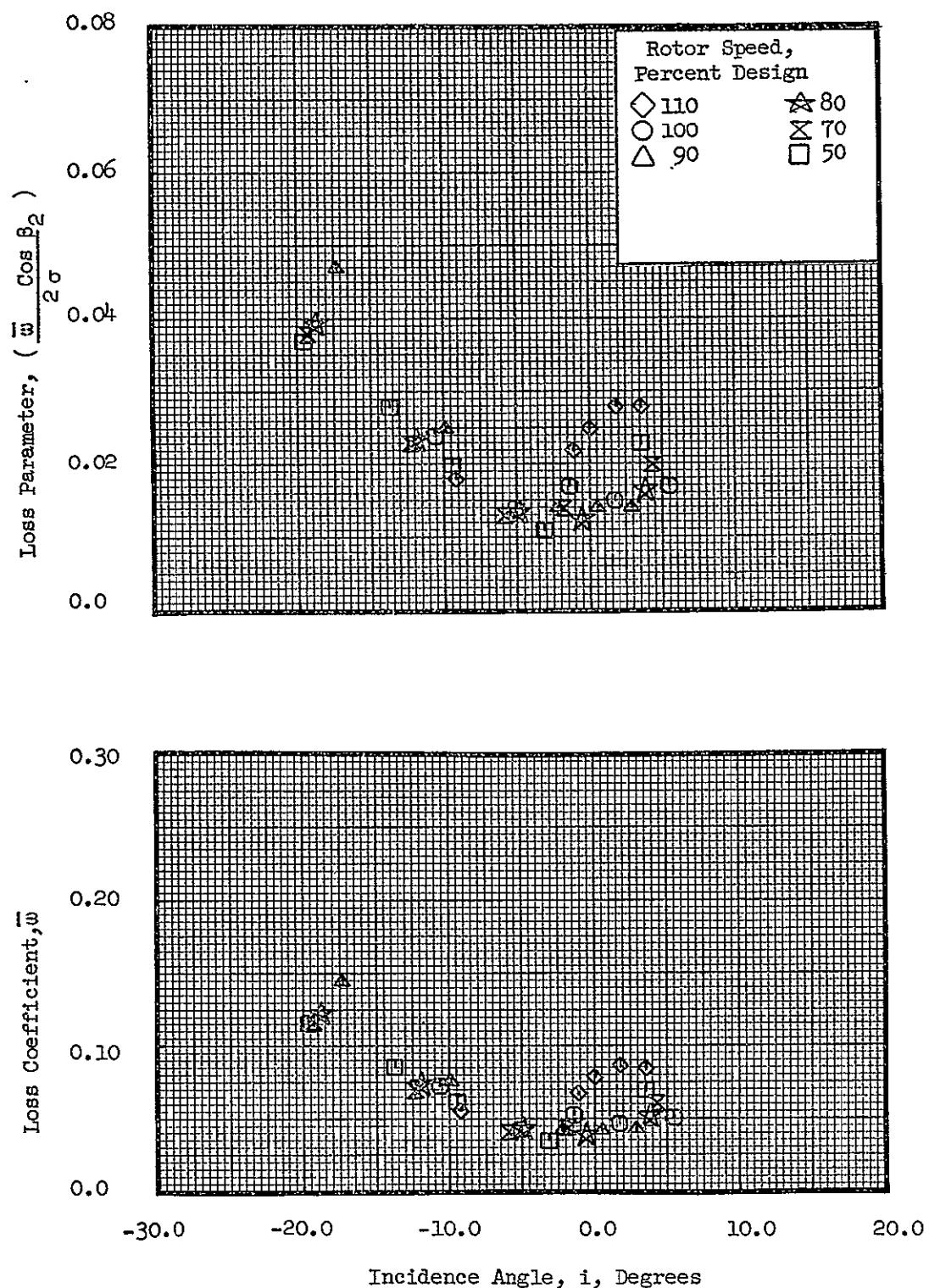


Figure 14 (b). Stator Blade Element Data with Undistorted Inlet Flow, at 10% Immersion from Tip.

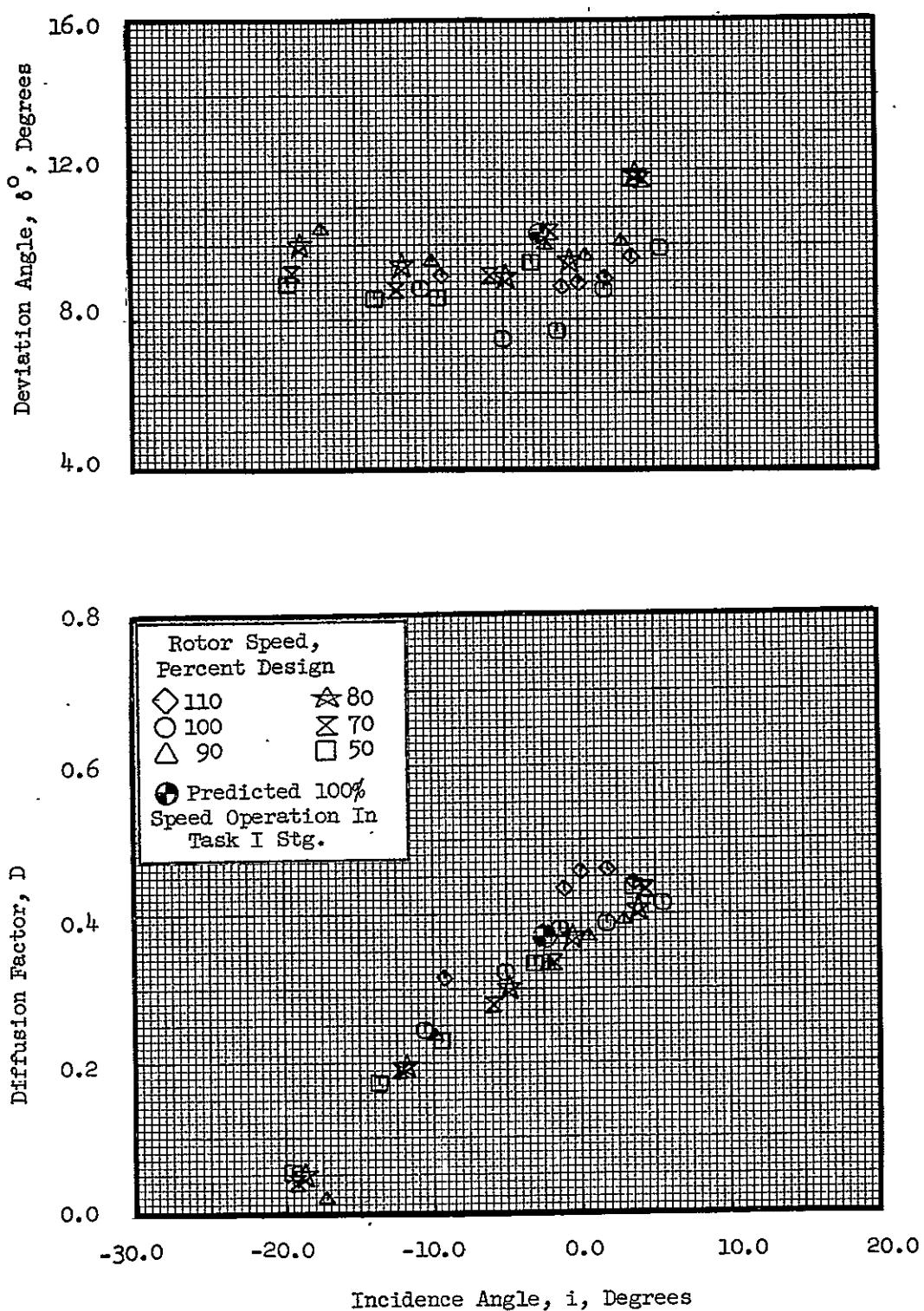


Figure 14 (b). Stator Blade Element Data with Undistorted Inlet Flow, at 10% Immersion from Tip (Concluded).

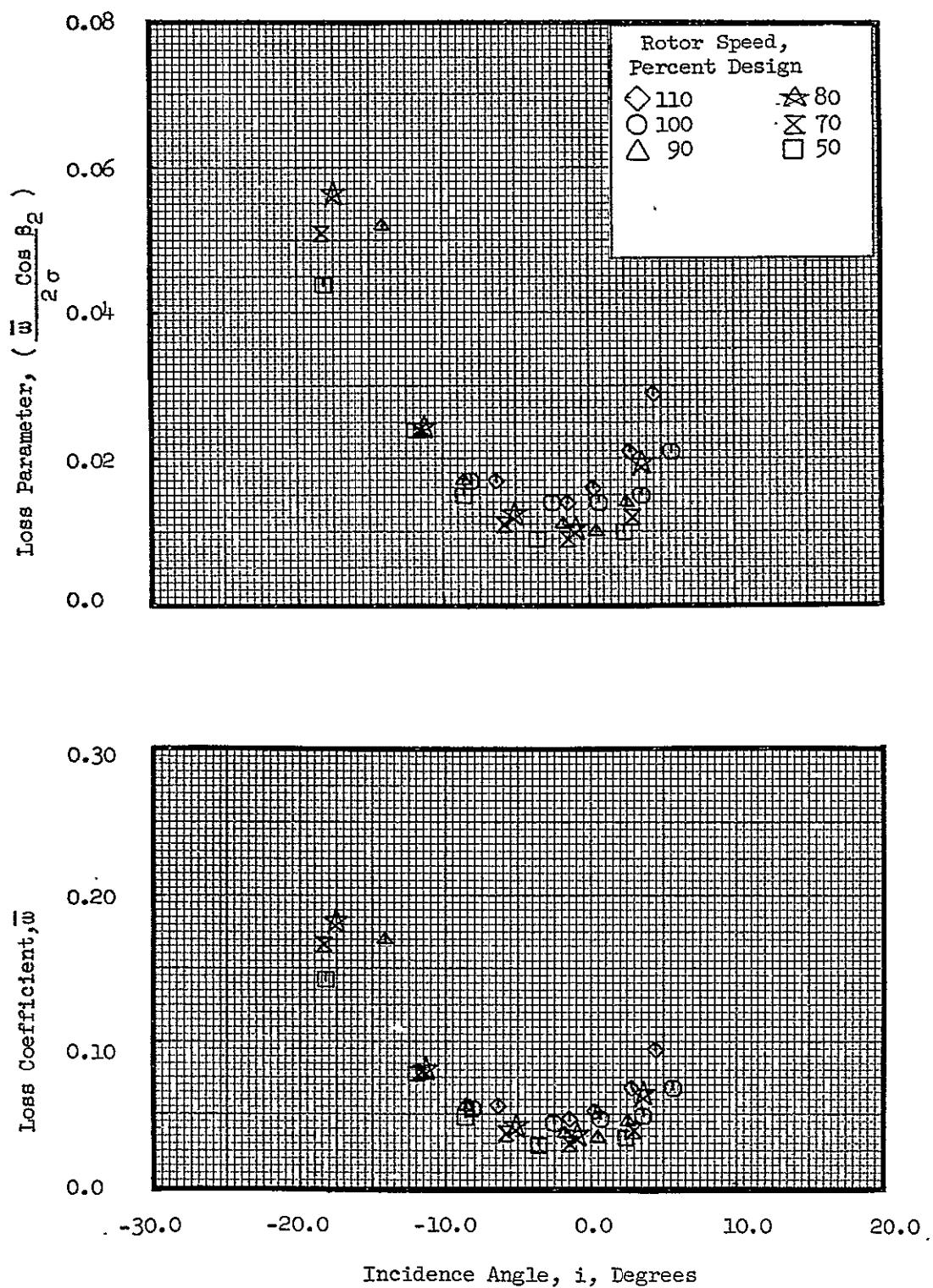


Figure 14 (c). Stator Blade Element Data with Undistorted Inlet Flow, at 30% Immersion from Tip.

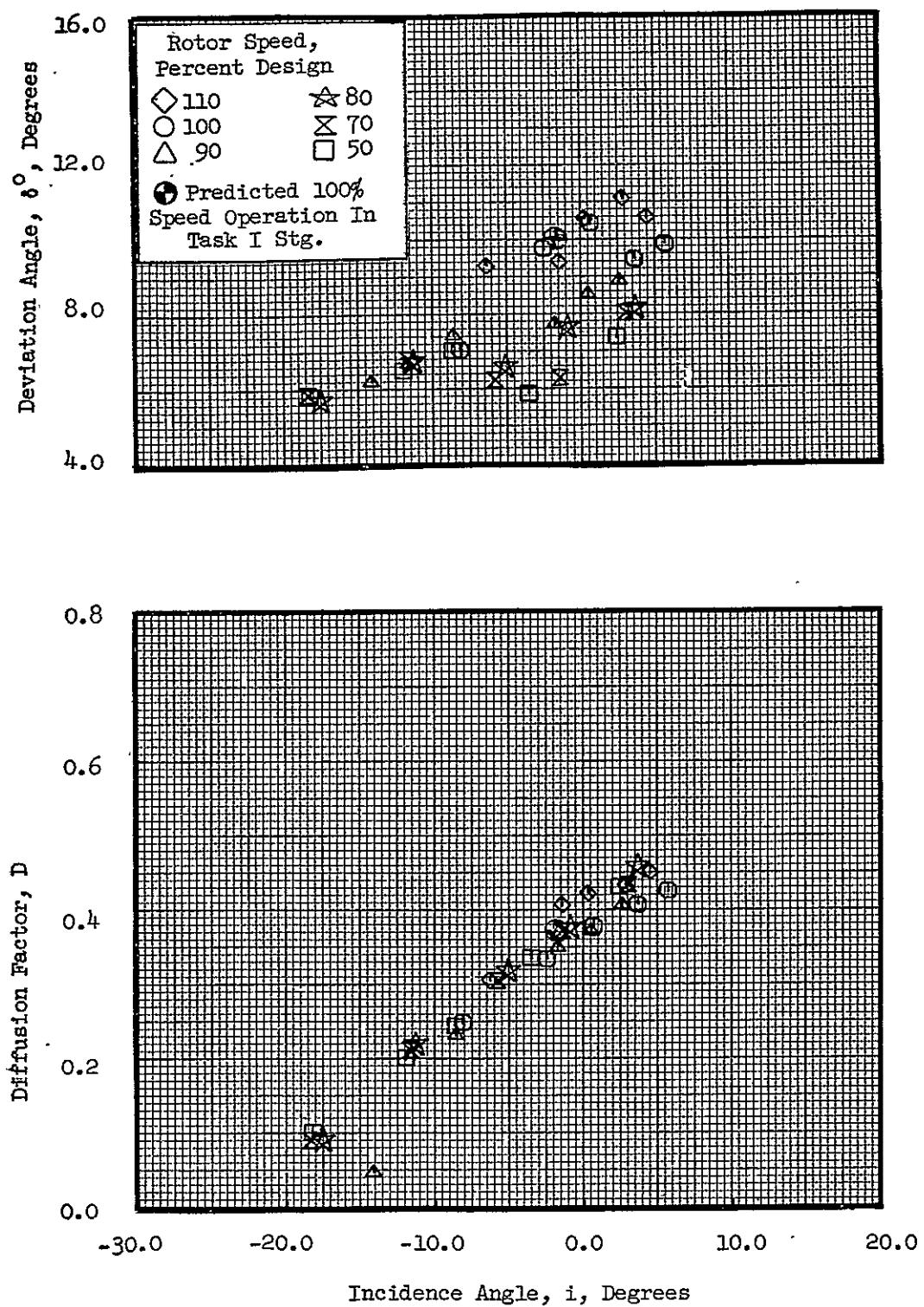


Figure 14 (c). Stator Blade Element Data with Undistorted Inlet Flow, at 30% Immersion from Tip (Concluded).

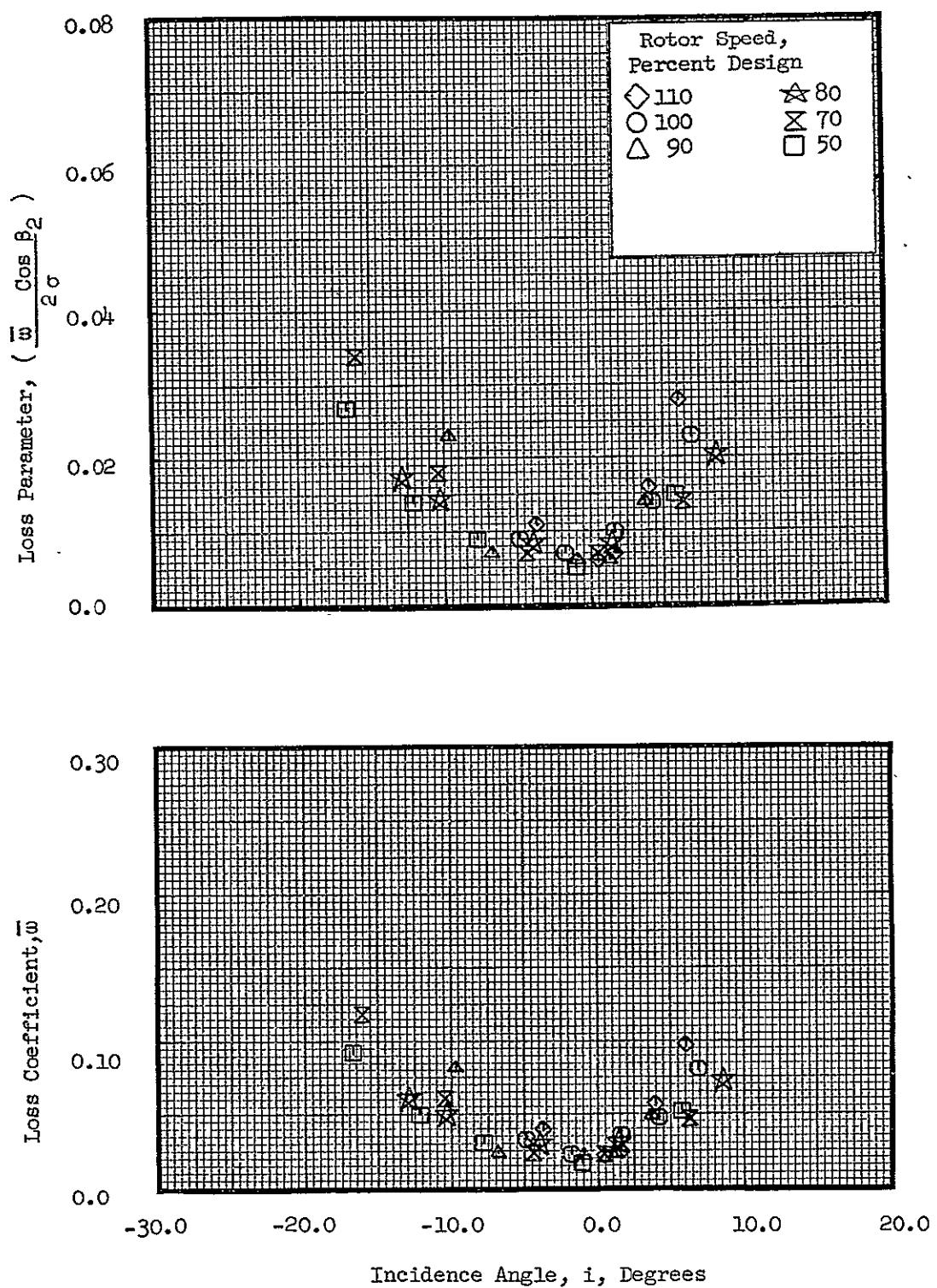


Figure 14 (d). Stator Blade Element Data with Undistorted Inlet Flow, at 50% Immersion from Tip.

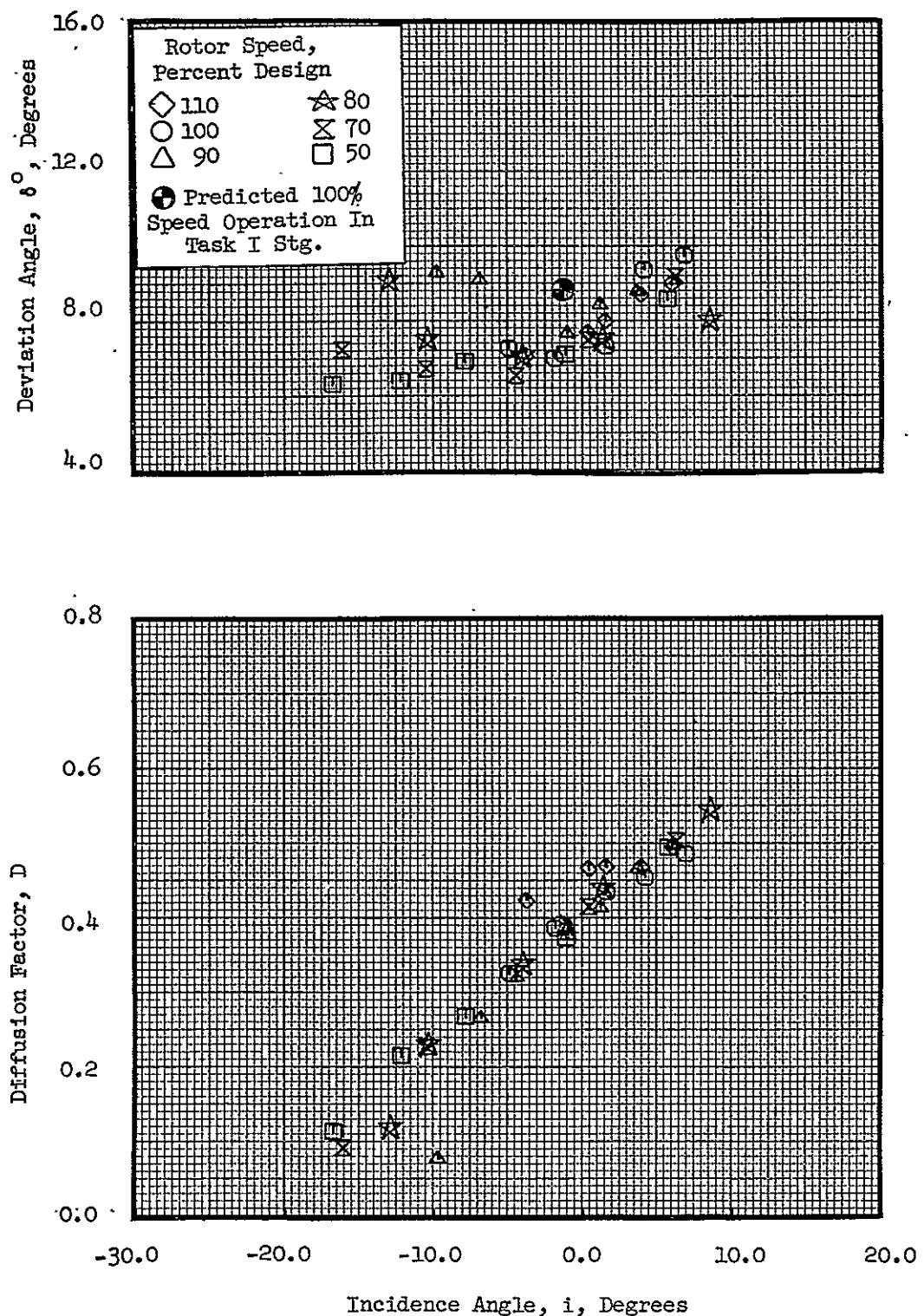


Figure 14 (d). Stator Blade Element Data with Undistorted Inlet Flow, at 50% Immersion from Tip (Concluded).

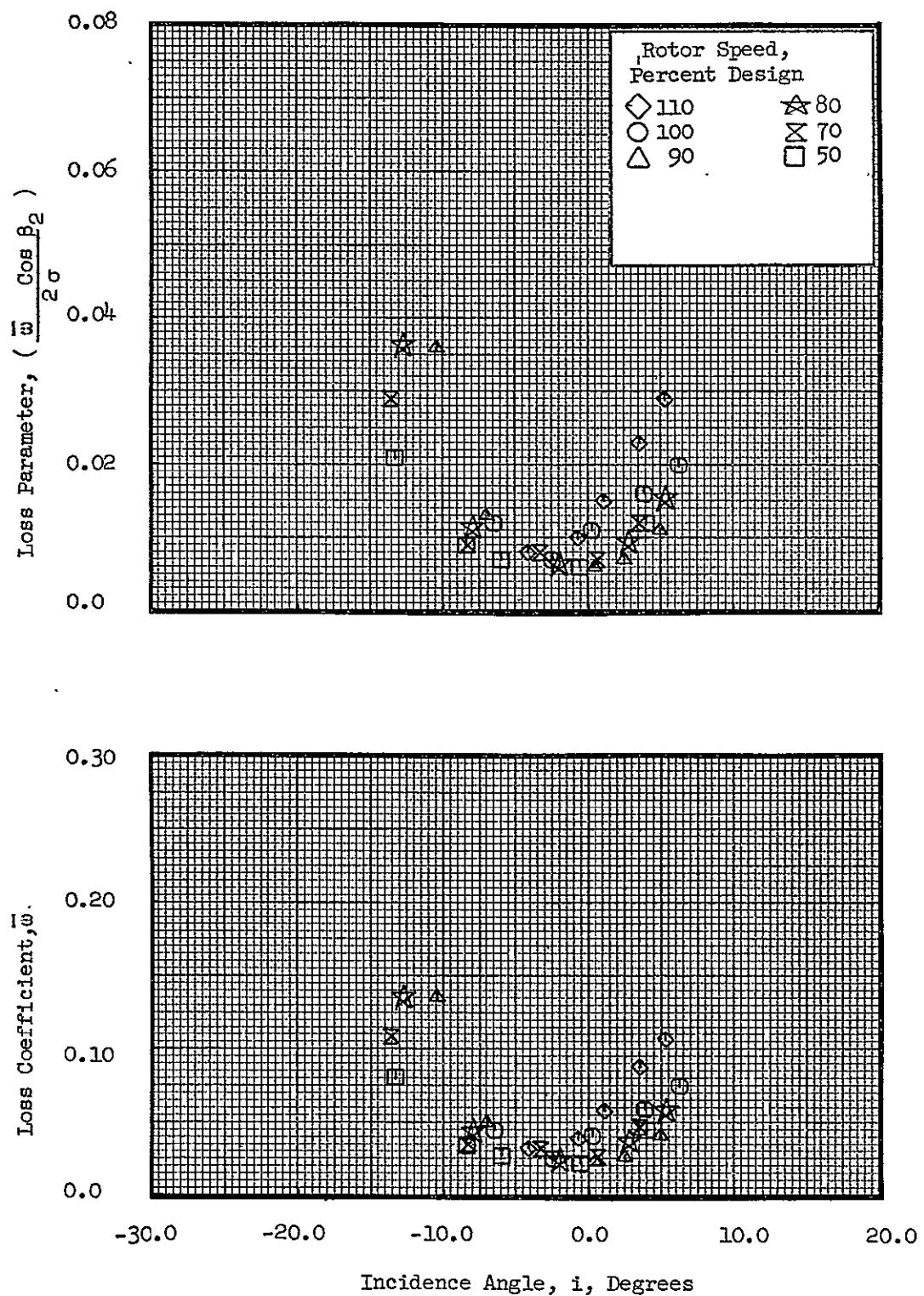


Figure 14 (e). Stator Blade Element Data with Undistorted Inlet Flow, at 70% Immersion from Tip.

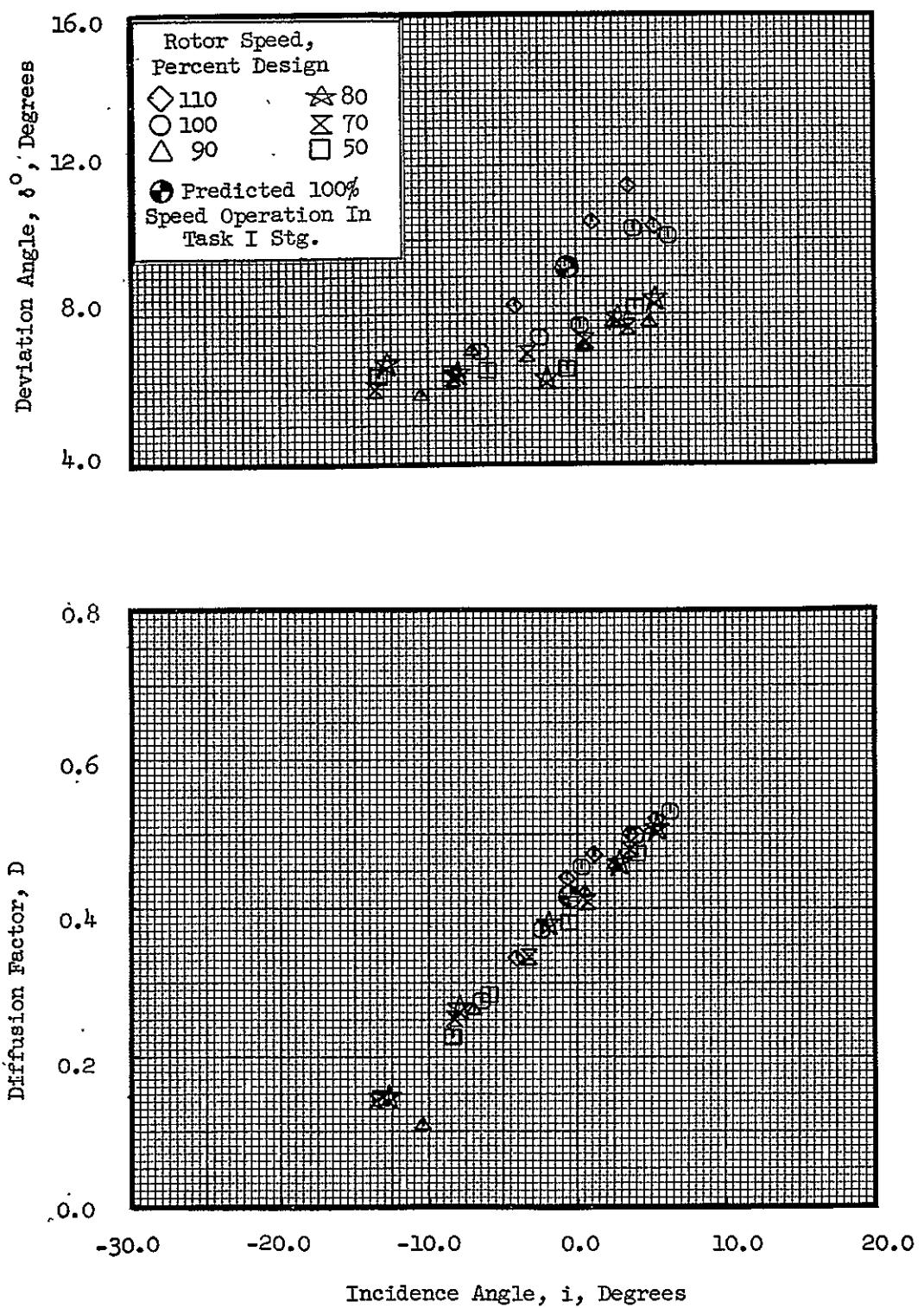


Figure 14 (e). Stator Blade Element Data with Undistorted Inlet Flow, at 70% Immersion from Tip (Concluded).

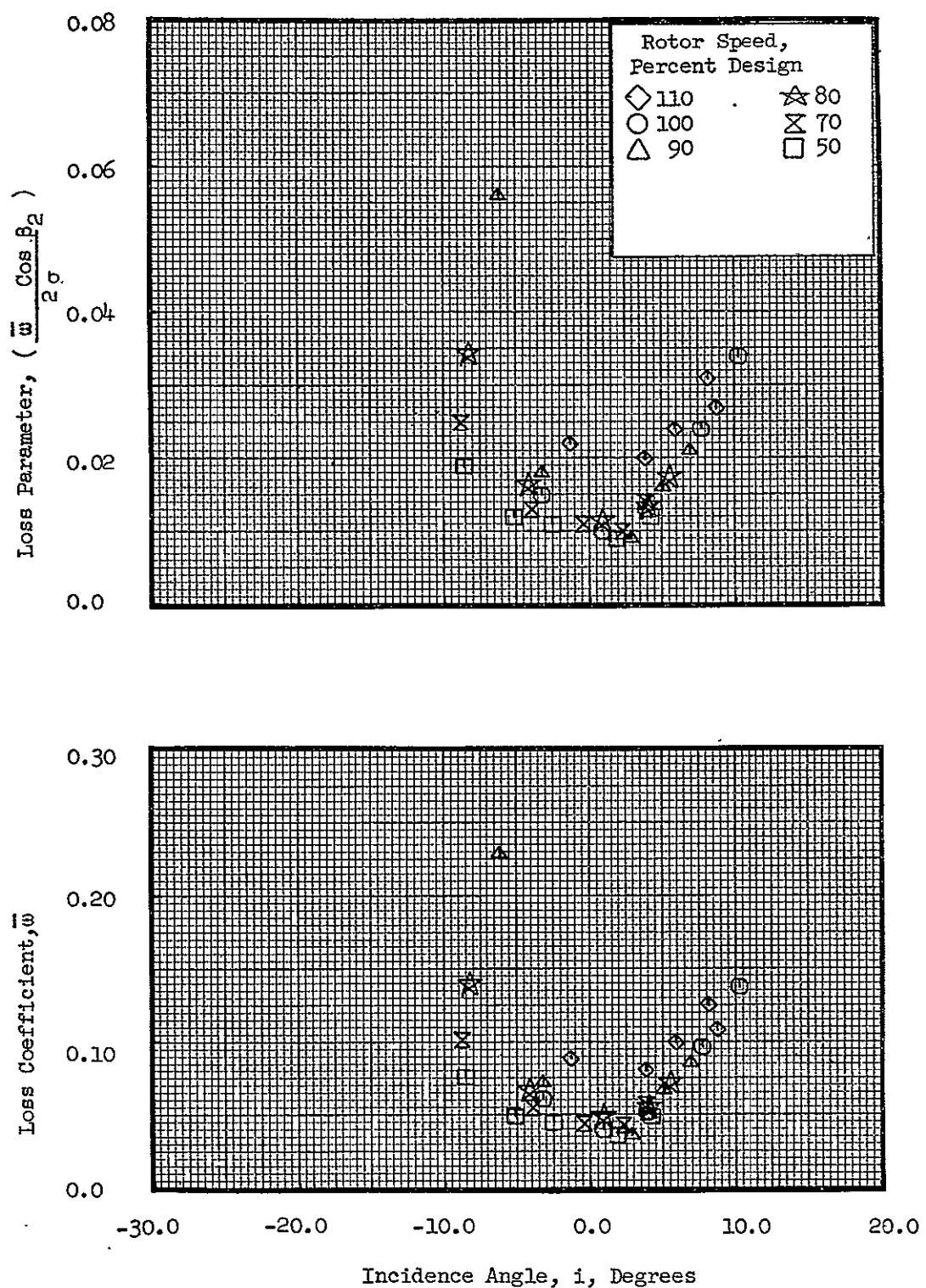


Figure 14 (f). Stator Blade Element Data with Undistorted Inlet Flow, at 90% Immersion from Tip.

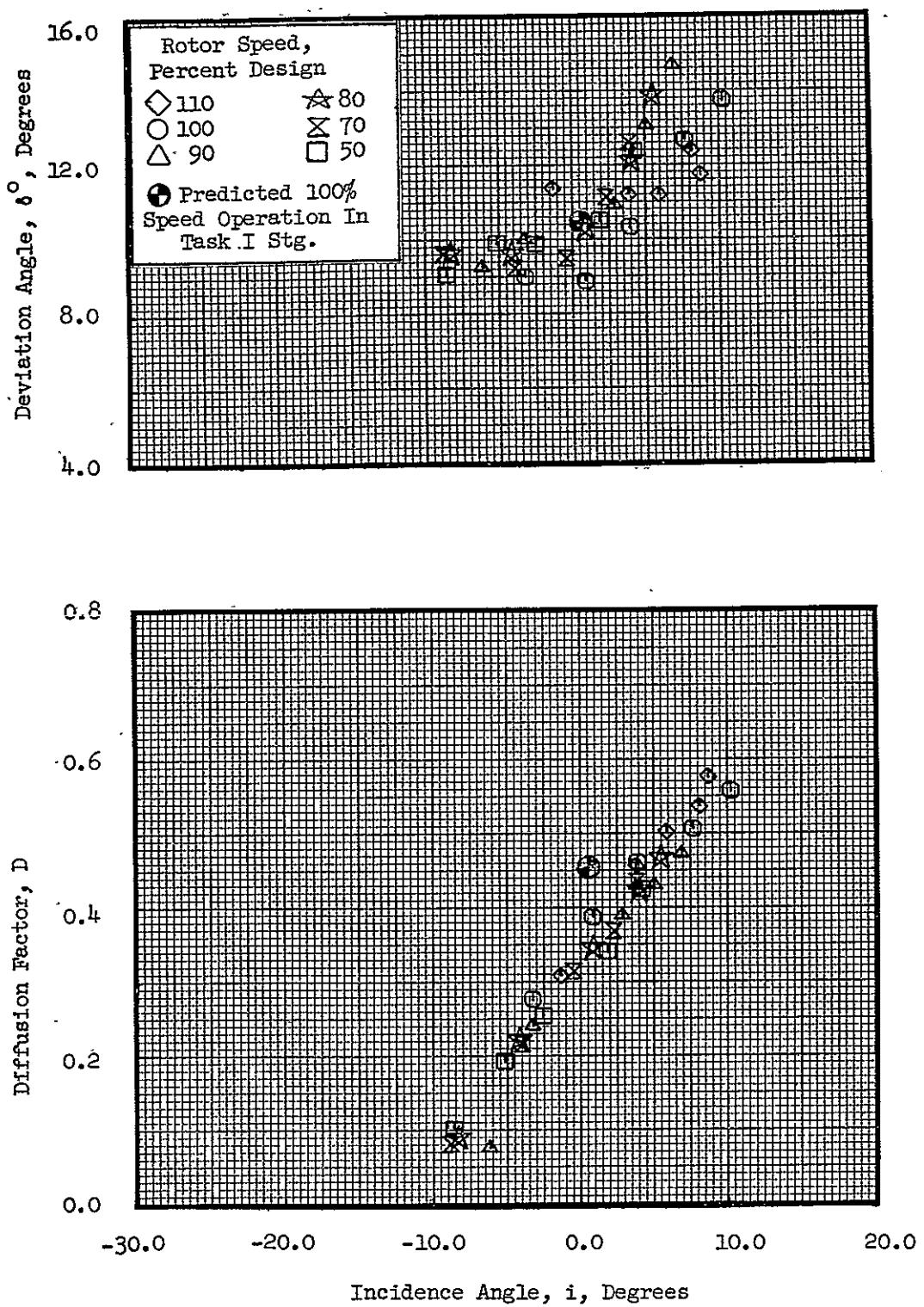


Figure 14 (f). Stator Blade Element Data with Undistorted Inlet Flow, at 90% Immersion from Tip (Concluded).

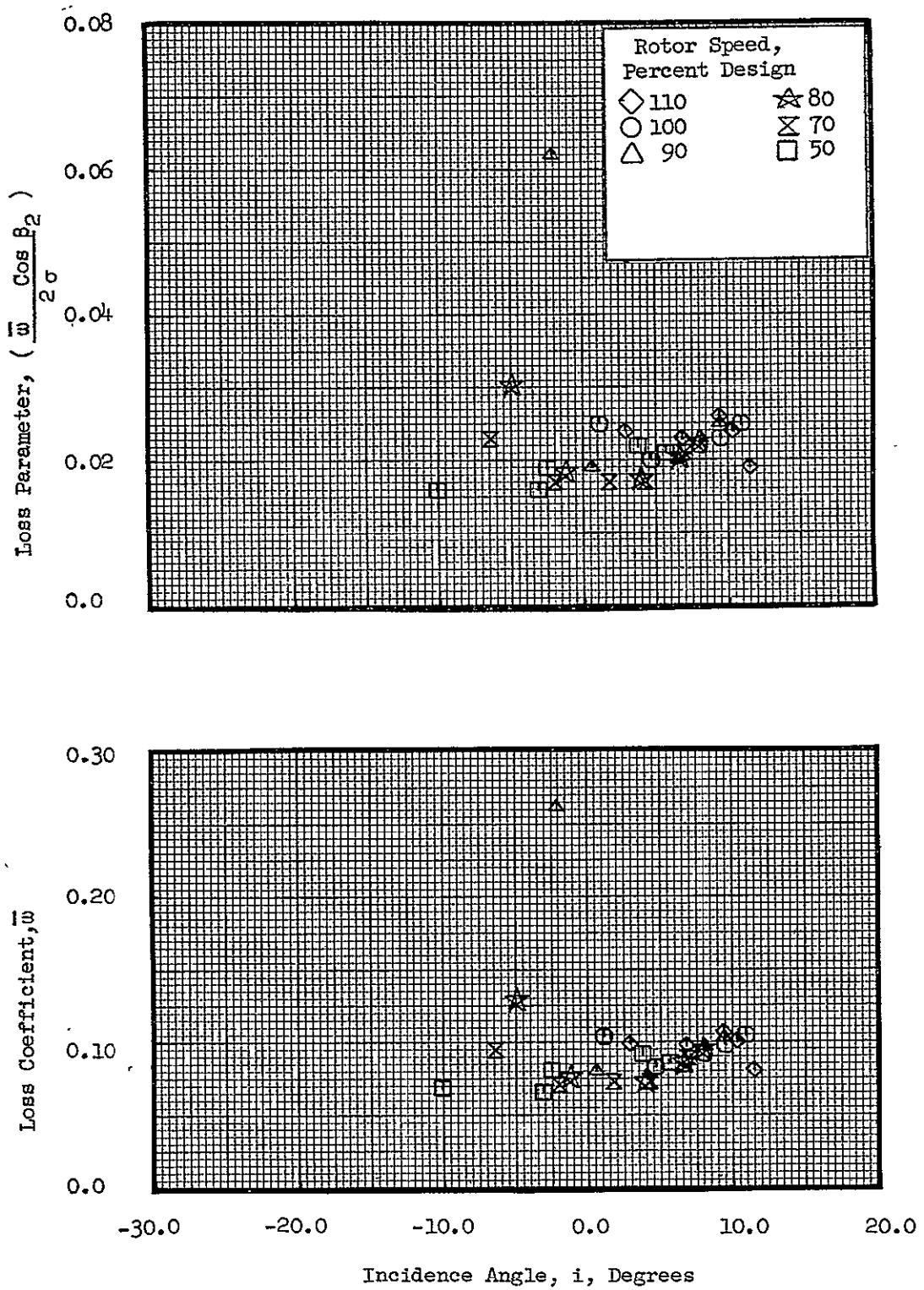


Figure 14 (g). Stator Blade Element Data with Undistorted Inlet Flow, at 95% Immersion from Tip.

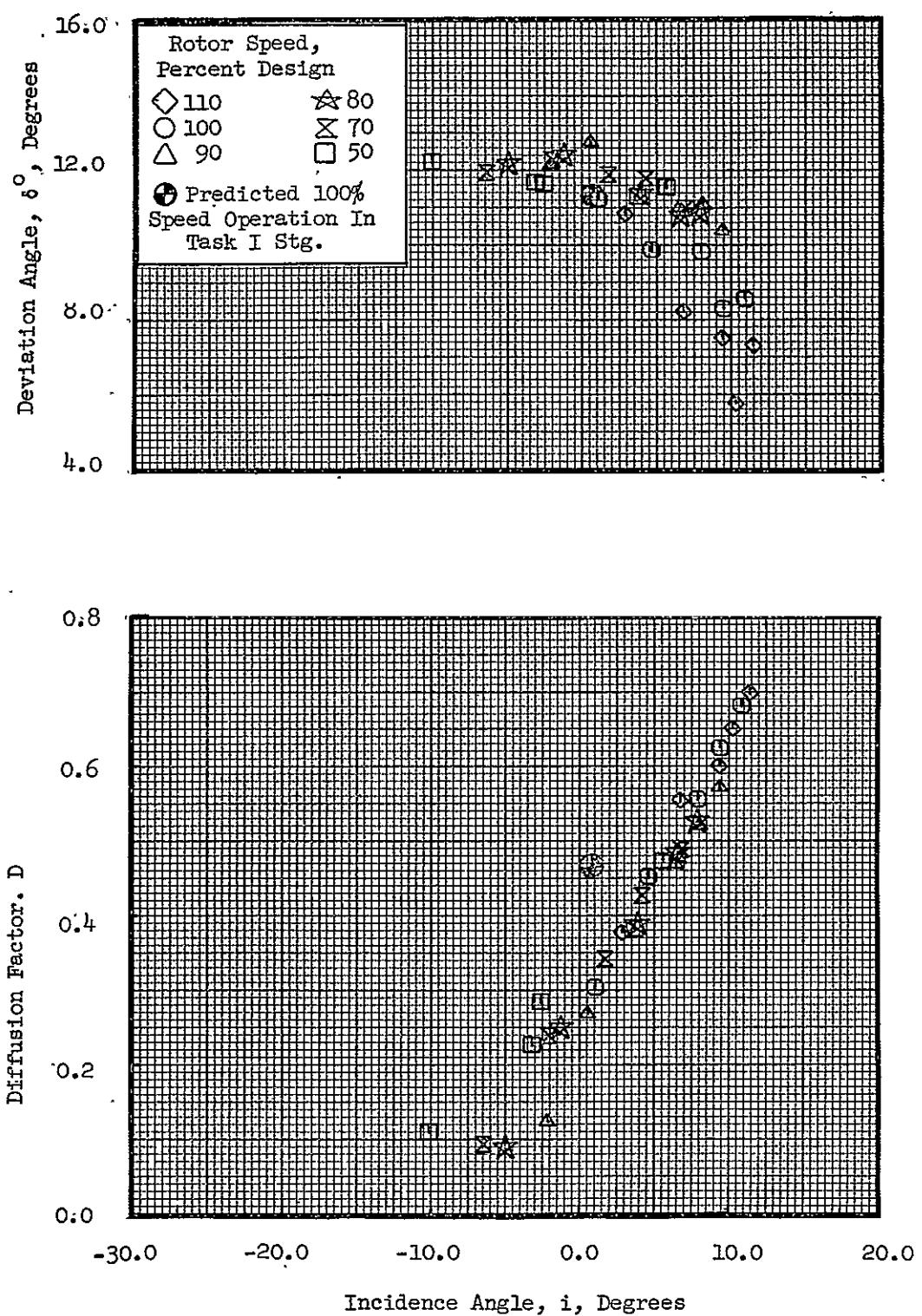


Figure 14 (g)... Stator Blade Element Data with Undistorted Inlet Flow, at 95% Immersion from Tip (Concluded).

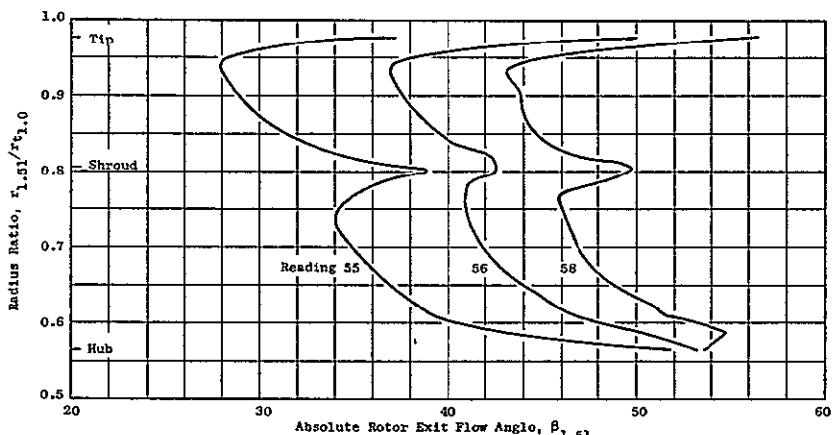
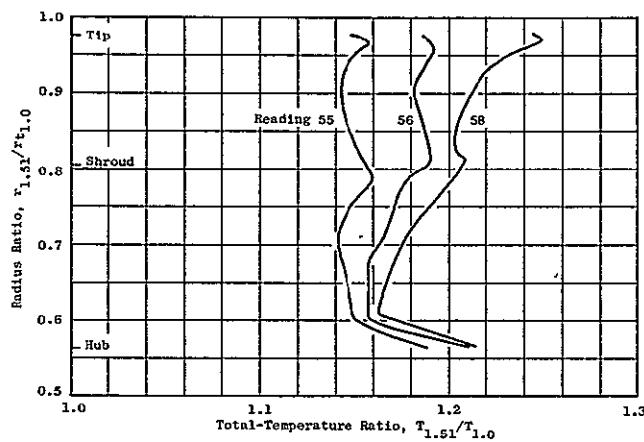
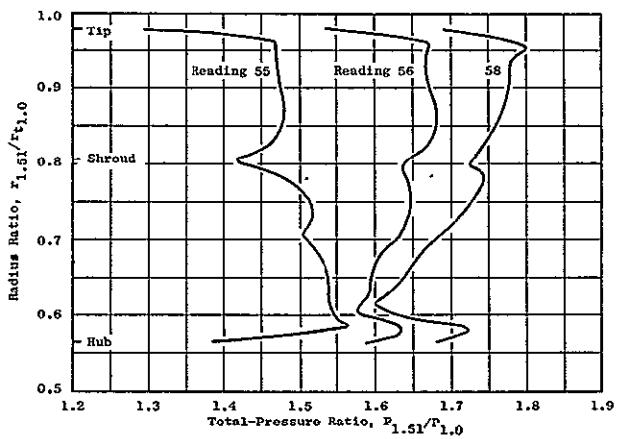


Figure 15. Continuous Traverse Data at Rotor Exit Plane 1.51 at 100% Speed with Undistorted Inlet Flow for Readings 55 (Max. Flow), 56 (Near Peak Efficiency), and 58 (Near Stall).

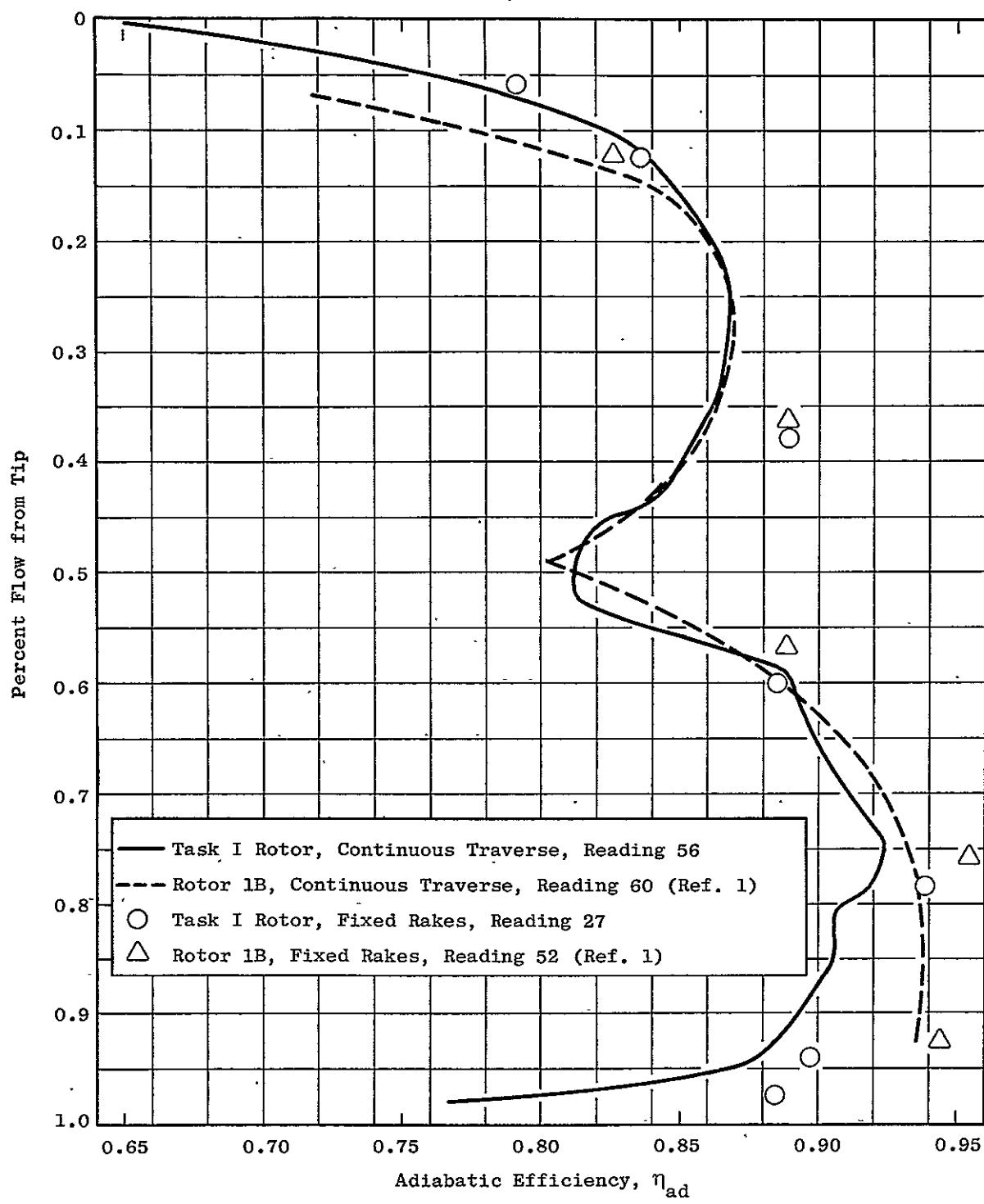


Figure 16 (a). Radial Profiles of Adiabatic Efficiency at 100% Speed  
Obtained in the Task I Stage and Rotor 1B Tests, Near  
Peak Efficiency.

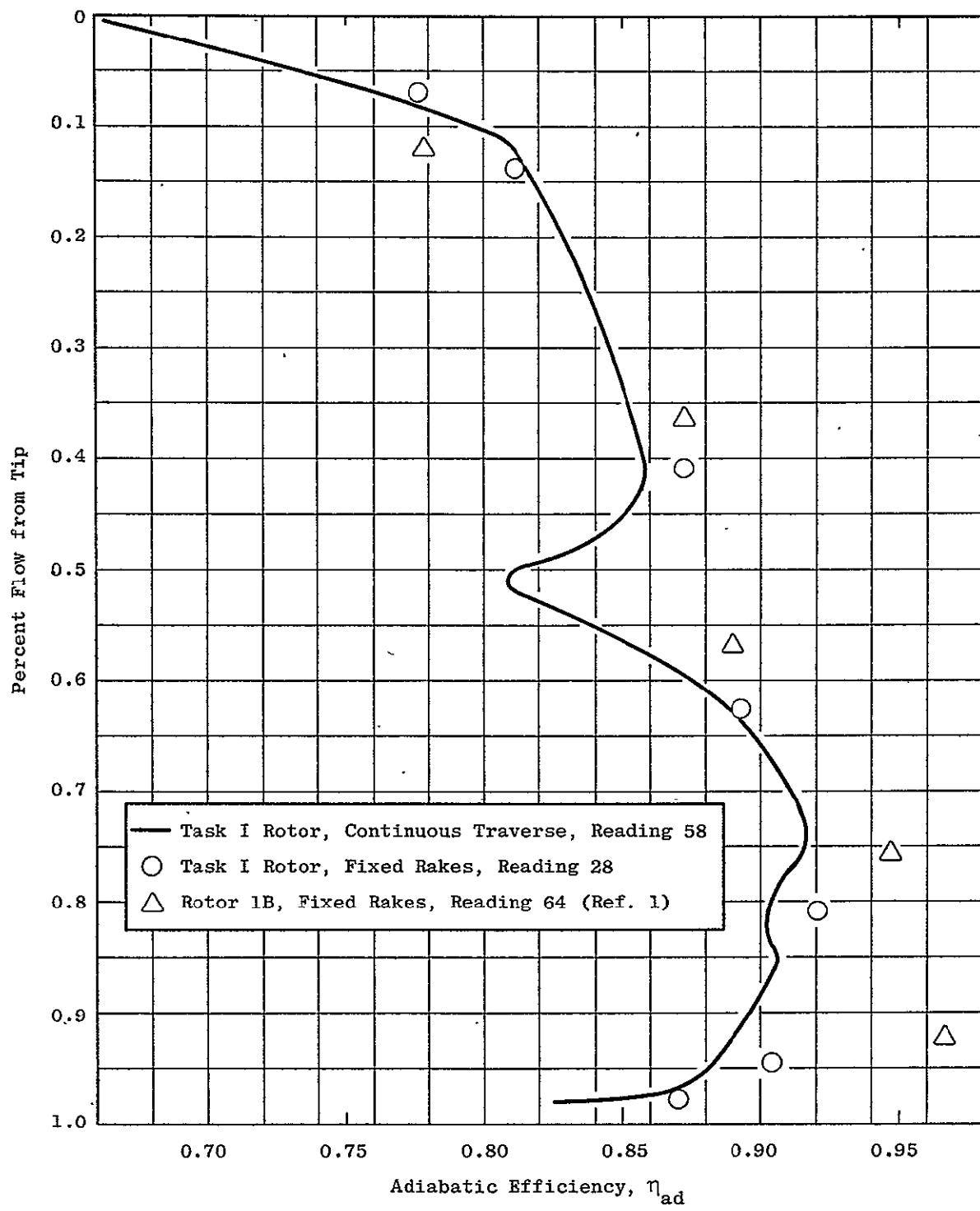


Figure 16 (b). Radial Profiles of Adiabatic Efficiency at 100% Speed Obtained in the Task I Stage and Rotor 1B Tests, Near Stall.

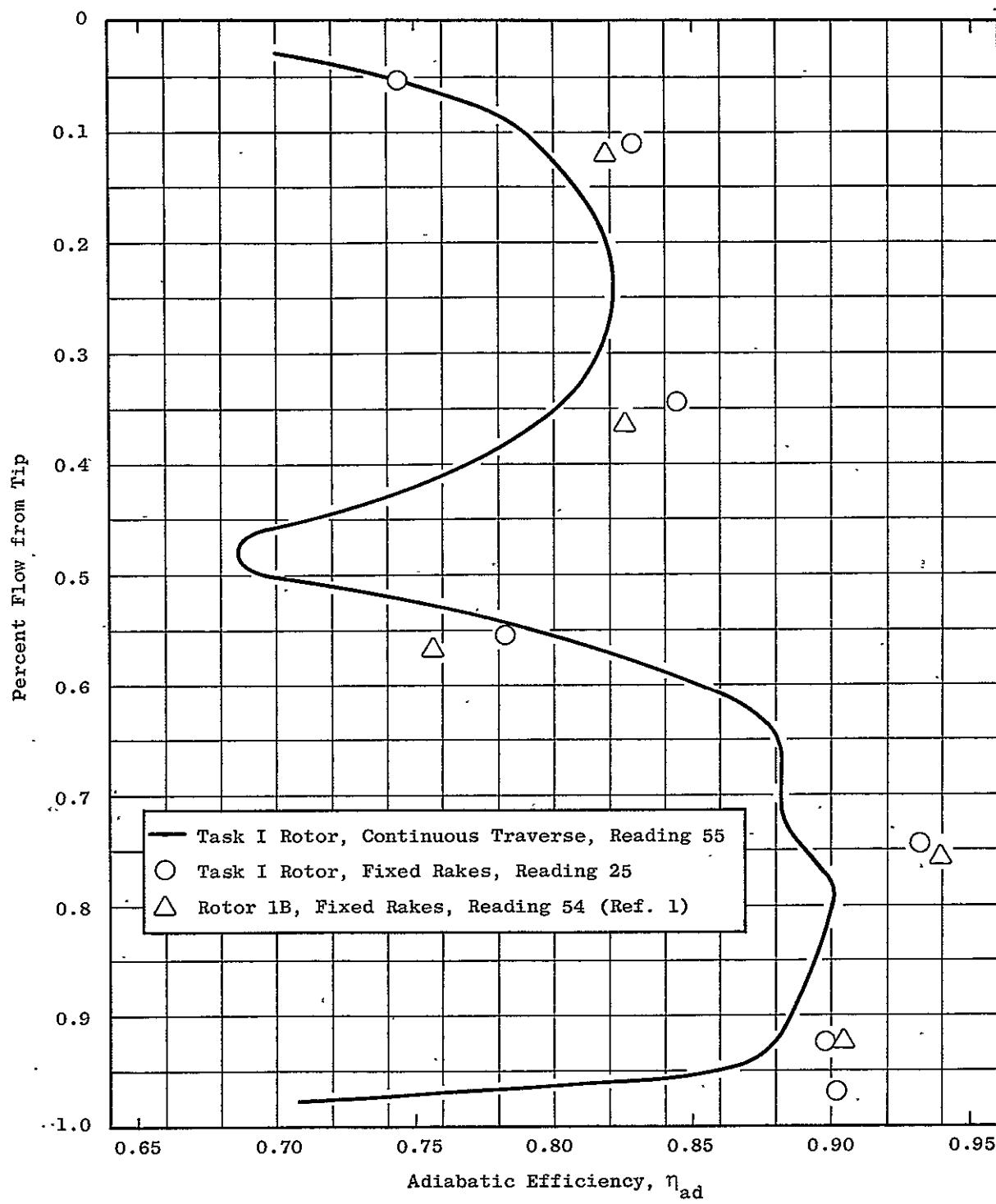


Figure 16 (c). Radial Profiles of Adiabatic Efficiency at 100% Speed  
Obtained in the Task I Stage and Rotor 1B Tests,  
Maximum Flow.

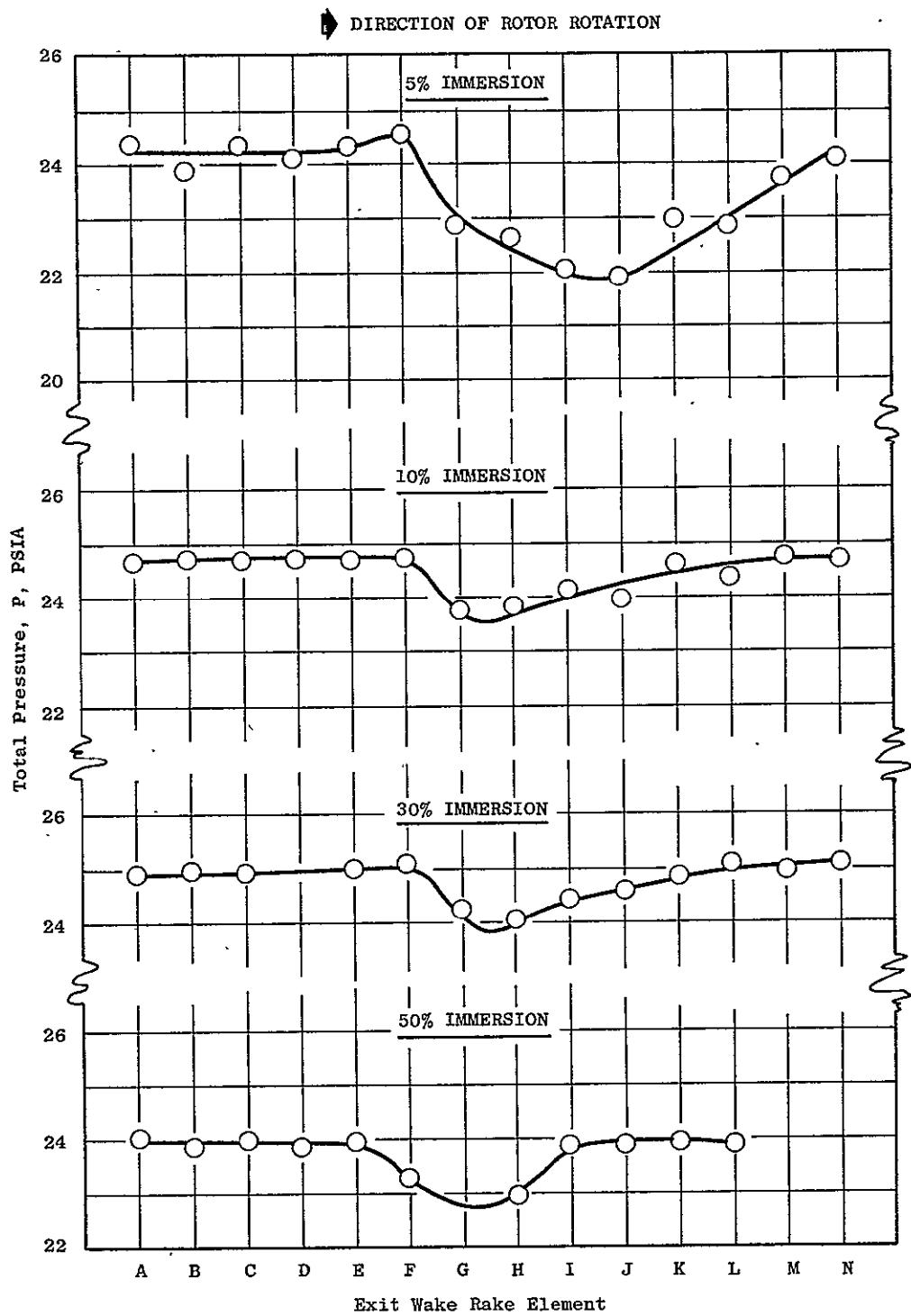


Figure 17 (a). Stator Exit Total-Pressure Wake Profiles at 100% Speed with Undistorted Inlet Flow, Near Peak Efficiency, Reading 27.

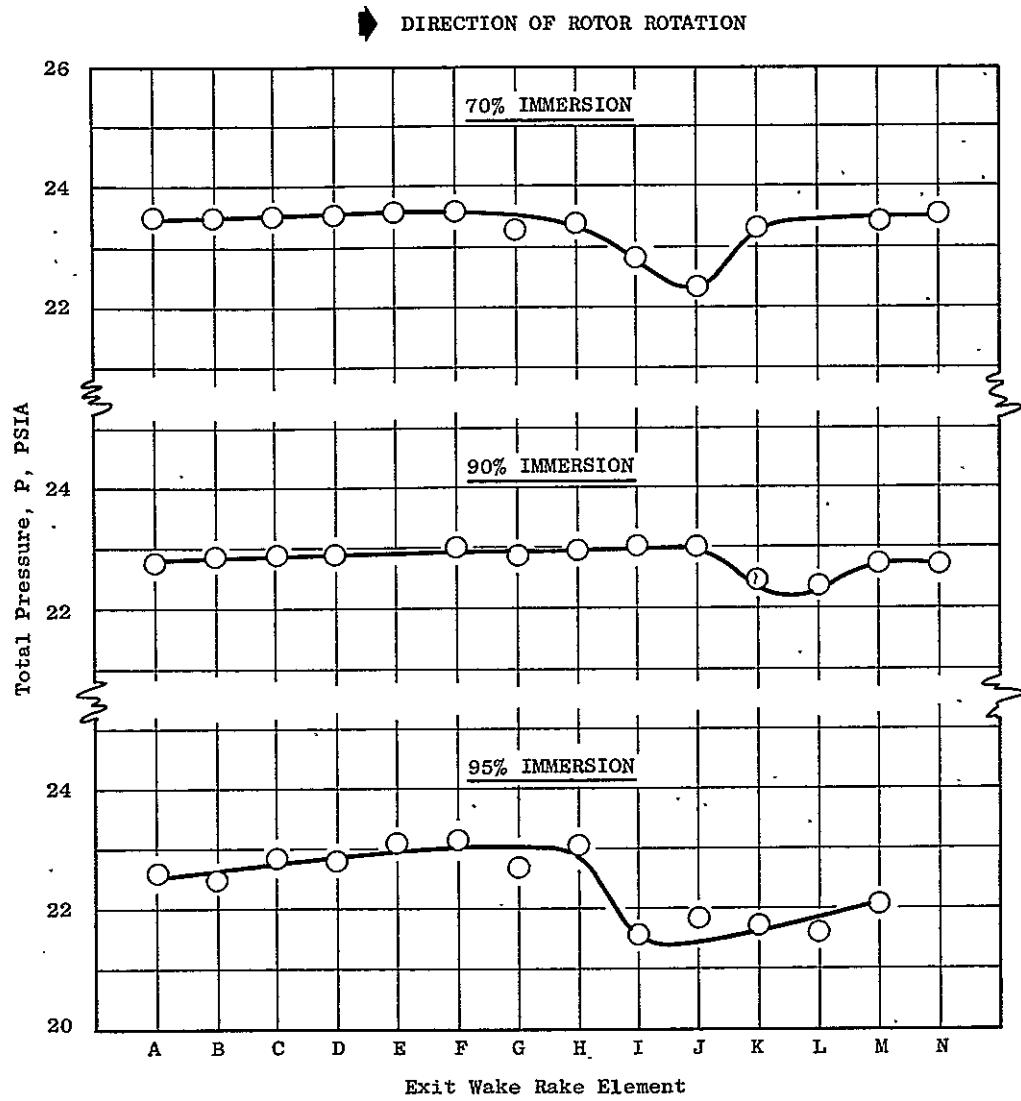


Figure 17 (a). Stator Exit Total-Pressure Wake Profiles at 100% Speed with Undistorted Inlet Flow, Near Peak Efficiency, Reading 27 (Concluded).

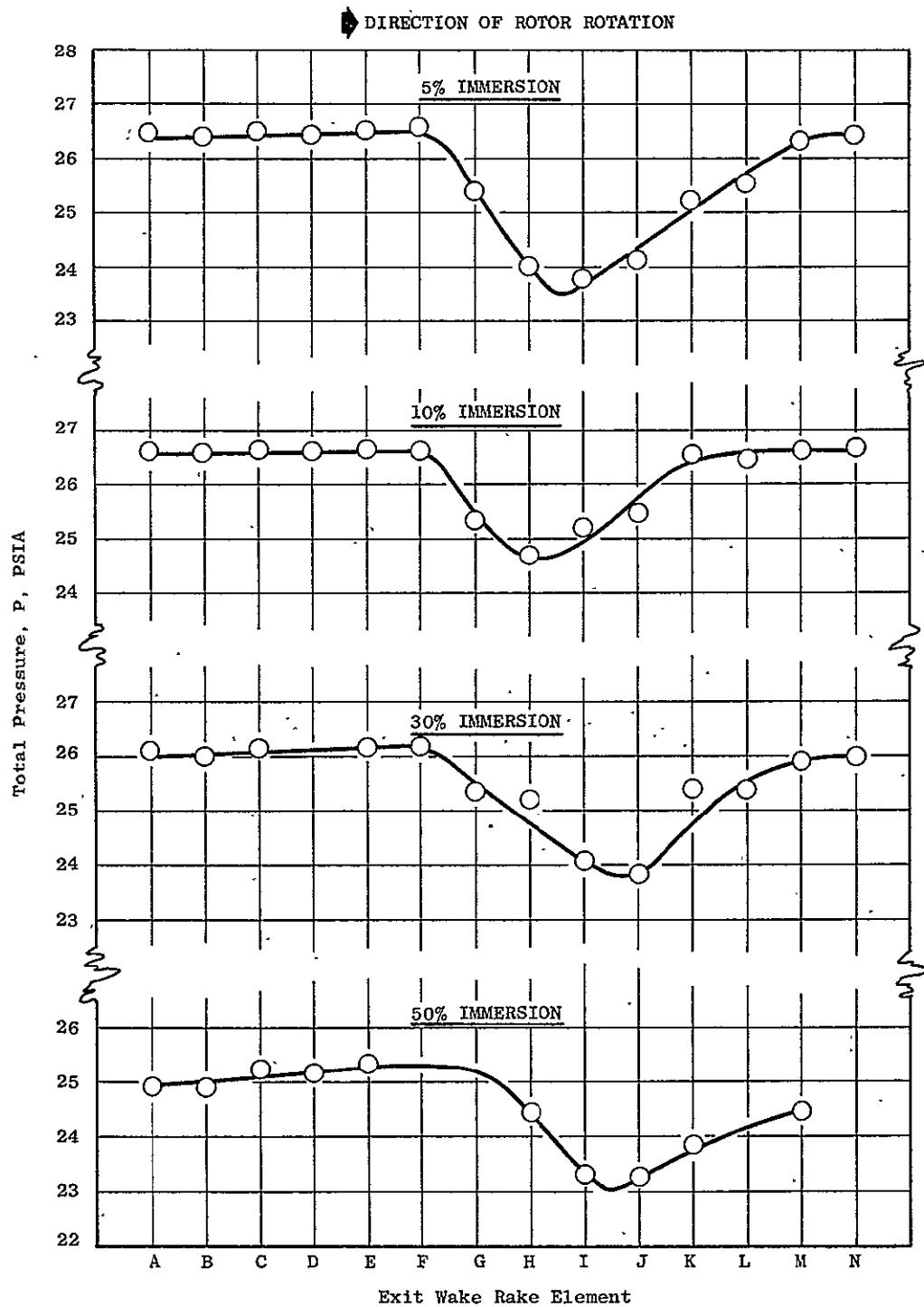


Figure 17 (b). Stator Exit Total-Pressure Wake Profiles at 100% Speed with Undistorted Inlet Flow, Near Stall, Reading 64.

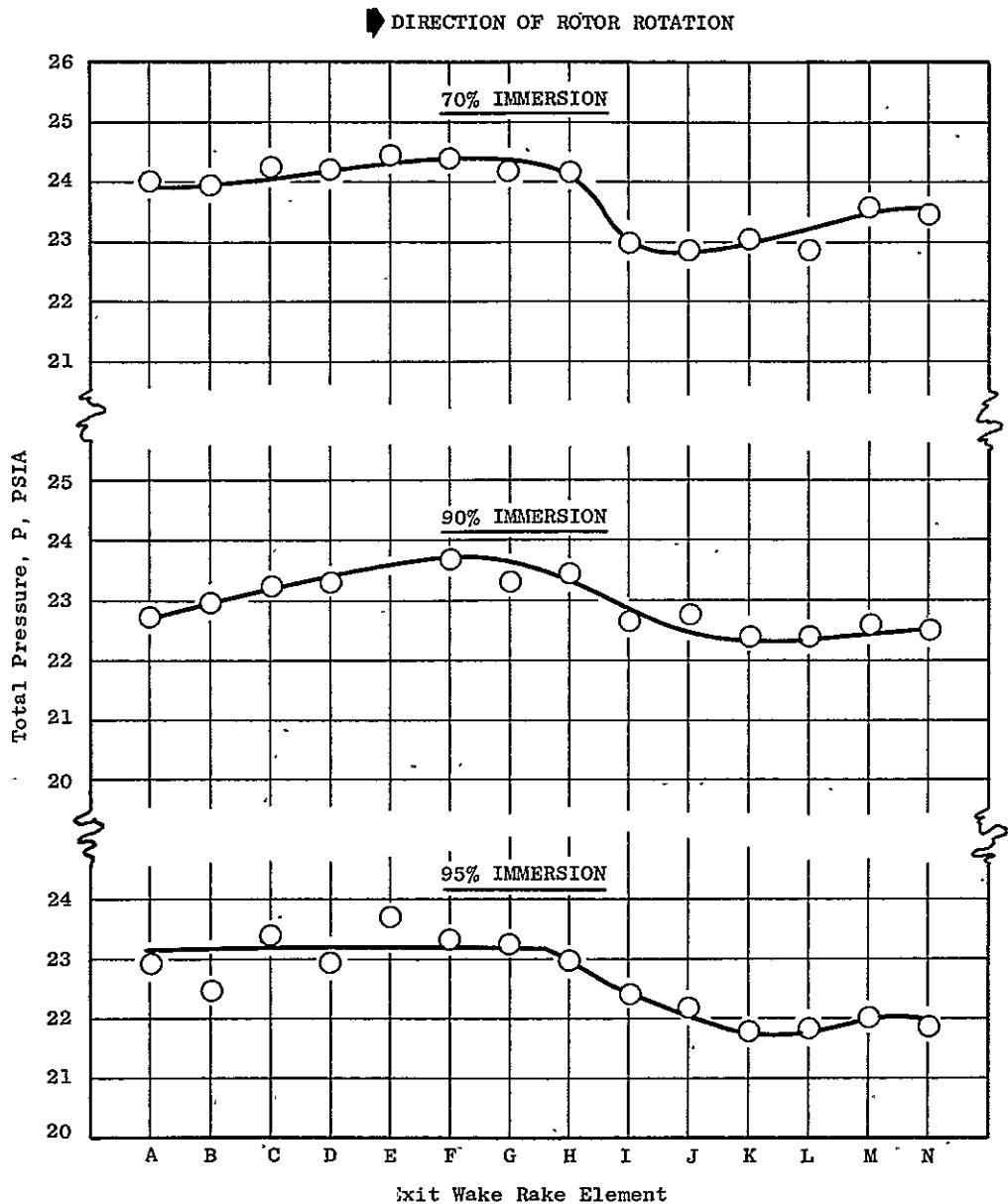


Figure 17 (b). Stator Exit Total-Pressure Wake Profiles at 100% Speed with Undistorted Inlet Flow, Near Stall, Reading 64 (Concluded).

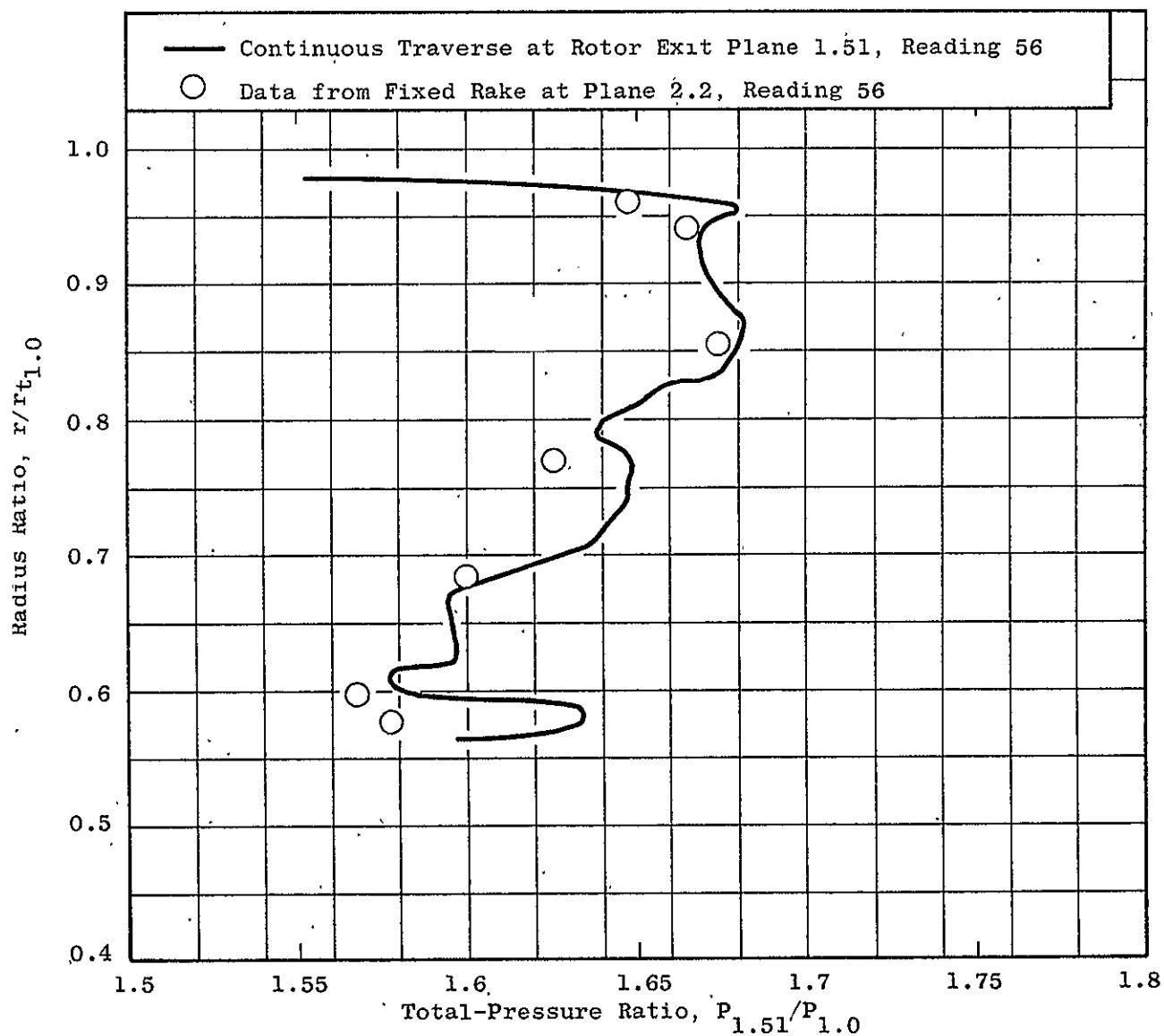


Figure 18 (a). Comparison of Radial Profiles and Rotor Total-Pressure Ratio at 100% Speed, Near Peak Efficiency; Obtained from Fixed and Traversing Instruments.

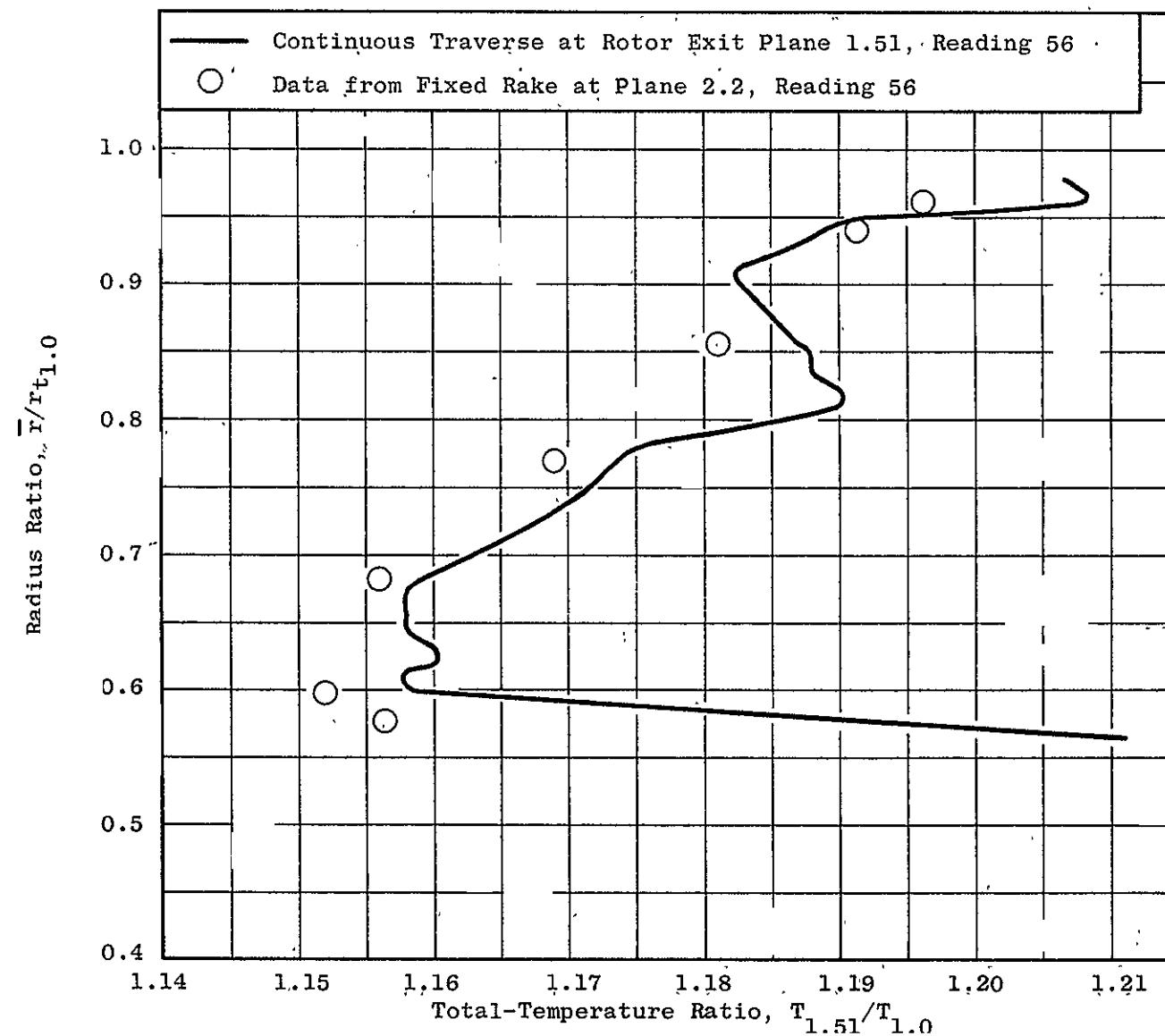


Figure 18 (b). Comparison of Radial Profiles and Rotor Total-Temperature Ratio at 100% Speed Near Peak Efficiency Obtained from Fixed and Traversing Instruments.

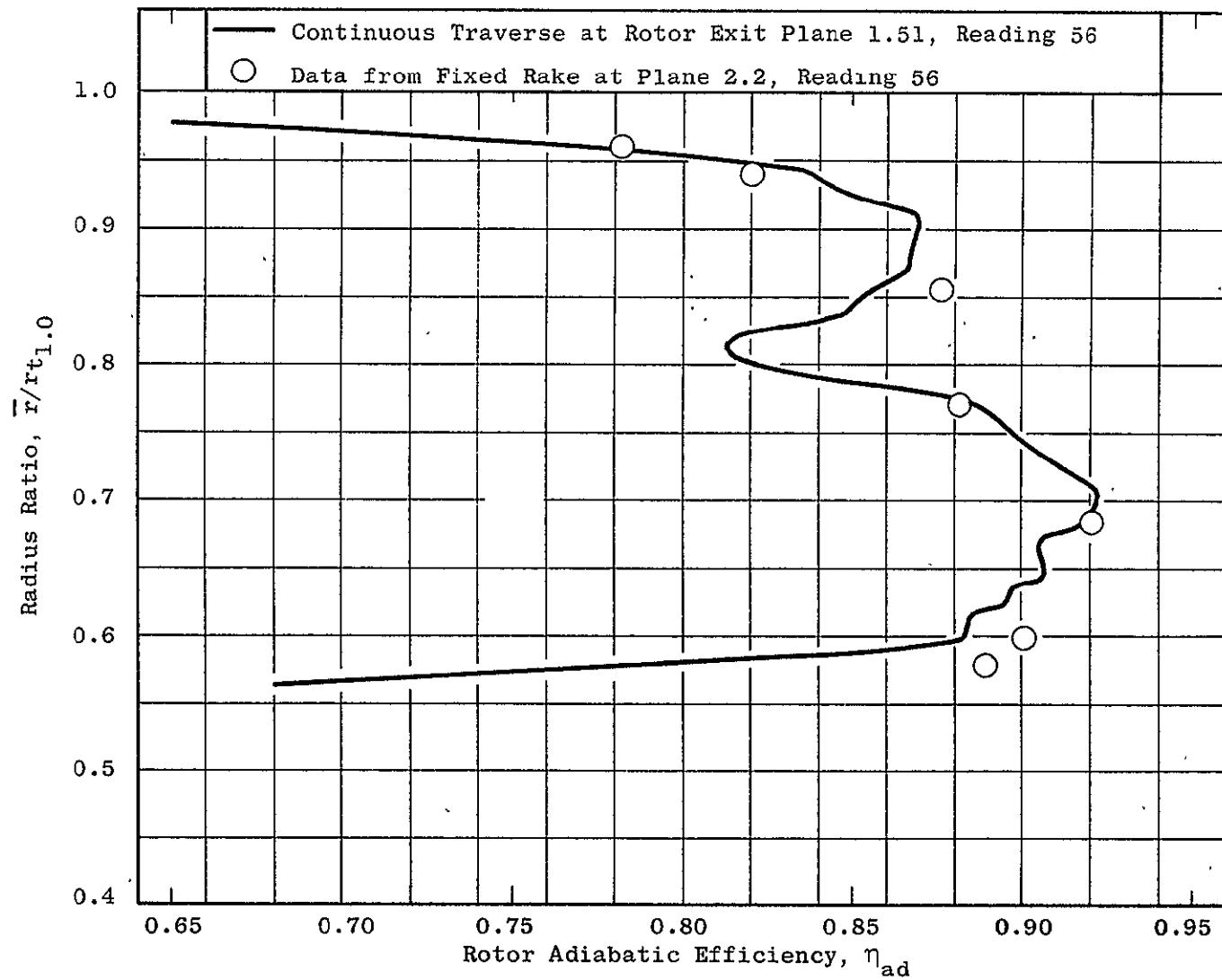


Figure 18 (c). Comparison of Radial Profiles and Rotor Adiabatic Efficiency at 100% Speed Near Peak Efficiency Obtained from Fixed and Traversing Instruments.

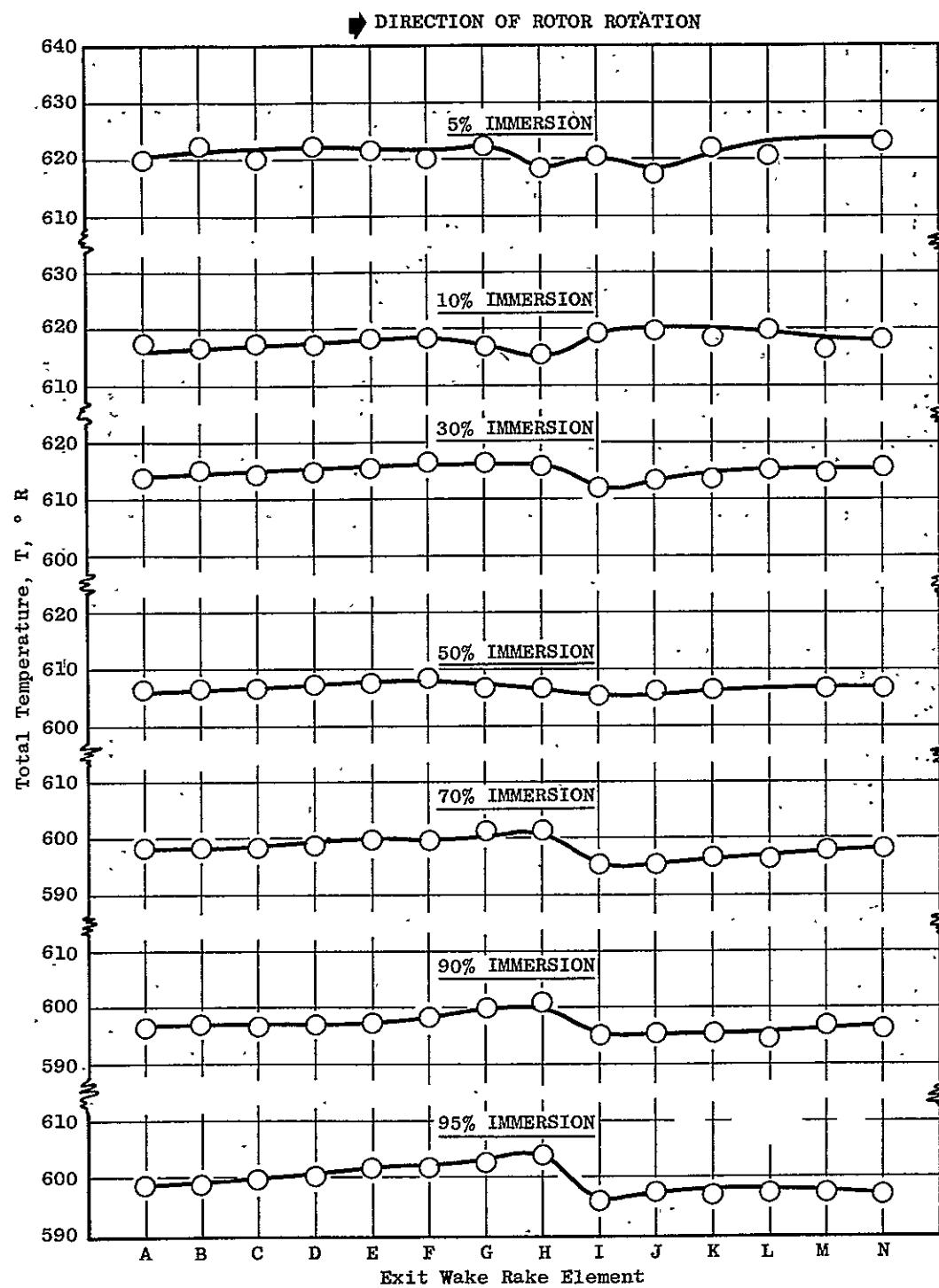


Figure 19 (a). Stator Exit Total-Temperature Wake Profiles at 100% Speed with Undistorted Inlet Flow, Near Peak Efficiency, Reading 27.

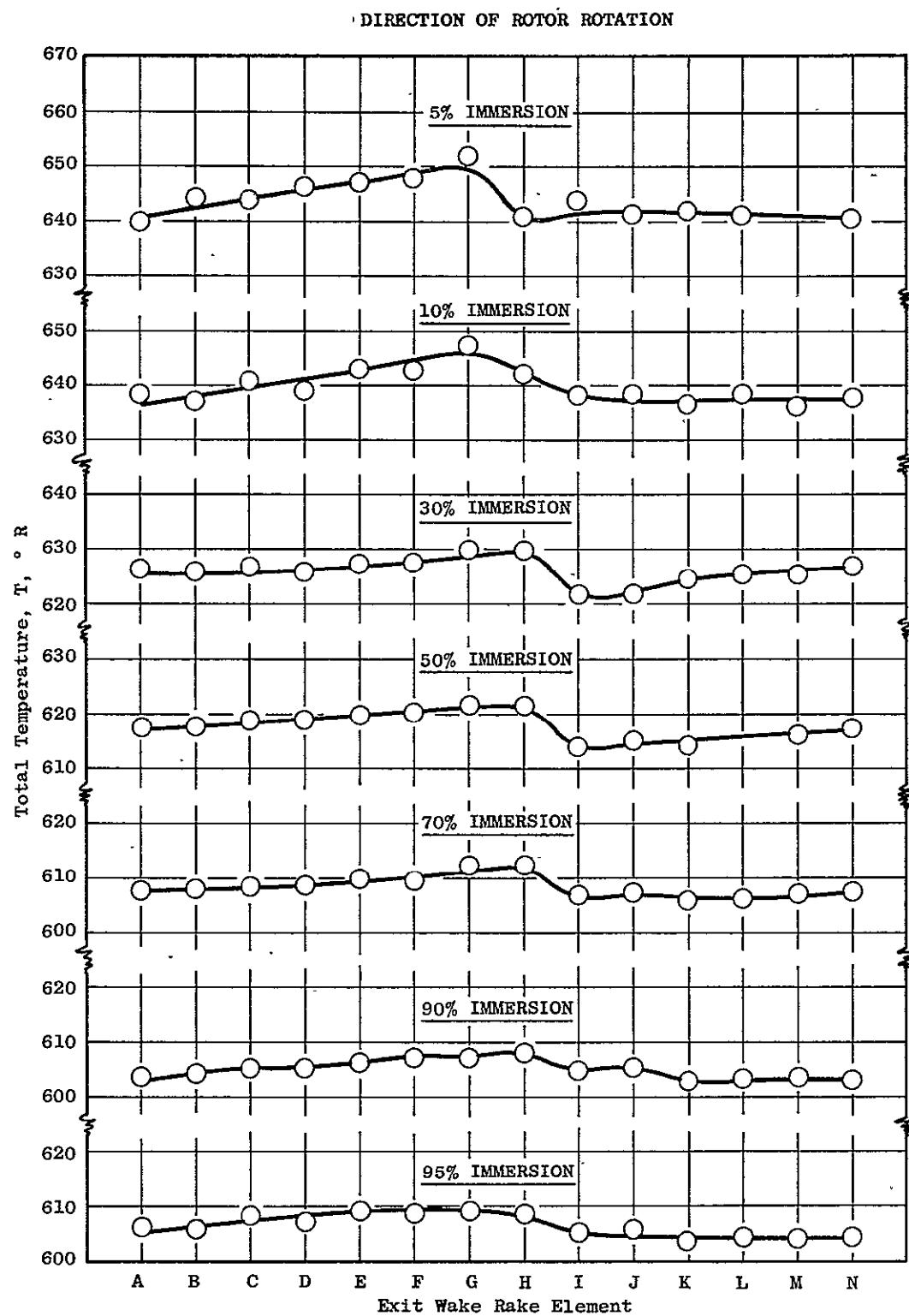


Figure 19 (b). Stator Exit Total-Temperature Wake Profiles at 100% Speed with Undistorted Inlet Flow, Near Stall, Reading 64.

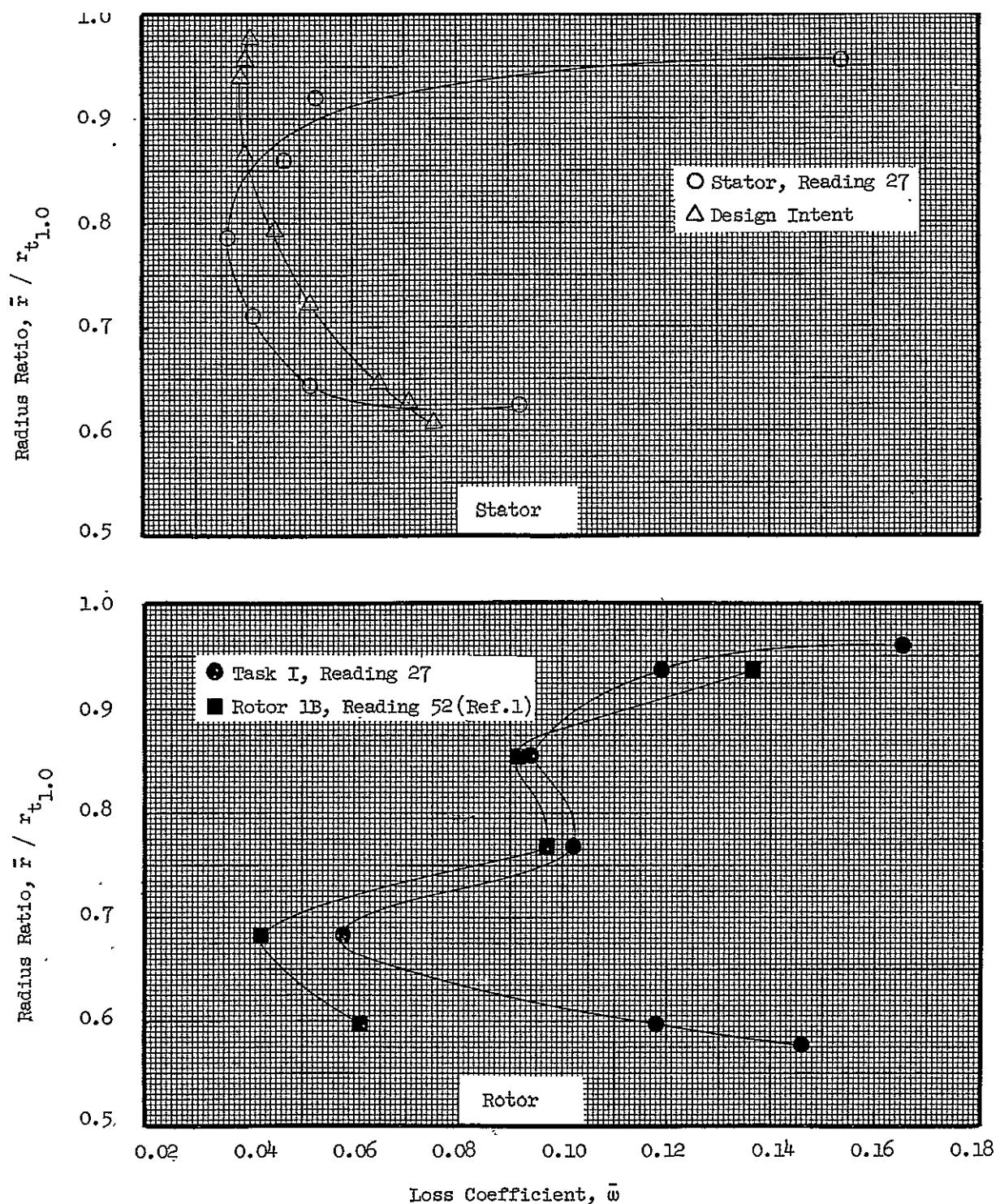


Figure 20. Radial Profiles of Rotor and Stator Loss Coefficients at 100% Speed Near Peak Efficiency.

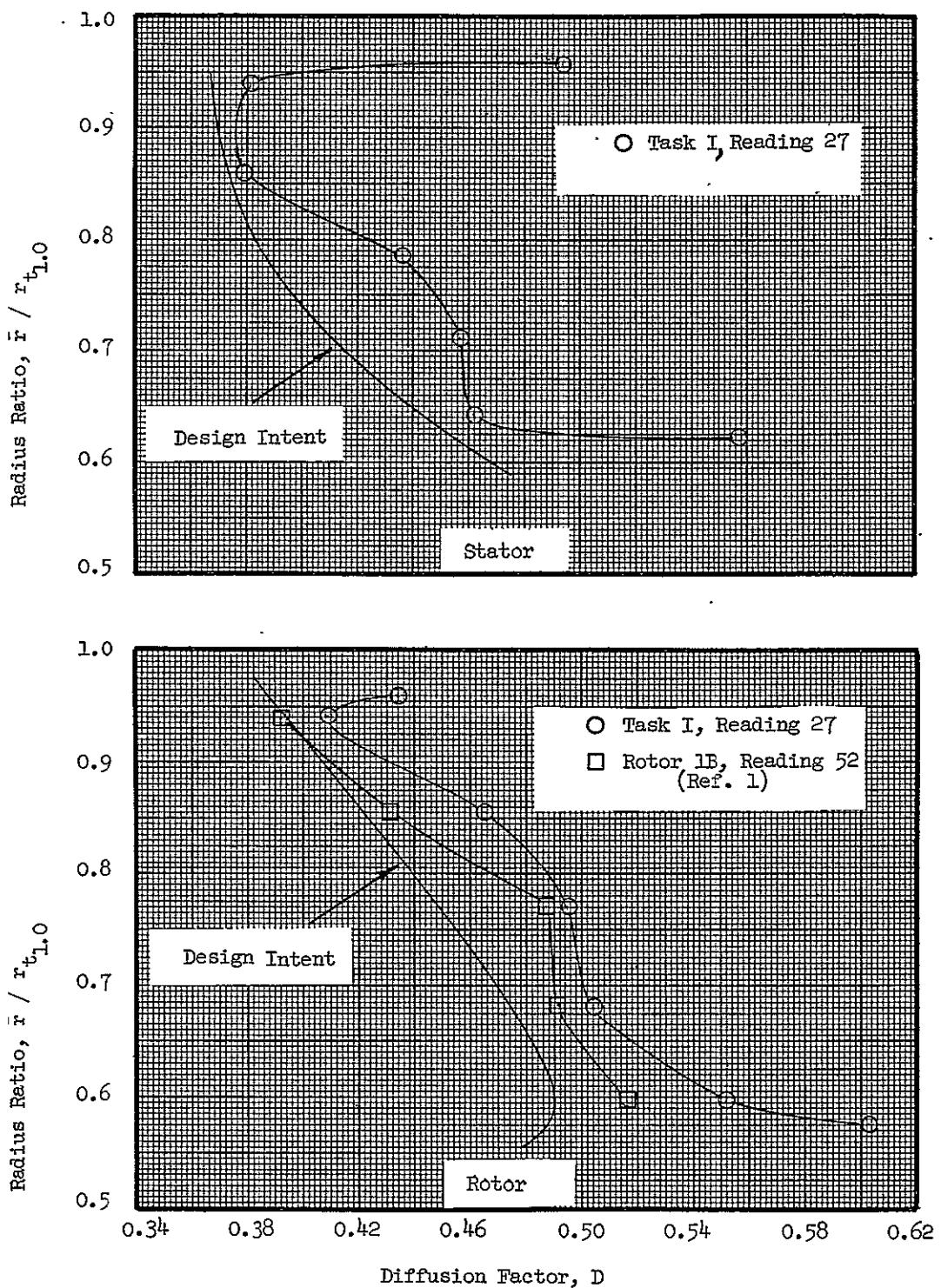


Figure 21. Radial Profiles of Rotor and Stator Diffusion Factors at 100% Speed Near Peak Efficiency.

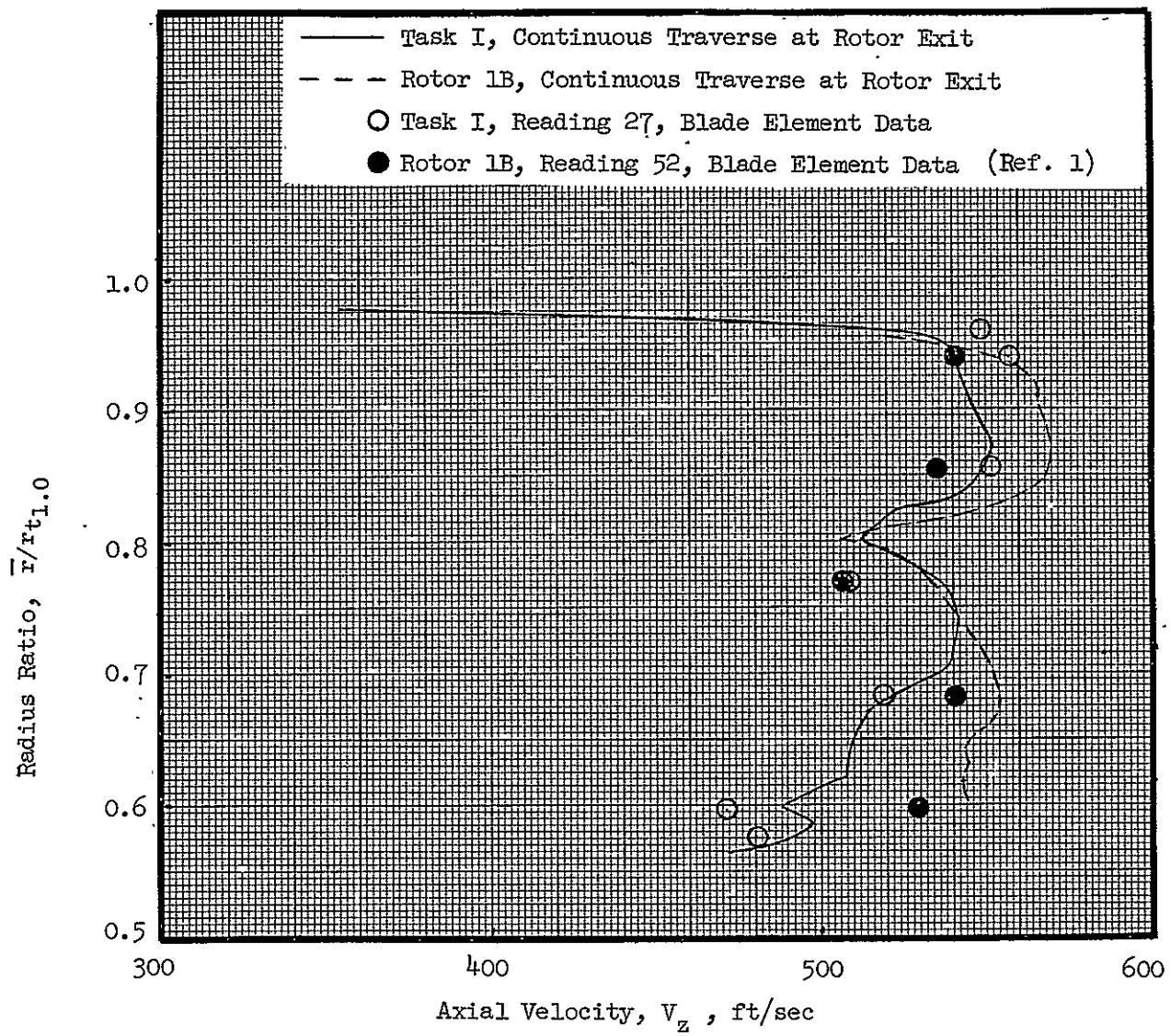


Figure 22 (a). Radial Profiles of Rotor Axial Velocities at 100% Speed Near Peak Efficiency.



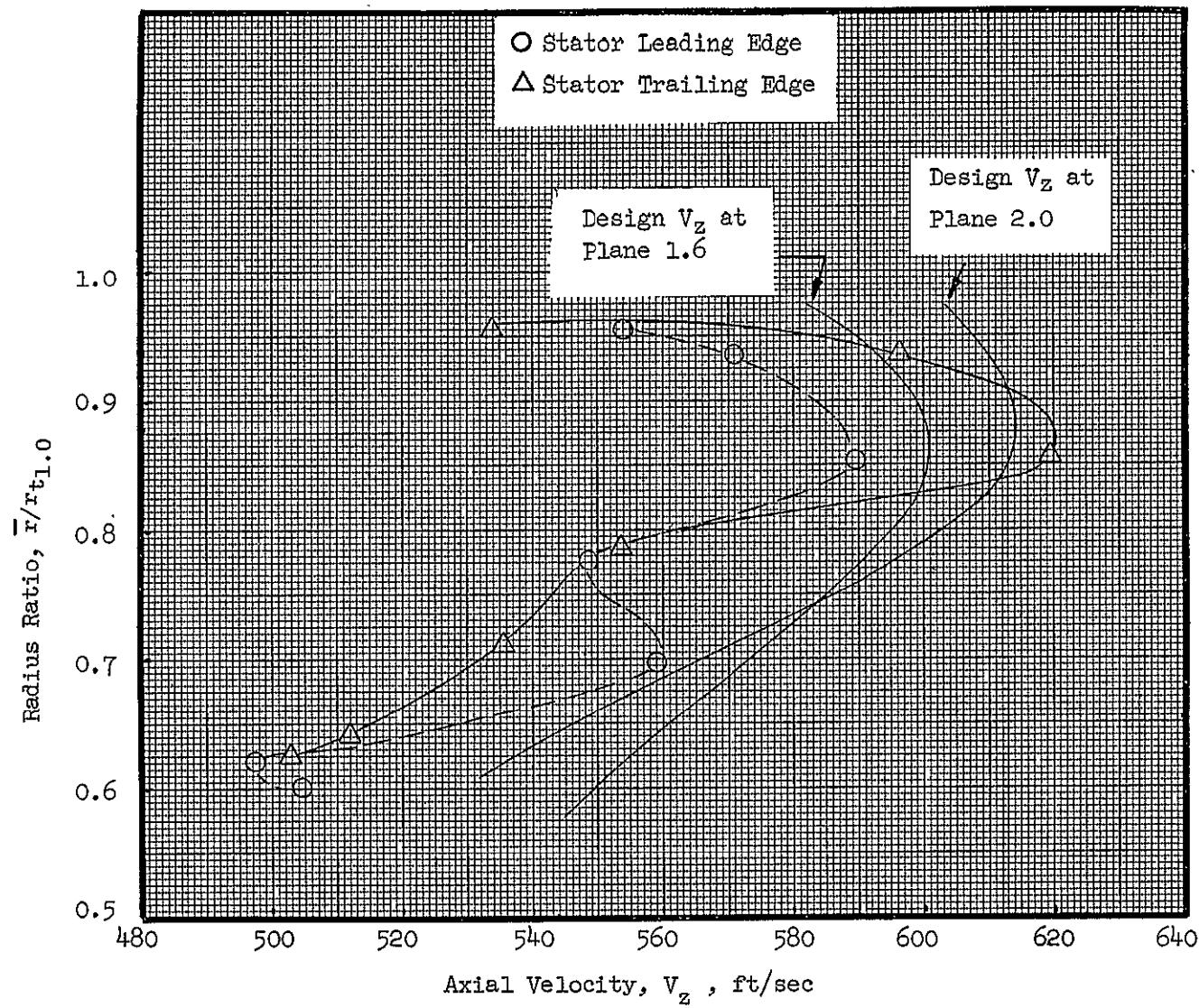


Figure 22 (b). Radial Profiles of Stator Axial Velocities at 100% Speed Near Peak Efficiency.

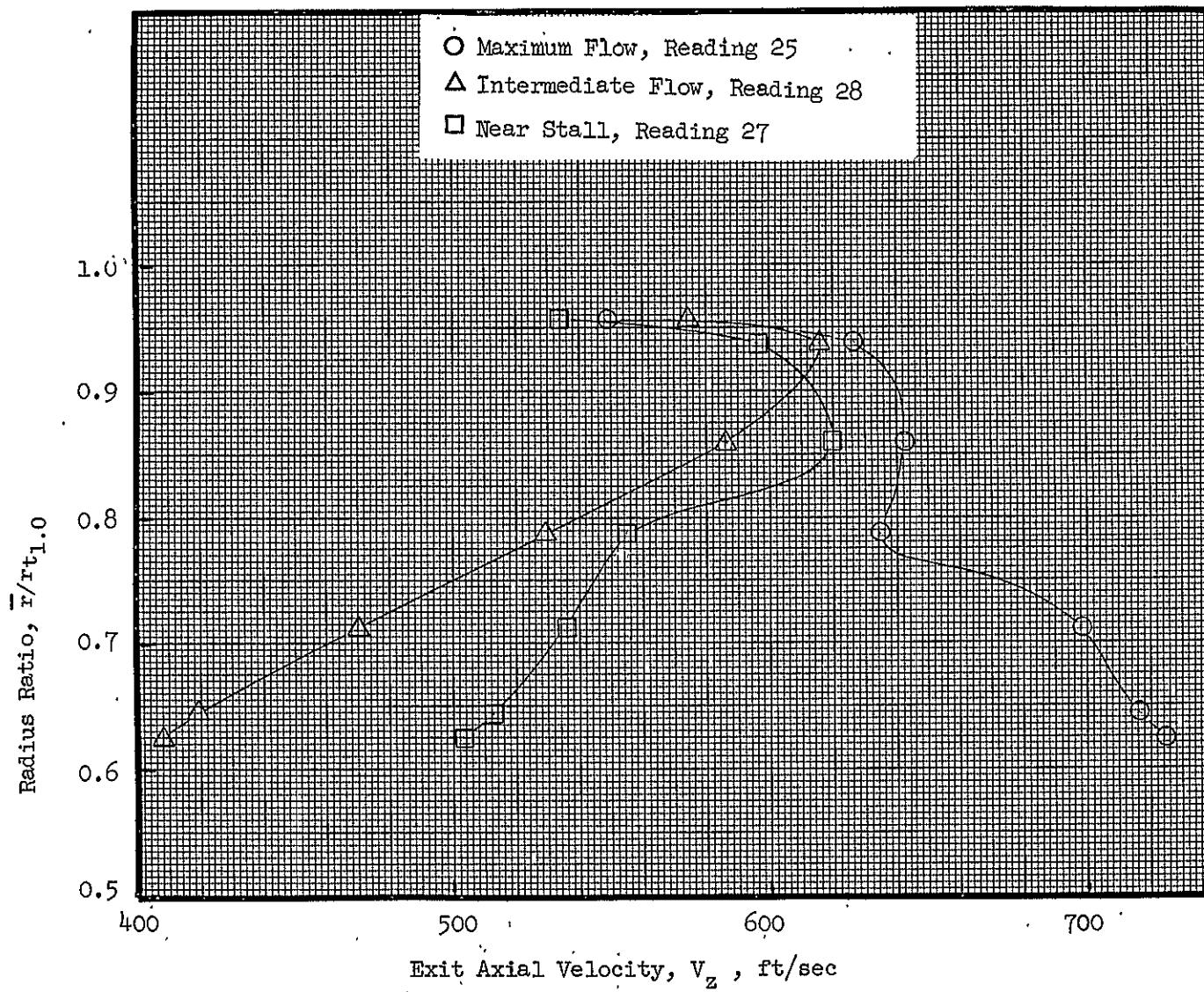


Figure 23. Stator Exit Axial Velocity Profiles at 100% Speed.

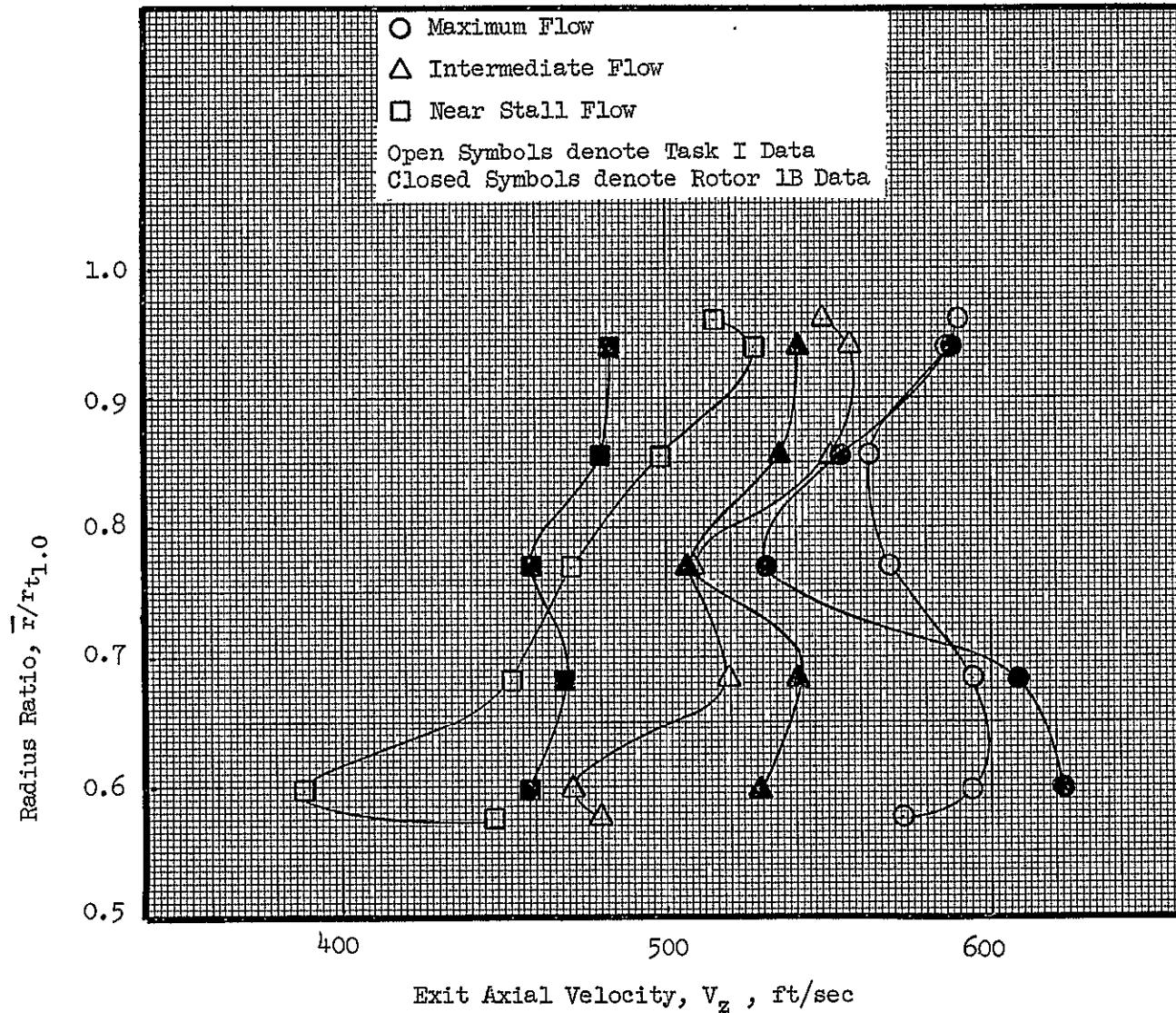


Figure 24. Rotor Exit Axial Velocity Profiles at 100% Speed.

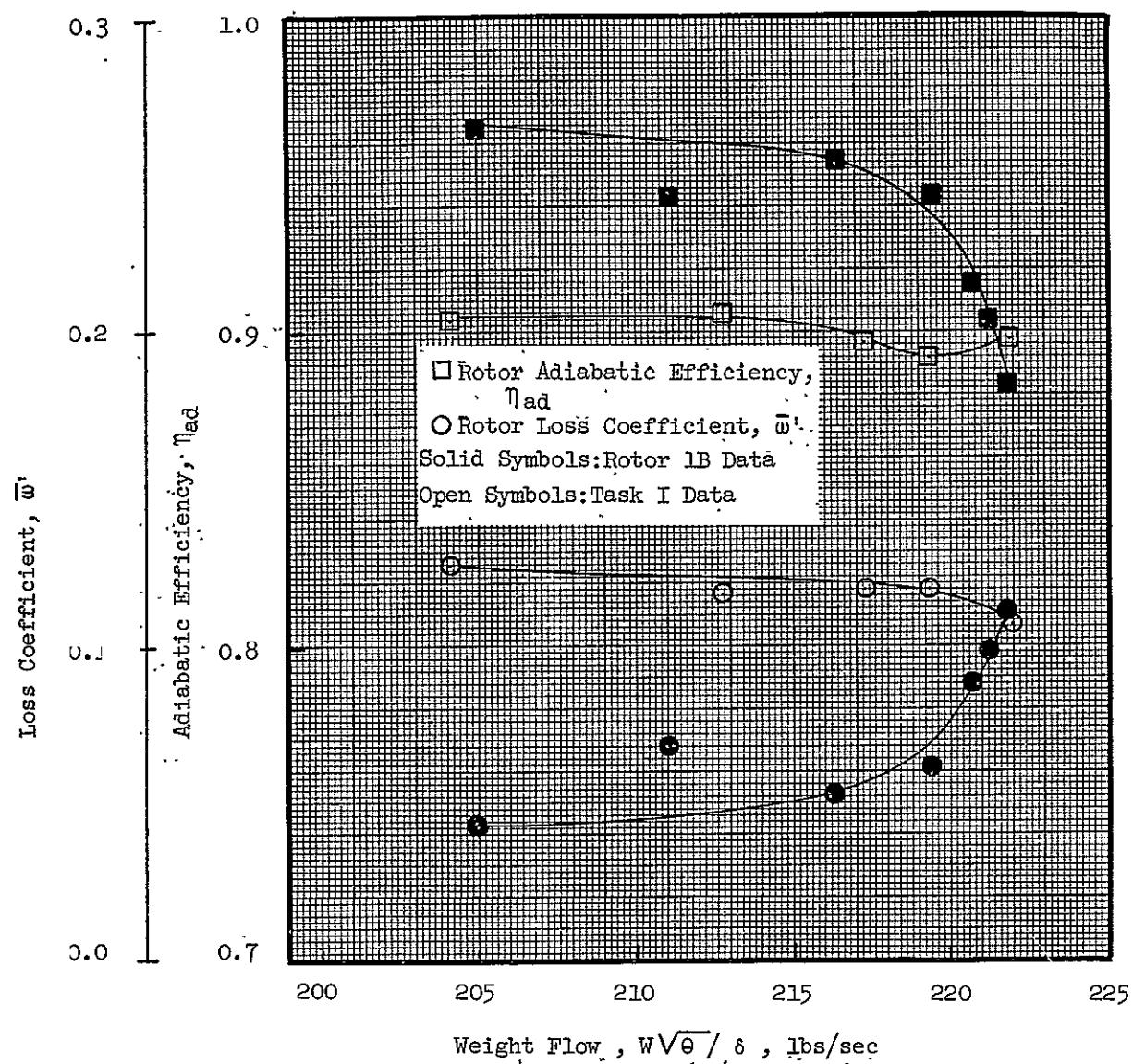


Figure 25 (a). Variations of Rotor Performance Parameters with Weight Flow at 100% Speed; 90% Immersion from Tip.

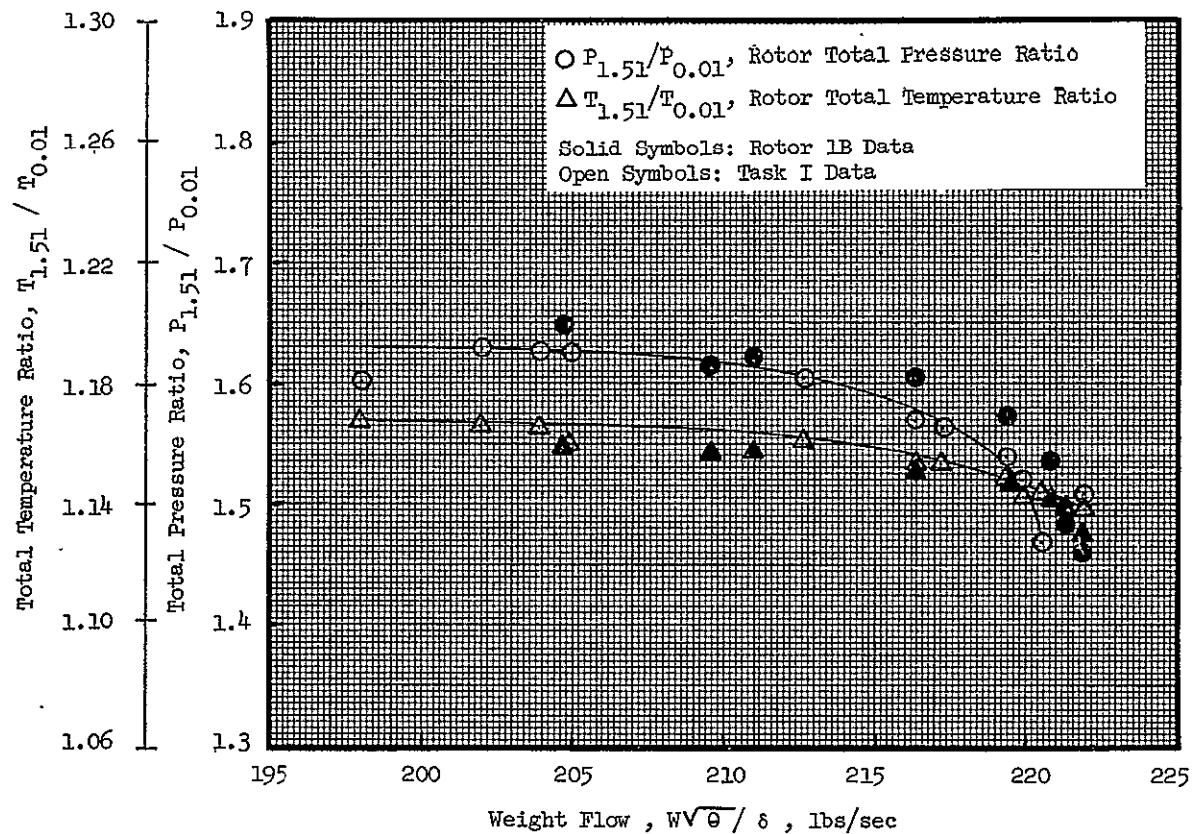


Figure 25 (a). Variations of Rotor Performance Parameters with Weight Flow at 100% Speed; 90% Immersion from Tip (Continued).

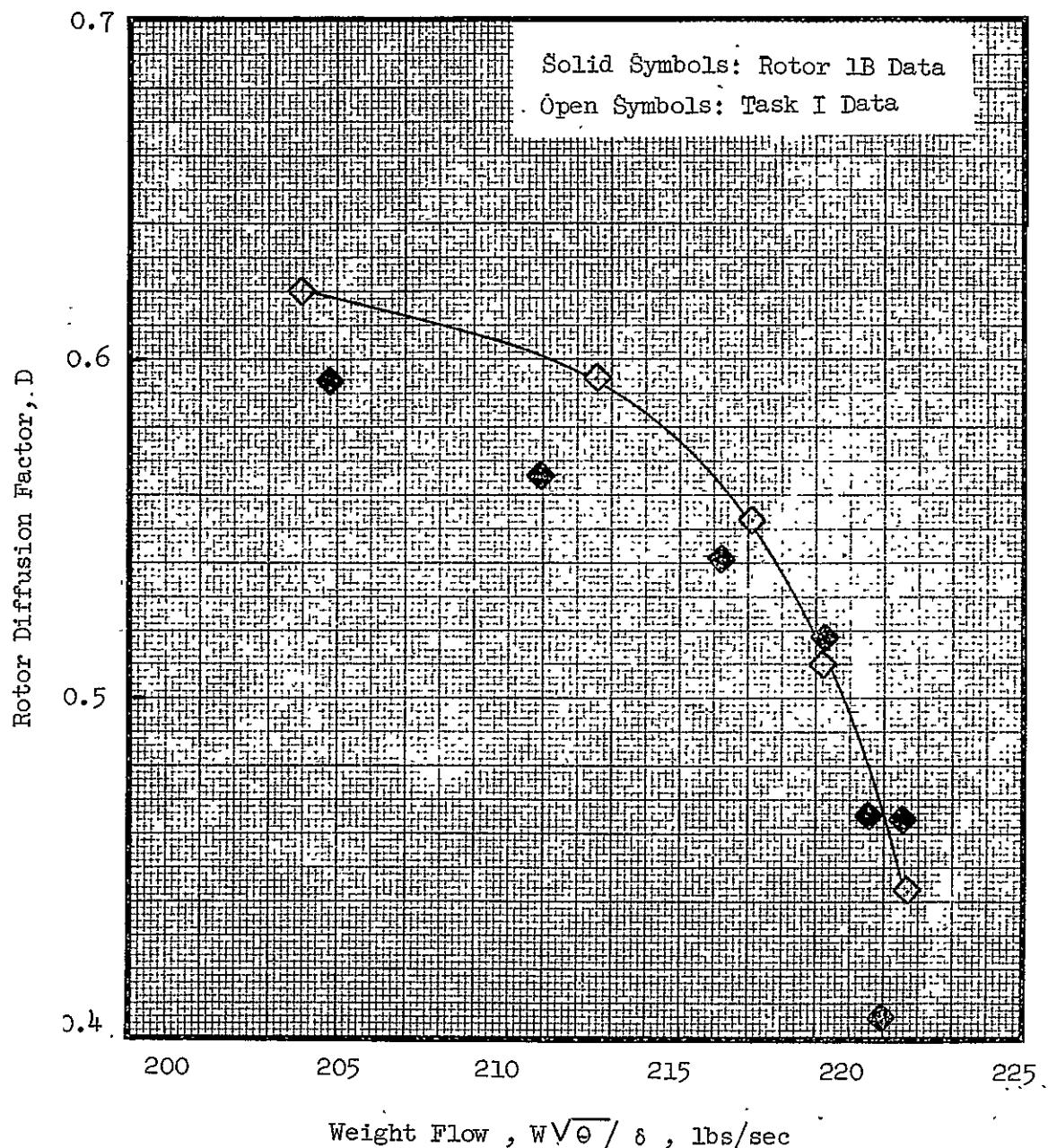


Figure 25(a) Variations of Rotor Performance Parameters With Weight Flow at 100% Speed; 90% Immersion From Tip (Continued)

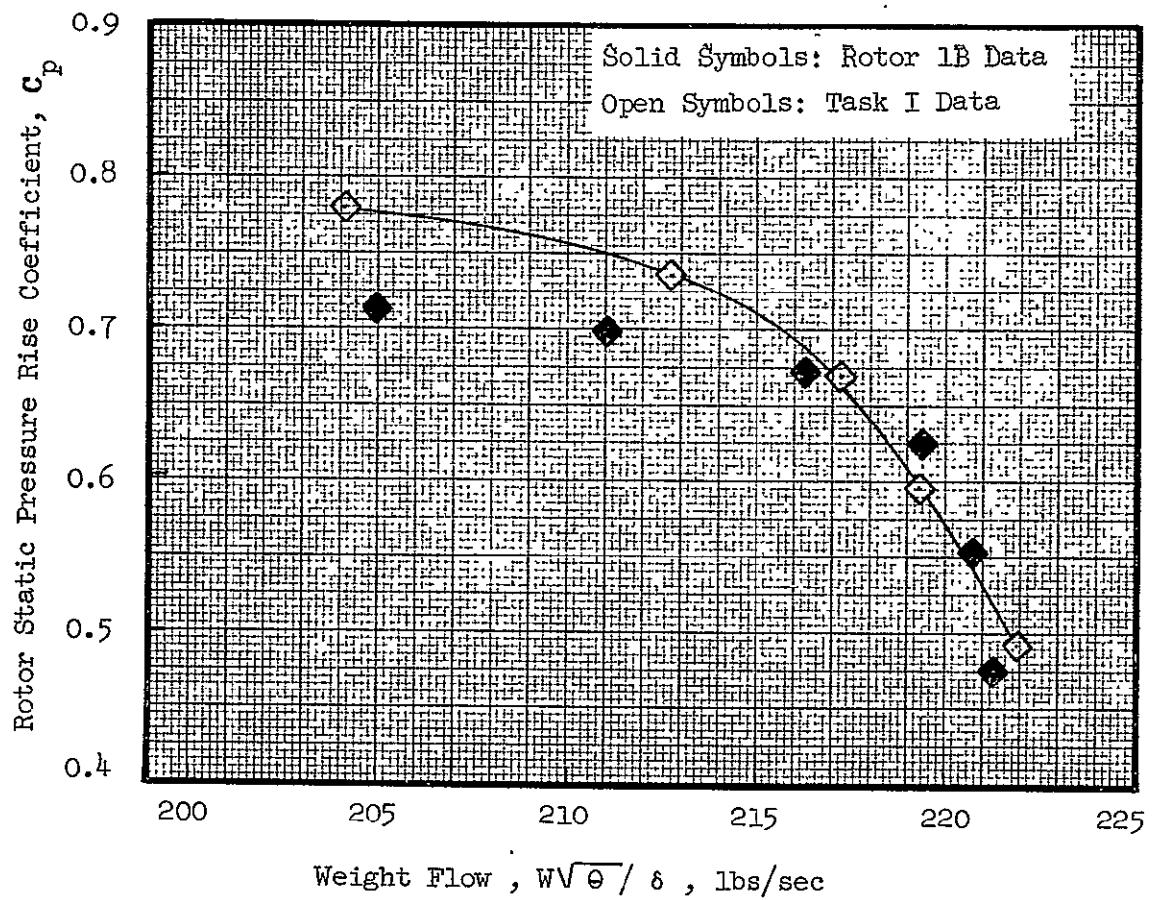


Figure 25(a) Variations of Rotor Performance Parameters With Weight Flow at 100% Speed; 90% Immersion From Tip (Continued)

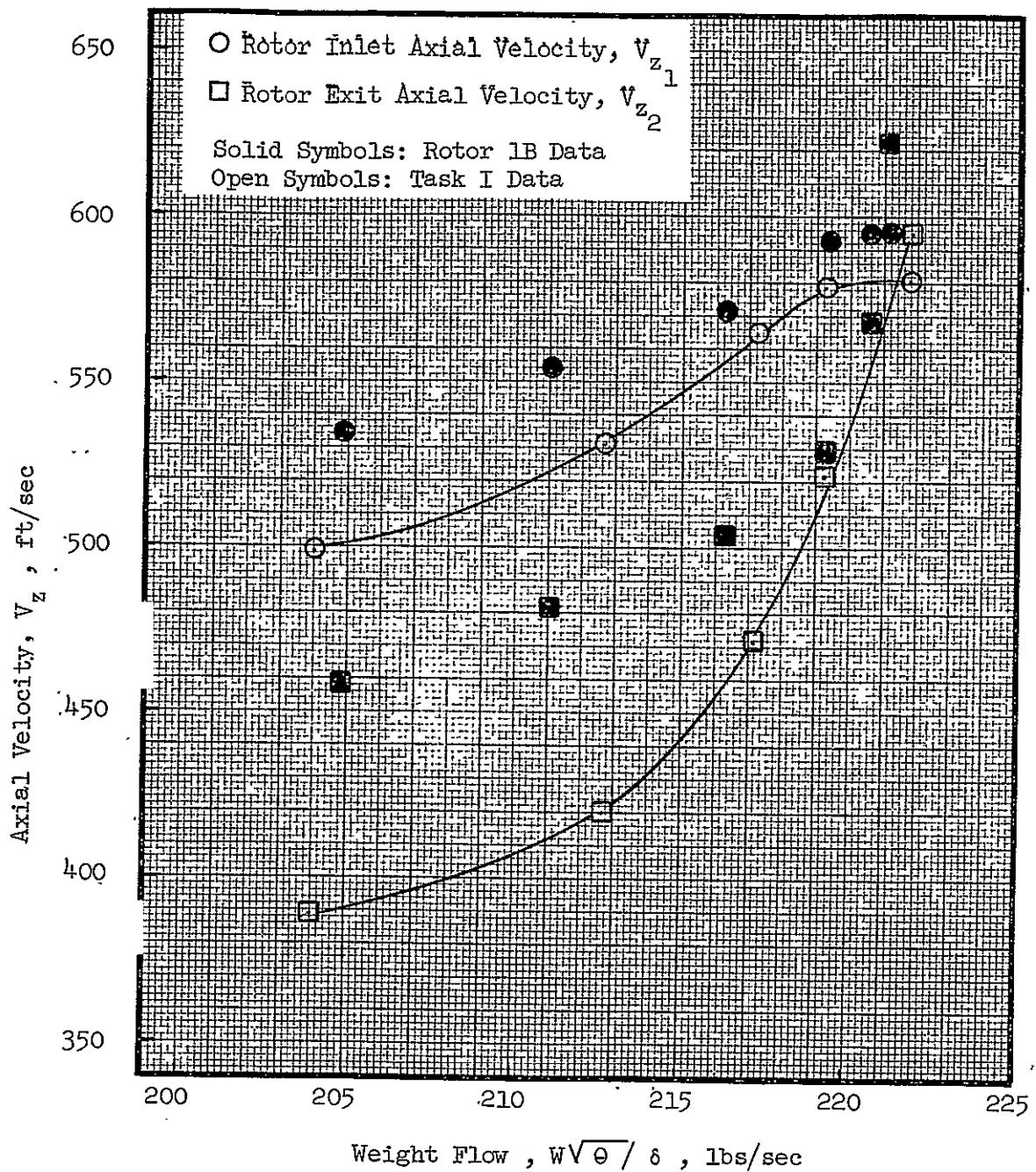


Figure 25(a) Variations of Rotor Performance Parameters With Weight Flow at 100% Speed; 90% Immersion From Tip (Concluded)

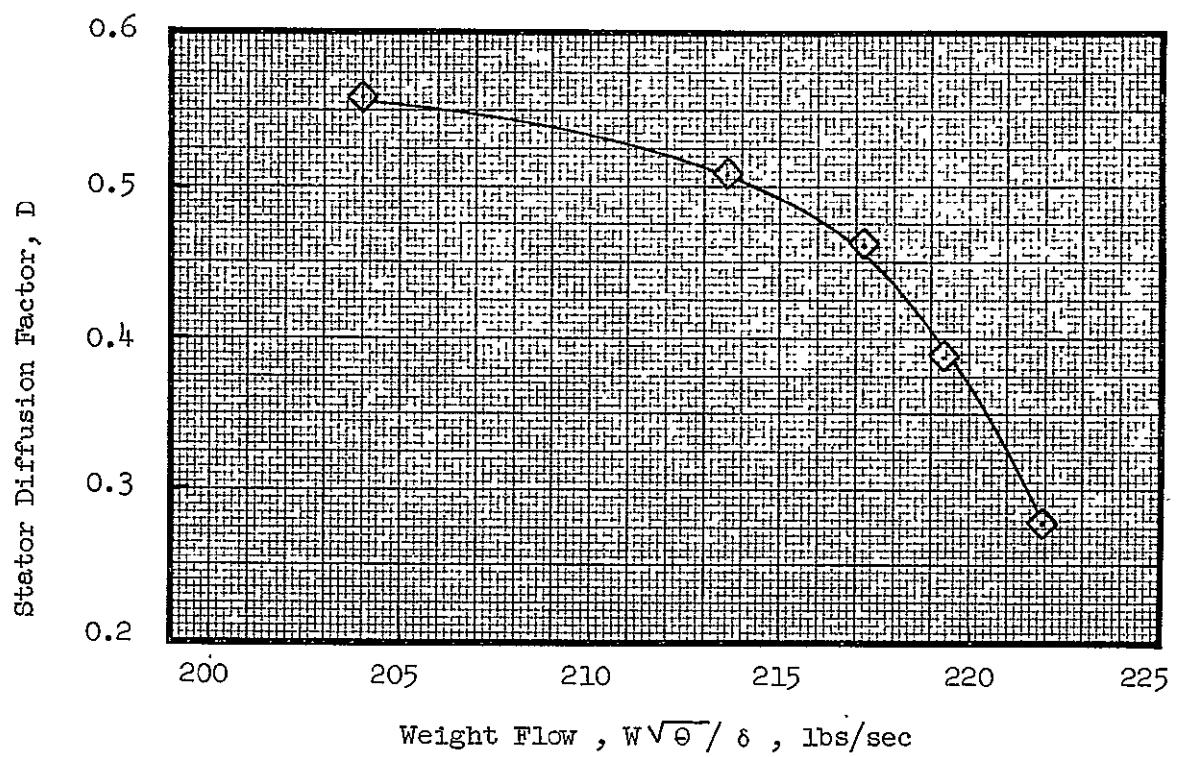


Figure 25(b) Variations of Stator Performance Parameters With Weight Flow at 100% Speed; 90% Immersion From Tip

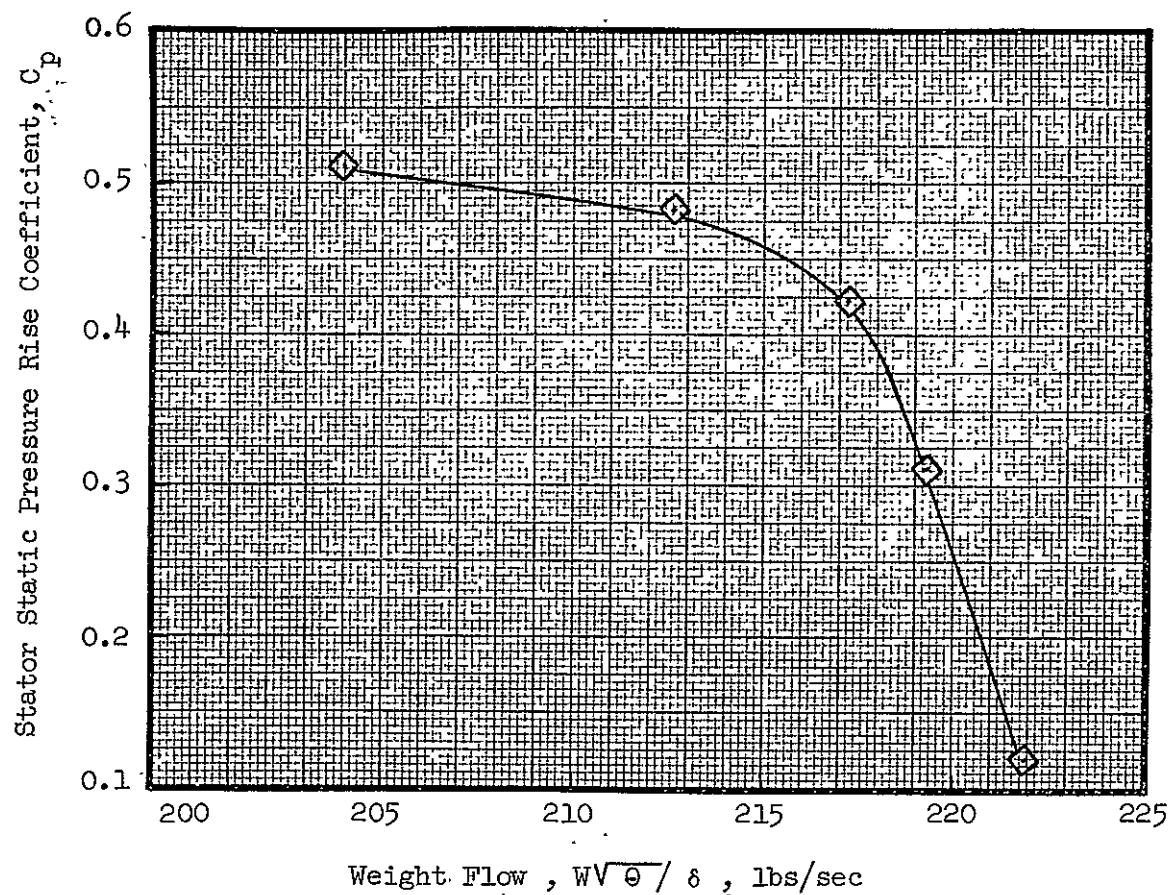


Figure 25(b) Variations of Stator Performance Parameters With Weight Flow at 100% Speed; 90% Immersion From Tip (Continued)

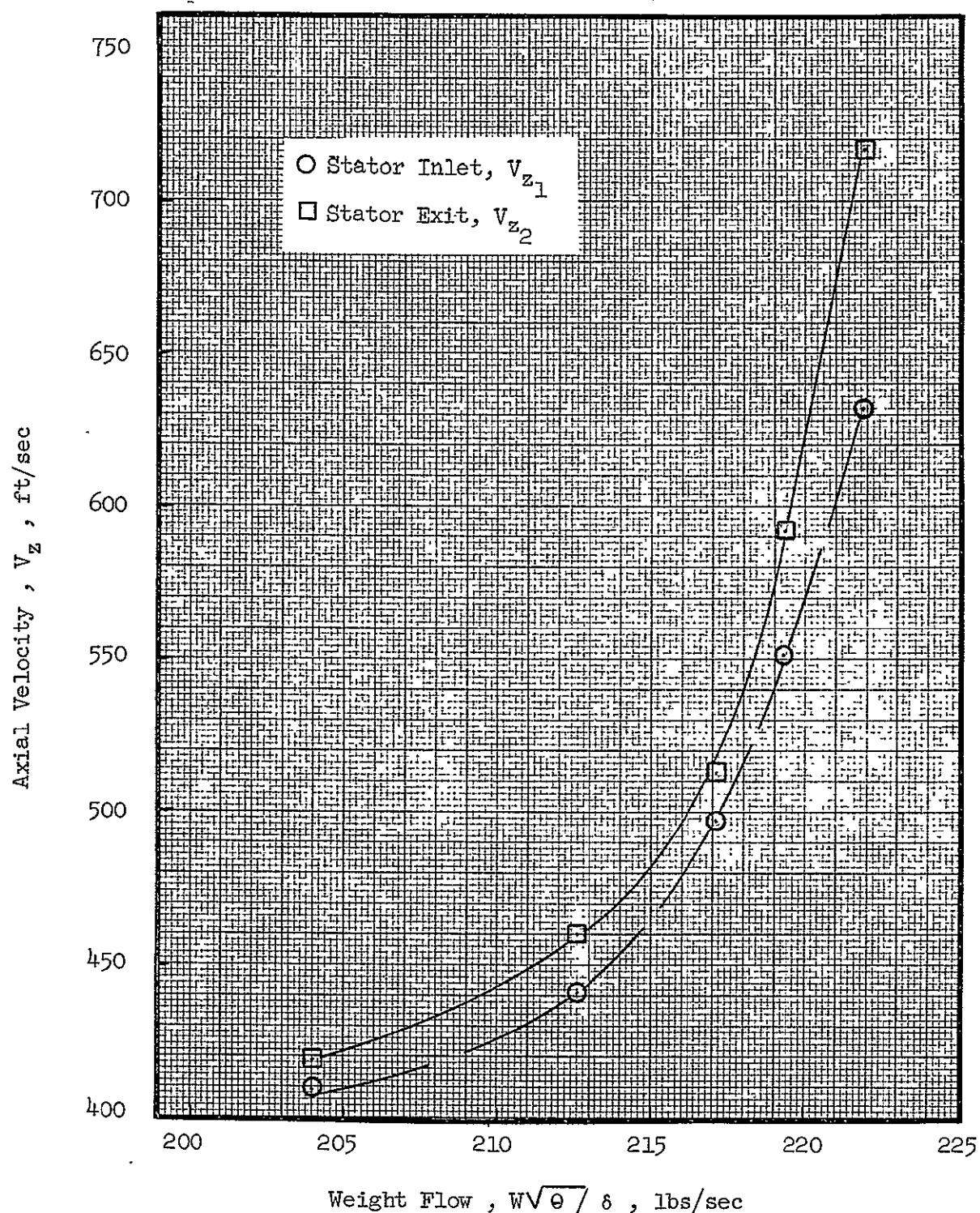


Figure 25(b) Variations of Stator Performance Parameters With Weight Flow at 100% Speed; 90% Immersion From Tip (Concluded)

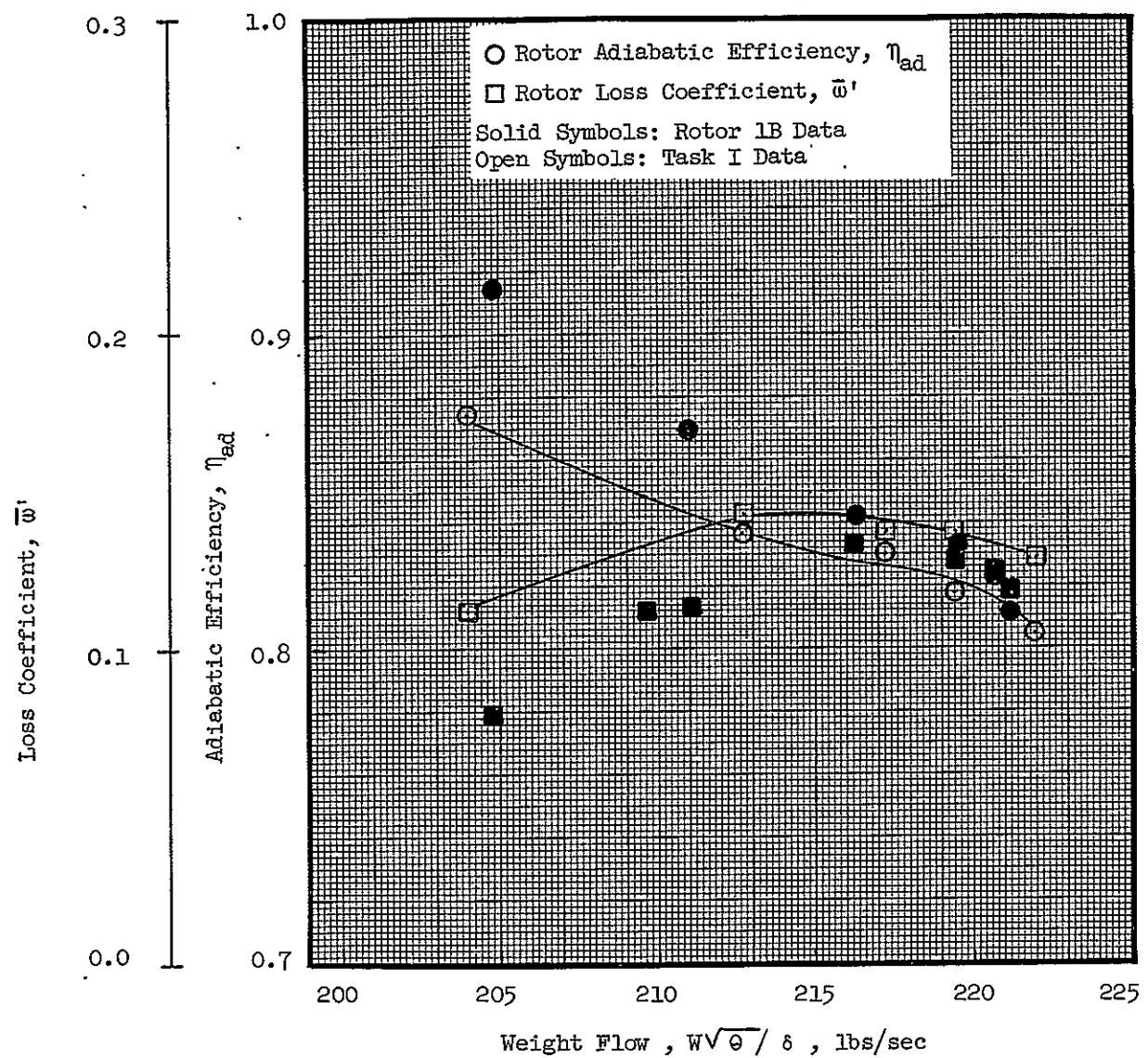


Figure 25 (c). Variations of Rotor Performance Parameters with Weight Flow at 100% Speed; 10% Immersion from Tip.

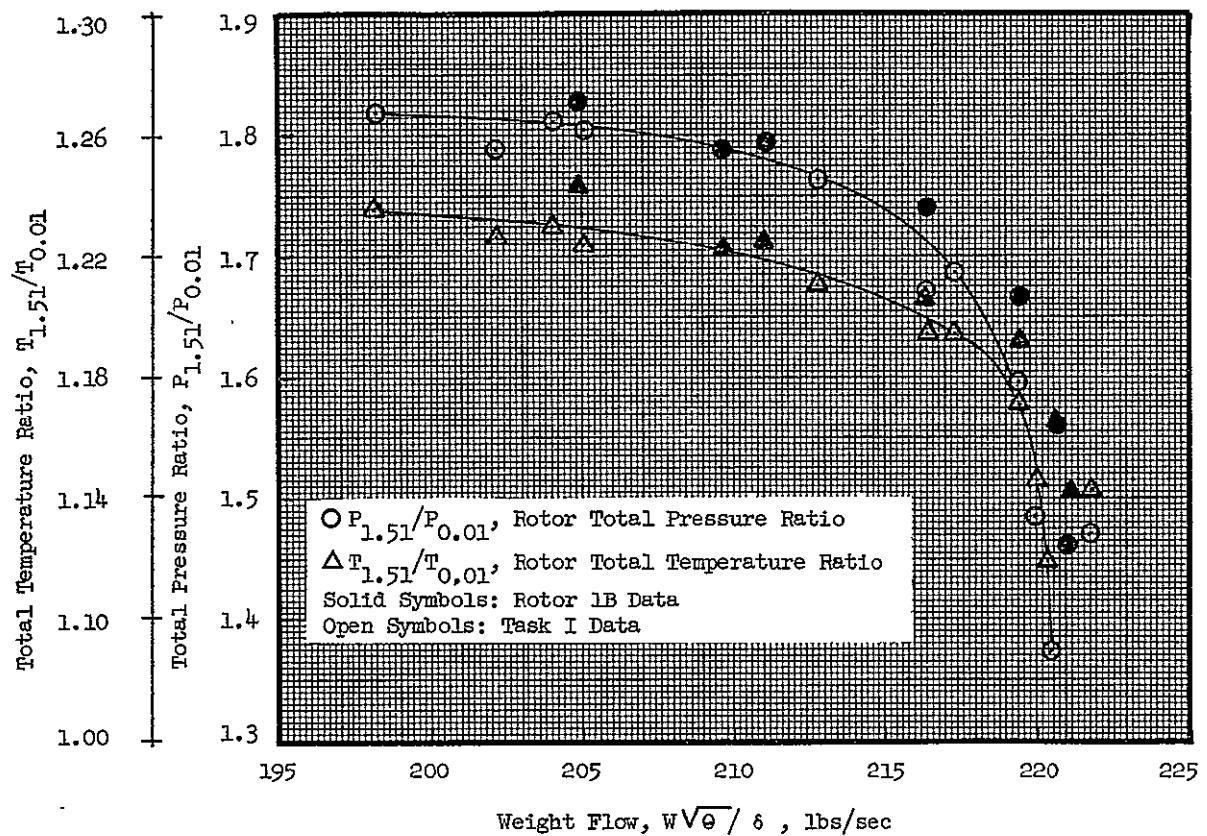


Figure 25 (c). Variations of Rotor Performance Parameters with Weight Flow at 100% Speed; 10% Immersion from Tip (Continued).

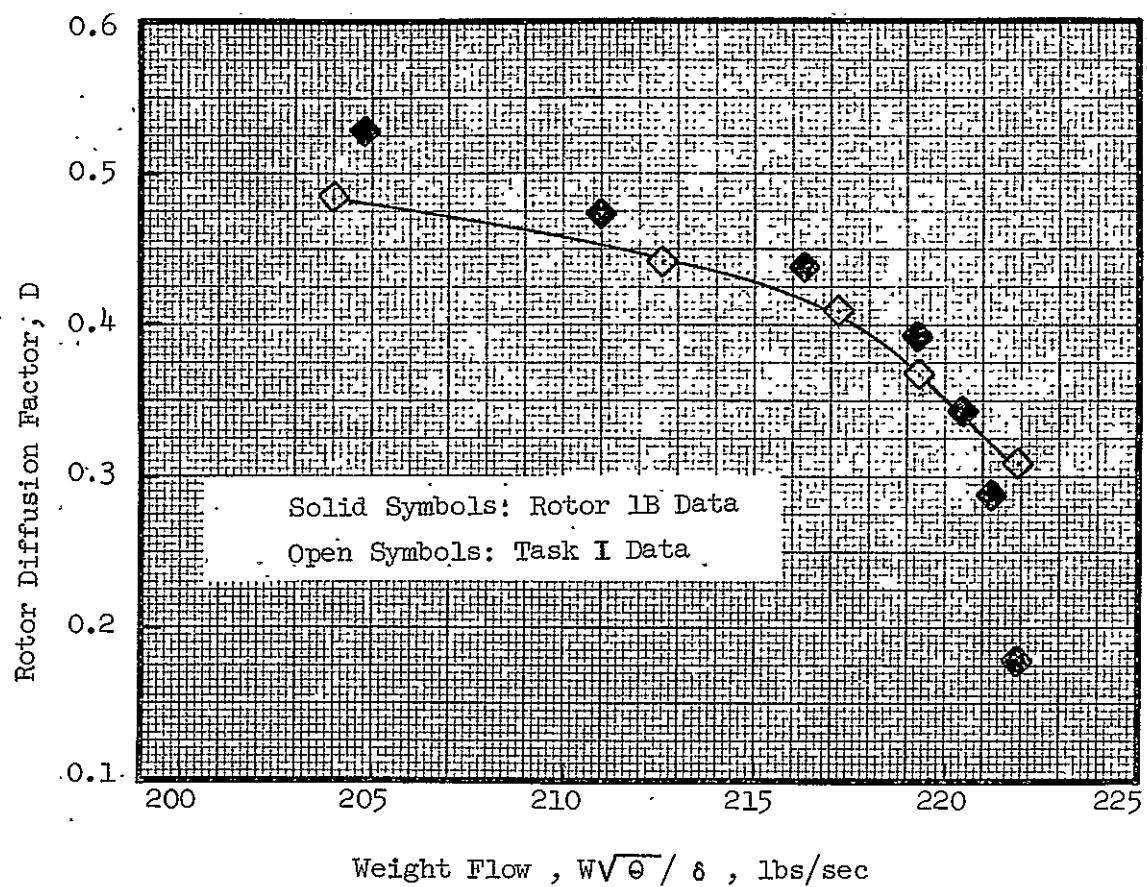


Figure 25(c) Variations of Rotor Performance Parameters With Weight Flow at 100% Speed; 10% Immersion From Tip (Continued)

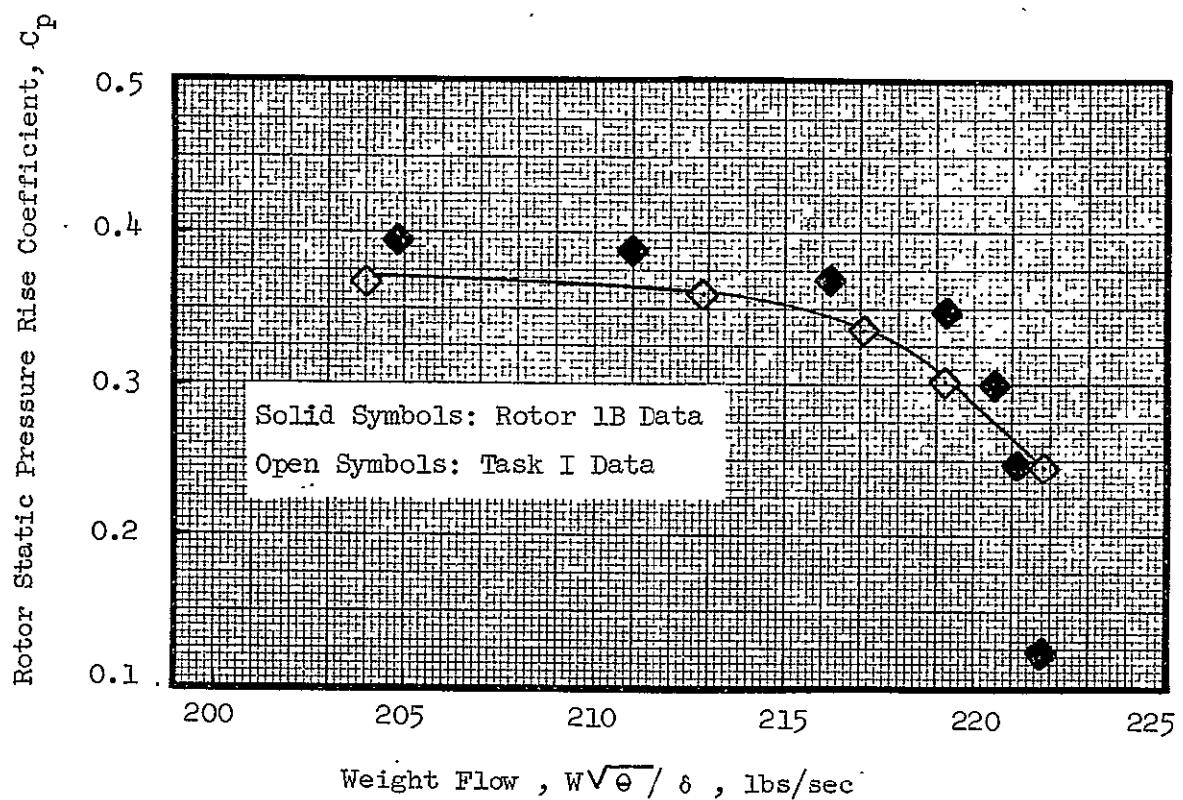


Figure 25(c) Variations of Rotor Performance Parameters With Weight Flow at 100% Speed; 10% Immersion From Tip (Continued)

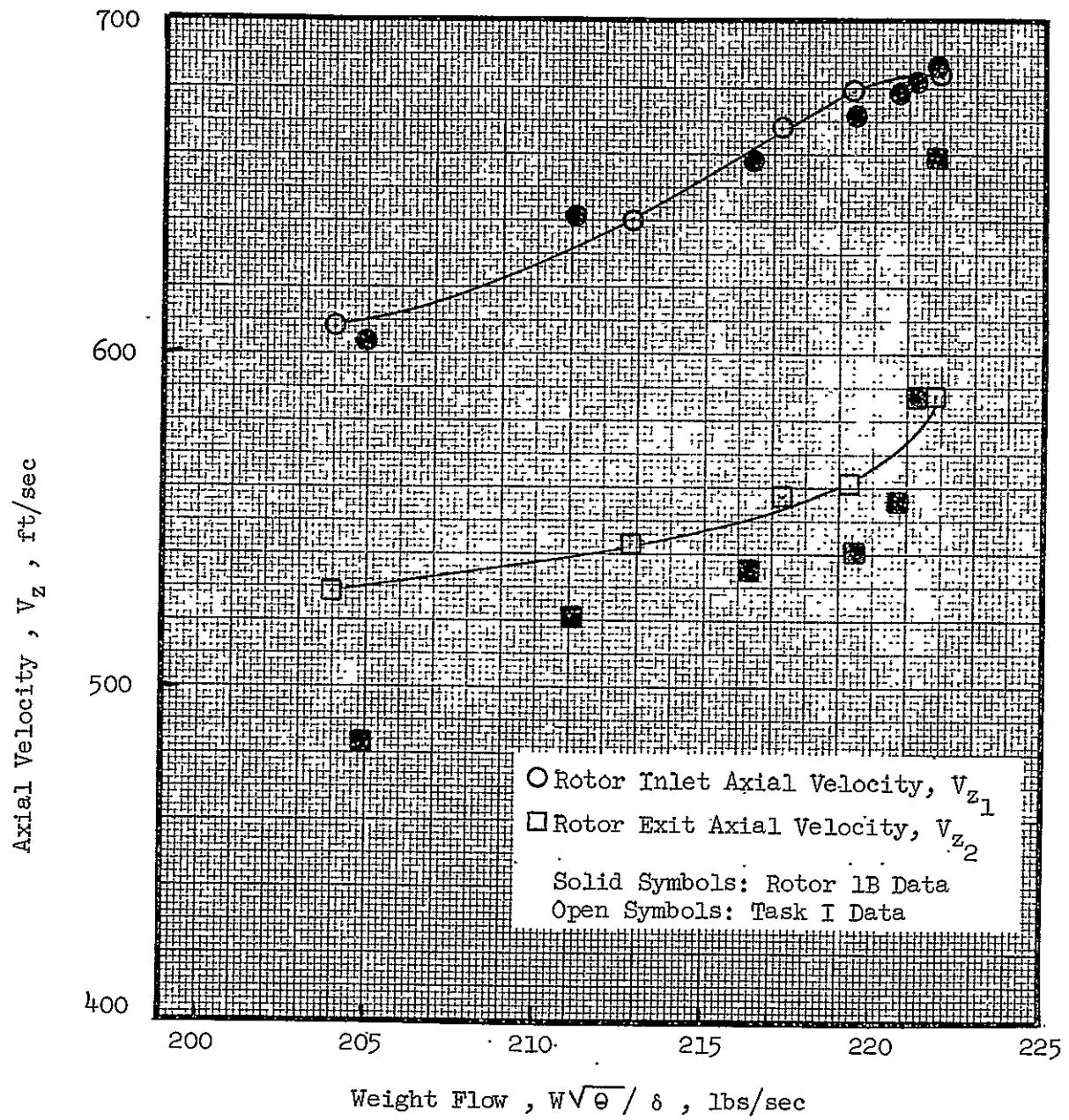


Figure 25(c) Variations of Rotor Performance Parameters With Weight Flow at 100% Speed; 10% Immersion From Tip (Concluded)

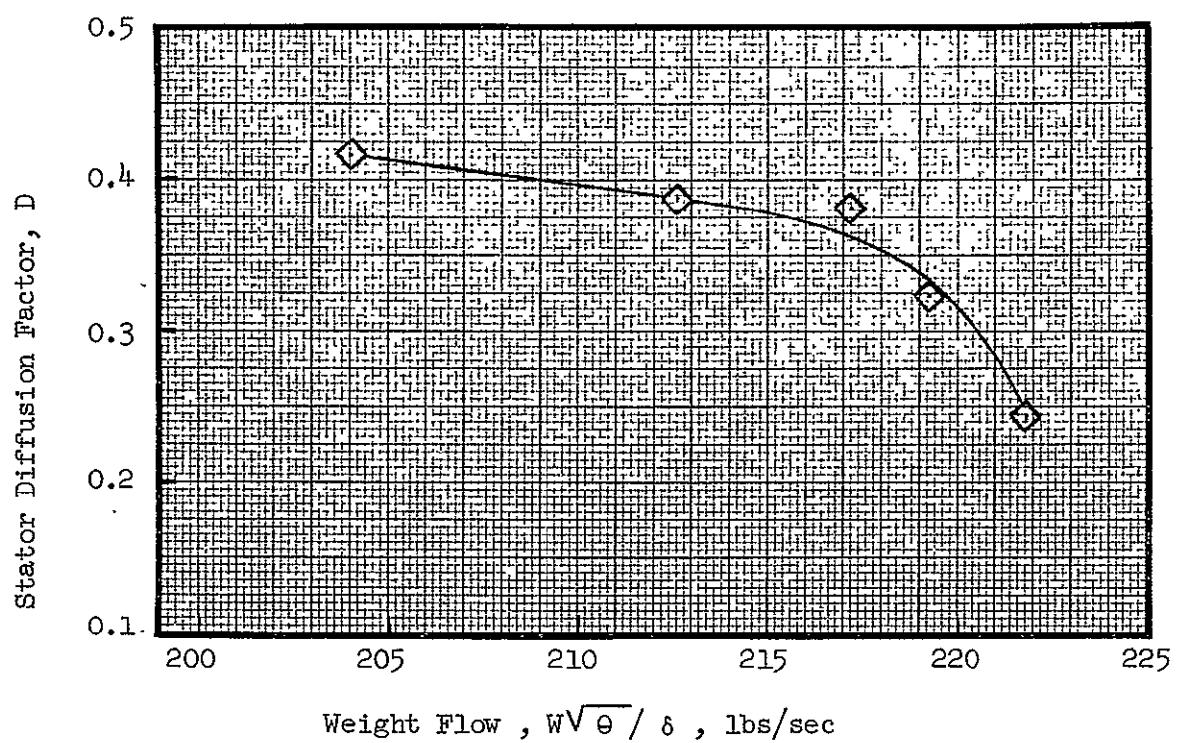


Figure 25(d) Variations of Stator Performance Parameters With Weight Flow at 100% Speed; 10% Immersion From Tip

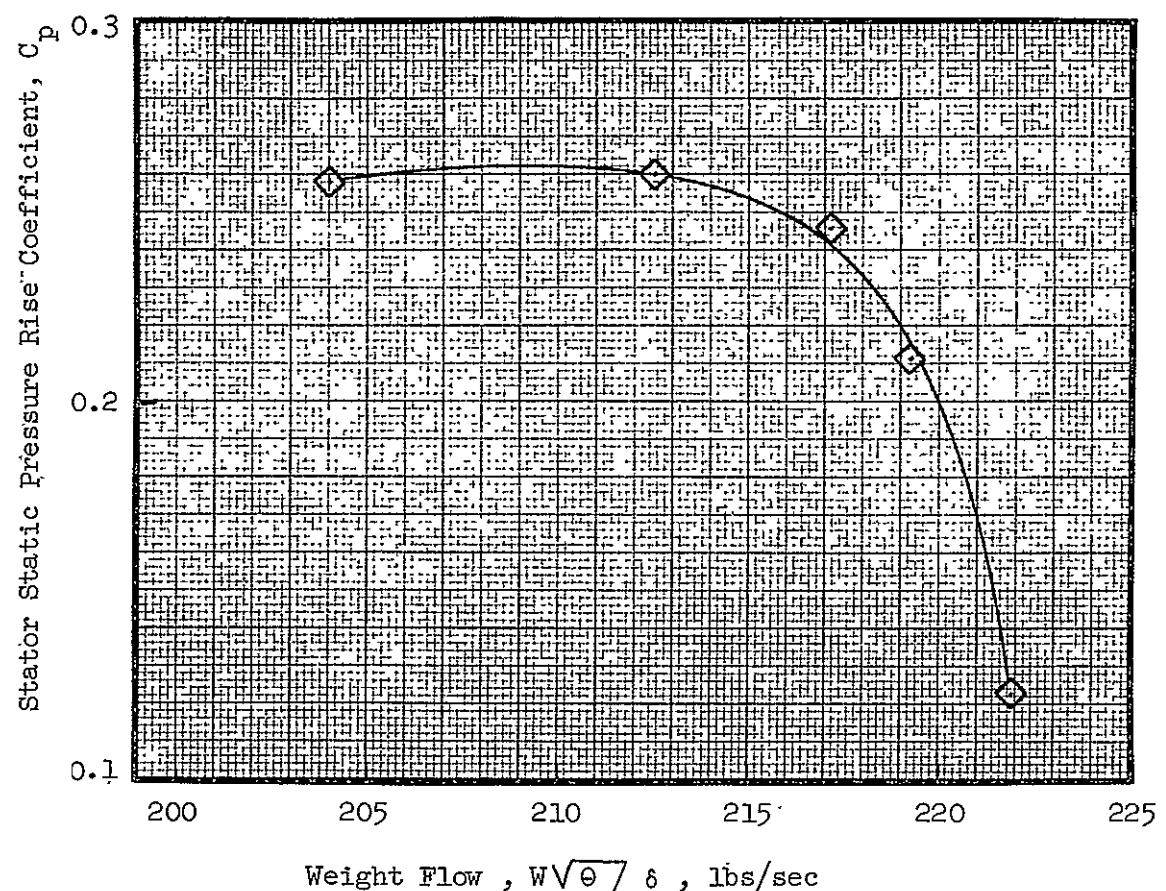


Figure 25(d) Variations of Stator Performance Parameters With Weight Flow at 100% Speed; 10% Immersion From Tip (Continued)

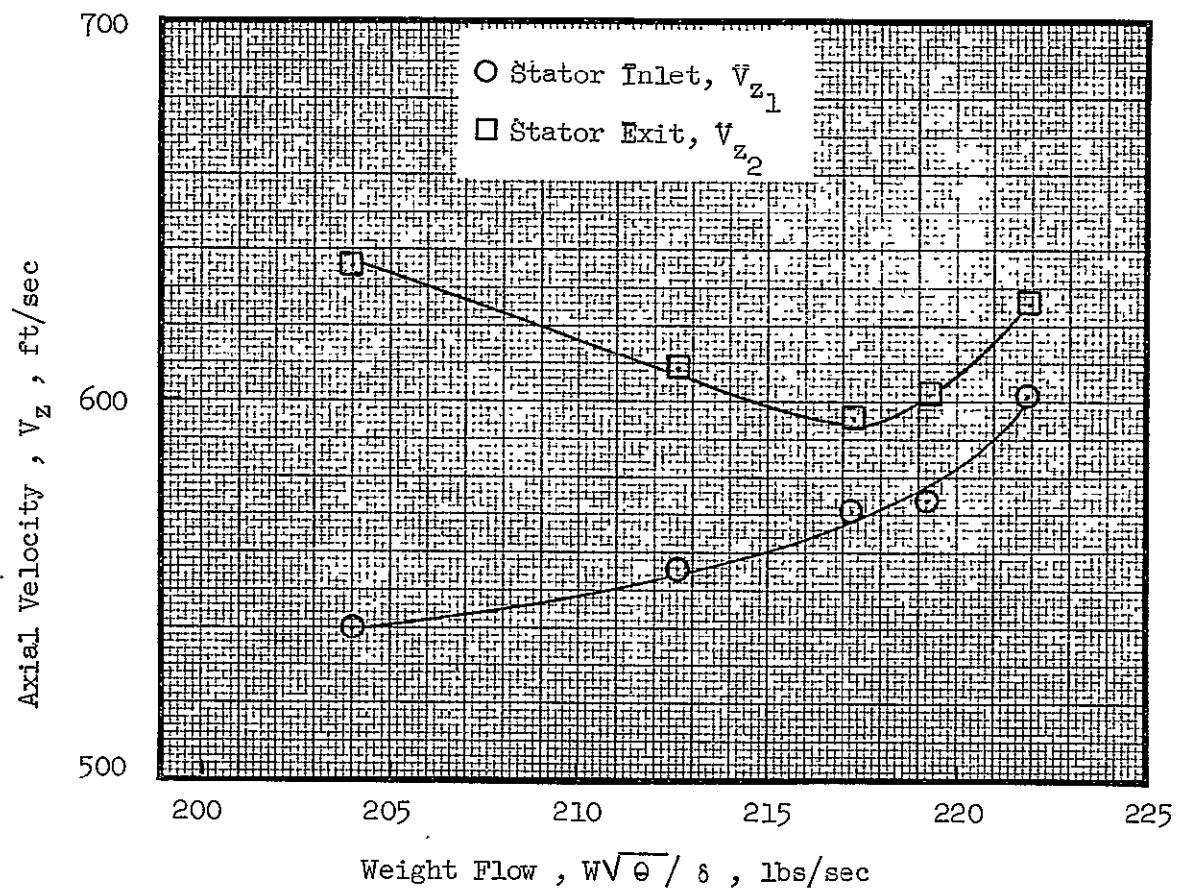


Figure 25(d) Variations of Stator Performance Parameters With Weight Flow at 100% Speed; 10% Immersion From Tip (Concluded)

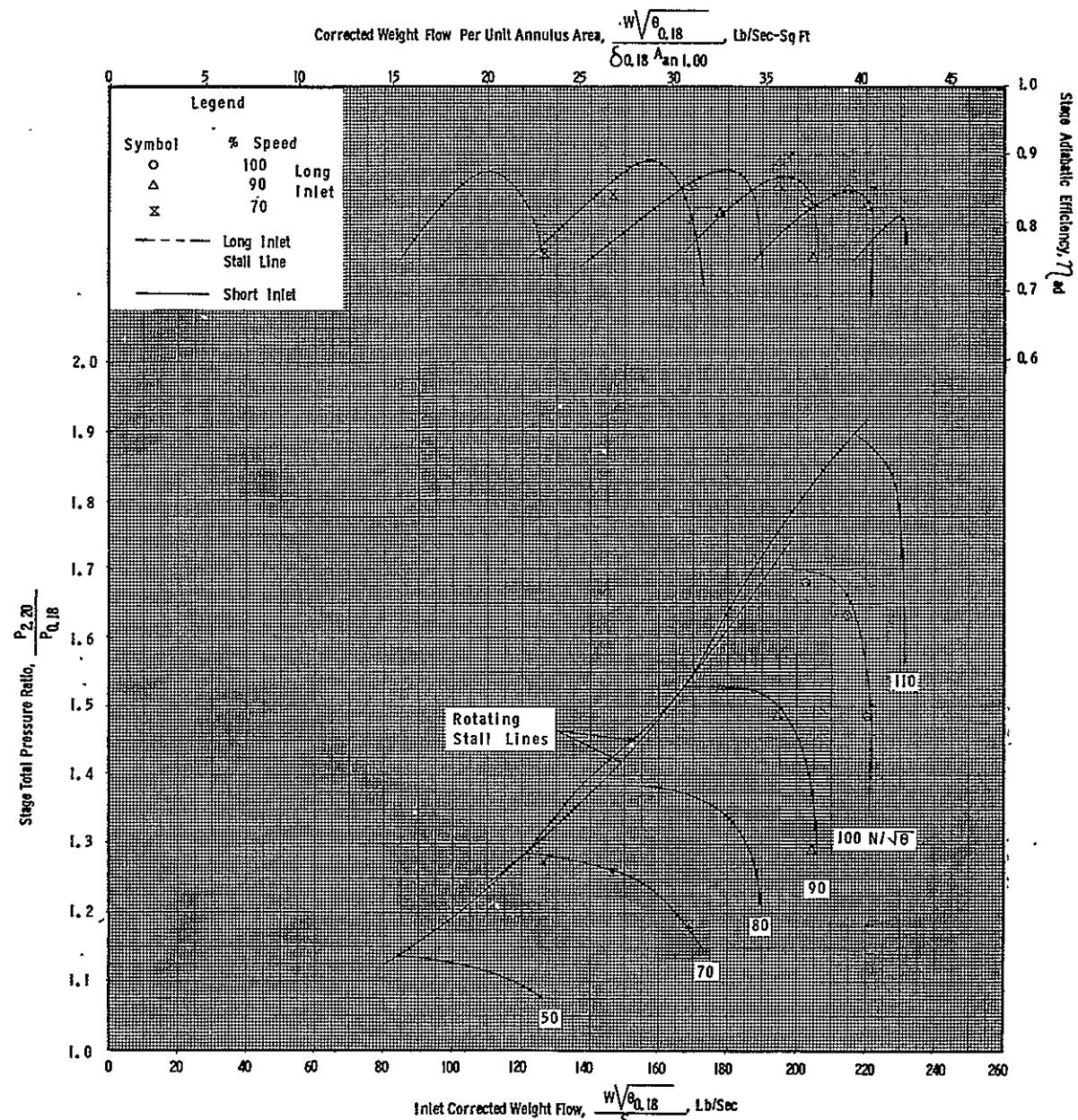


Figure 26. Stage Performance Map with Undistorted Inlet Flow and Long Inlet Duct.

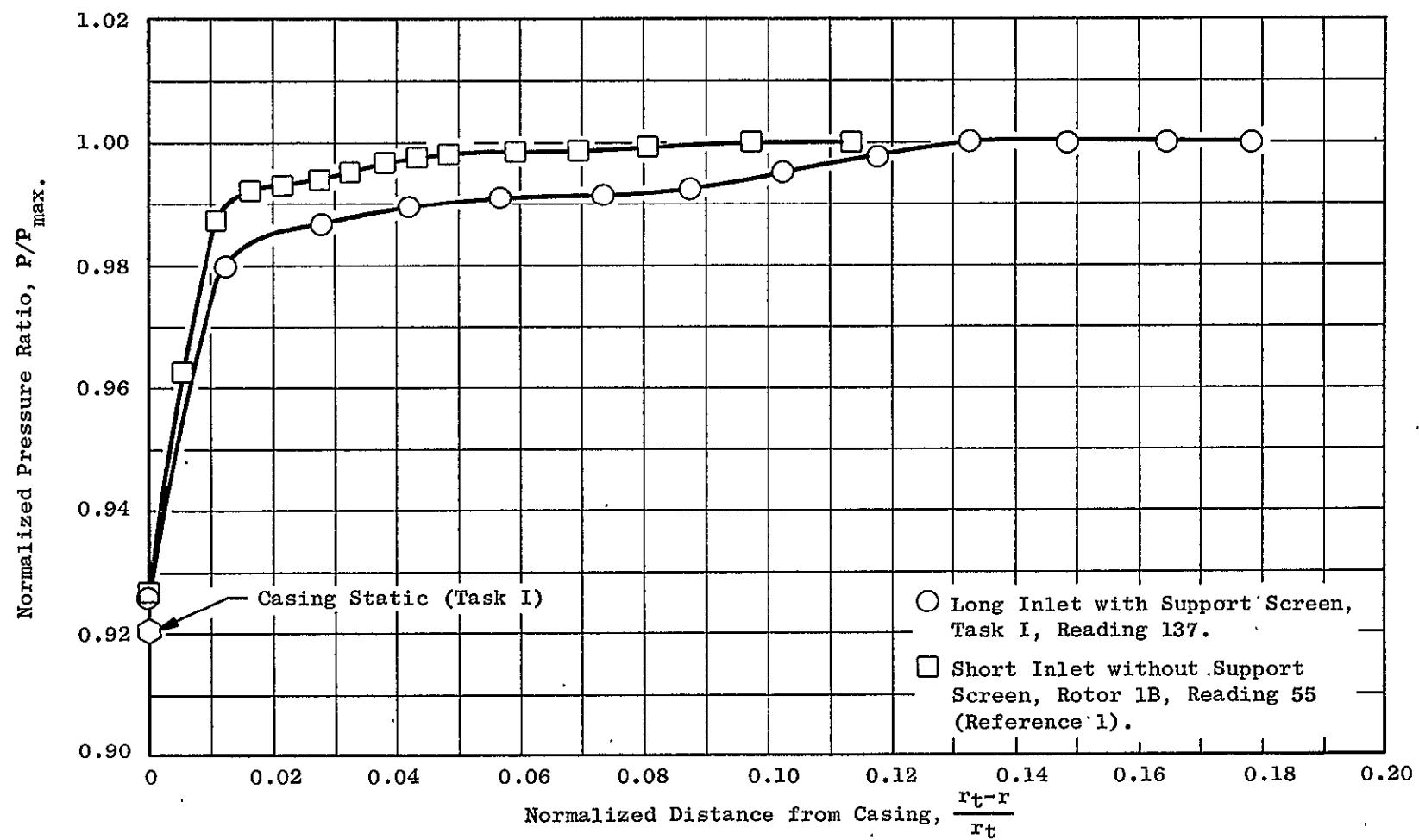


Figure 27. Comparison of Inlet Casing Boundary Layer Profiles at 100% Speed, Undistorted Inlet Flow, Between Long Inlet Duct with Distortion Support Screen and Short Inlet Duct without Distortion Support Screen.

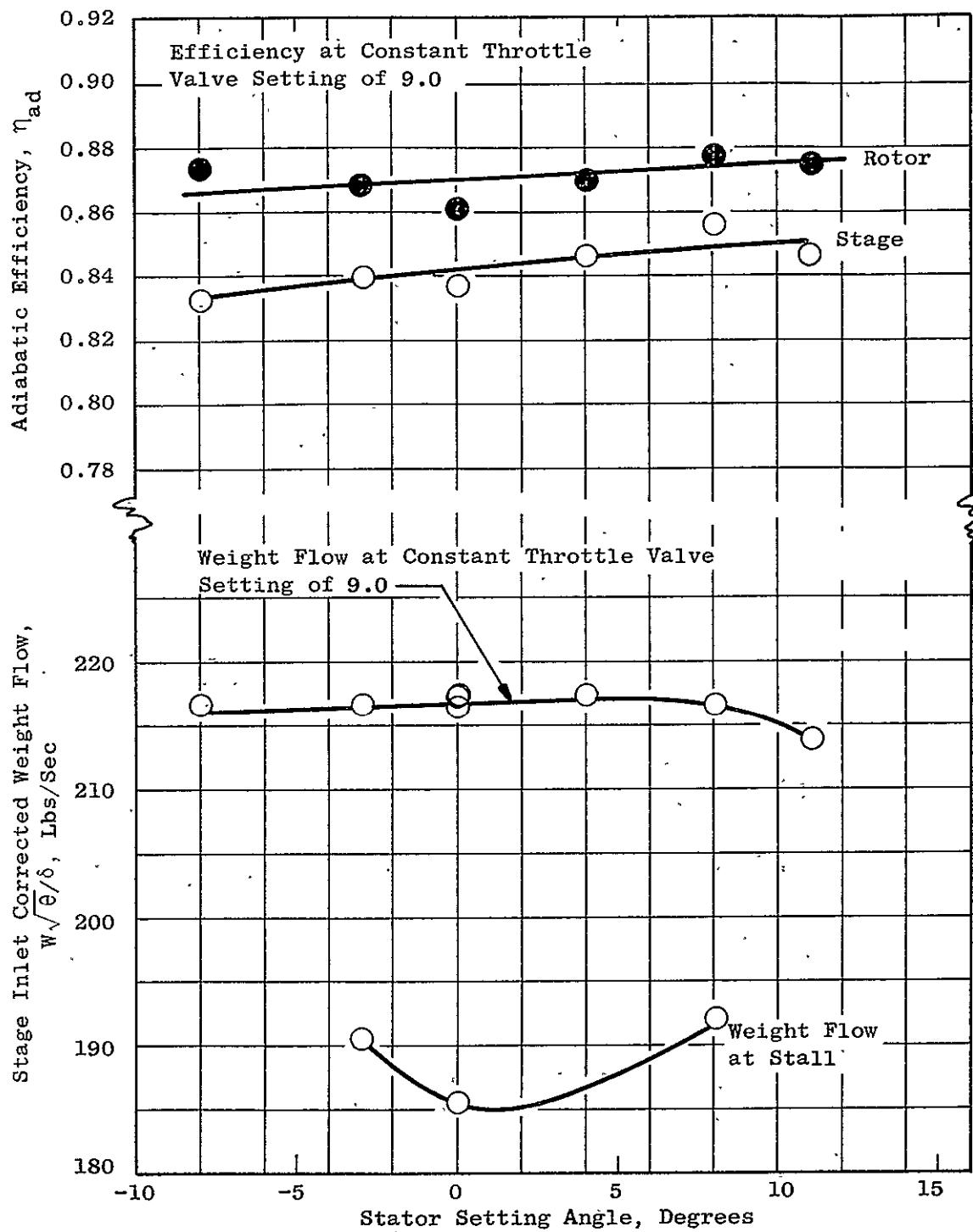


Figure 28. Variation of Weight Flow and Efficiency with Stator Setting Angle.

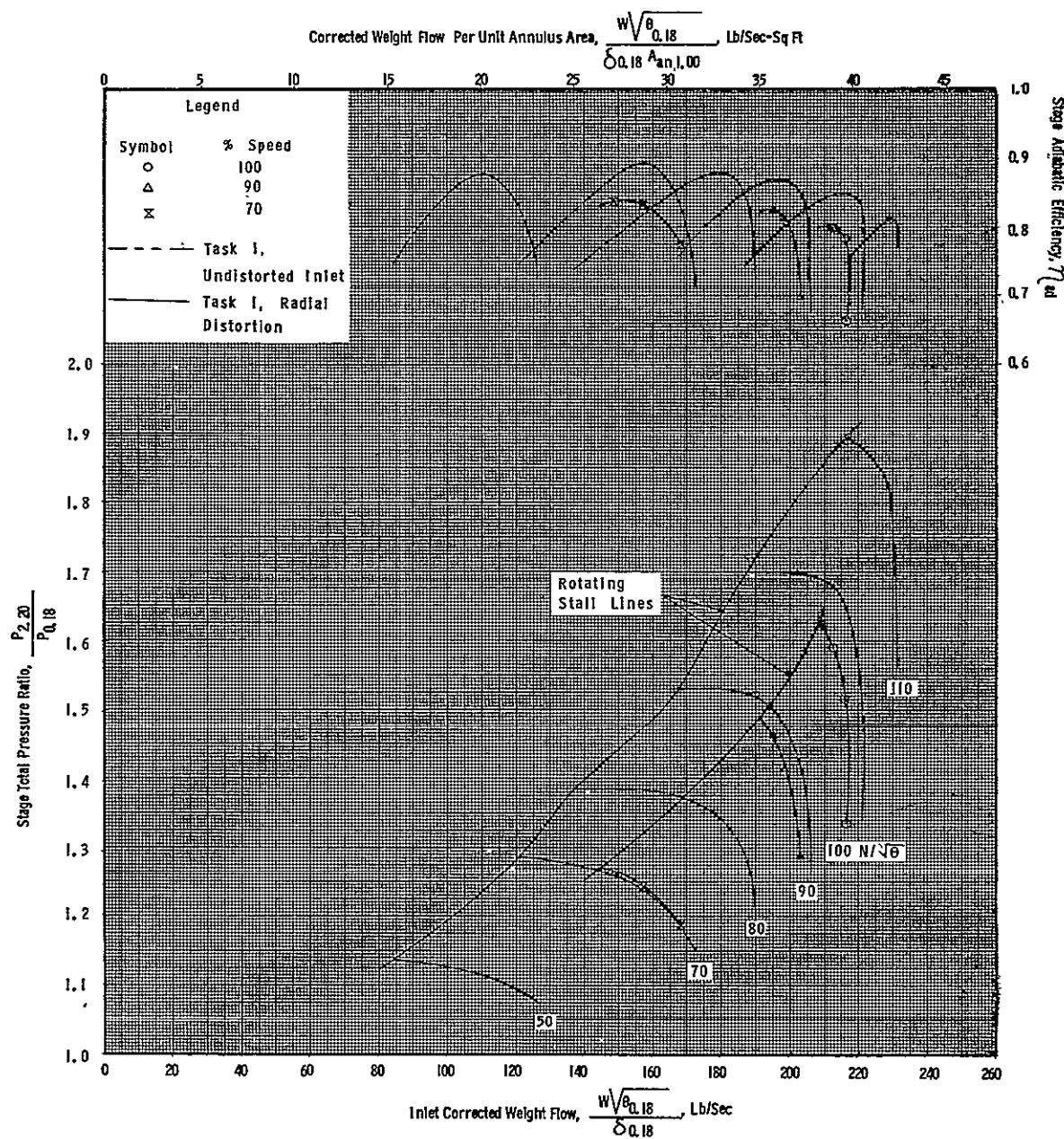


Figure 29. Stage Performance Map with Inlet Tip-Radial Distortion.

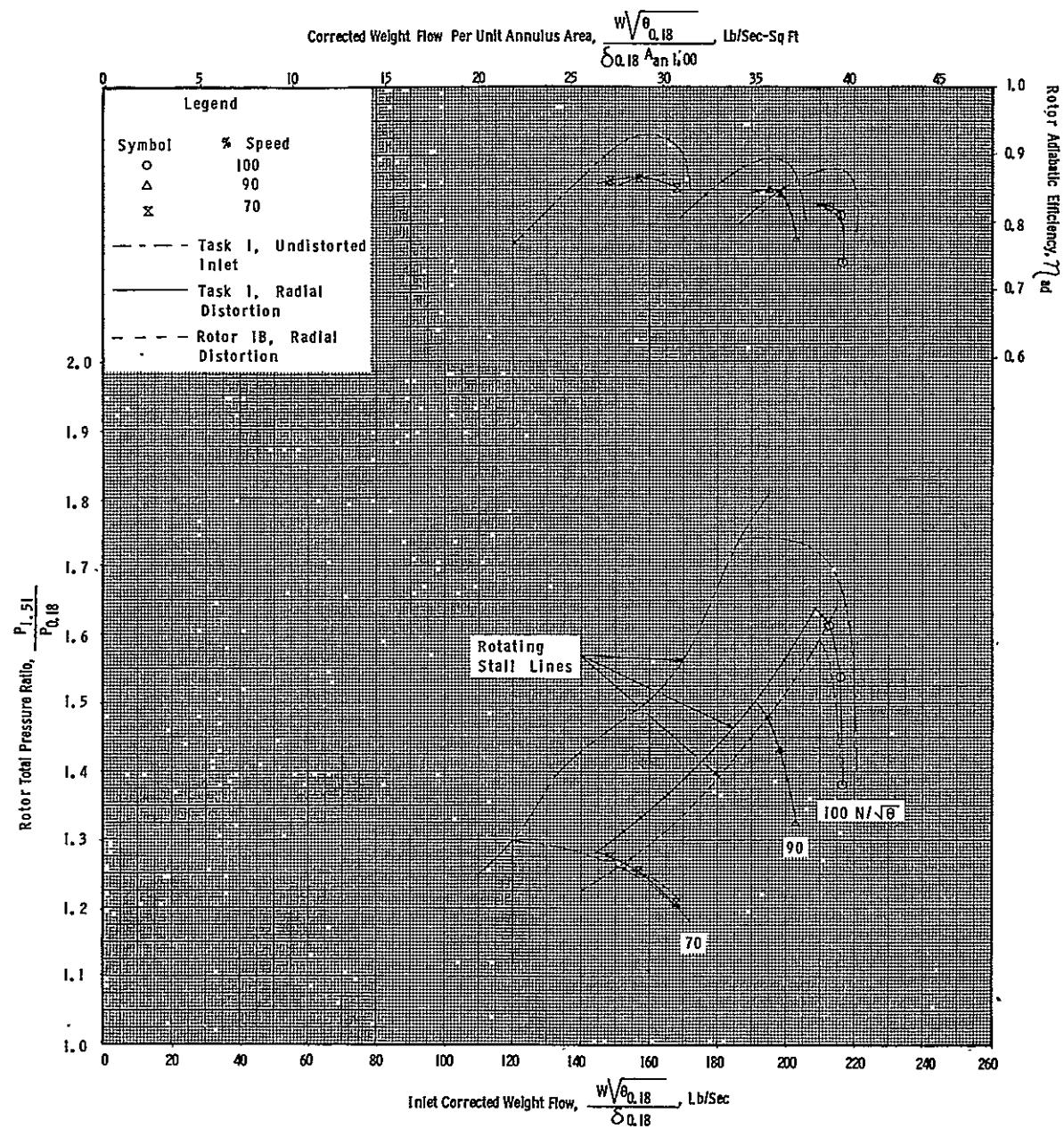


Figure 30. Rotor Performance Map with Inlet Tip-Radial Distortion.

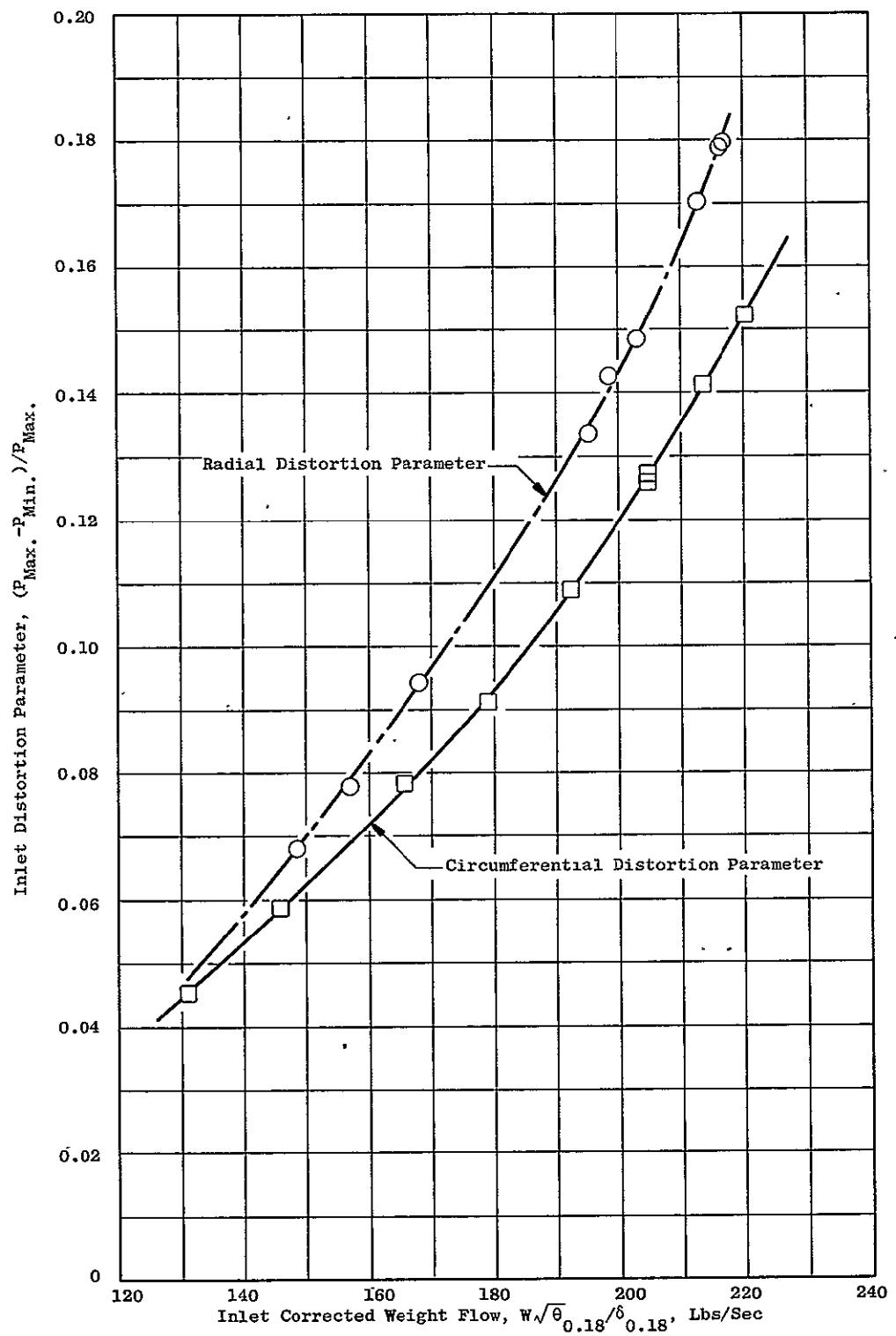


Figure 31. Variation of Inlet Distortion Parameter for Radial and Circumferential Distortion Tests.

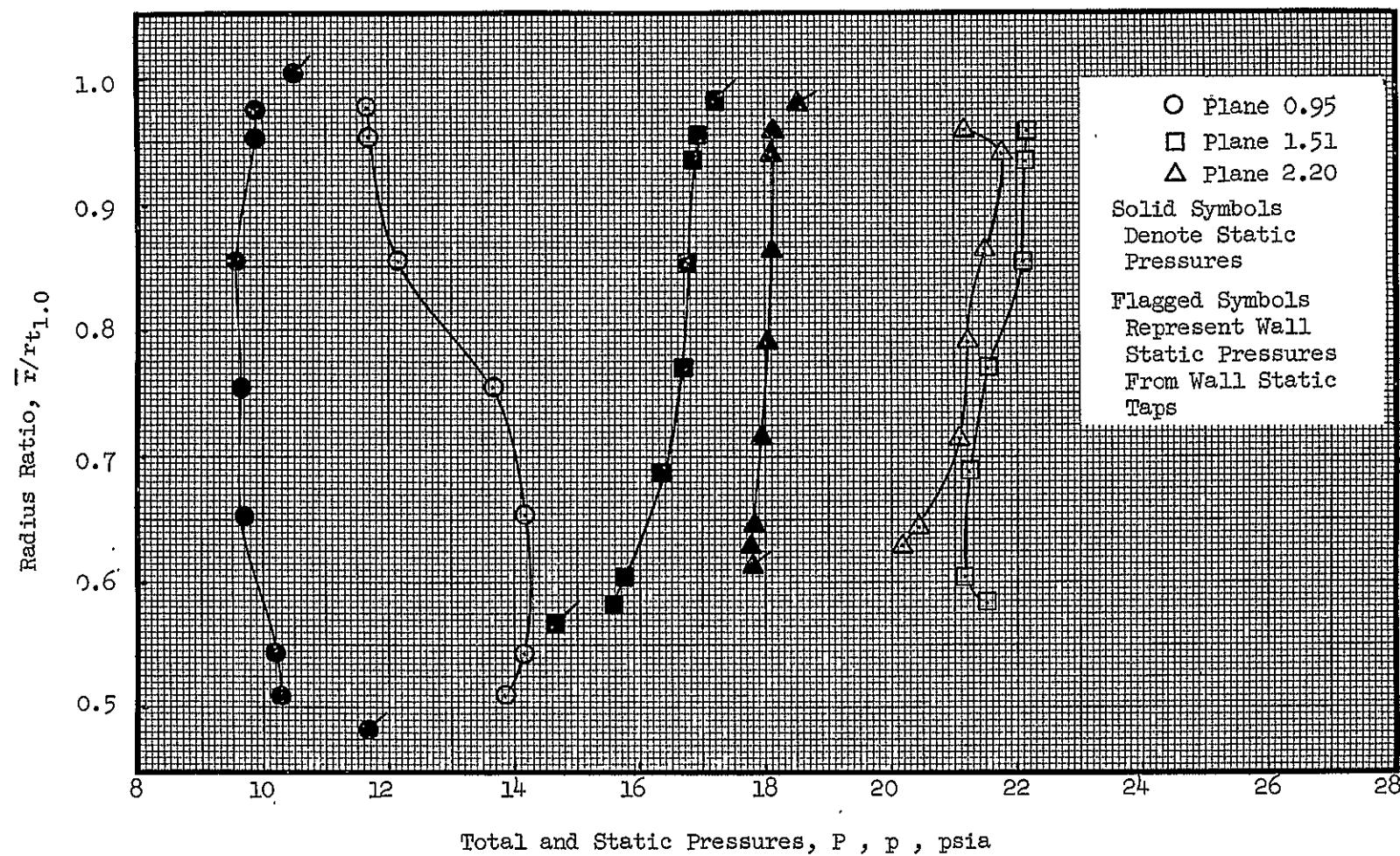


Figure 32. Radial Profiles of Fluid Conditions at 100% Speed Near Stall with Inlet Tip-Radial Distortion, Reading 82.

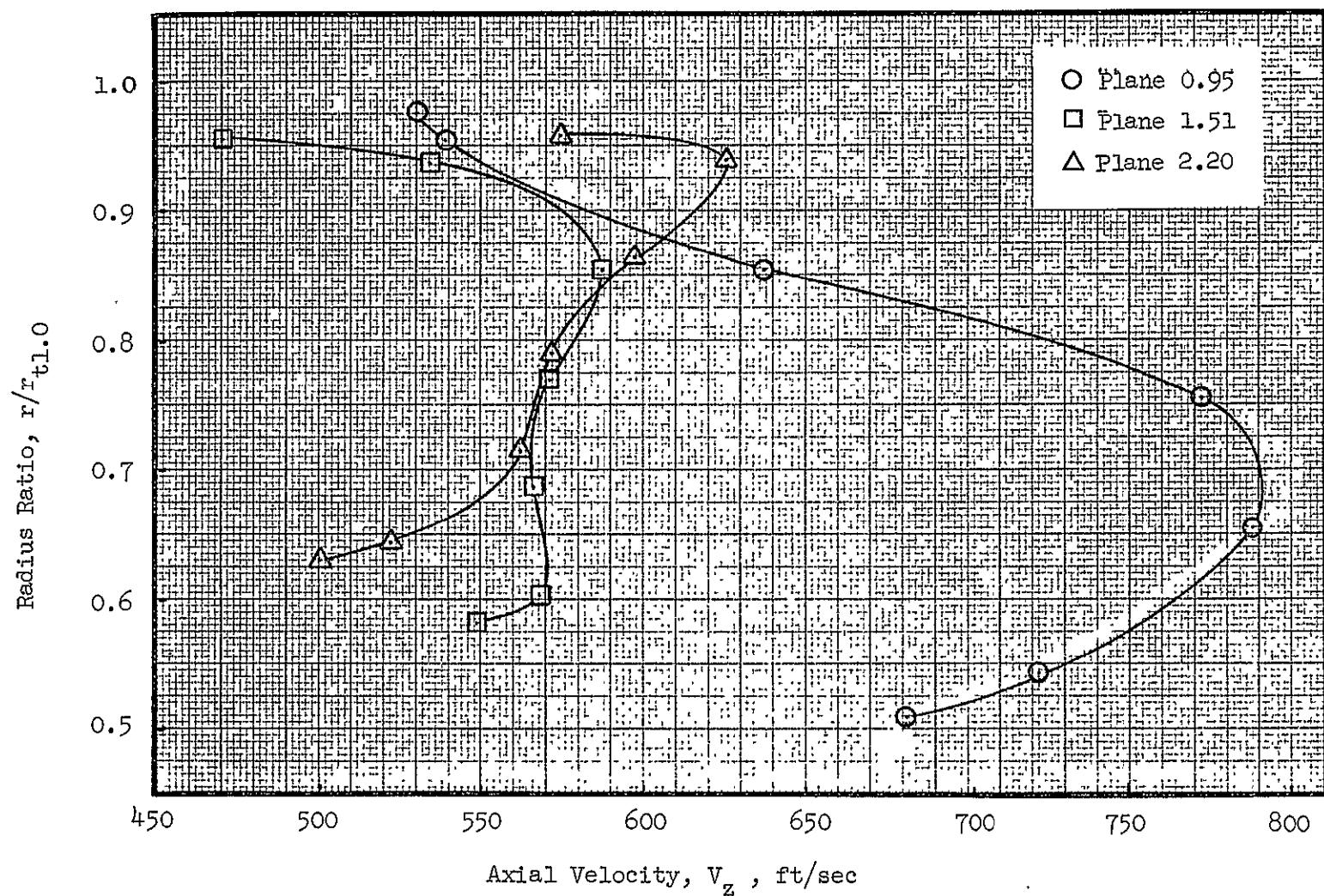


Figure 32. Radial Profiles of Fluid Conditions at 100% Speed Near Stall with Inlet Tip-Radial Distortion, Reading 82 (Continued).

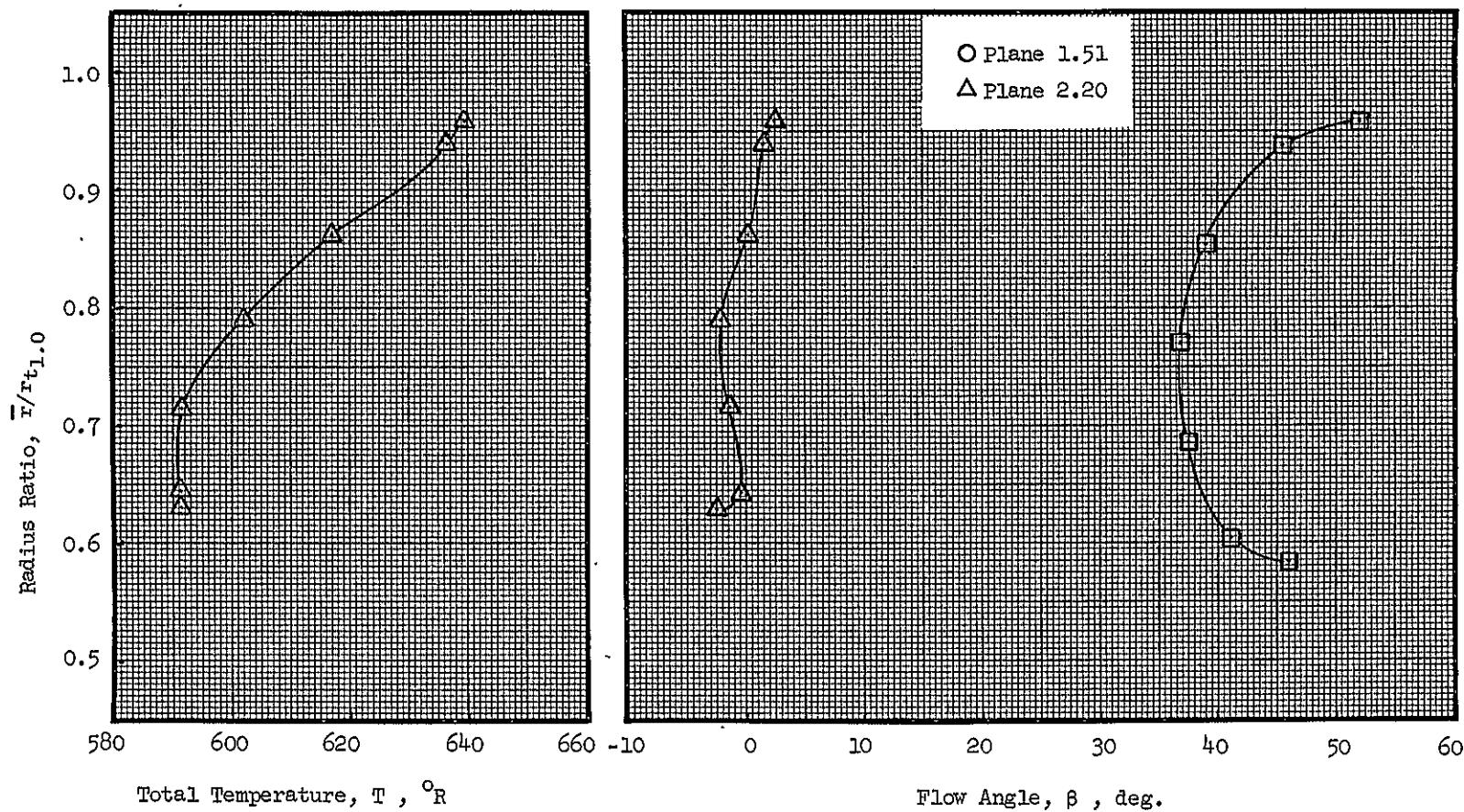


Figure 32. Radial Profiles of Fluid Conditions at 100% Speed Near Stall with Inlet Tip-Radial Distortion, Reading 82 (Concluded).

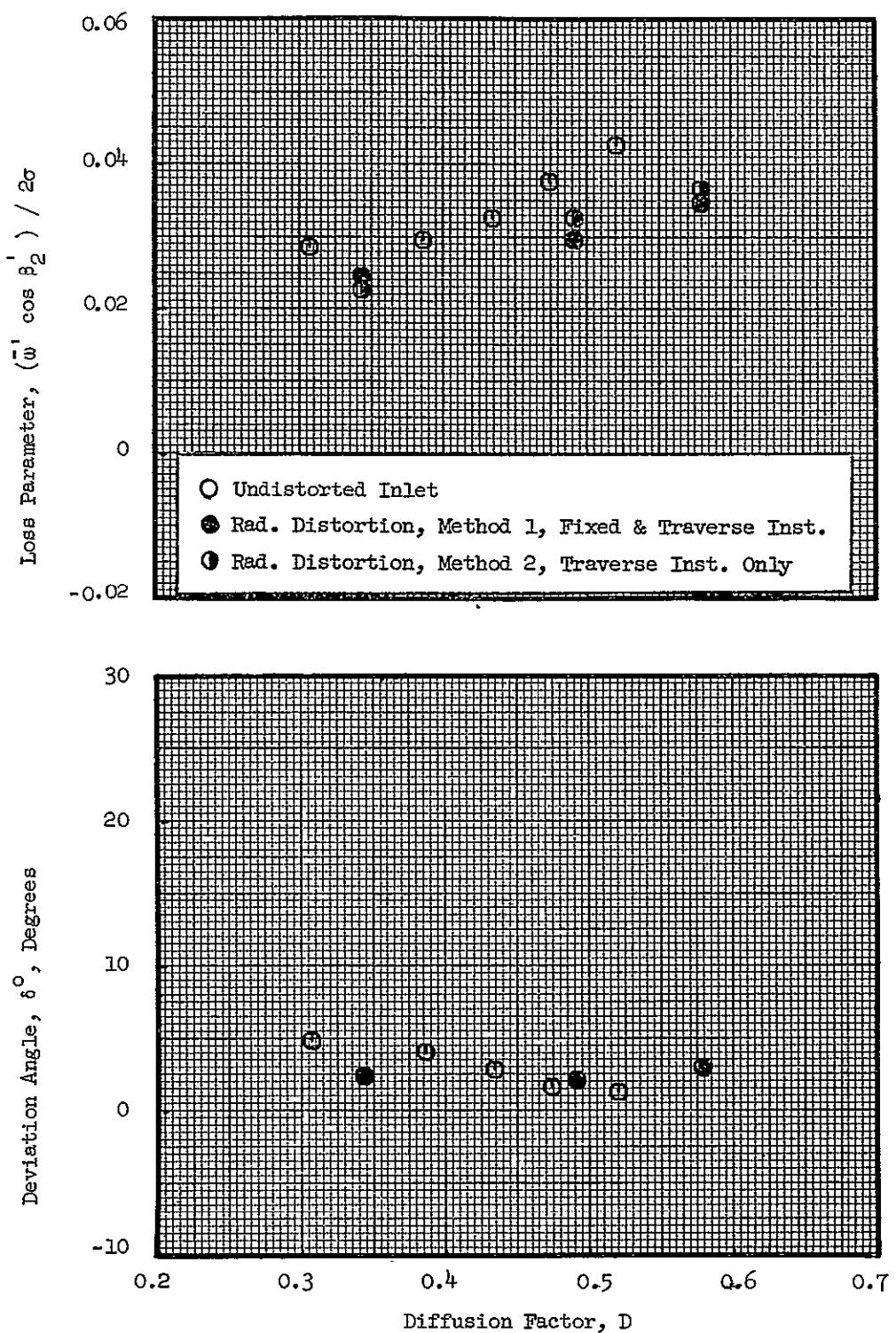


Figure 33 (a). Rotor Blade Element Data with Inlet Tip-Radial Distortion, at 5% Immersion from Tip.

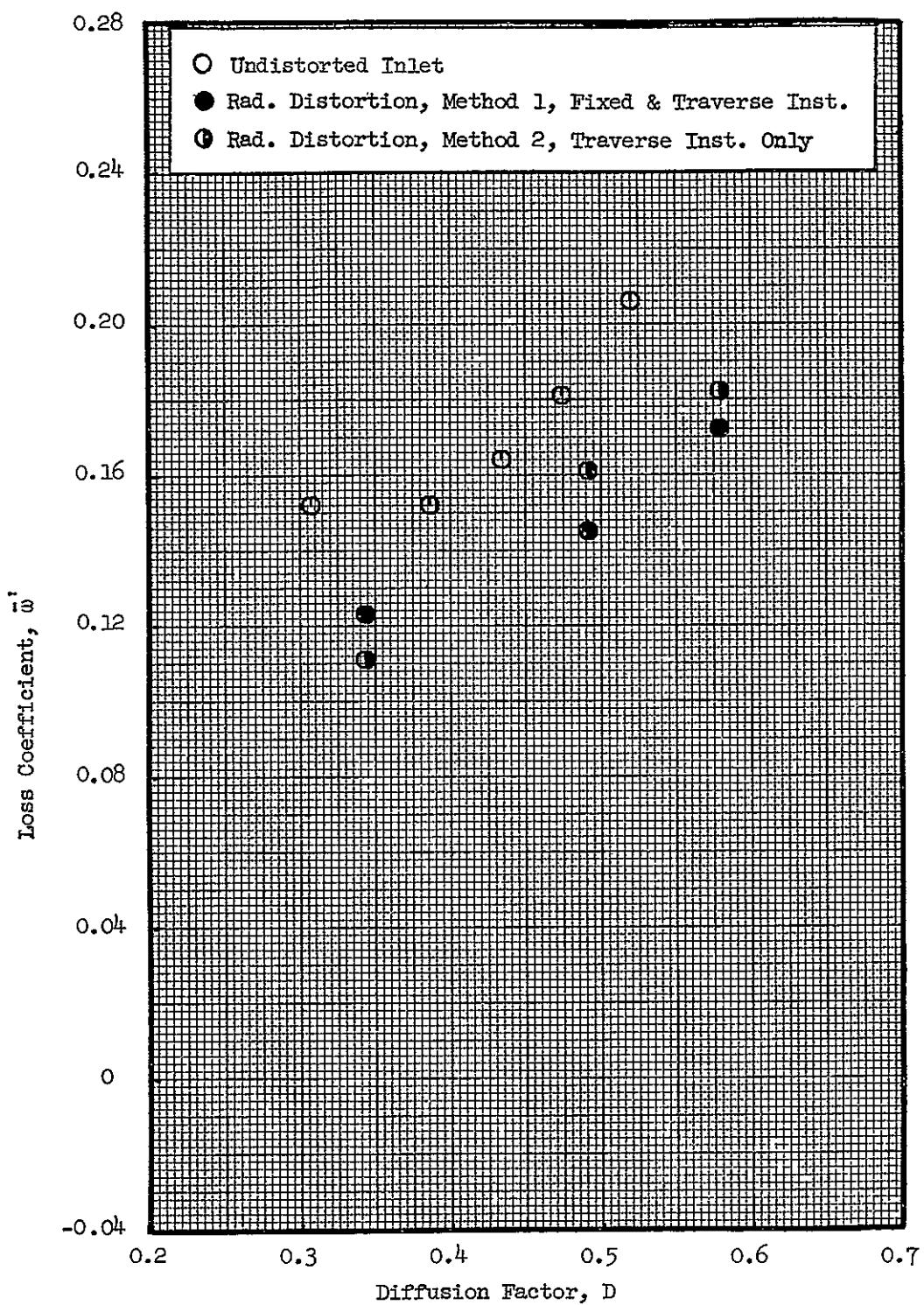


Figure 33 (a). Rotor Blade Element Data with Inlet Tip-Radial Distortion, at 5% Immersion from Tip (Concluded).

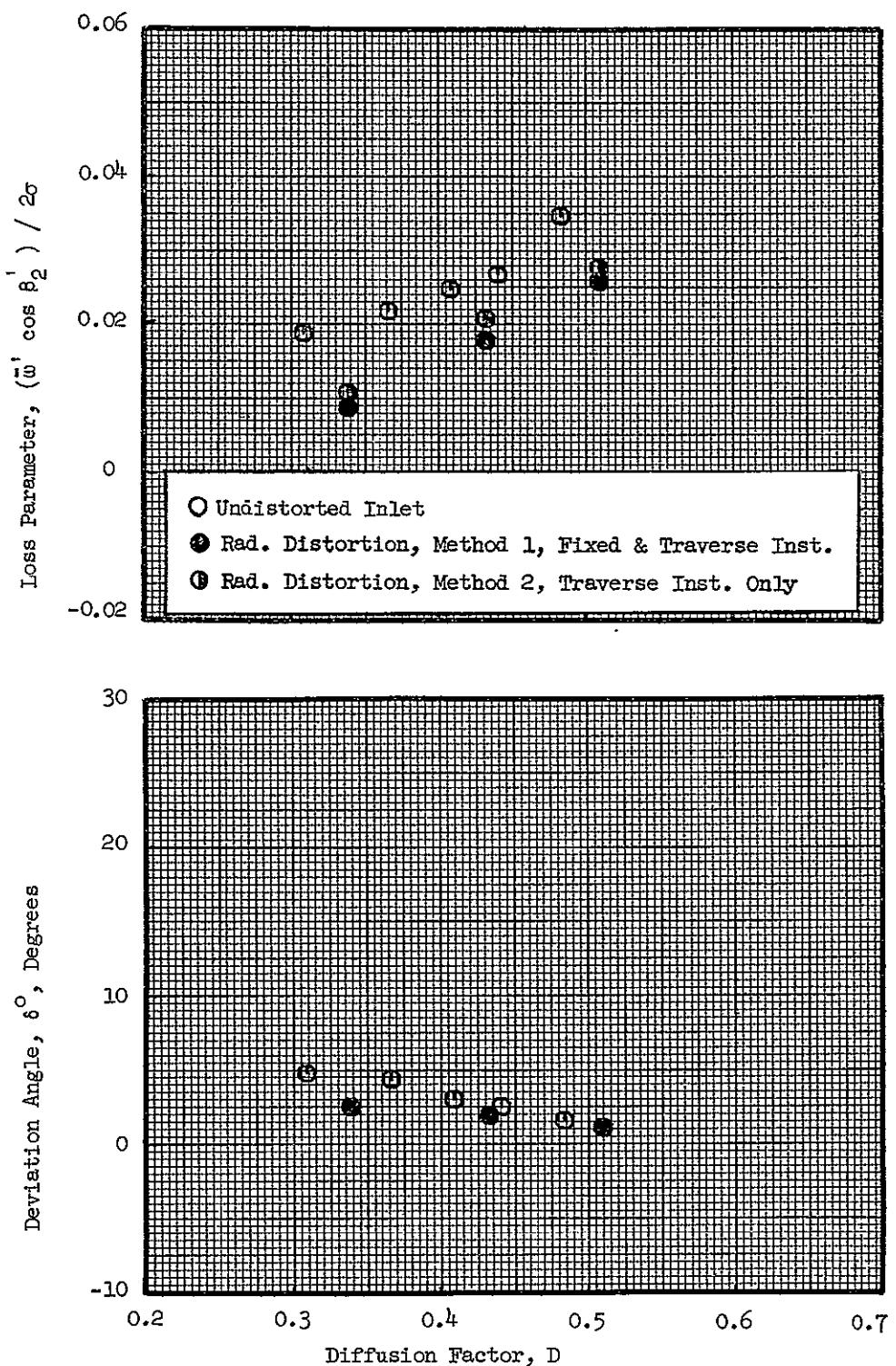


Figure 33 (b). Rotor Blade Element Data with Inlet Tip-Radial Distortion, at 10% Immersion from Tip.

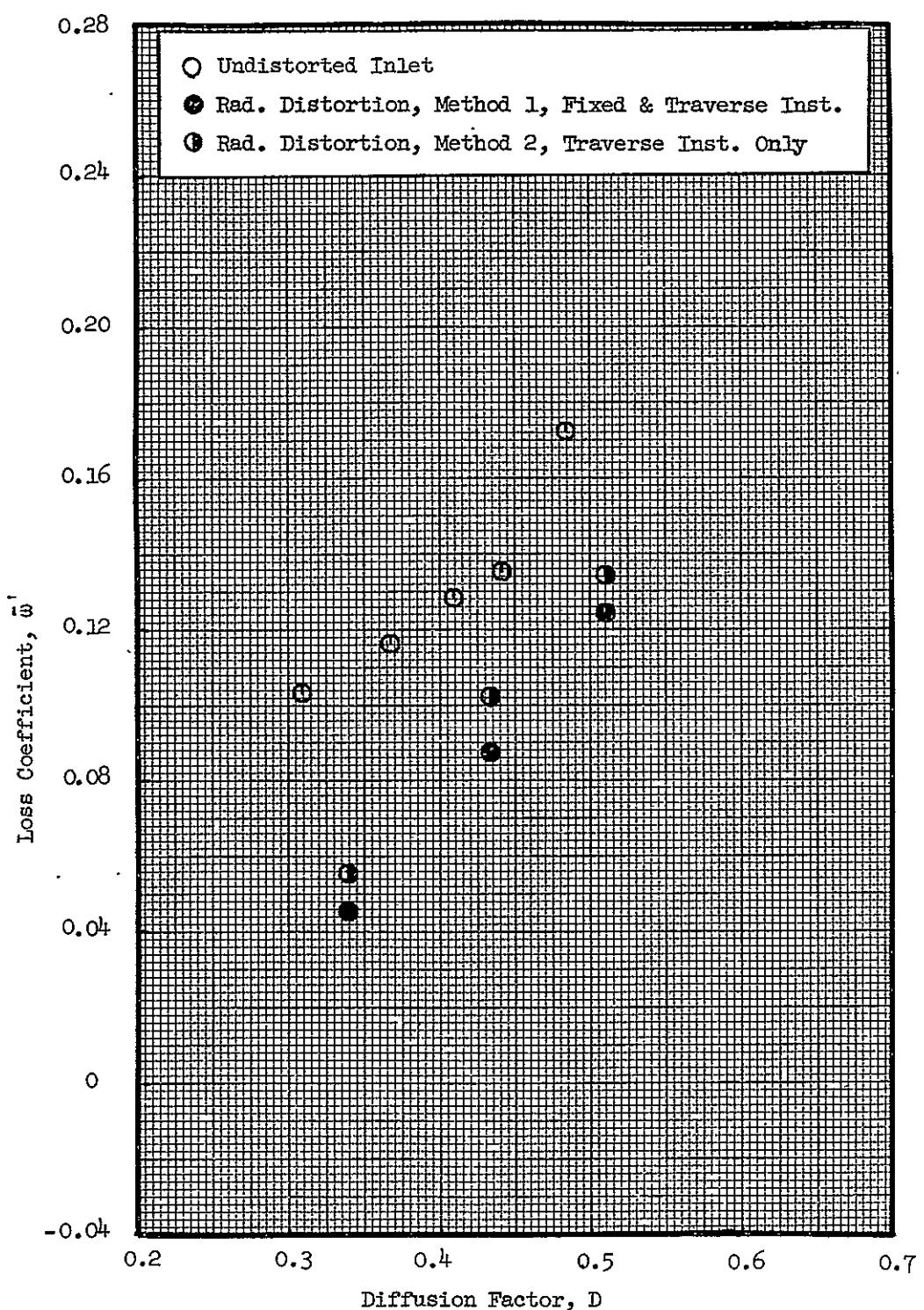


Figure 33 (b). Rotor Blade Element Data with Inlet Tip-Radial Distortion, at 10% Immersion from Tip (Concluded).

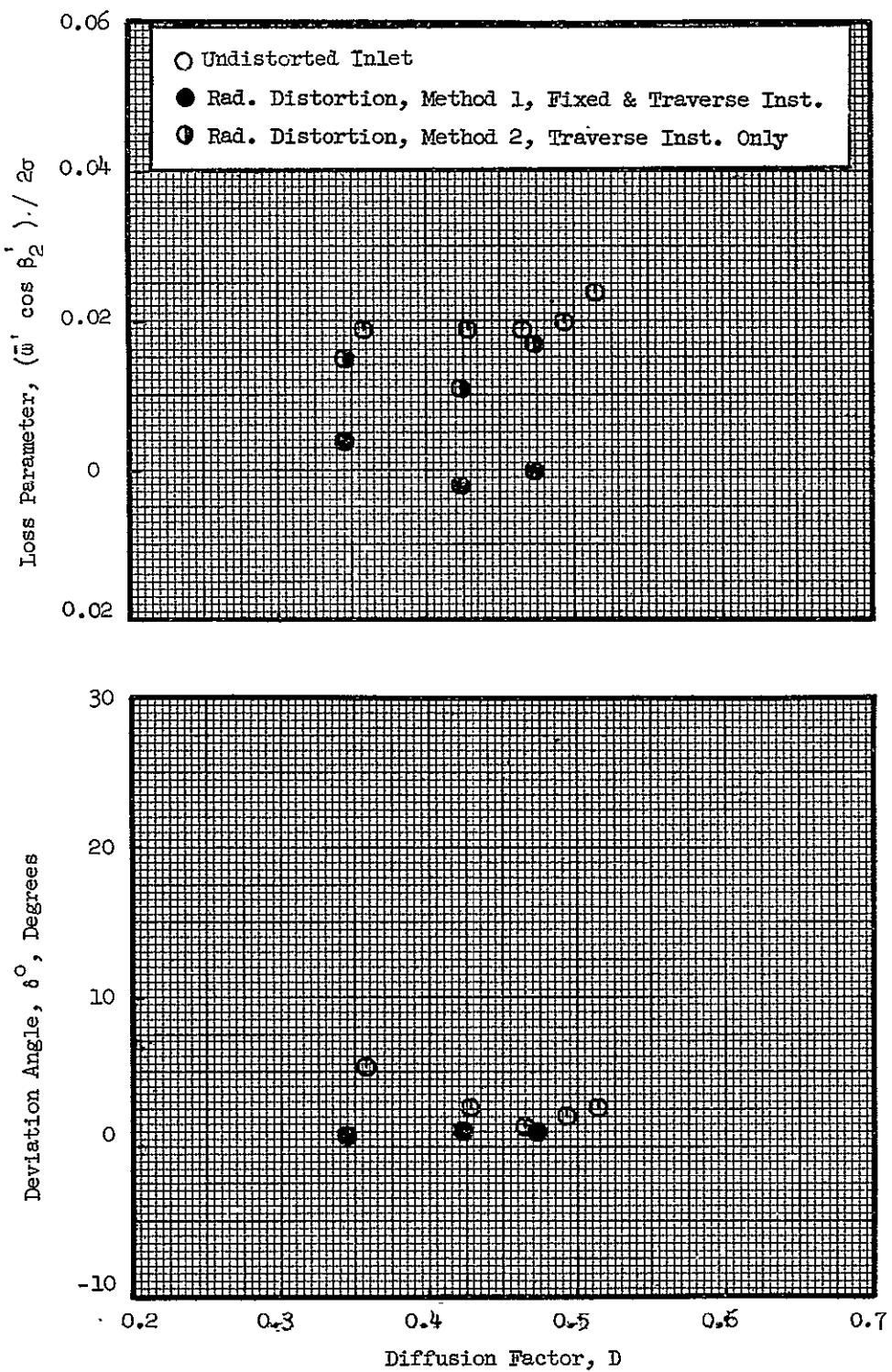


Figure 33 (c). Rotor Blade Element Data with Inlet Tip-Radial Distortion, at 30% Immersion from Tip.

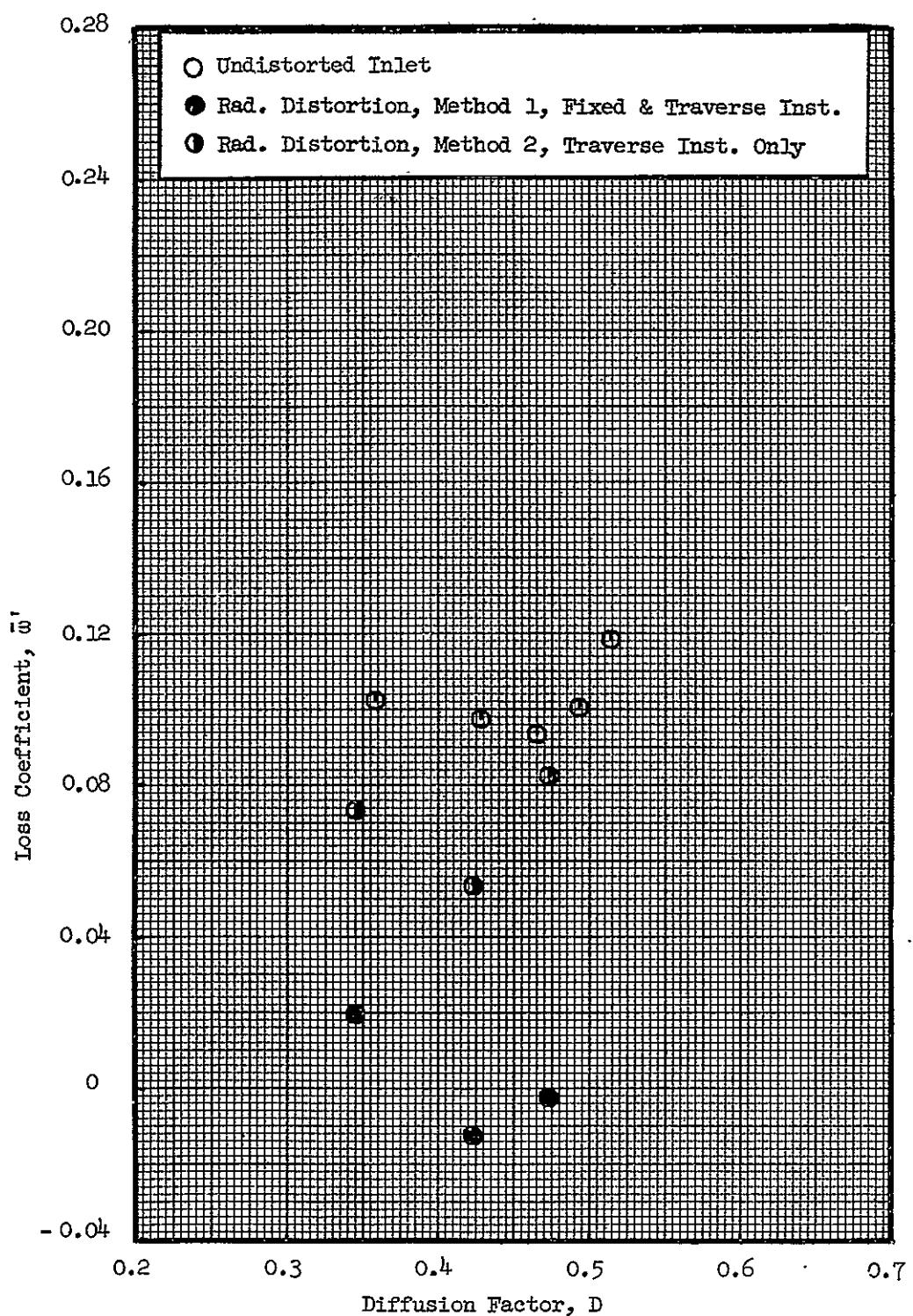


Figure 33 (c). Rotor Blade Element Data with Inlet Tip-Radial Distortion, at 30% Immersion from Tip (Concluded).

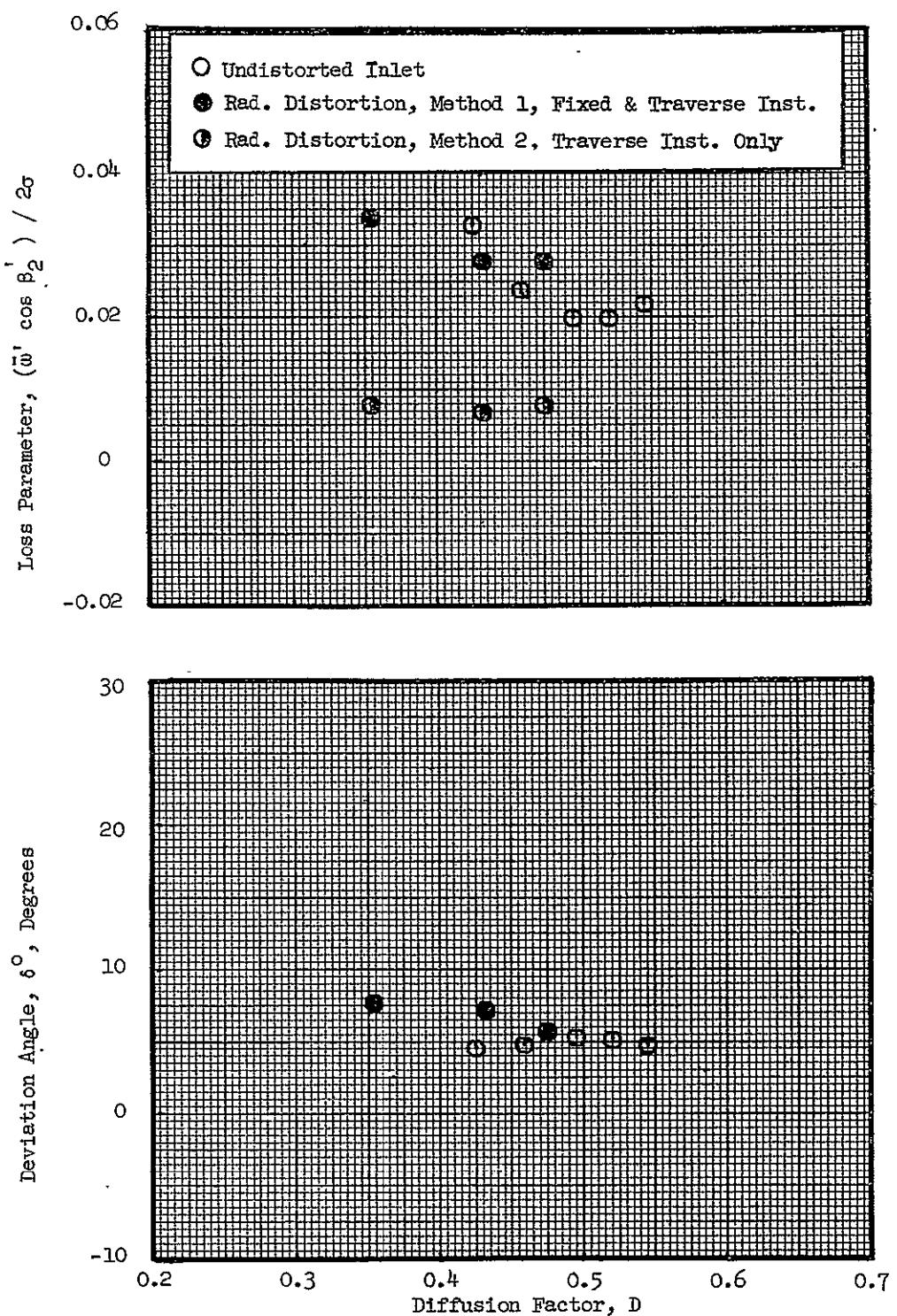


Figure 33 (d). Rotor Blade Element Data with Inlet Tip-Radial Distortion, at 50% Immersion from Tip.

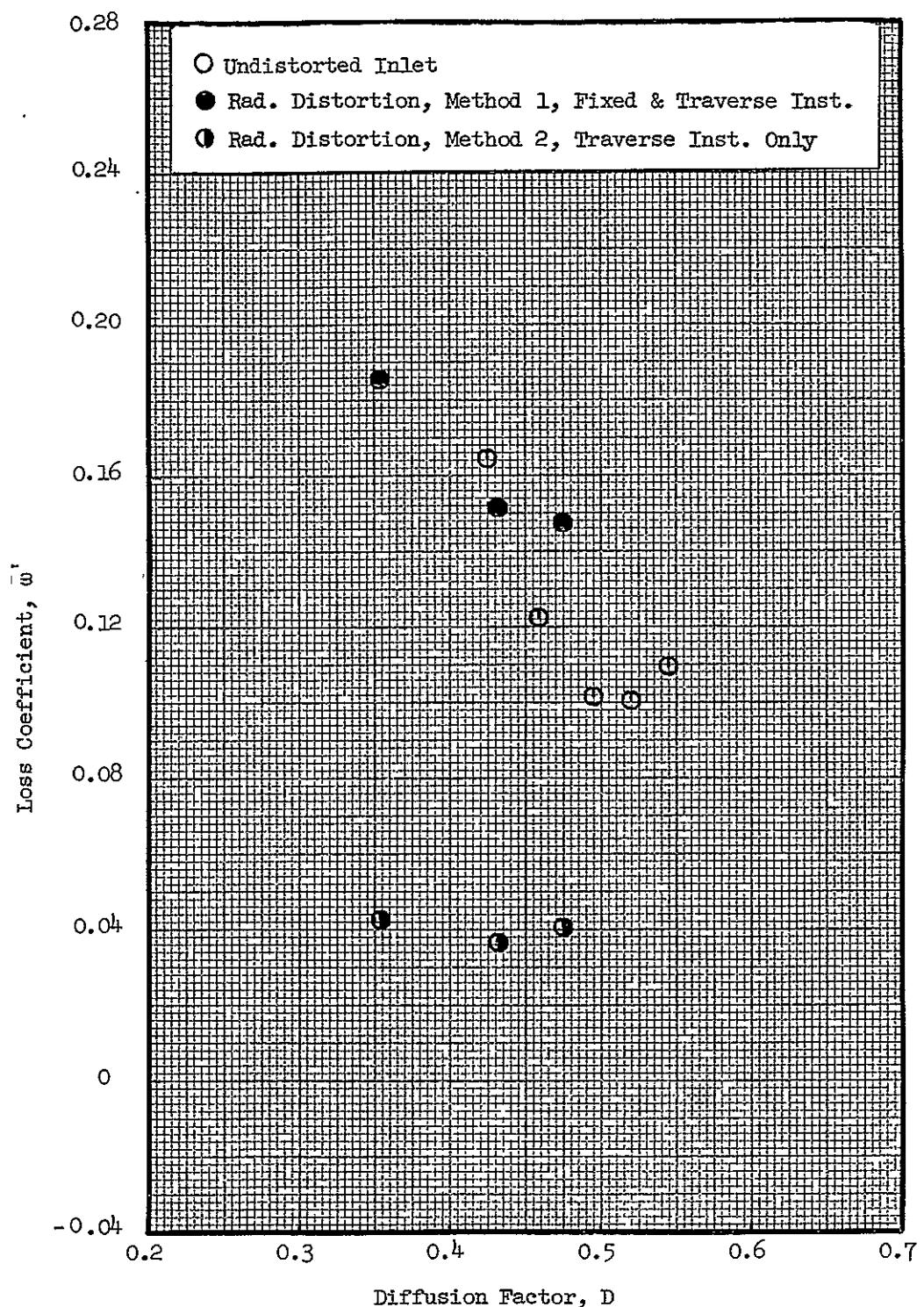


Figure 33 (d). Rotor Blade Element Data with Inlet Tip-Radial Distortion, at 50% Immersion from Tip (Concluded).

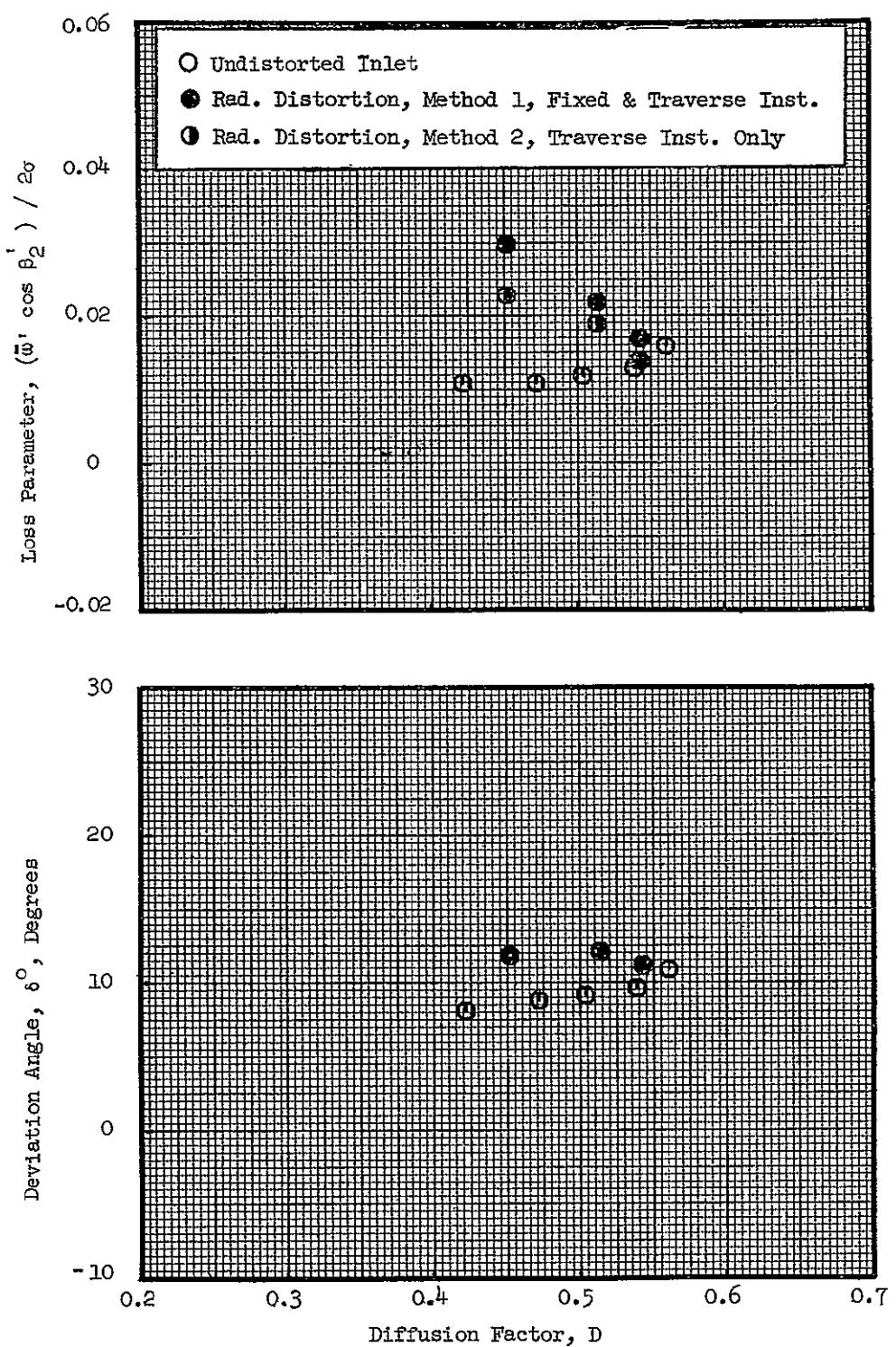


Figure 33 (e). Rotor Blade Element Data with Inlet Tip-Radial Distortion, at 70% Immersion from Tip.

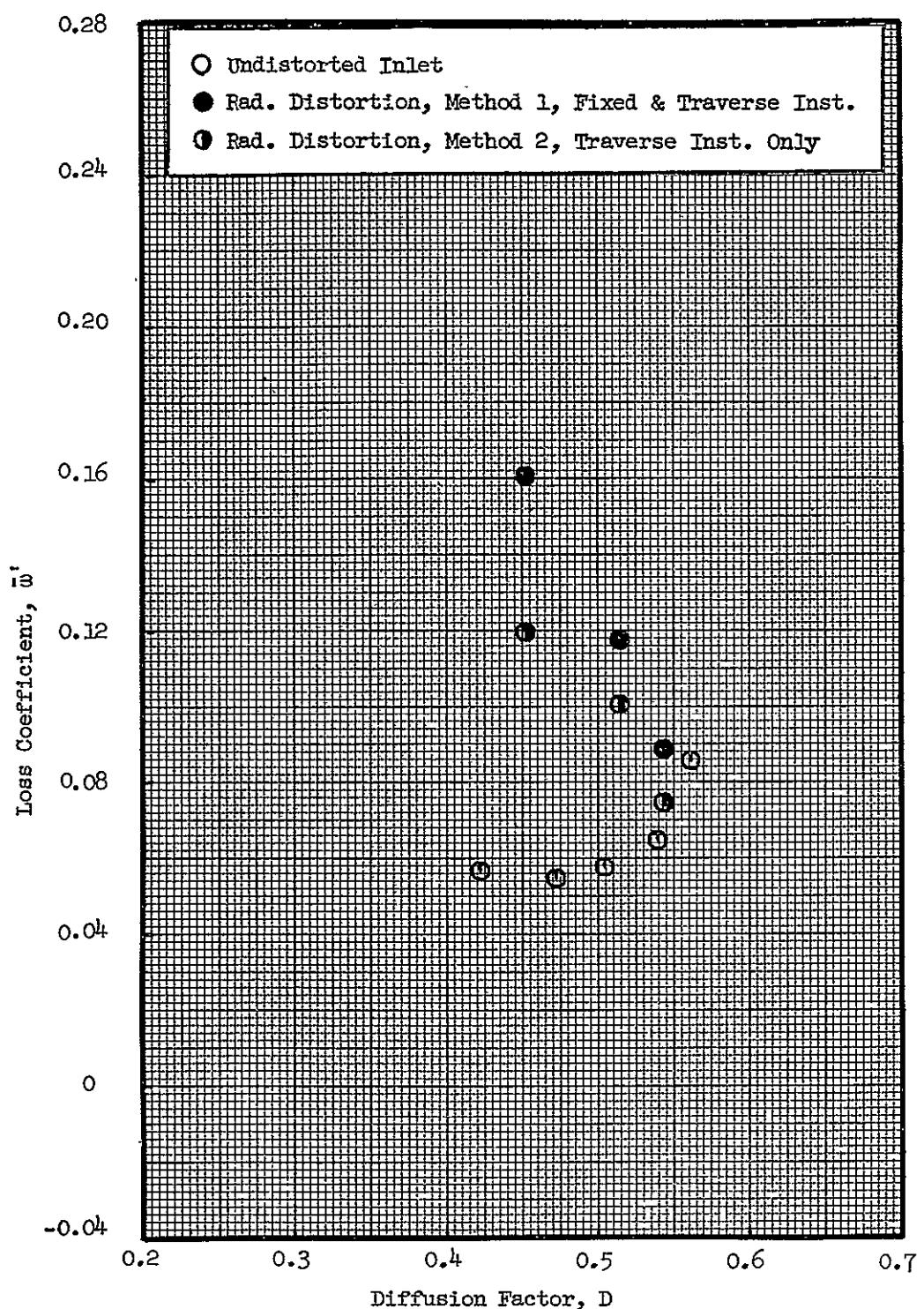


Figure 33 (e). Rotor Blade Element Data with Inlet Tip-Radial Distortion, at 70% Immersion from Tip (Concluded).

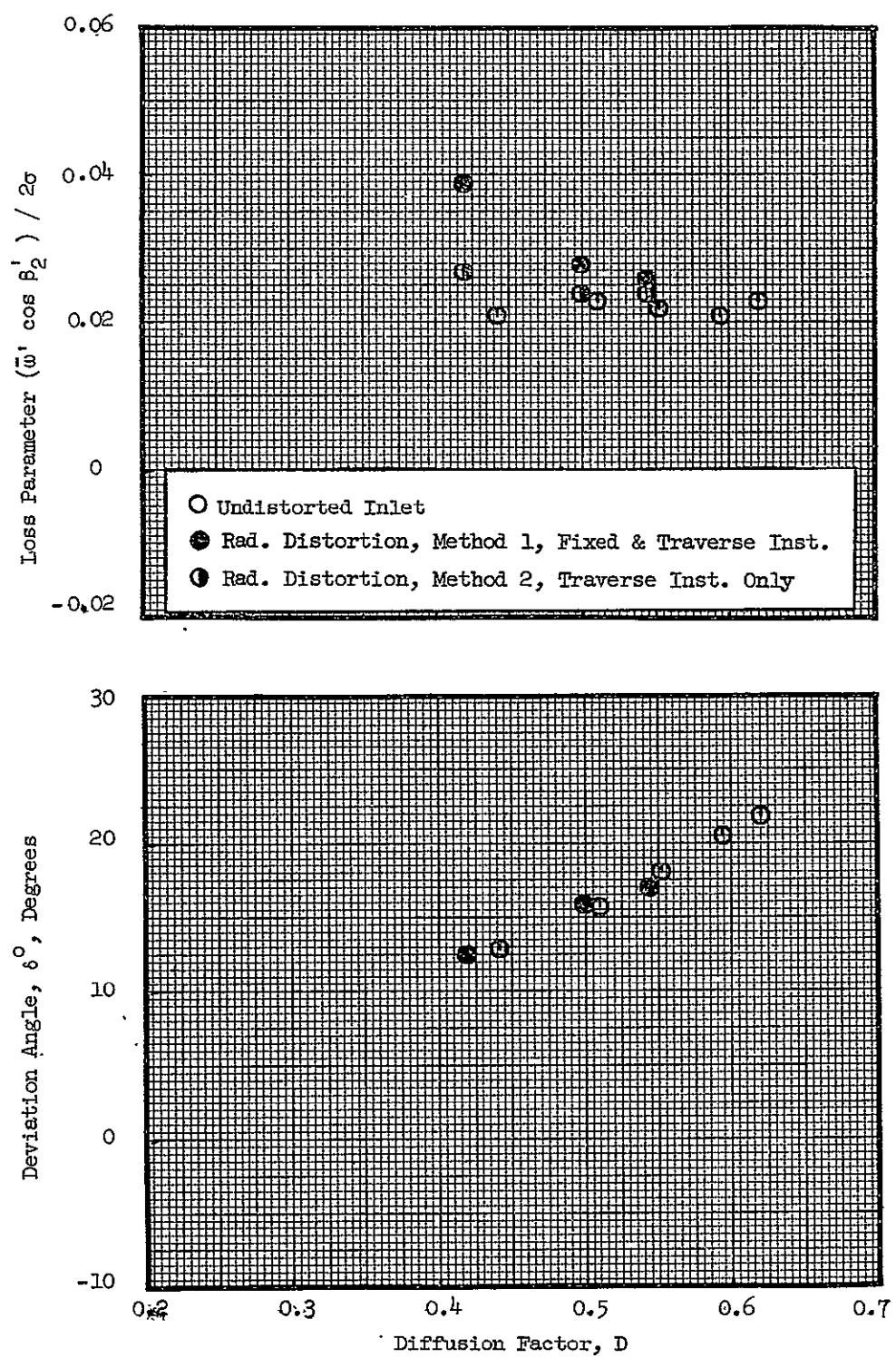


Figure 33 (f). Rotor Blade Element Data with Inlet Tip-Radial Distortion, at 90% Immersion from Tip.

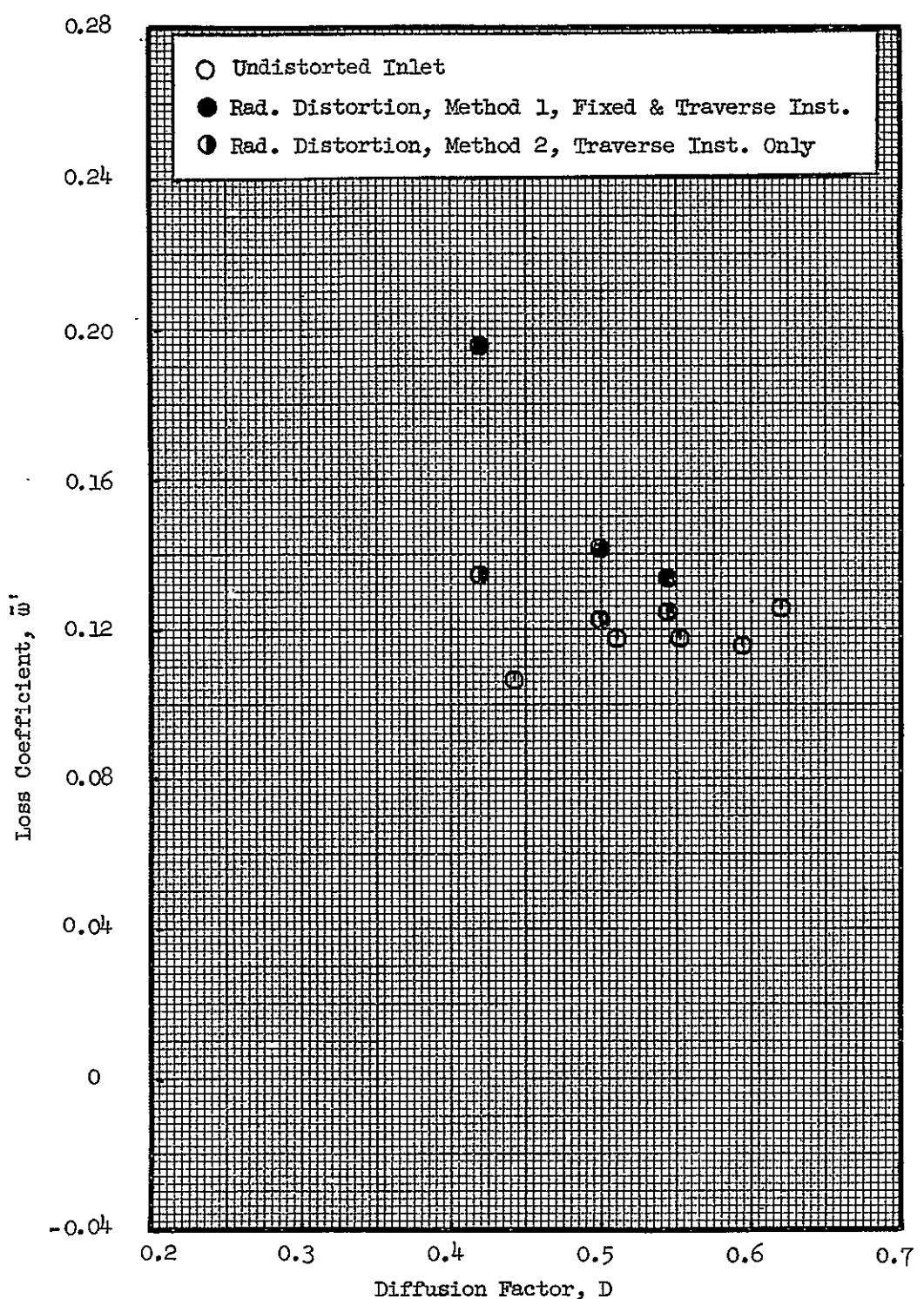


Figure 33 (f). Rotor Blade Element Data with Inlet Tip-Radial Distortion, at 90% Immersion from Tip (Concluded).

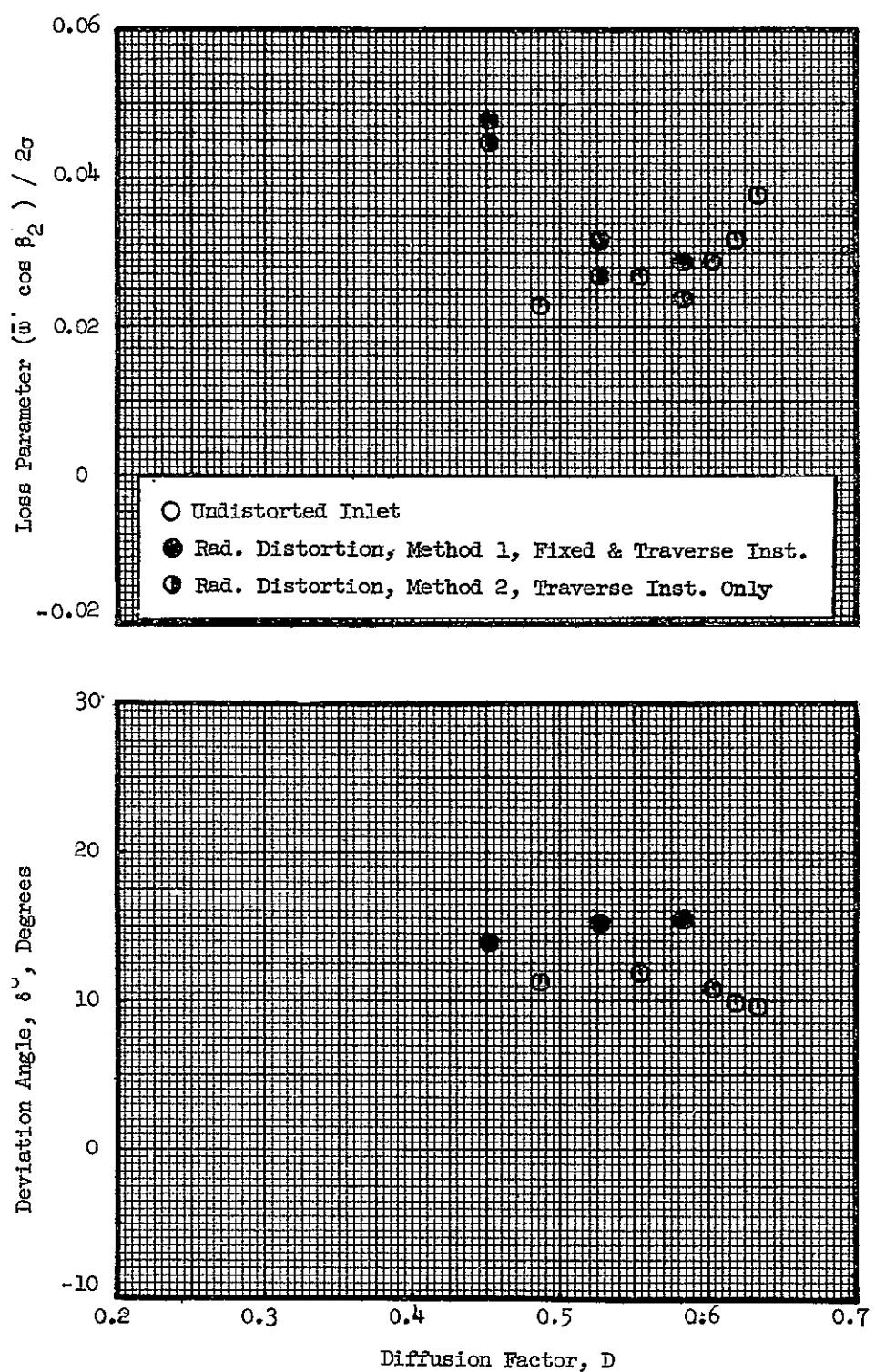


Figure 33 (g). Rotor Blade Element Data with Inlet Tip-Radial Distortion, at 95% Immersion from Tip.

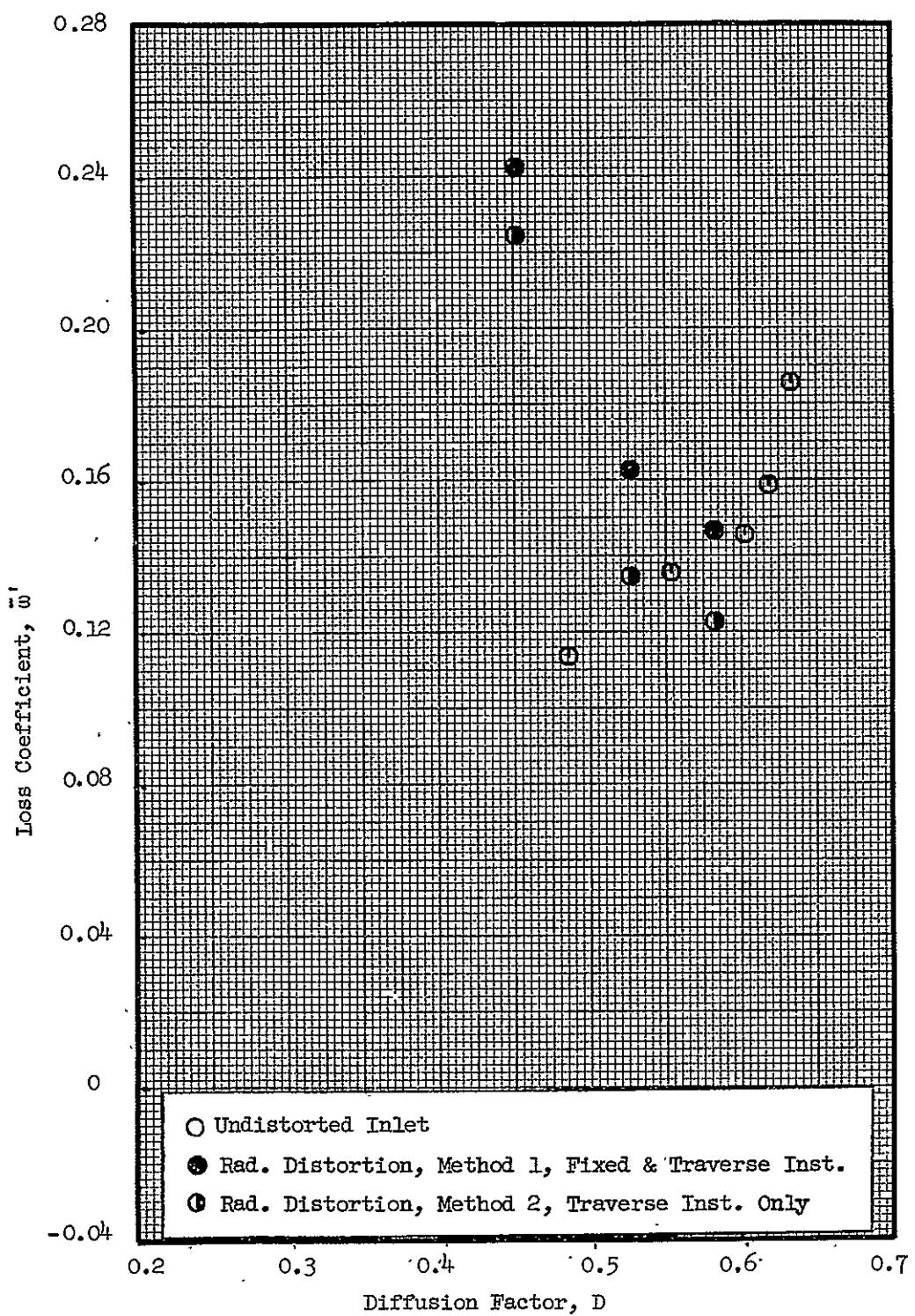


Figure 33 (g). Rotor Blade Element Data with Inlet Tip-Radial Distortion, at 95% Immersion from Tip (Concluded).

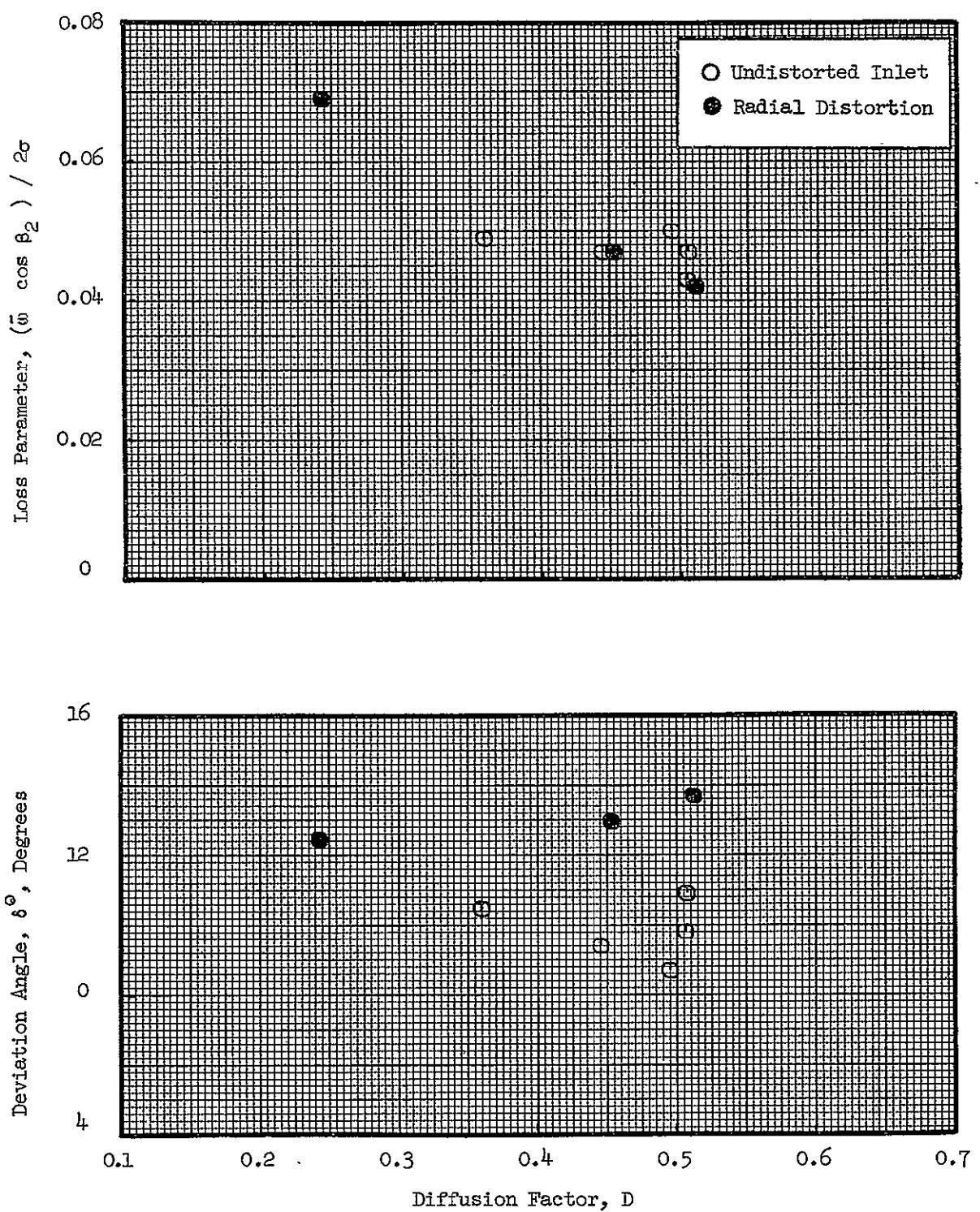


Figure 34 (a). Stator Blade Element Data with Inlet Tip-Radial Distortion, at 5% Immersion from Tip.

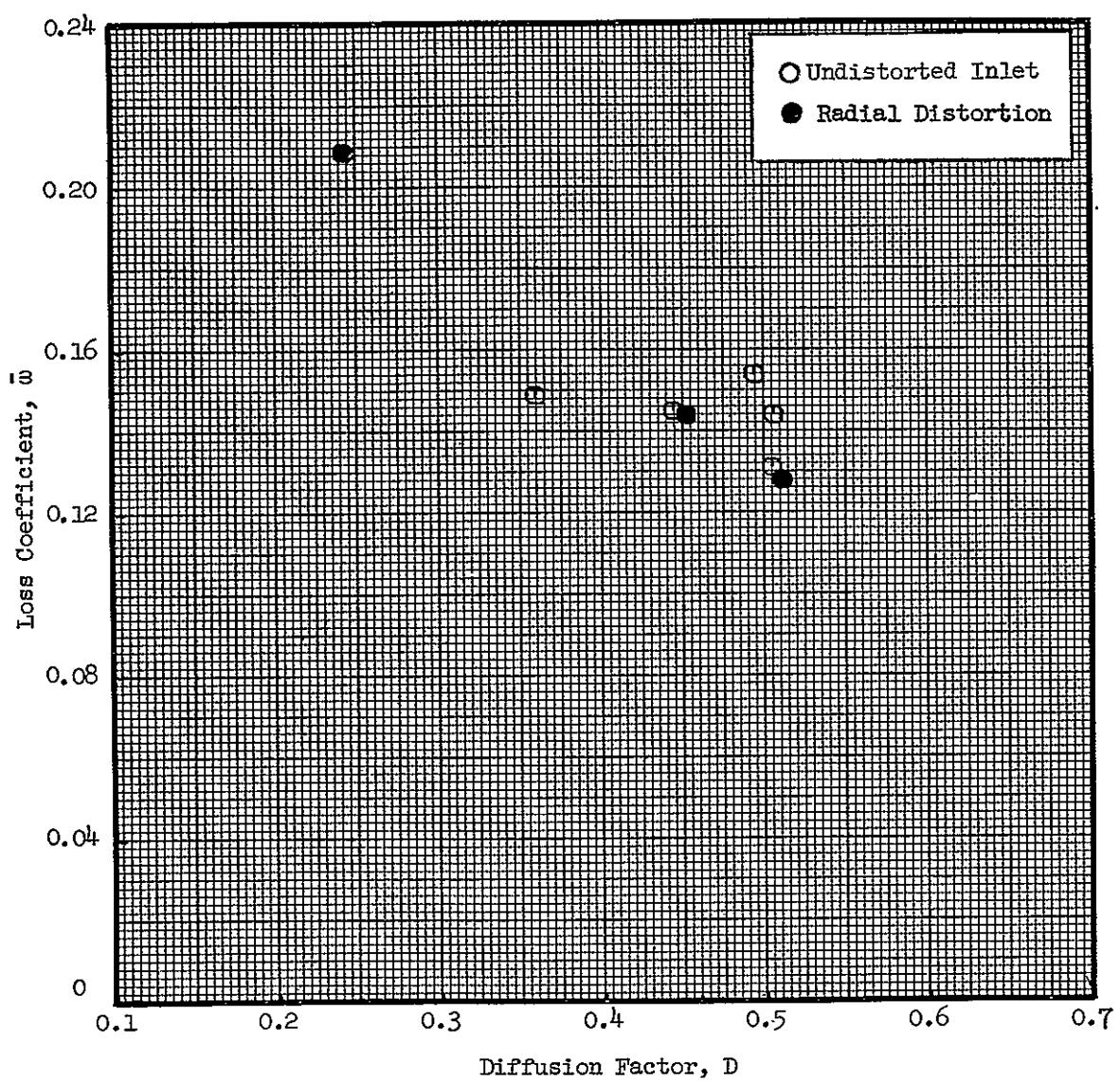


Figure 34 (a). Stator Blade Element Data with Inlet Tip-Radial Distortion, at 5% Immersion from Tip (Concluded).

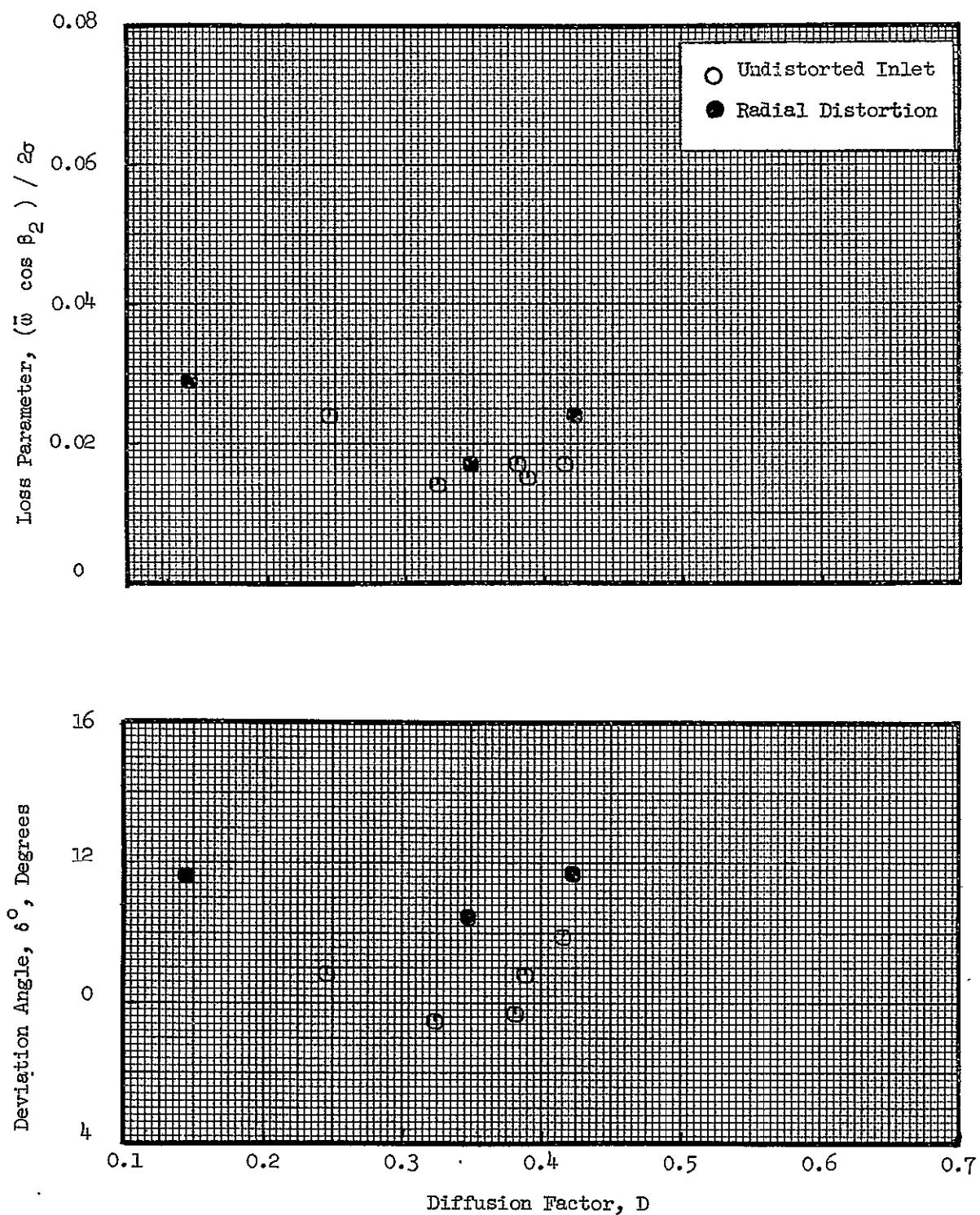


Figure 34 (b). Stator Blade Element Data with Inlet Tip-Radial Distortion, at 10% Immersion from Tip.

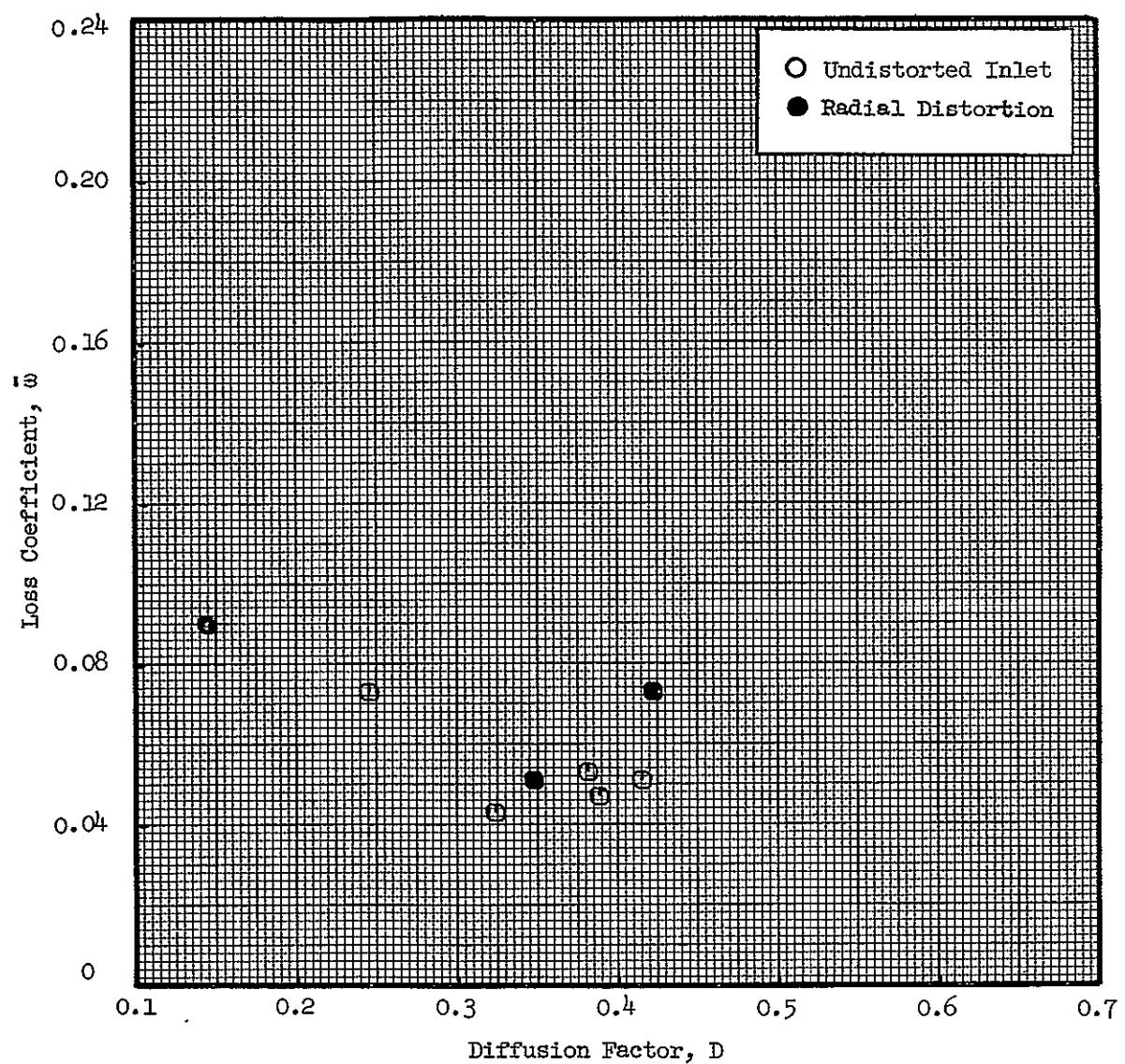


Figure 34 (b). Stator Blade Element Data with Inlet Tip-Radial Distortion, at 10% Immersion from Tip (Concluded).

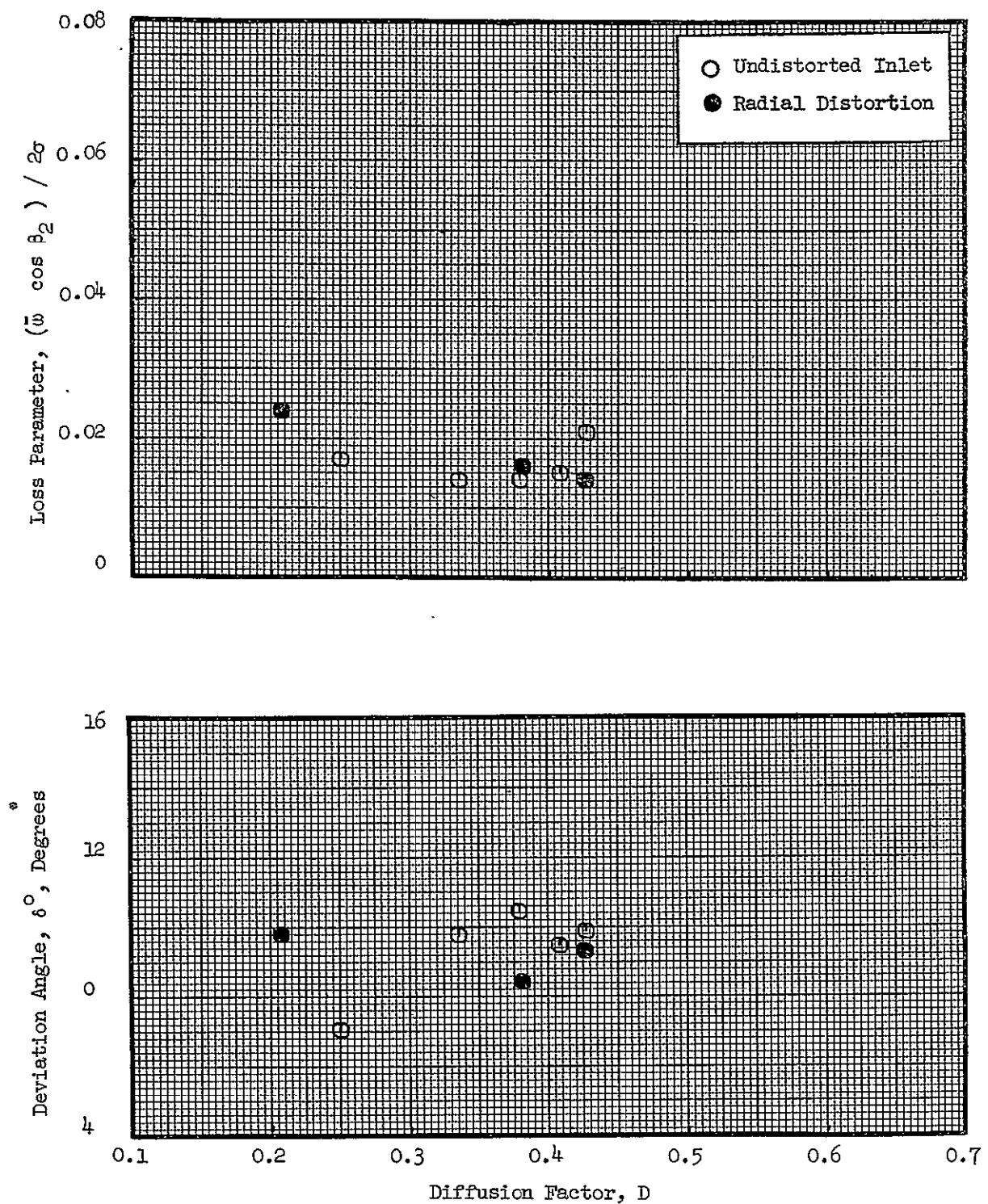


Figure 34 (c). Stator Blade Element Data with Inlet Tip-Radial Distortion, at 30% Immersion from Tip.

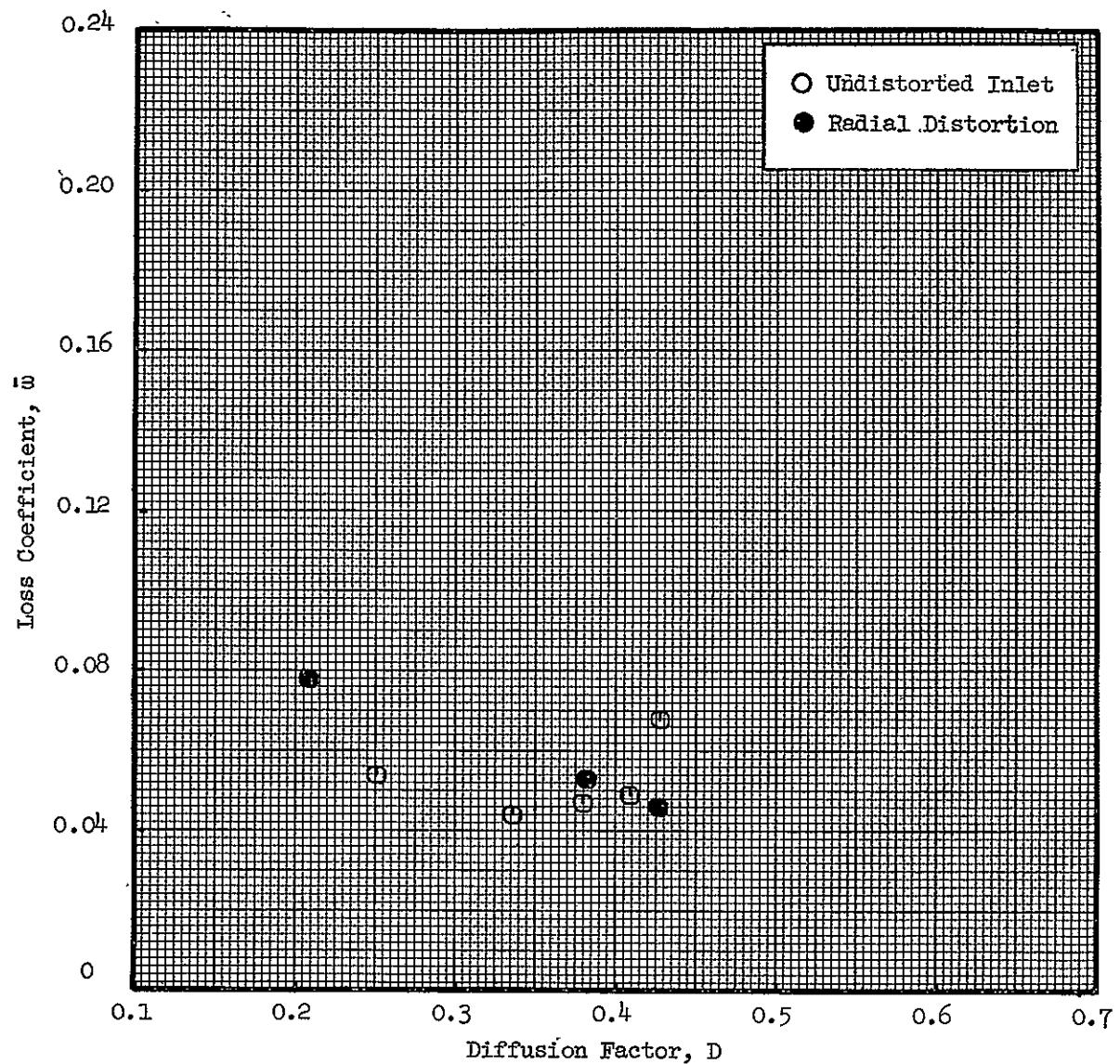


Figure 34 (c). Stator Blade Element Data with Inlet Tip-Radial Distortion, at 30% Immersion from Tip (Concluded).

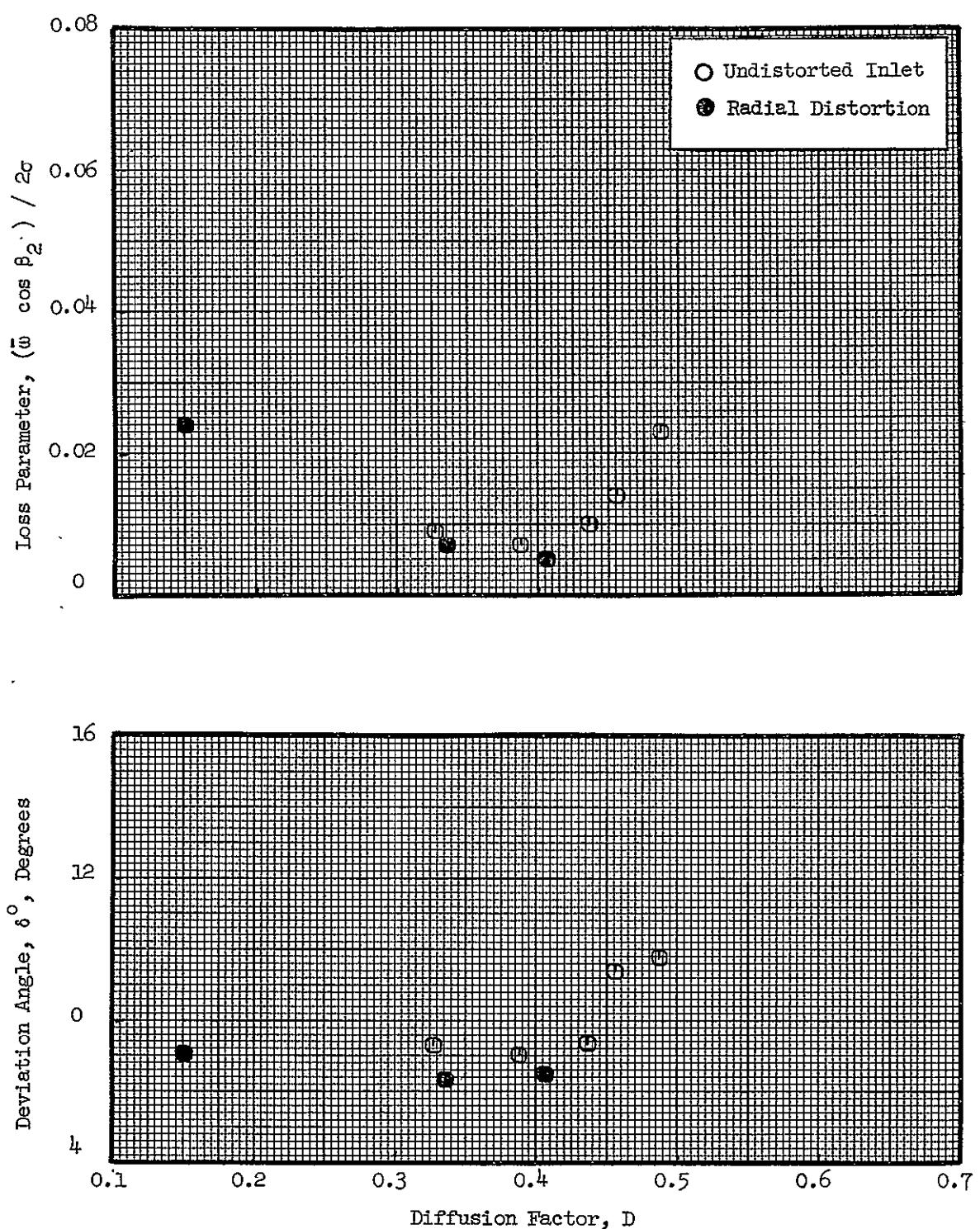


Figure 34 (d). Stator Blade Element Data with Inlet Tip-Radial Distortion, at 50% Immersion from Tip.

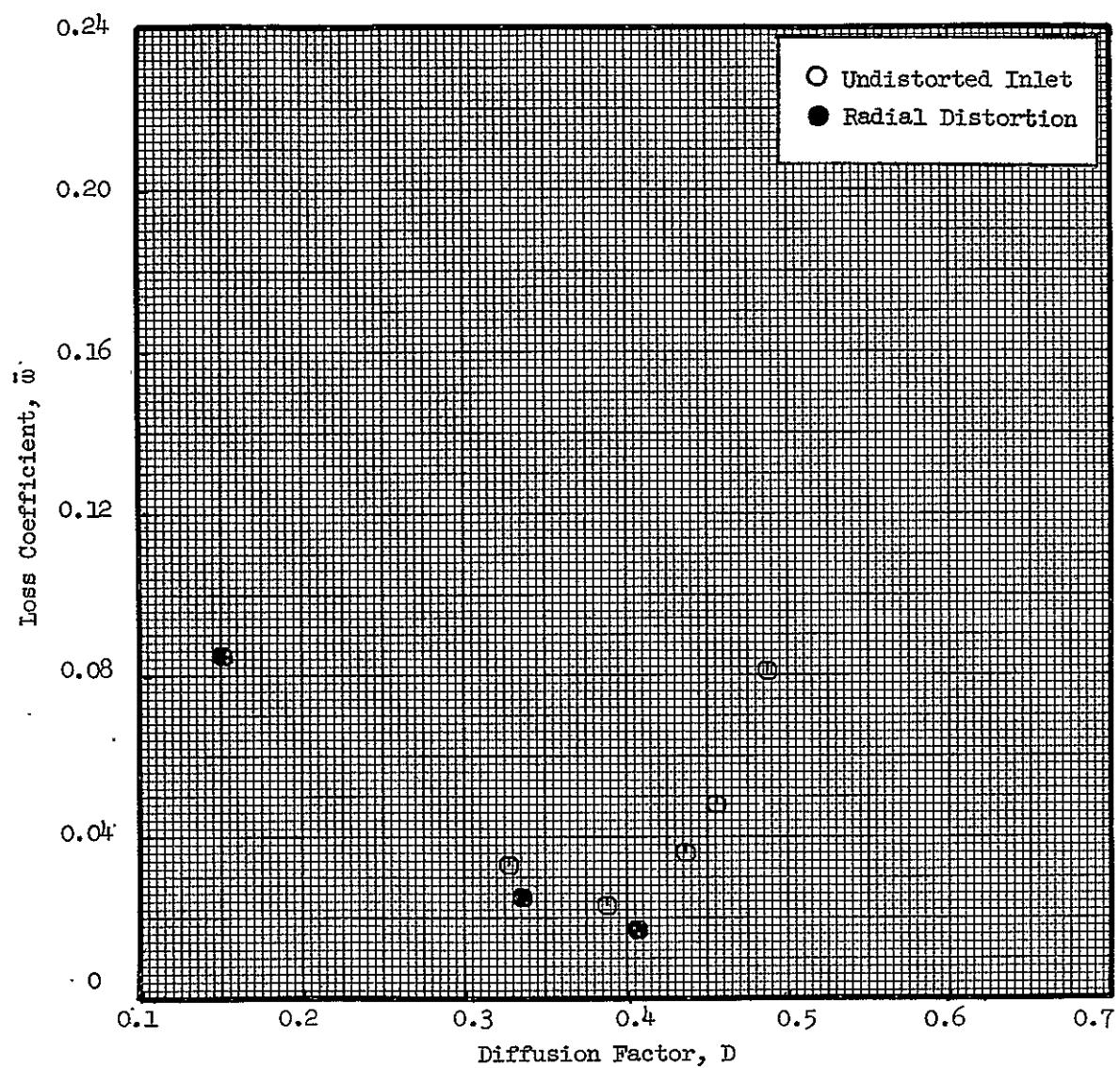


Figure 34 (d). Stator Blade Element Data with Inlet Tip-Radial Distortion, at 50% Immersion from Tip (Concluded).

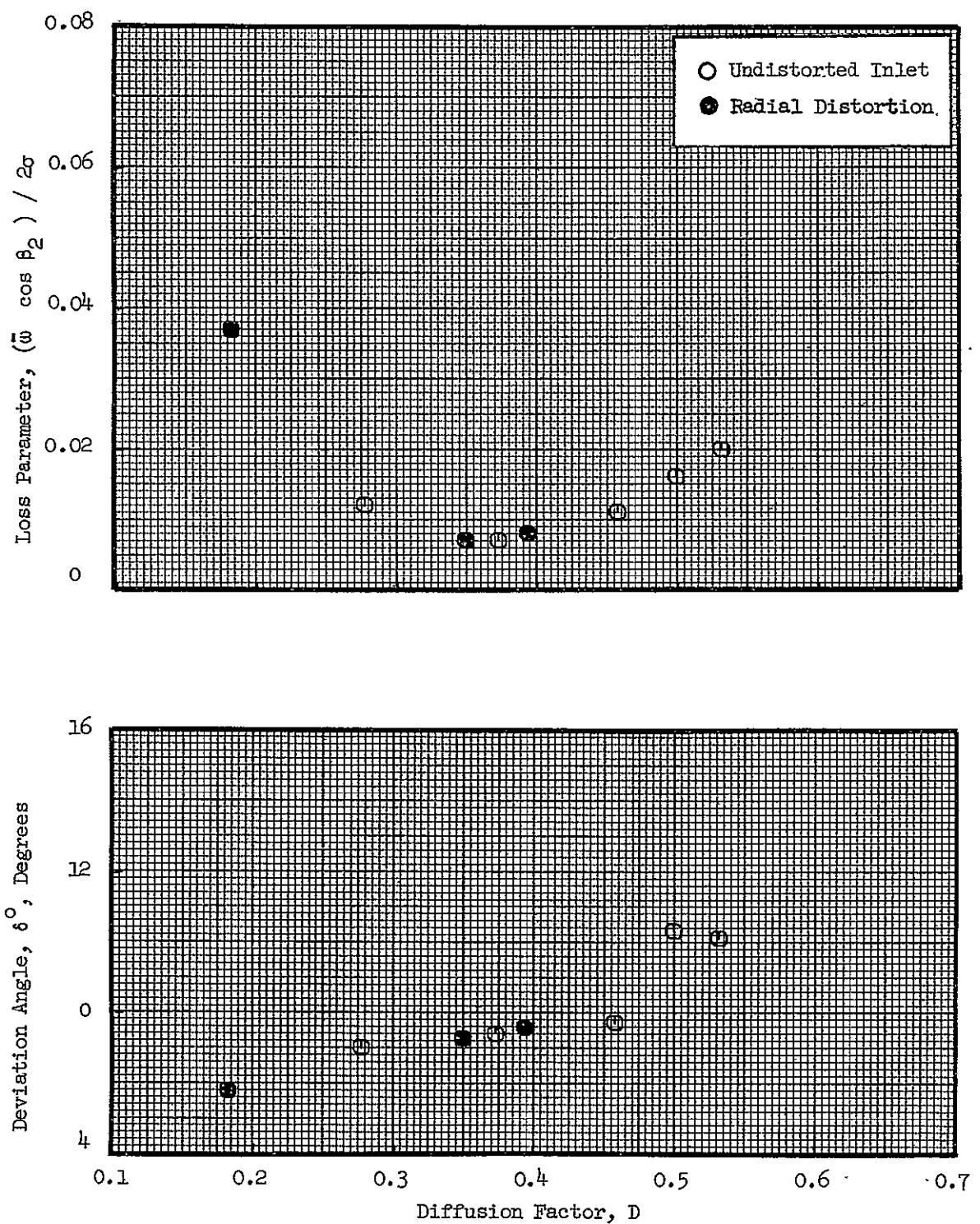


Figure 34 (e). Stator Blade Element Data with Inlet Tip-Radial Distortion, at 70% Immersion from Tip.

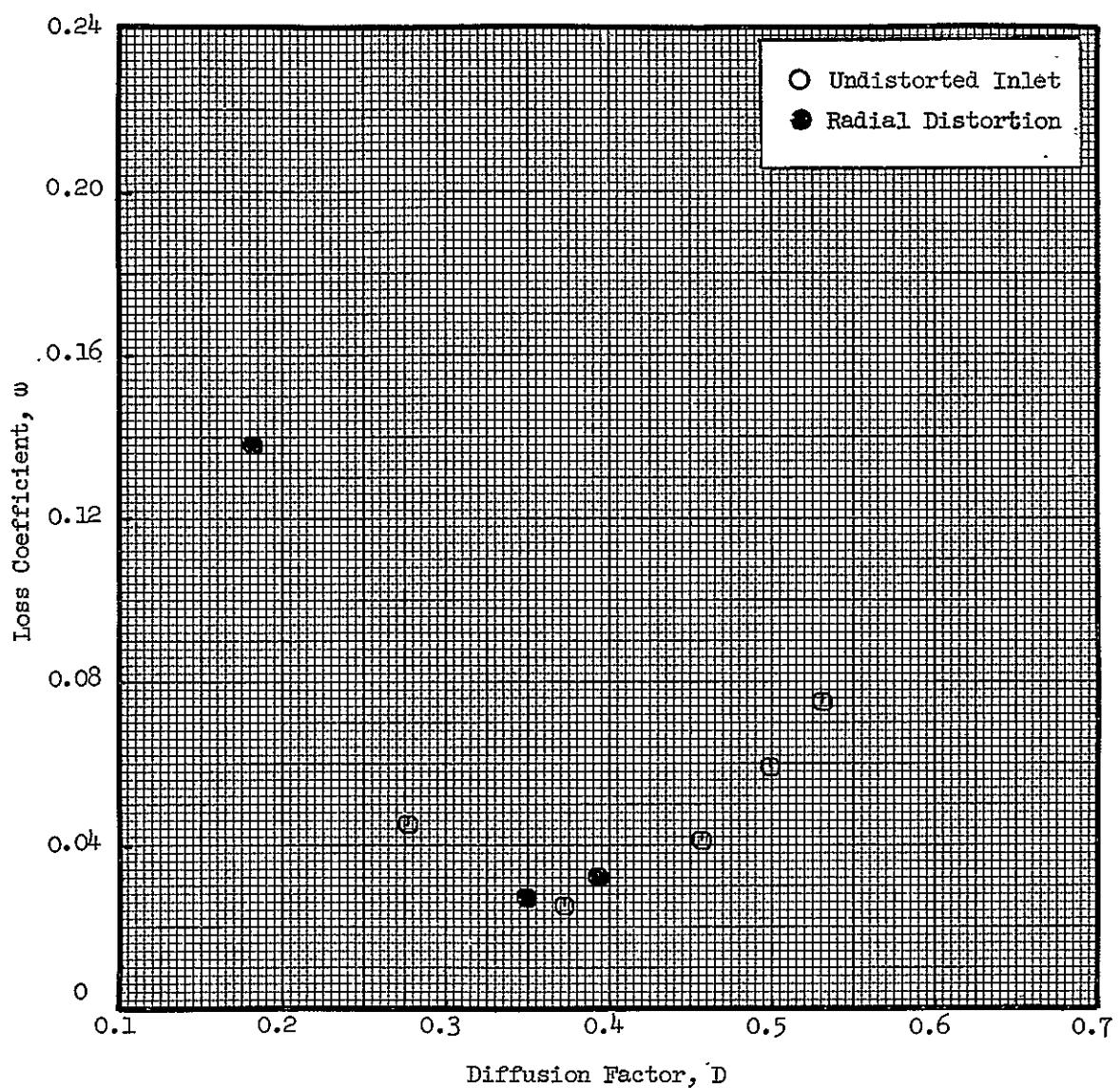


Figure 34 (e). Stator Blade Element Data with Inlet Tip-Radial Distortion, at 70% Immersion from Tip (Concluded)

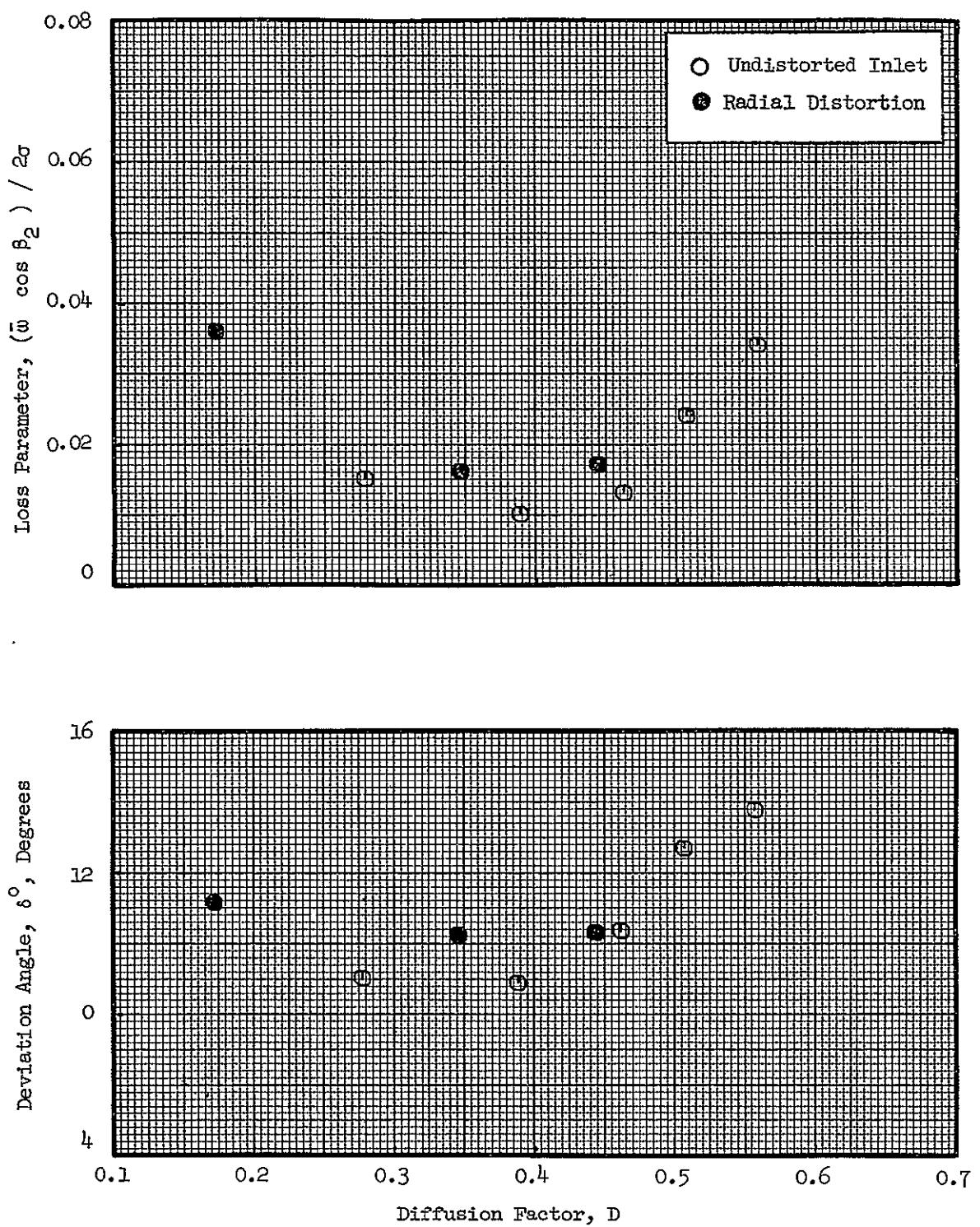


Figure 34 (f). Stator Blade Element Data with Inlet Tip-Radial Distortion, at 90% Immersion from Tip.

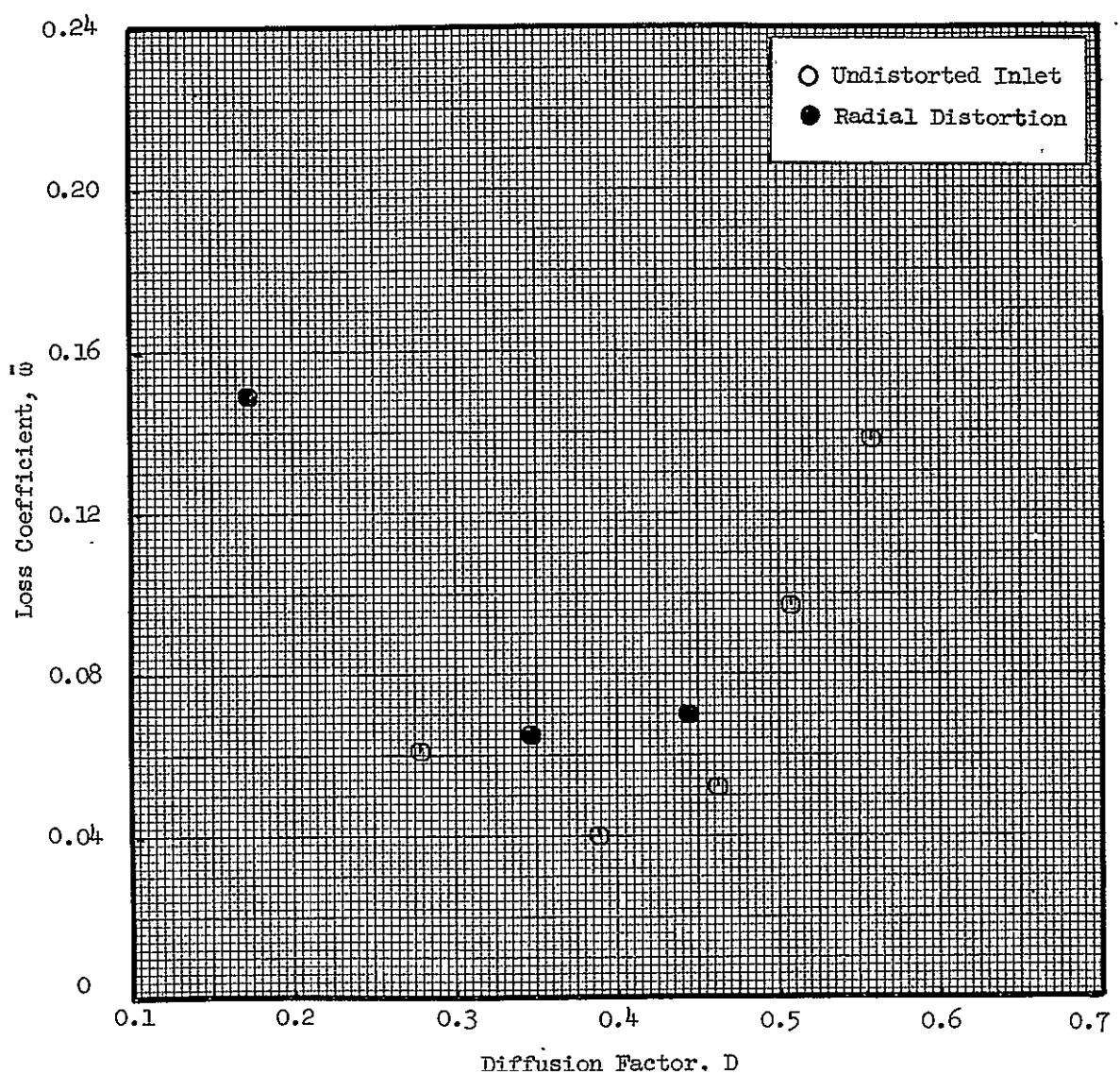


Figure 34 (f). Stator Blade Element Data with Inlet Tip-Radial Distortion, at 90% Immersion from Tip (Concluded).

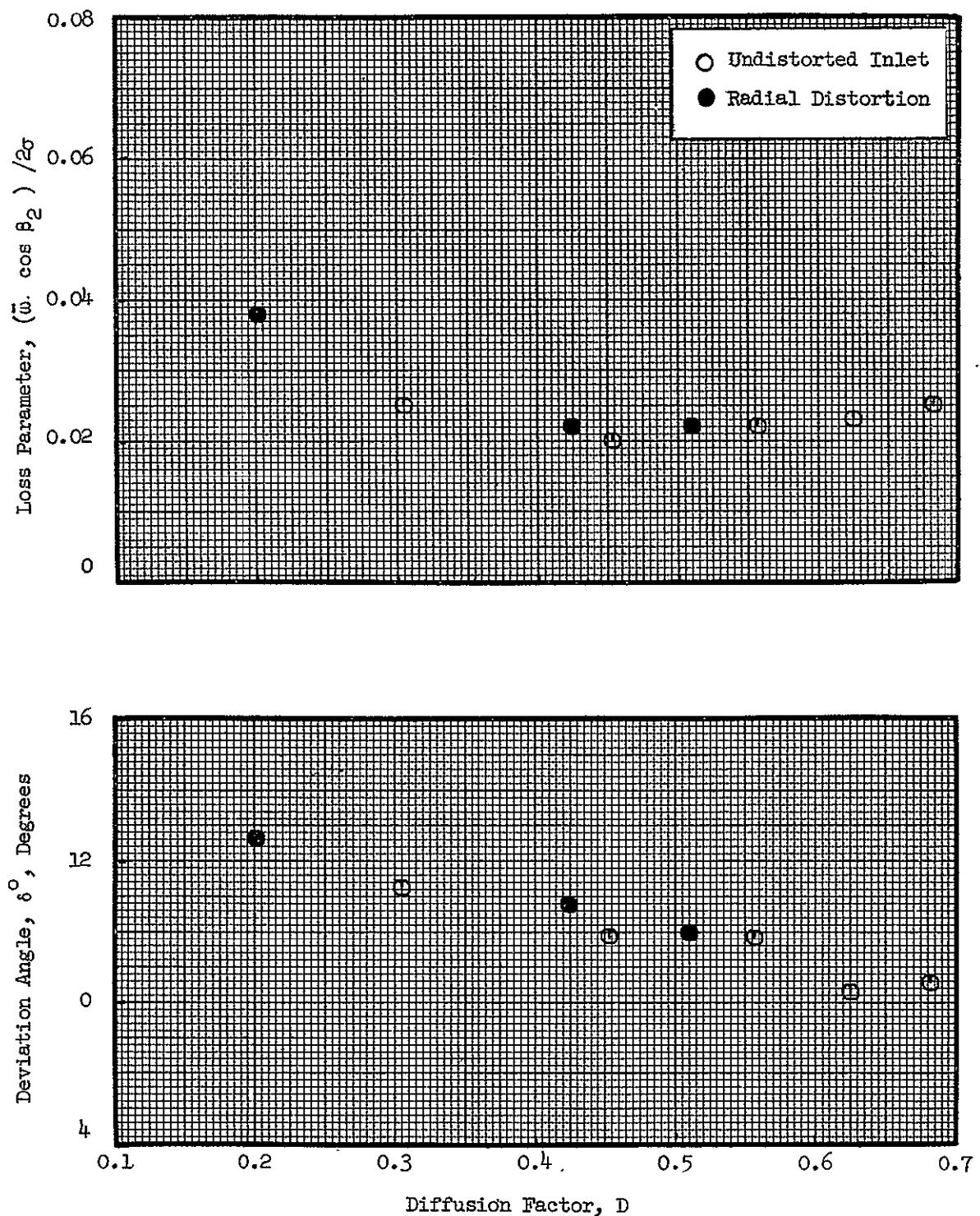


Figure 34 (g). Stator Blade Element Data with Inlet Tip-Radial Distortion, at 95% Immersion from Tip.

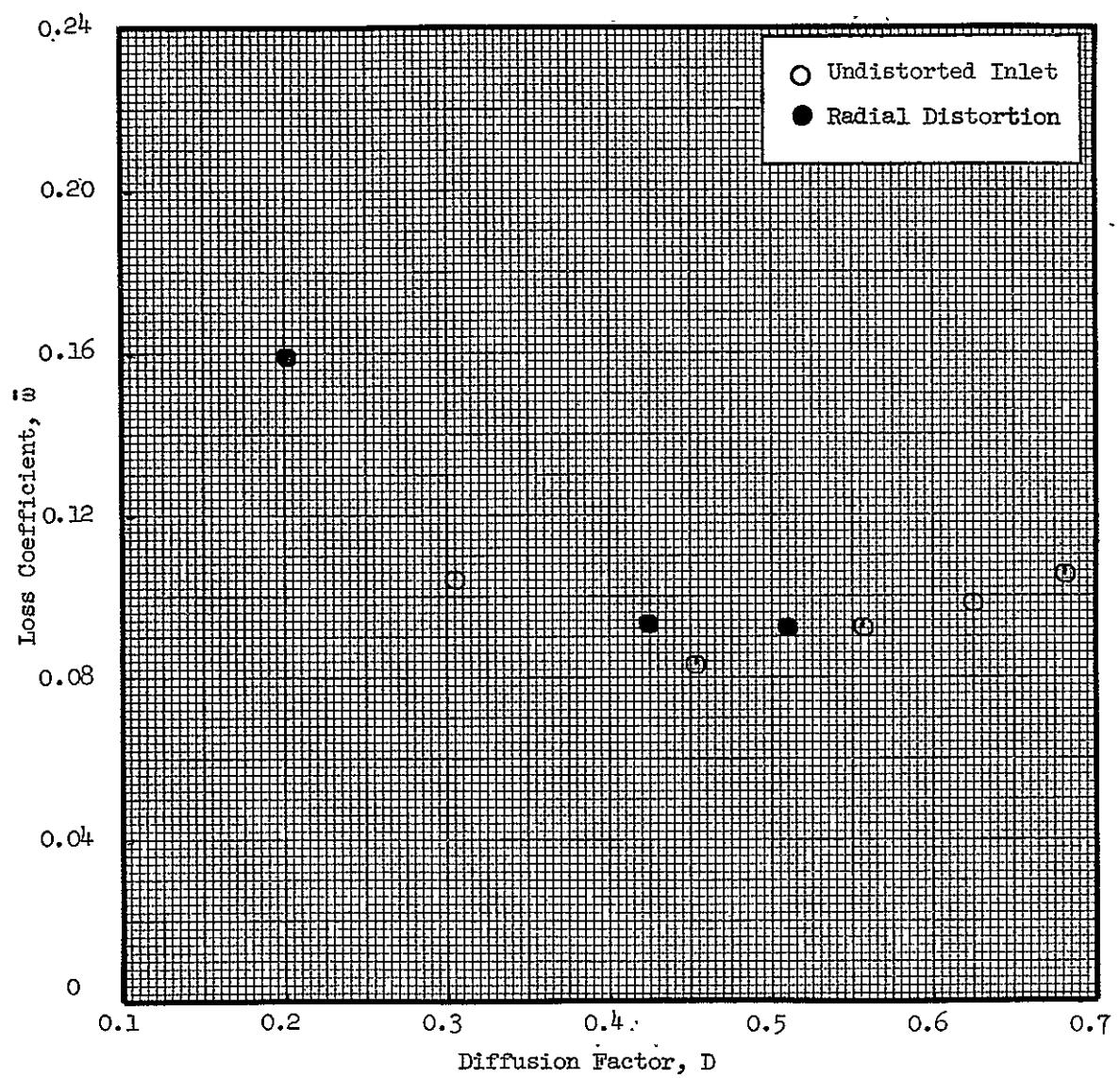


Figure 34 (g). Stator Blade Element Data with Inlet Tip-Radial Distortion, at 95% Immersion from Tip (Concluded).

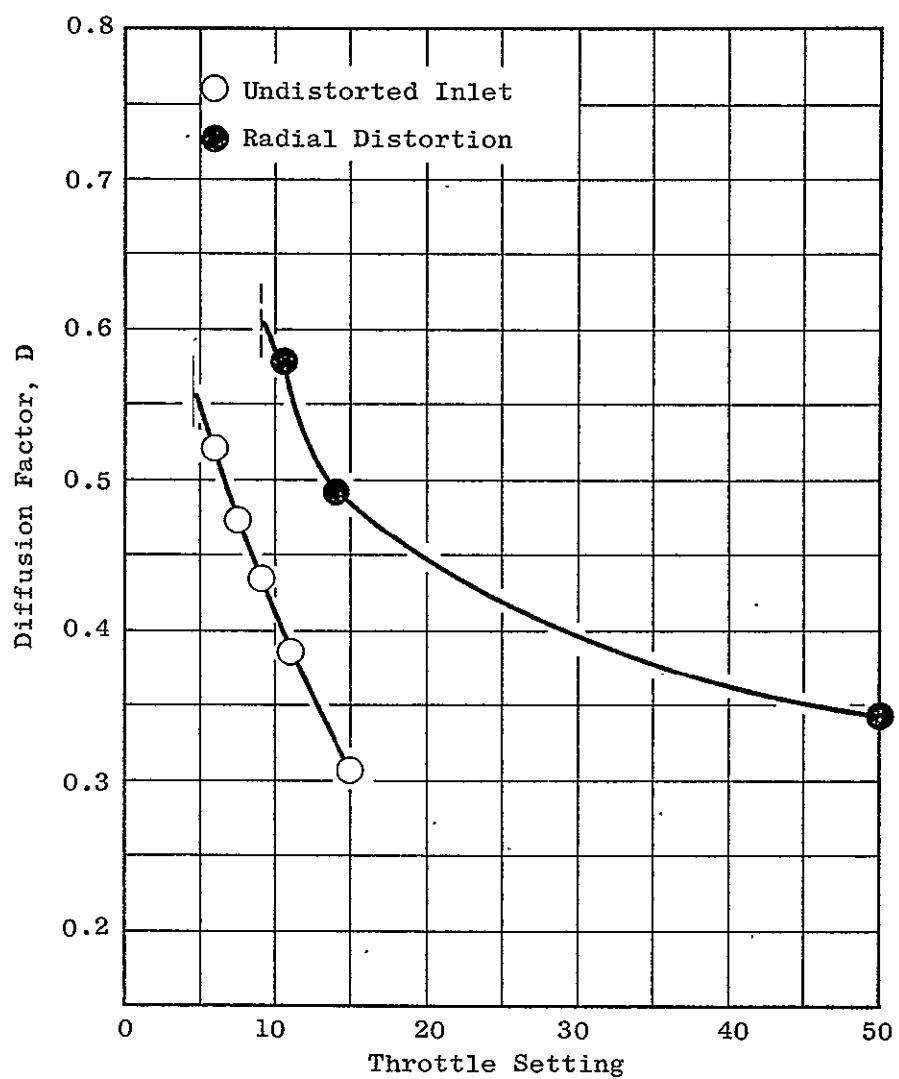


Figure 35 (a). Variation of Rotor Aerodynamic Loading Quantities with Throttle Setting at 100% Speed for Radial Distortion and Undistorted Inlet Flow, at 5% Immersion from Tip.

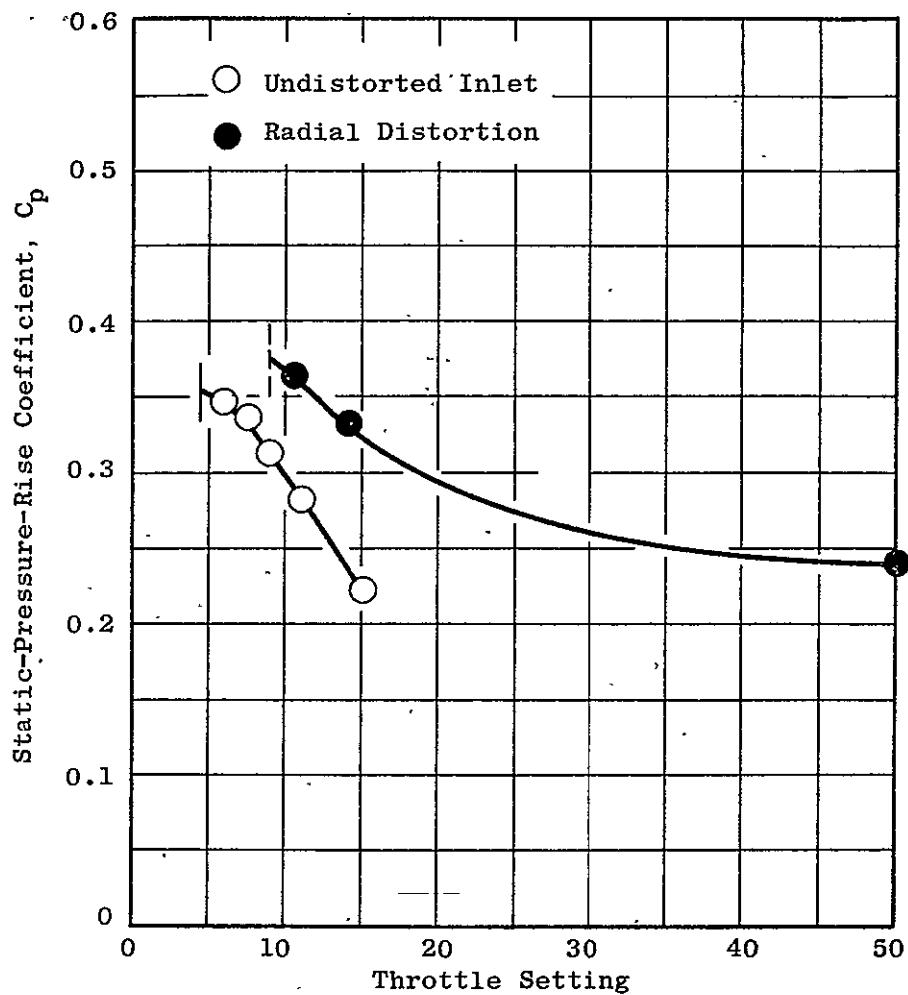


Figure 35 (a). Variation of Rotor Aerodynamic Loading Quantities with Throttle Setting at 100% Speed for Radial Distortion and Undistorted Inlet Flow, at 5% Immersion from Tip (Continued).

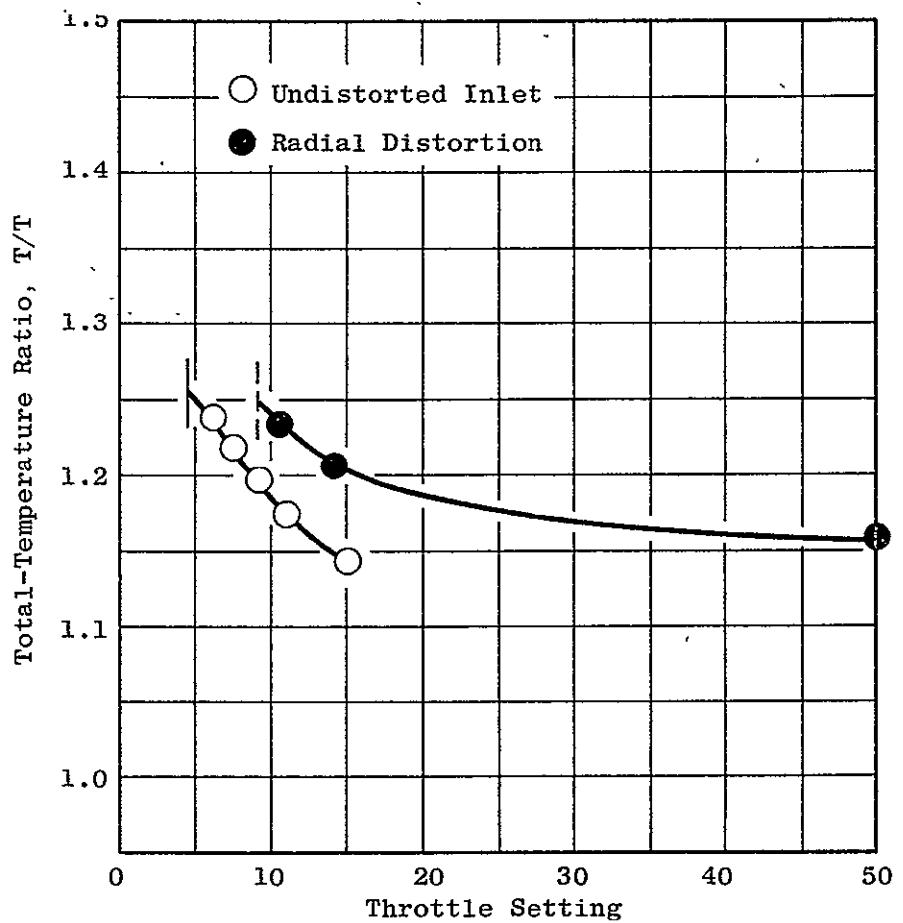


Figure 35 (a). Variation of Rotor Aerodynamic Loading Quantities with Throttle Setting at 100% Speed for Radial Distortion and Undistorted Inlet Flow, at 5% Immersion from Tip (Concluded).

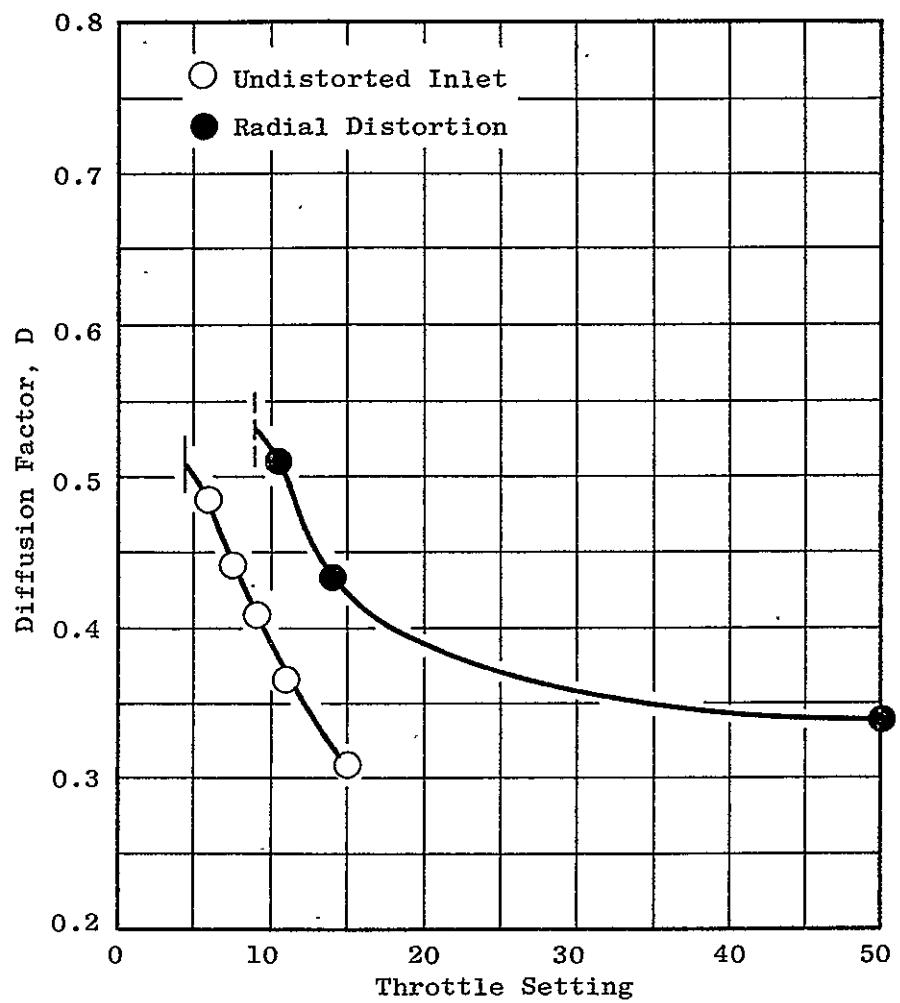


Figure 35 (b). Variation of Rotor Aerodynamic Loading Quantities with Throttle Setting at 100% Speed for Radial Distortion and Undistorted Inlet Flow, at 10% Immersion from Tip.

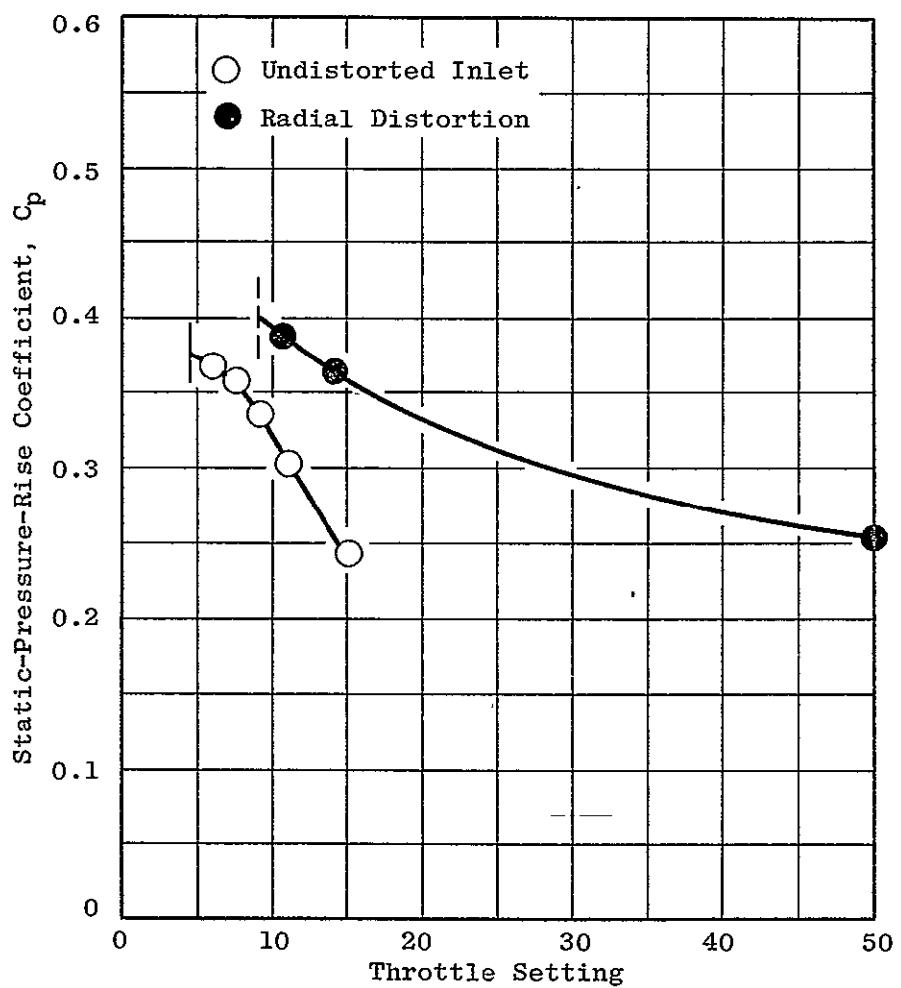


Figure 35 (b). Variation of Rotor Aerodynamic Loading Quantities with Throttle Setting at 100% Speed for Radial Distortion and Undistorted Inlet Flow, at 10% Immersion from Tip (Continued).

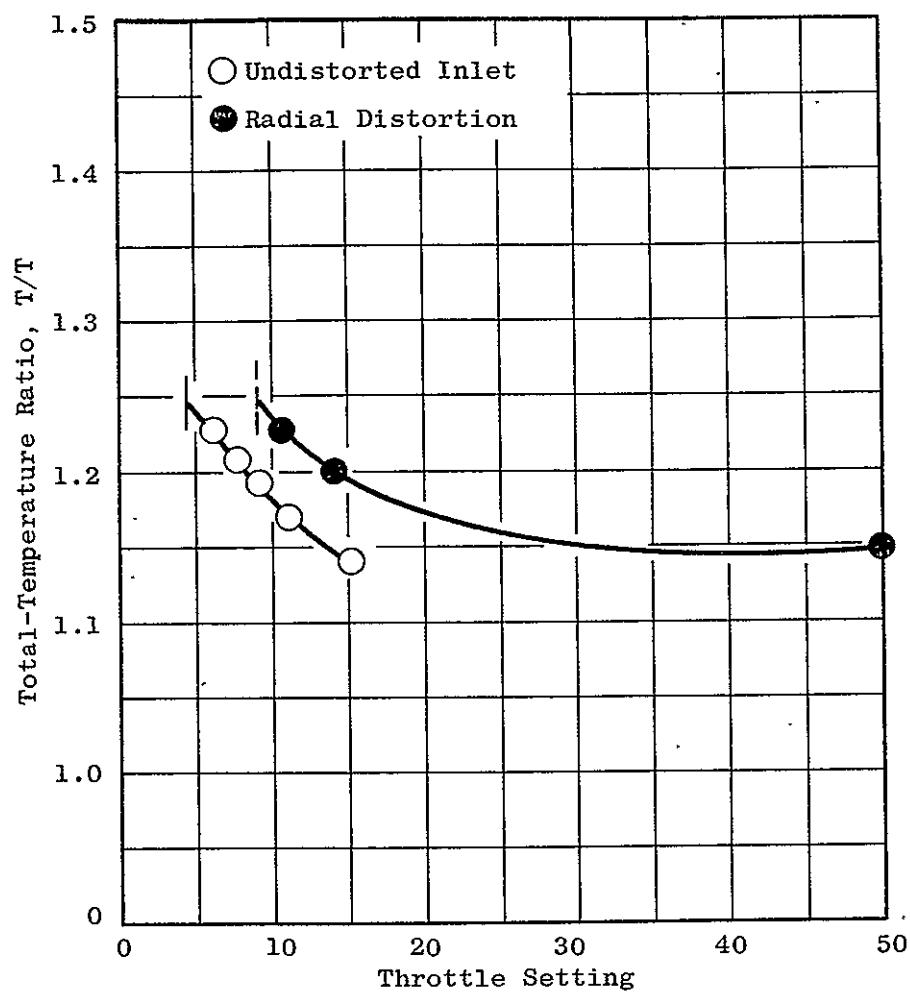


Figure 35 (b). Variation of Rotor Aerodynamic Loading Quantities with Throttle Setting at 100% Speed for Radial Distortion and Undistorted Inlet Flow, at 10% Immersion from Tip (Concluded).

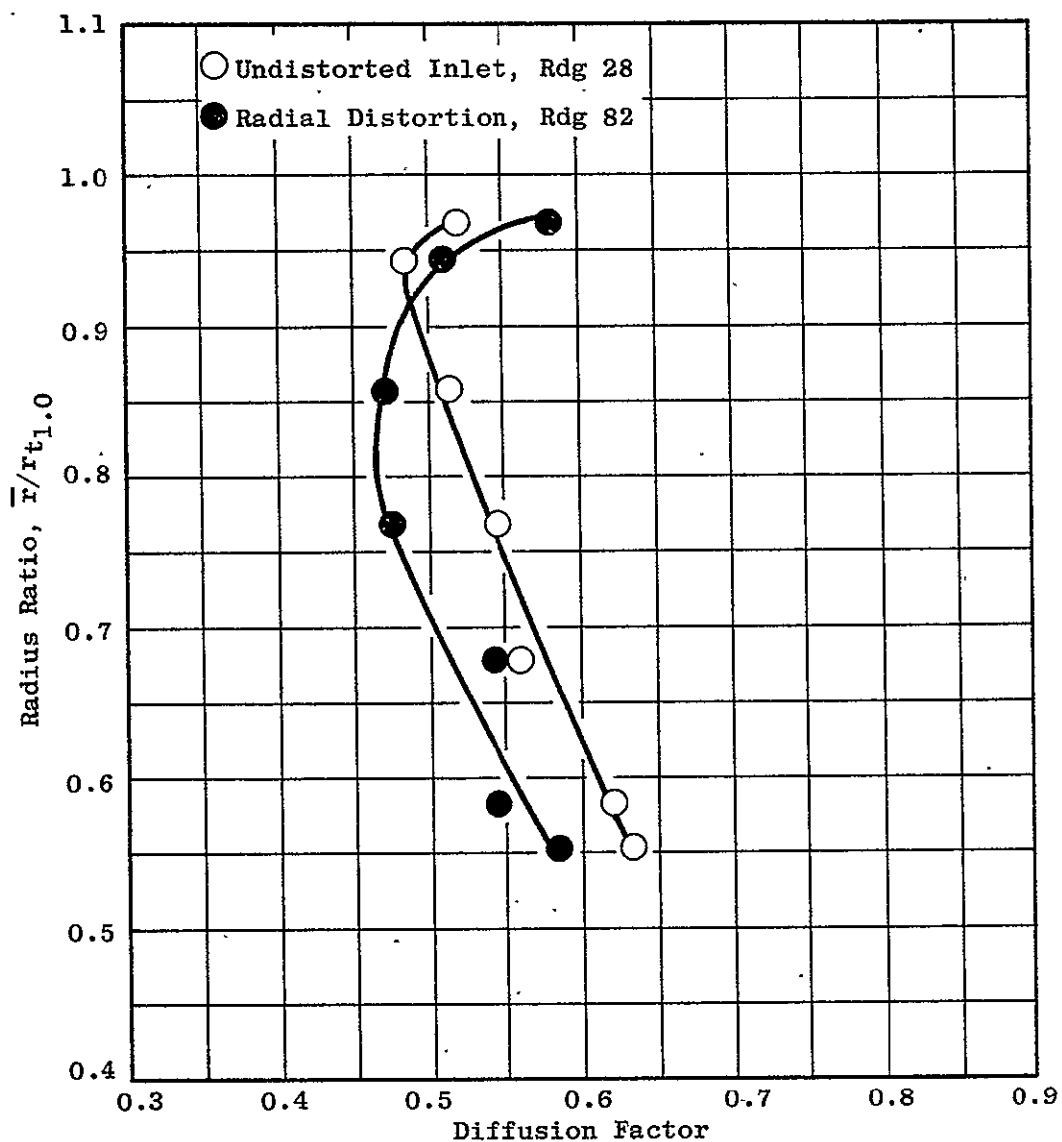


Figure 36 (a). Radial Variation of Rotor Diffusion Factor Near 100% Speed Stall for Radial Distortion and Undistorted Flow.

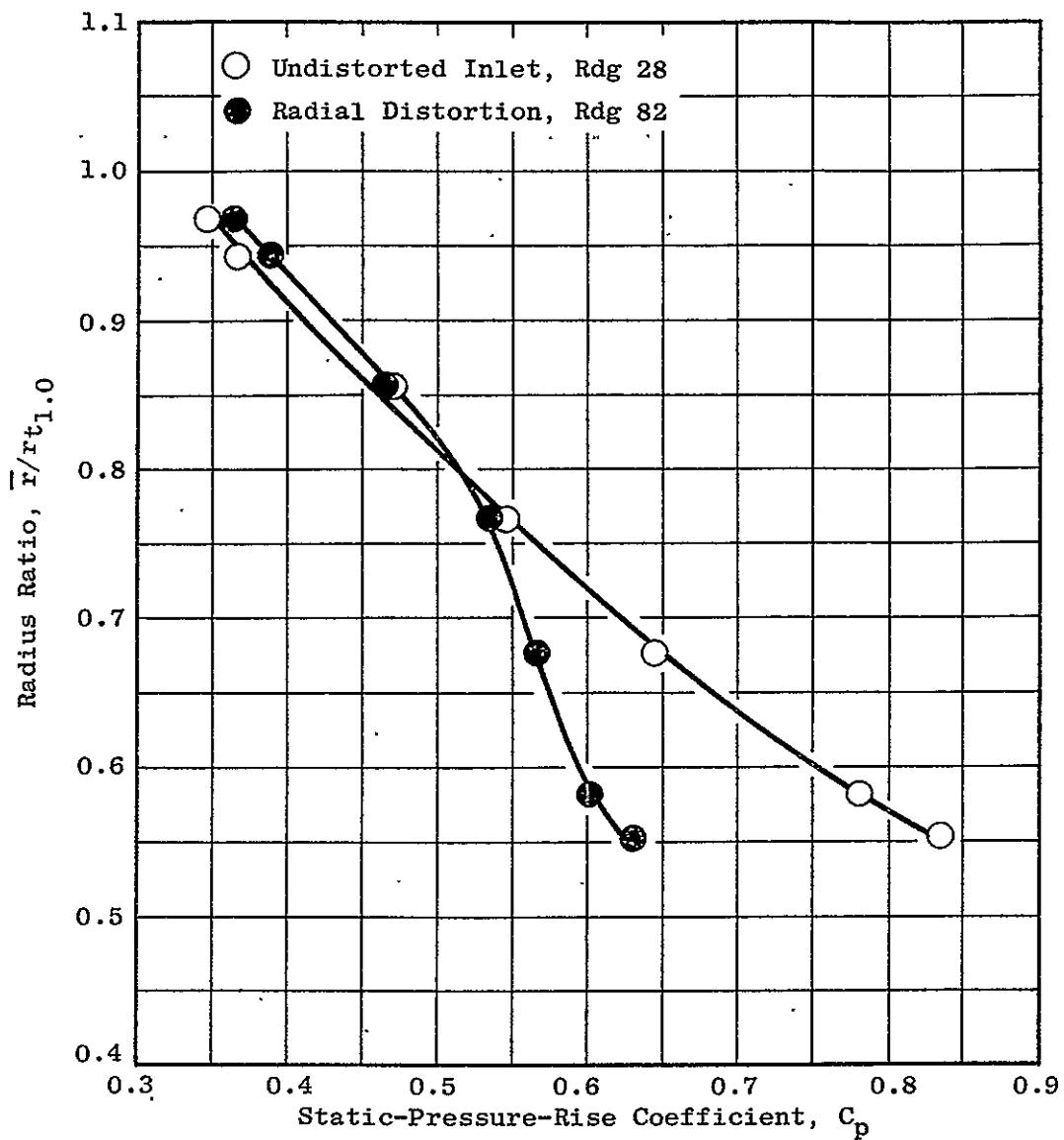


Figure 36 (b). Radial Variation of Rotor Static-Pressure-Rise Coefficient Near 100% Speed Stall for Radial Distortion and Undistorted Inlet Flow.

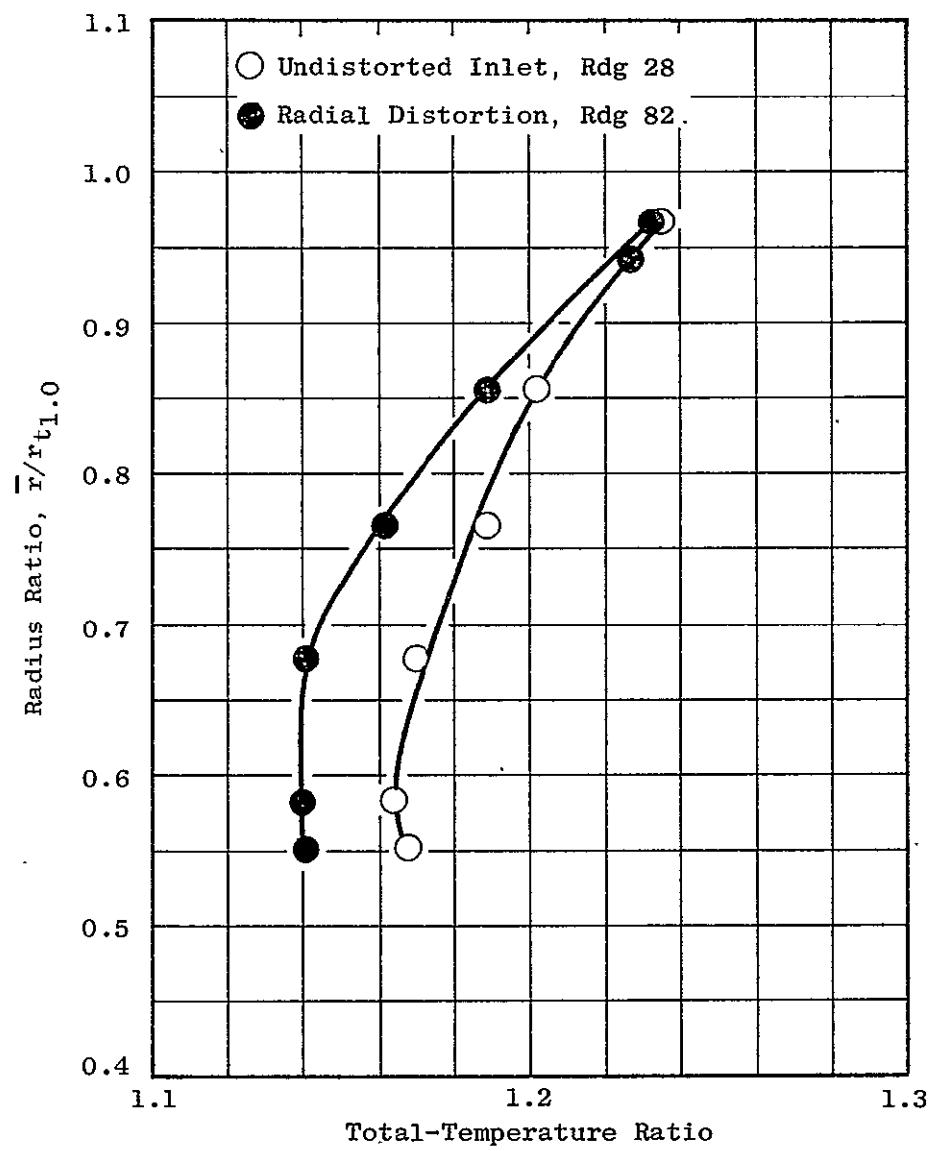


Figure 36 (c). Radial Variation of Rotor Total-Temperature Ratio Near 100% Speed Stall for Radial Distortion and Undistorted Inlet Flow.

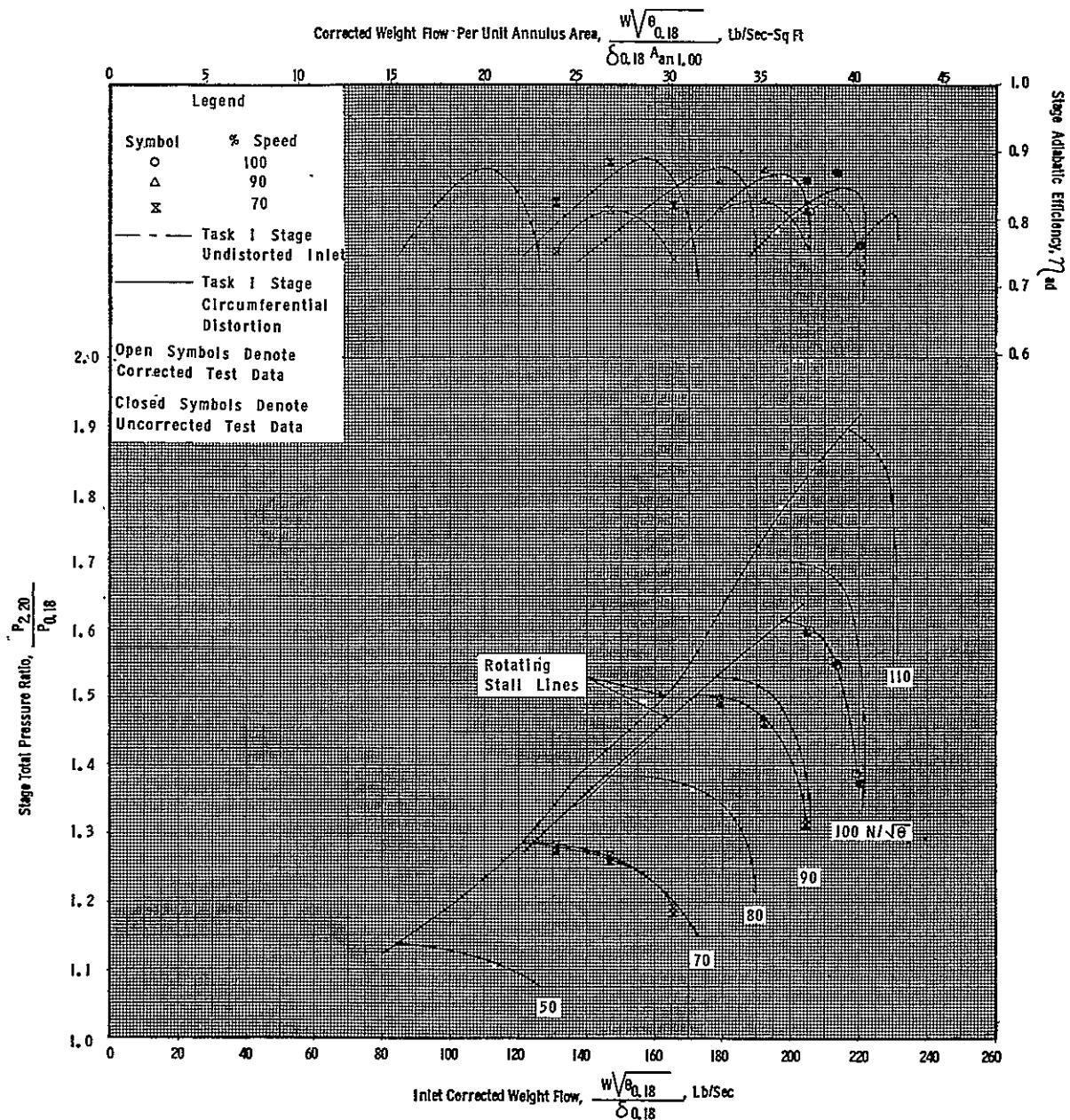


Figure 37. Stage Performance Map with Circumferential Inlet Flow Distortion.

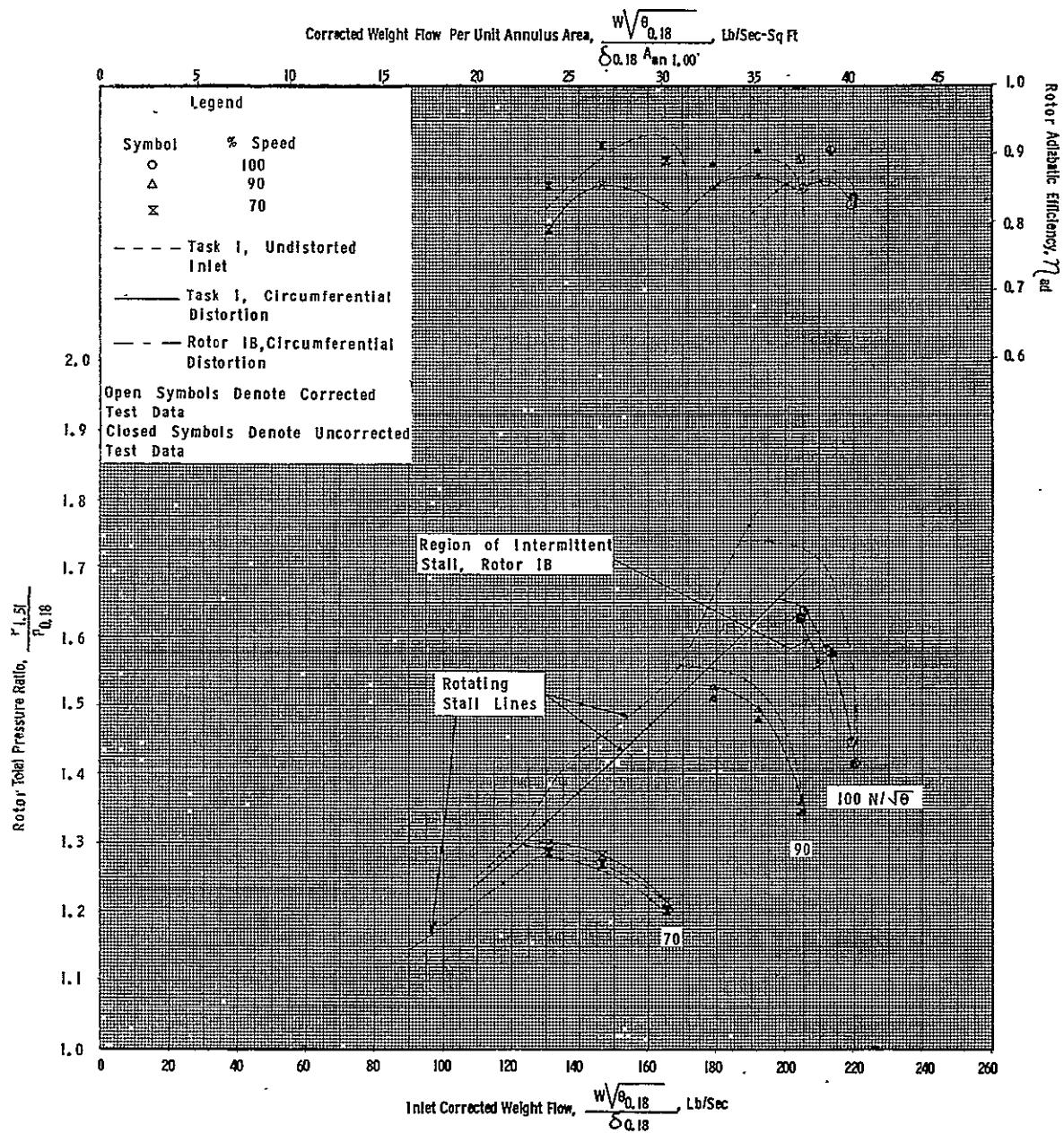


Figure 38. Rotor Performance Map with Circumferential Inlet Flow Distortion.

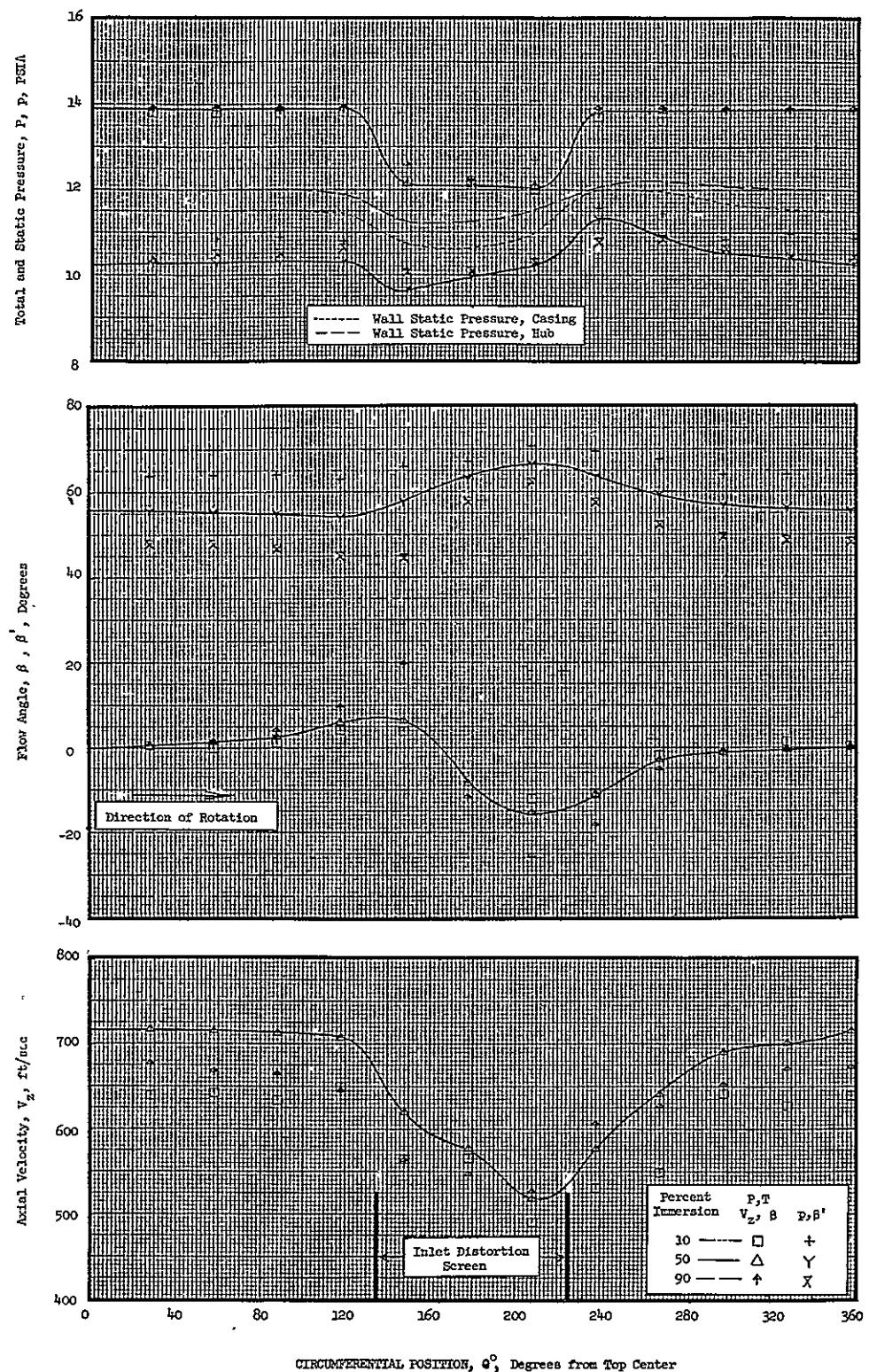


Figure 39 (a). Circumferential Variation of Flow Conditions at 100% Speed Near Stall with Circumferential Inlet Flow Distortion, Plane 0.95.

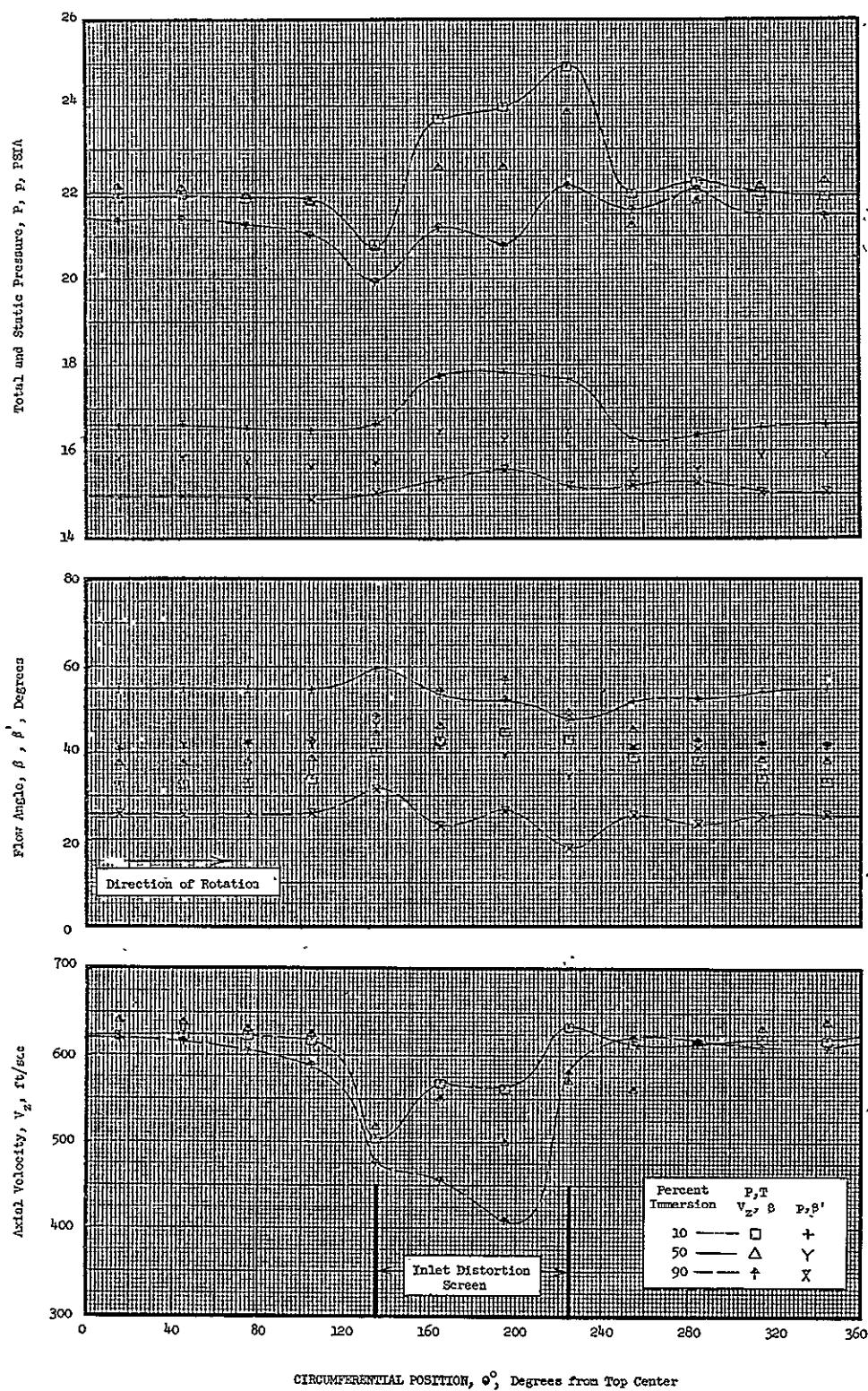


Figure 39 (b). Circumferential Variation of Flow Conditions at 100% Speed Near Stall with Circumferential Inlet Flow Distortion, Plane 1.51.

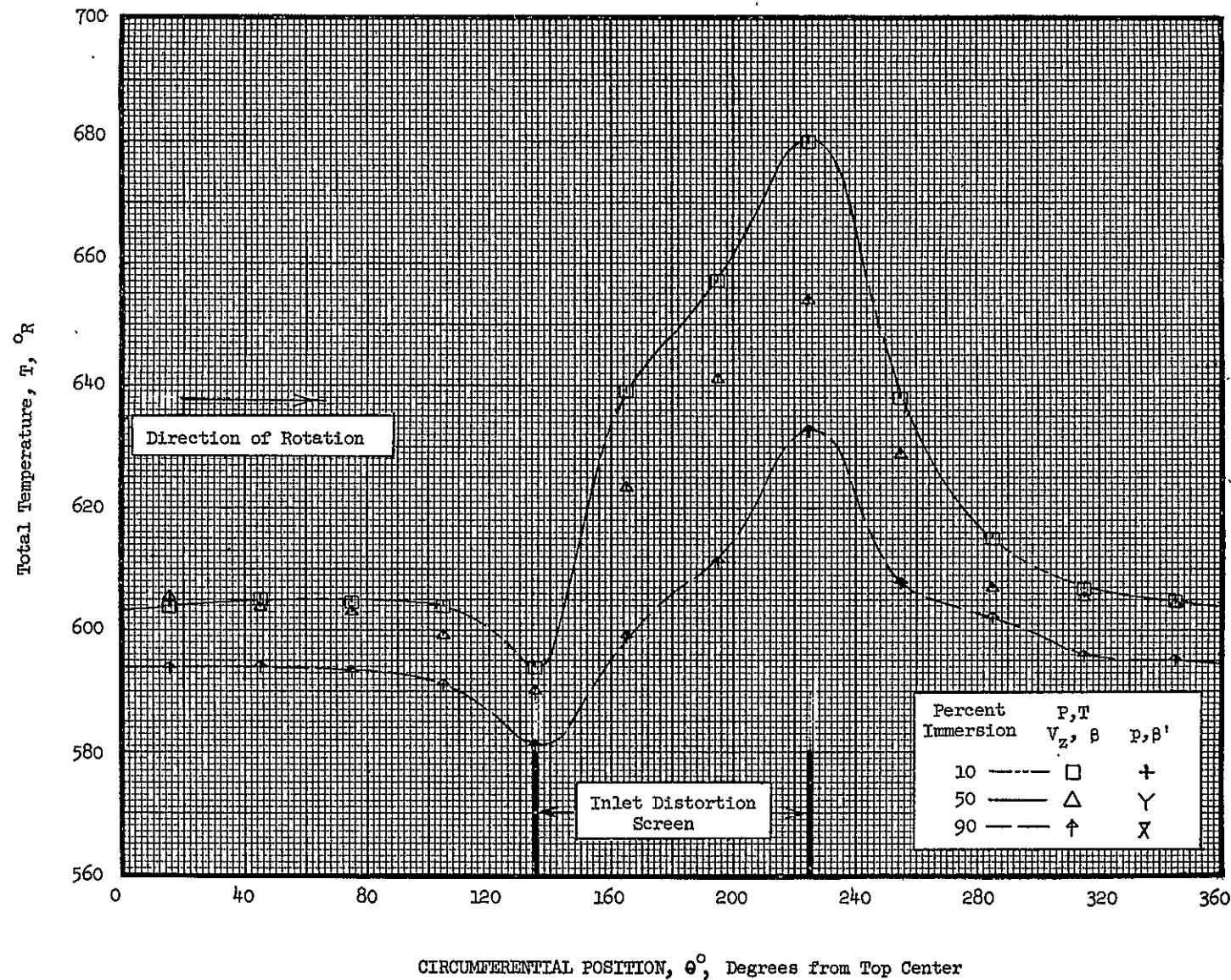


Figure 39 (b). Circumferential Variation of Flow Conditions at 100% Speed Near Stall with Circumferential Inlet Flow Distortion, Plane 1.51 (Concluded).

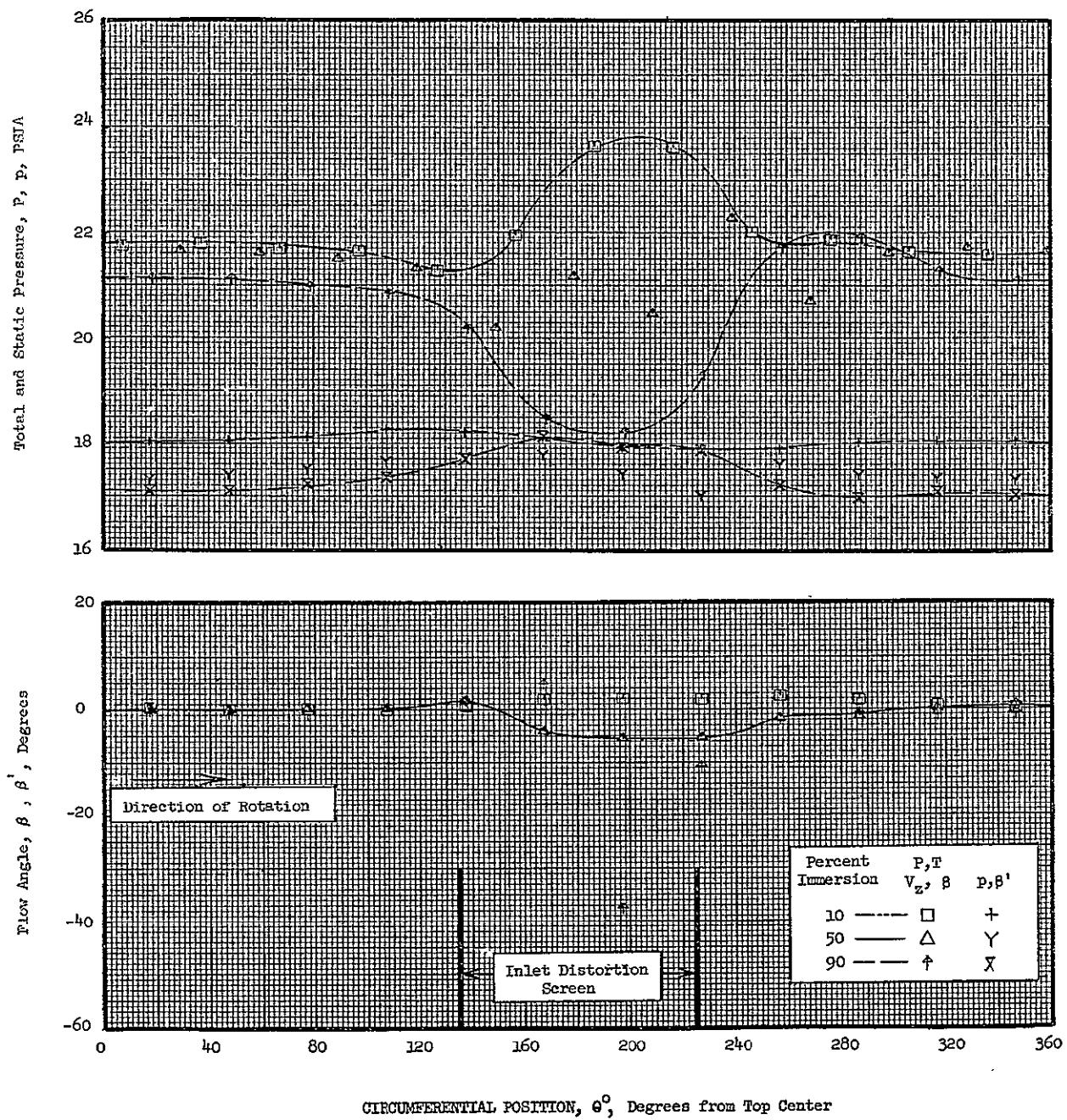


Figure 39 (c). Circumferential Variation of Flow Conditions at 100% Speed Near Stall with Circumferential Inlet Flow Distortion, Plane 2.20.

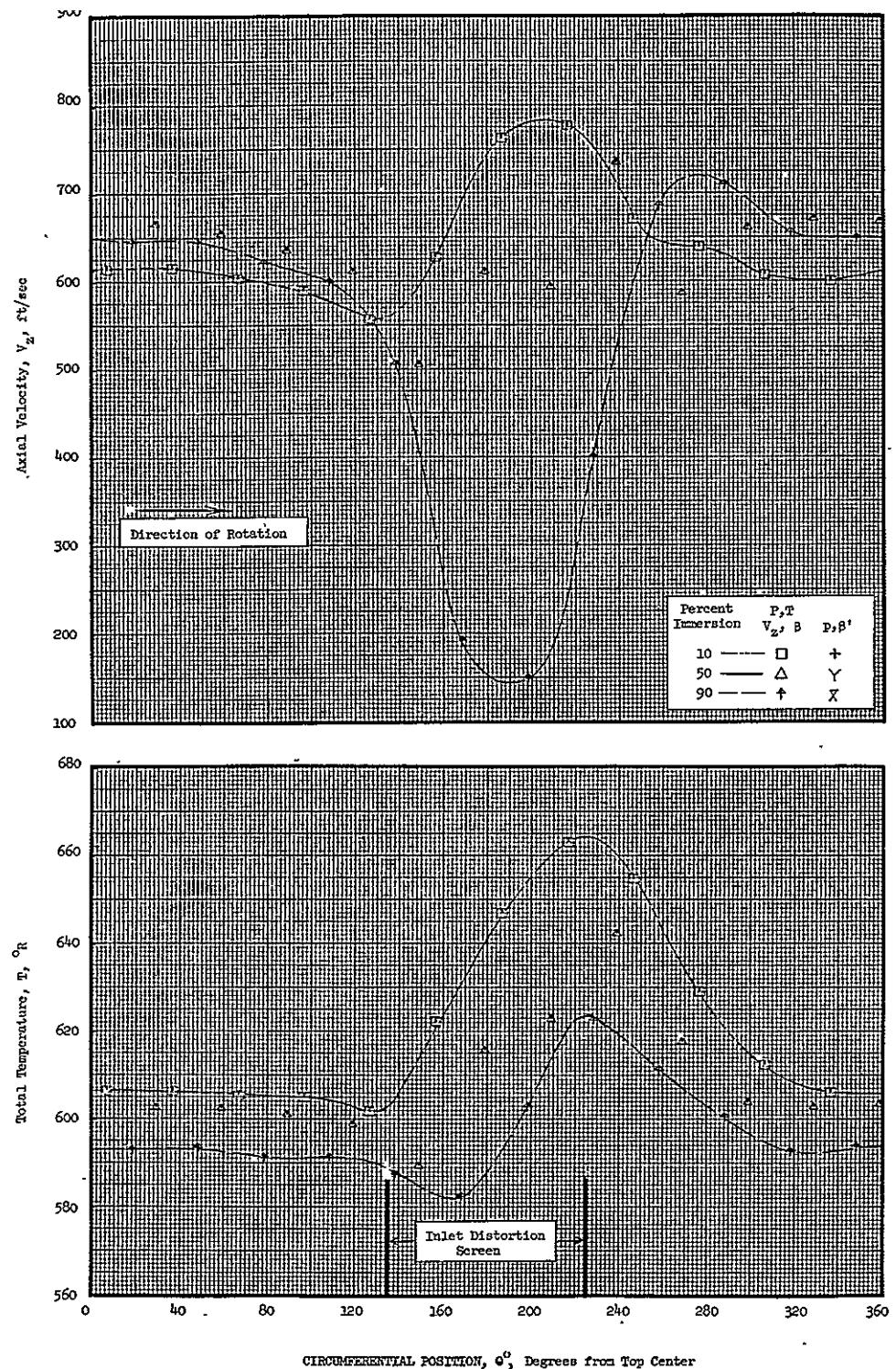


Figure 39 (c). Circumferential Variation of Flow Conditions at 100% Speed Near Stall with Circumferential Inlet Flow Distortion, Plane 2.20 (Concluded).

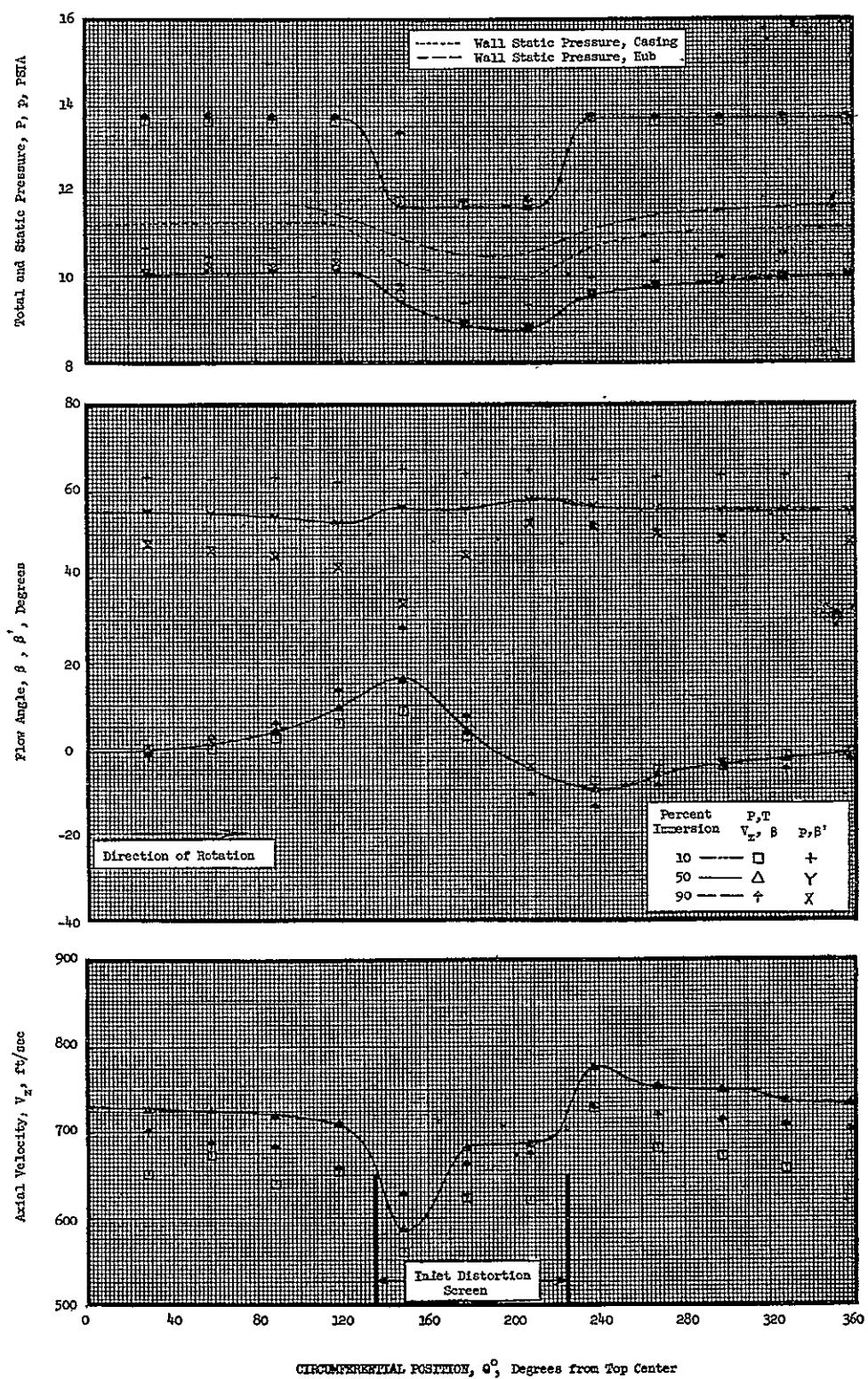


Figure 40 (a). Circumferential Variation of Flow Conditions at 100% Speed Maximum Weight Flow with Circumferential Inlet Flow Distortion, Plane 0.95.

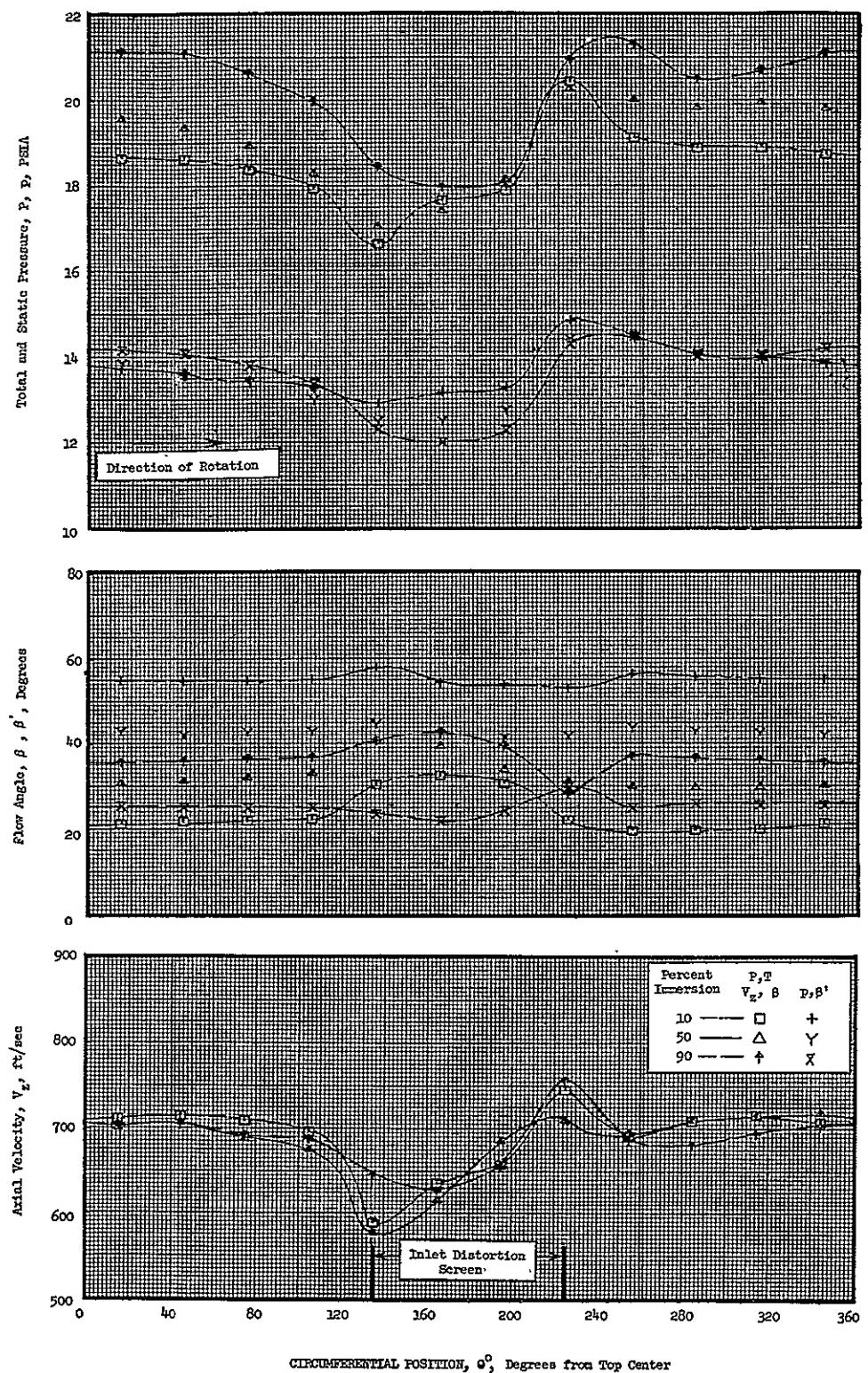


Figure 40 (b). Circumferential Variation of Flow Conditions at 100% Speed Maximum Weight Flow with Circumferential Inlet Flow Distortion, Plane 1.51.

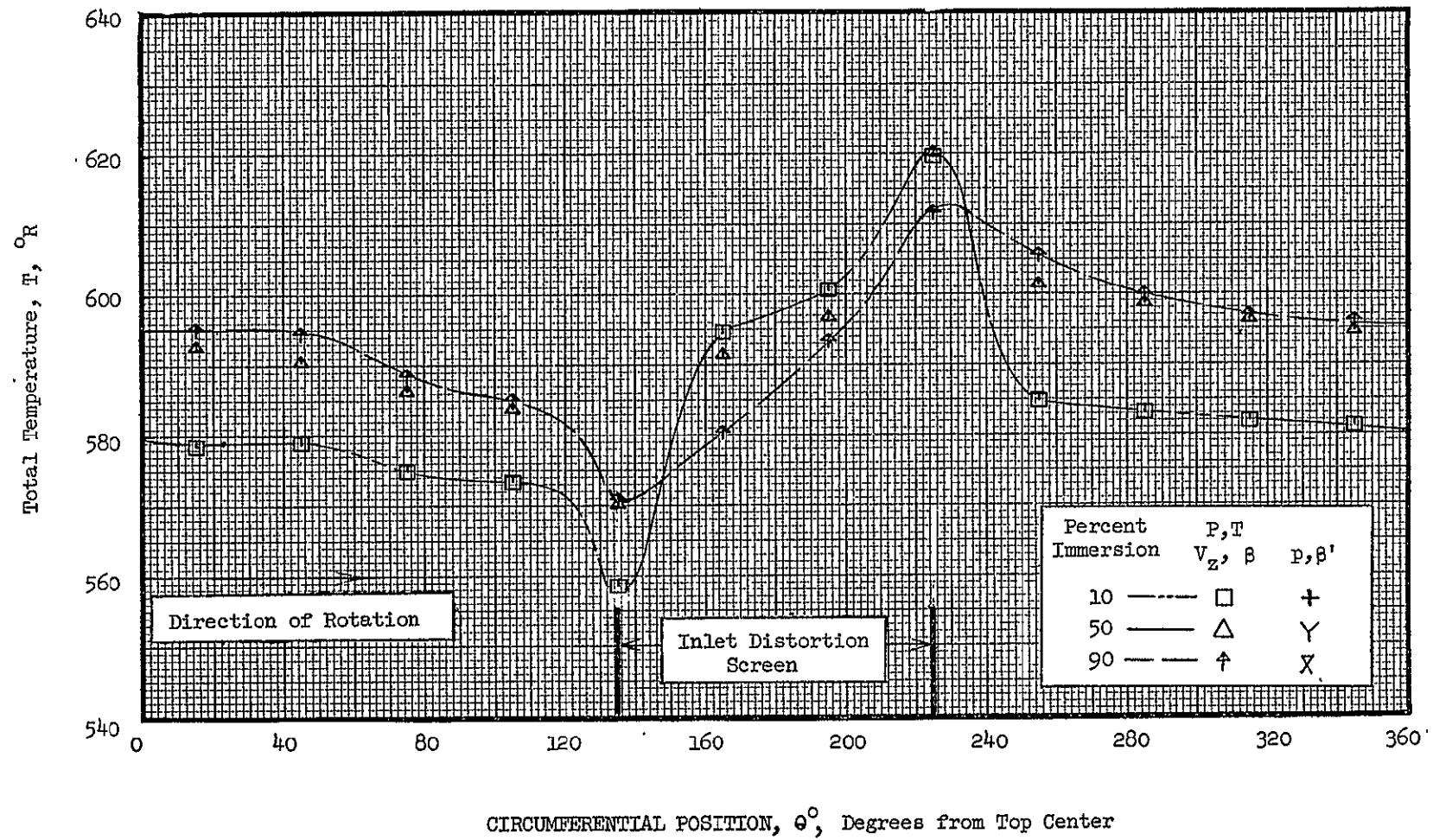


Figure 40 (b). Circumferential Variation of Flow Conditions at 100% Speed Maximum Weight Flow with Circumferential Inlet Flow Distortion, Plane 1.51 (Concluded).

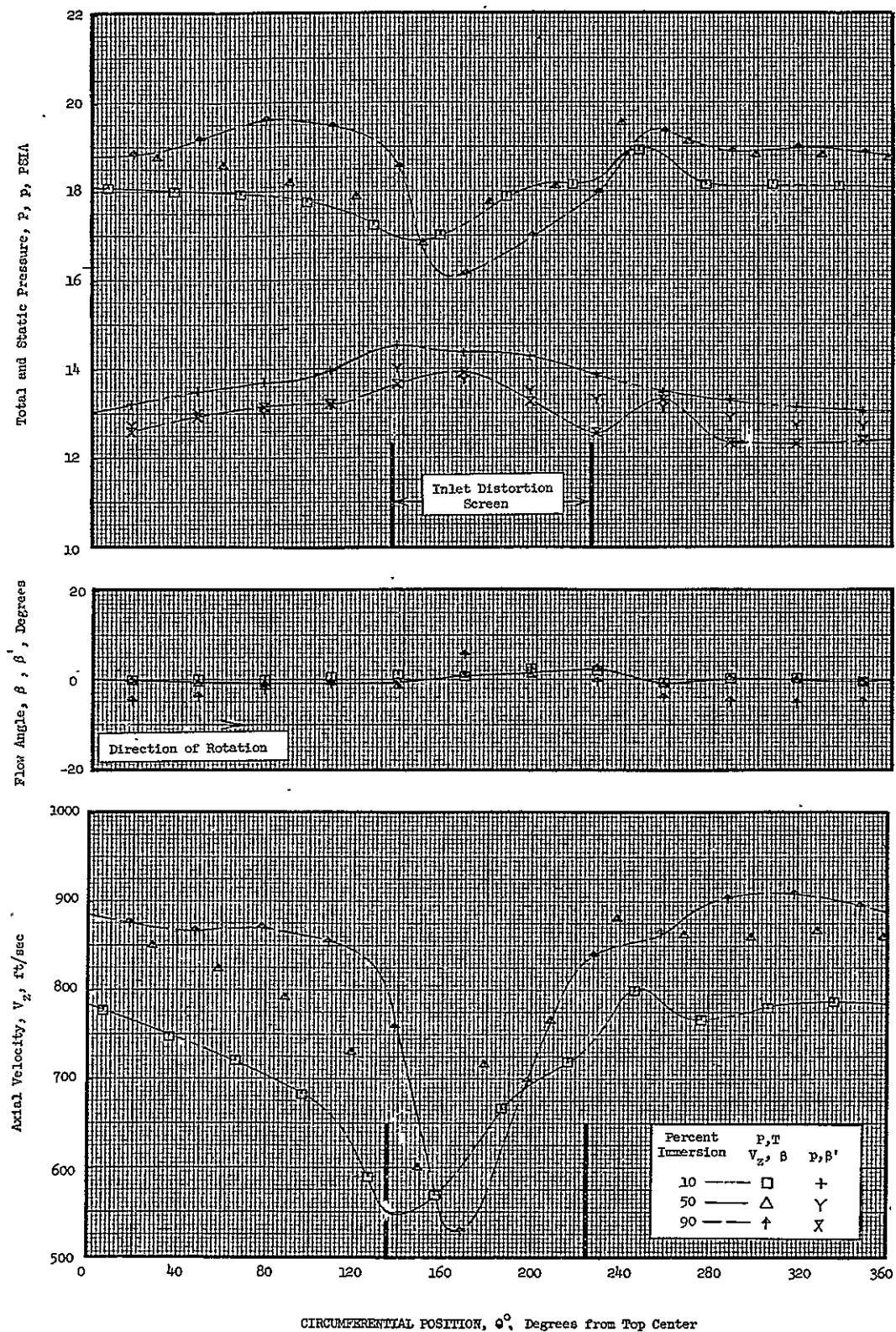


Figure 40 (c). Circumferential Variation of Flow Conditions at 100% Speed Maximum Weight Flow with Circumferential Inlet Flow Distortion, Plane 2.20.

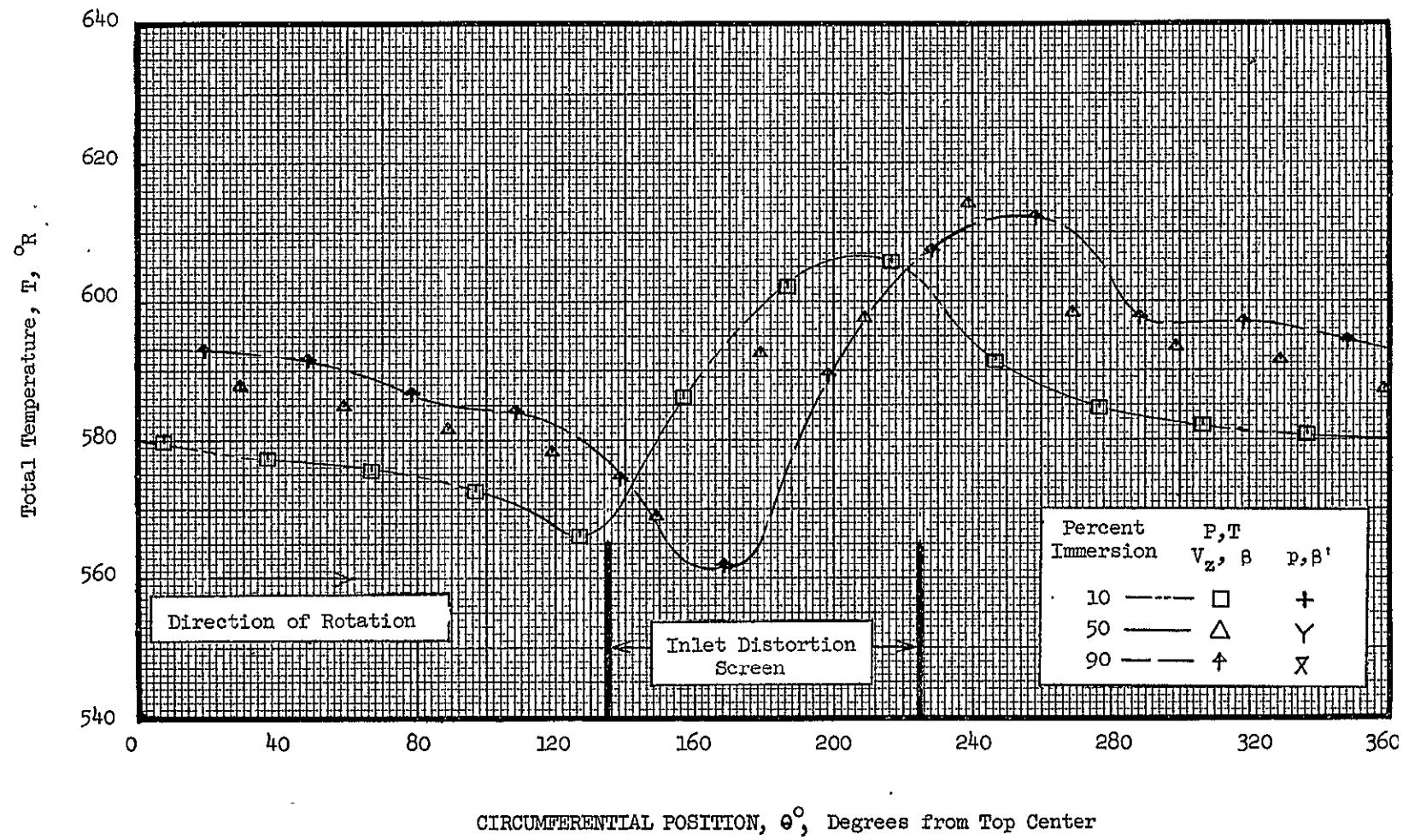


Figure 40 (c). Circumferential Variation of Flow Conditions at 100% Speed Maximum Weight Flow with Circumferential Inlet Flow Distortion, Plane 2.20 (Concluded).

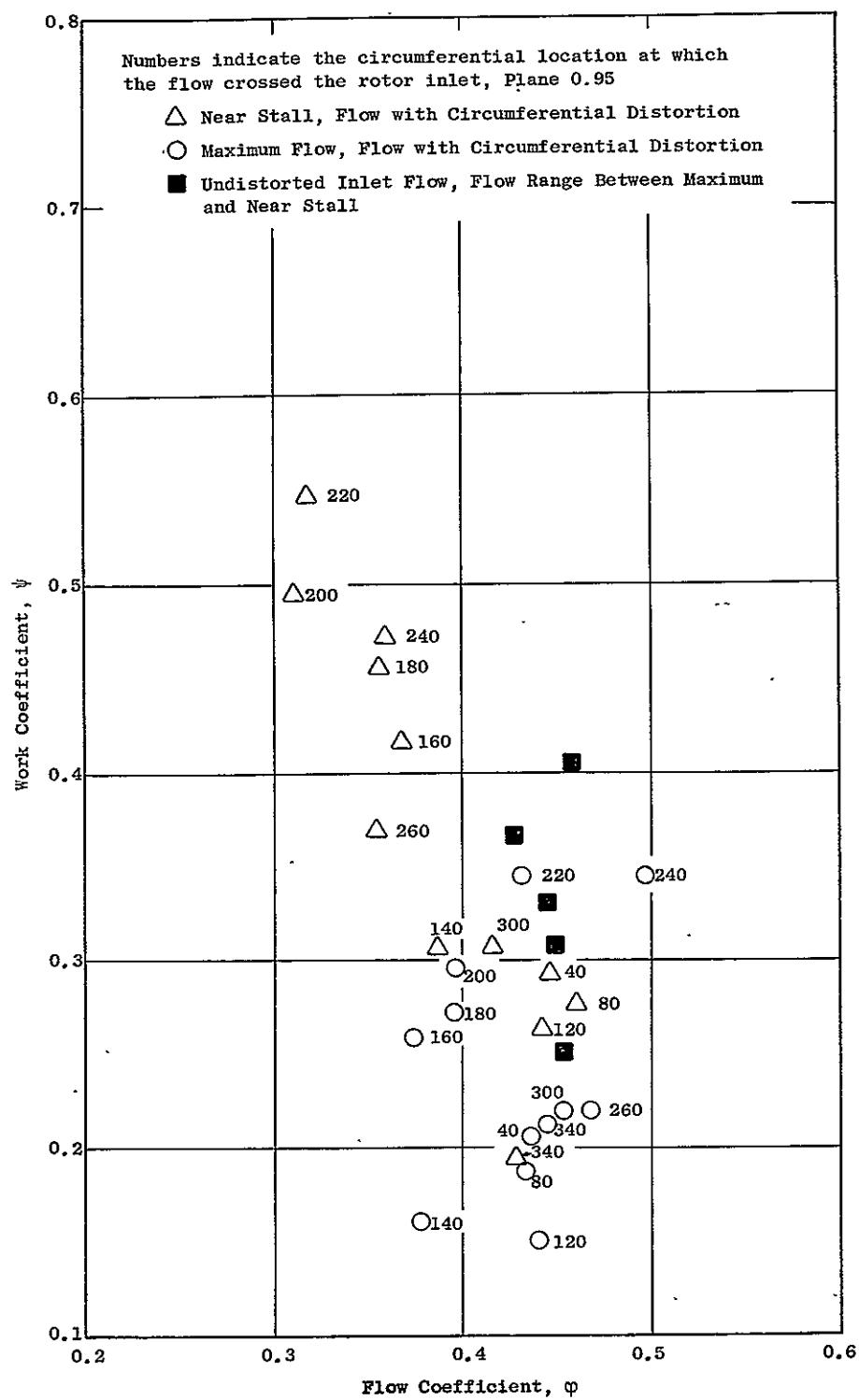


Figure 41 (a). Rotor Blade Element Work Coefficient - Flow Coefficient Characteristics, Uncorrected for Inlet Swirl and Axial Velocity Change at 100% Speed; 10% Immersion from Tip.

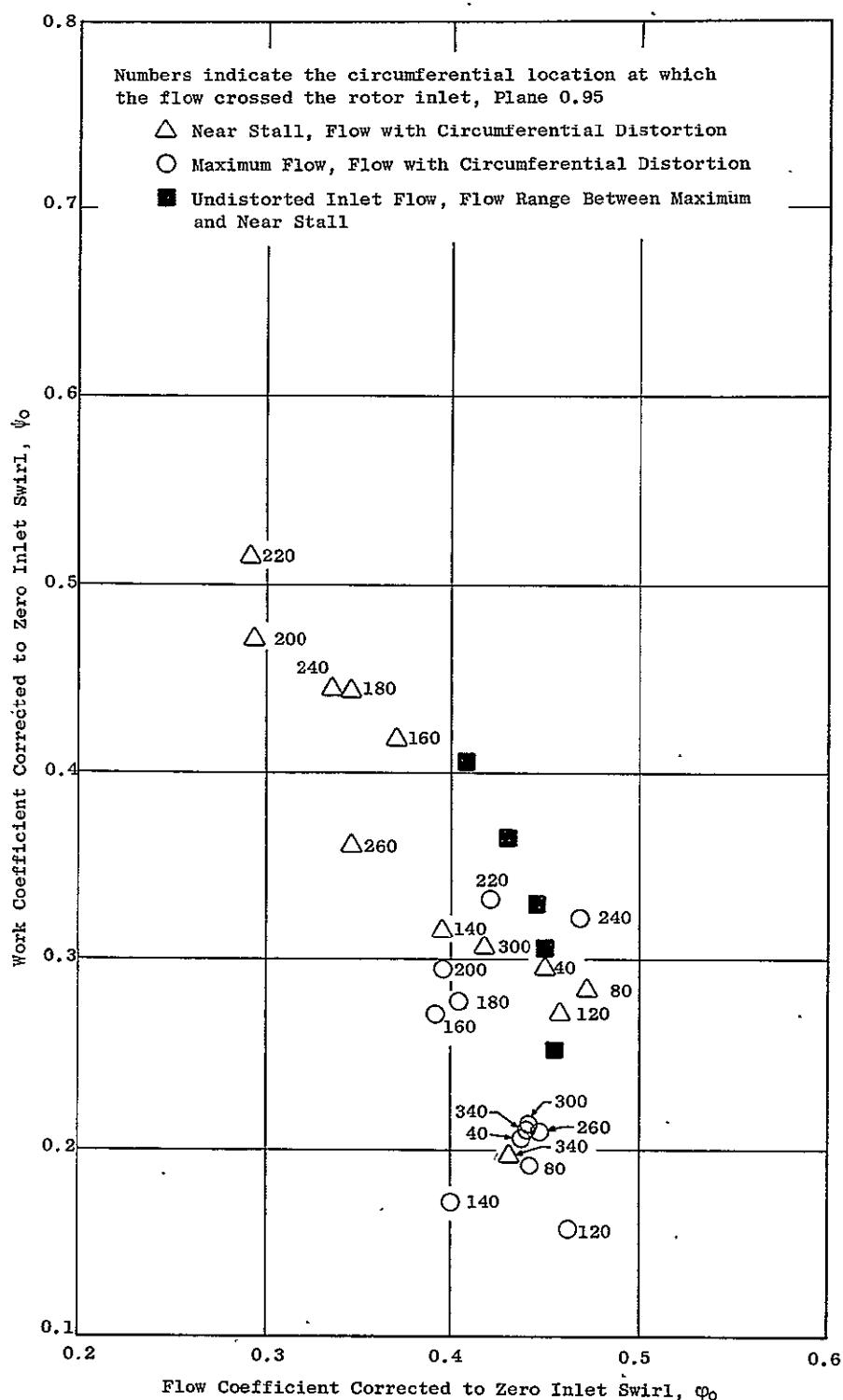


Figure 41 (b). Rotor Blade Element Work Coefficient - Flow Coefficient Characteristics, Corrected for Inlet Swirl at 100% Speed; 10% Immersion from Tip.

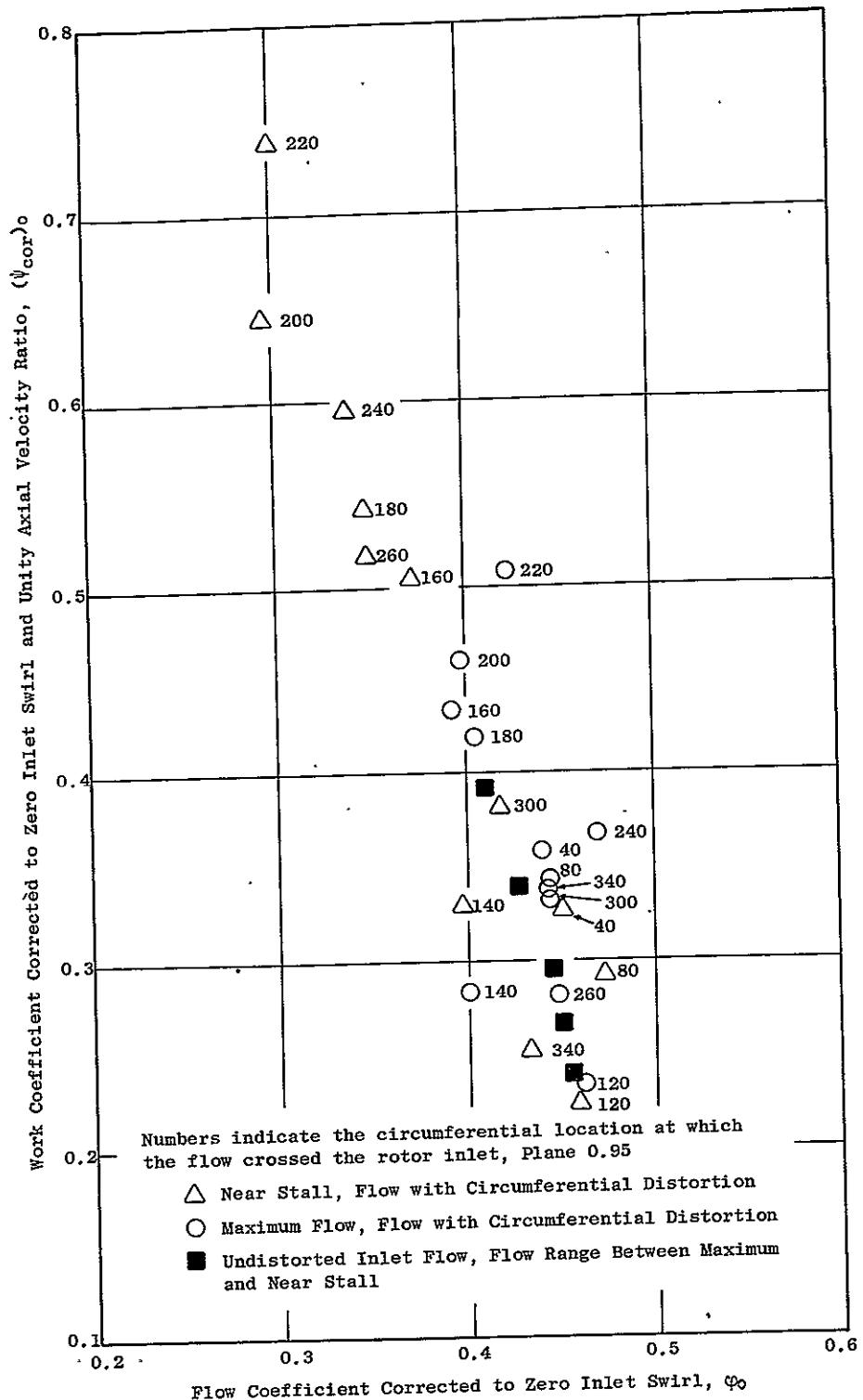


Figure 41 (c). Rotör Blade Element Work Coefficient - Flow Coefficient Characteristics, Corrected for Inlet Swirl and Axial Velocity Change at 100% Speed; 10% Immersion from Tip.

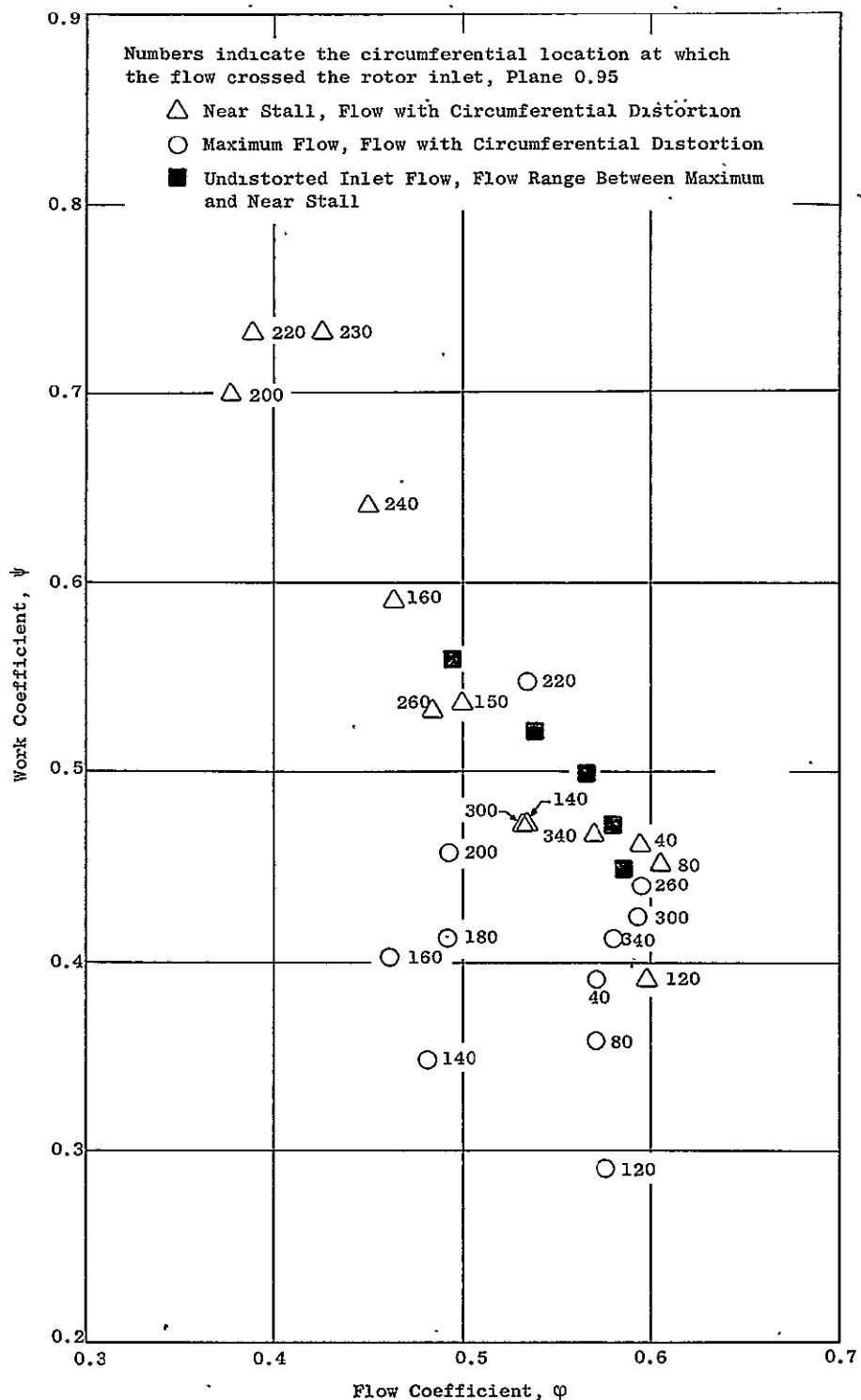


Figure 42 (a). Rotor Blade Element Work Coefficient - Flow Coefficient Characteristics, Uncorrected for Inlet Swirl and Axial Velocity Change at 100% Speed; 50% Immersion from Tip.

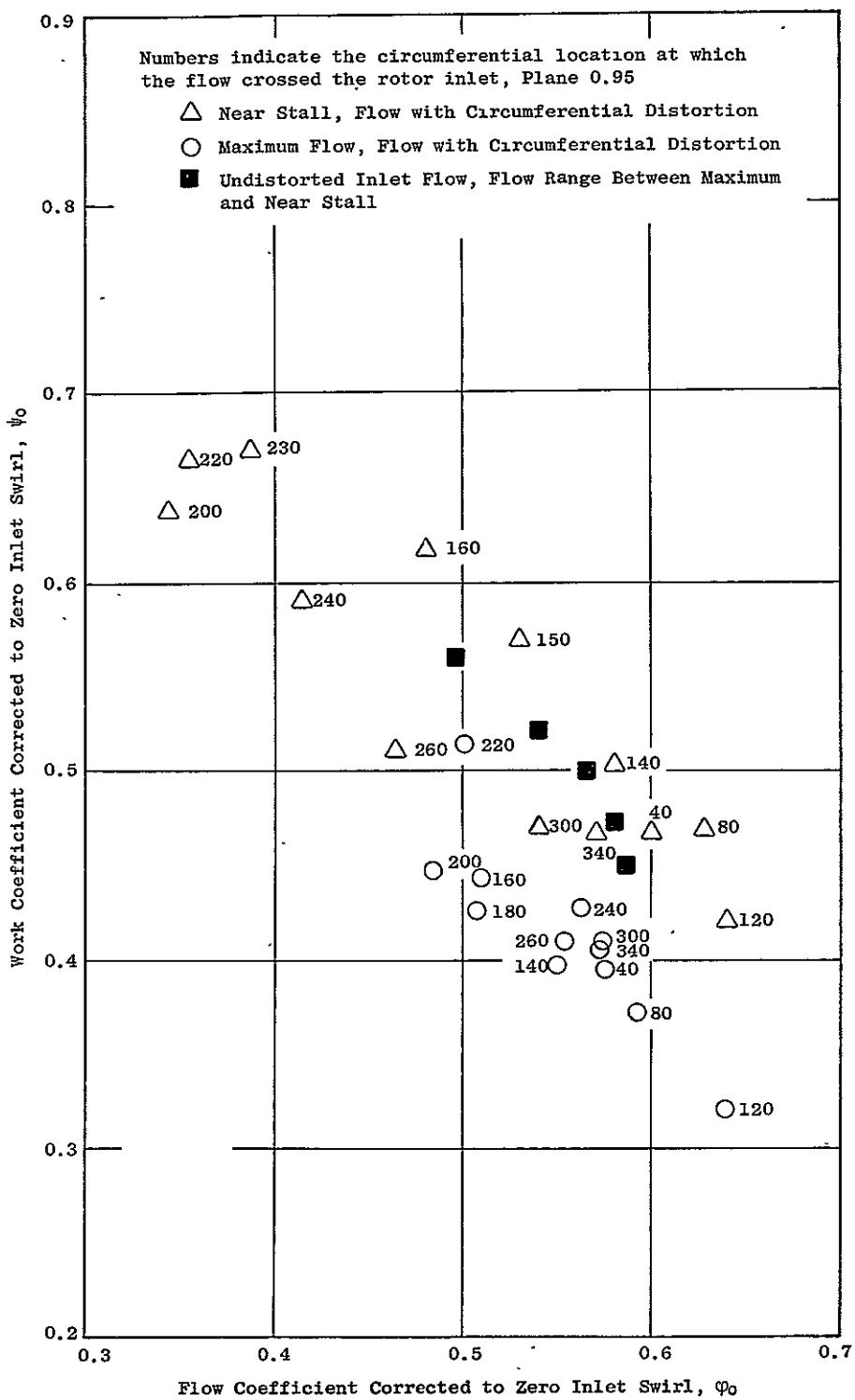


Figure 42 (b). Rotor Blade Element Work Coefficient - Flow Coefficient Characteristics, Corrected for Inlet Swirl at 100% Speed; 50% Immersion from Tip.

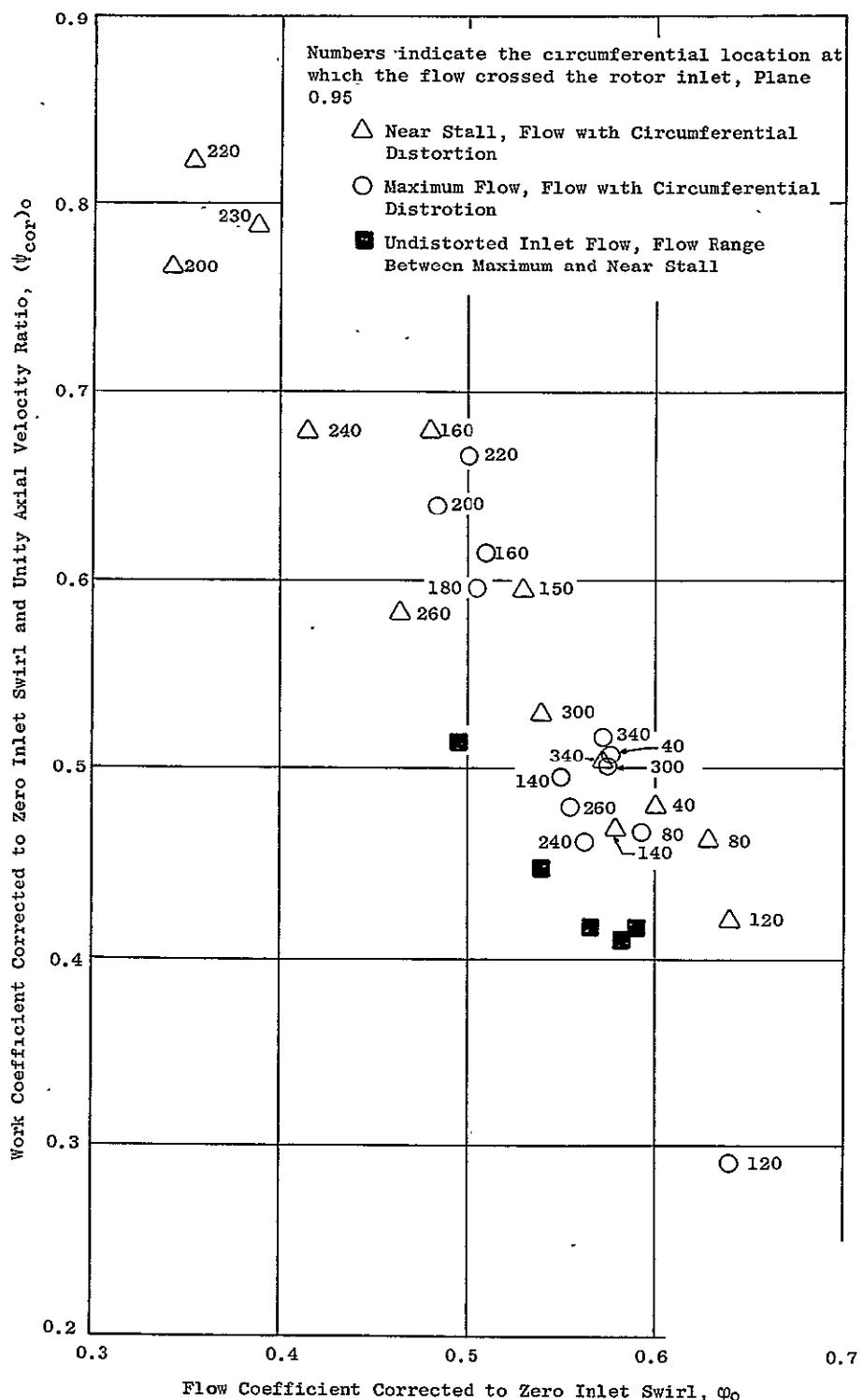


Figure 42 (c). Rotor Blade Element Work Coefficient - Flow Coefficient Characteristics, Corrected for Inlet Swirl and Axial Velocity Change at 100% Speed; 50% Immersion from Tip.

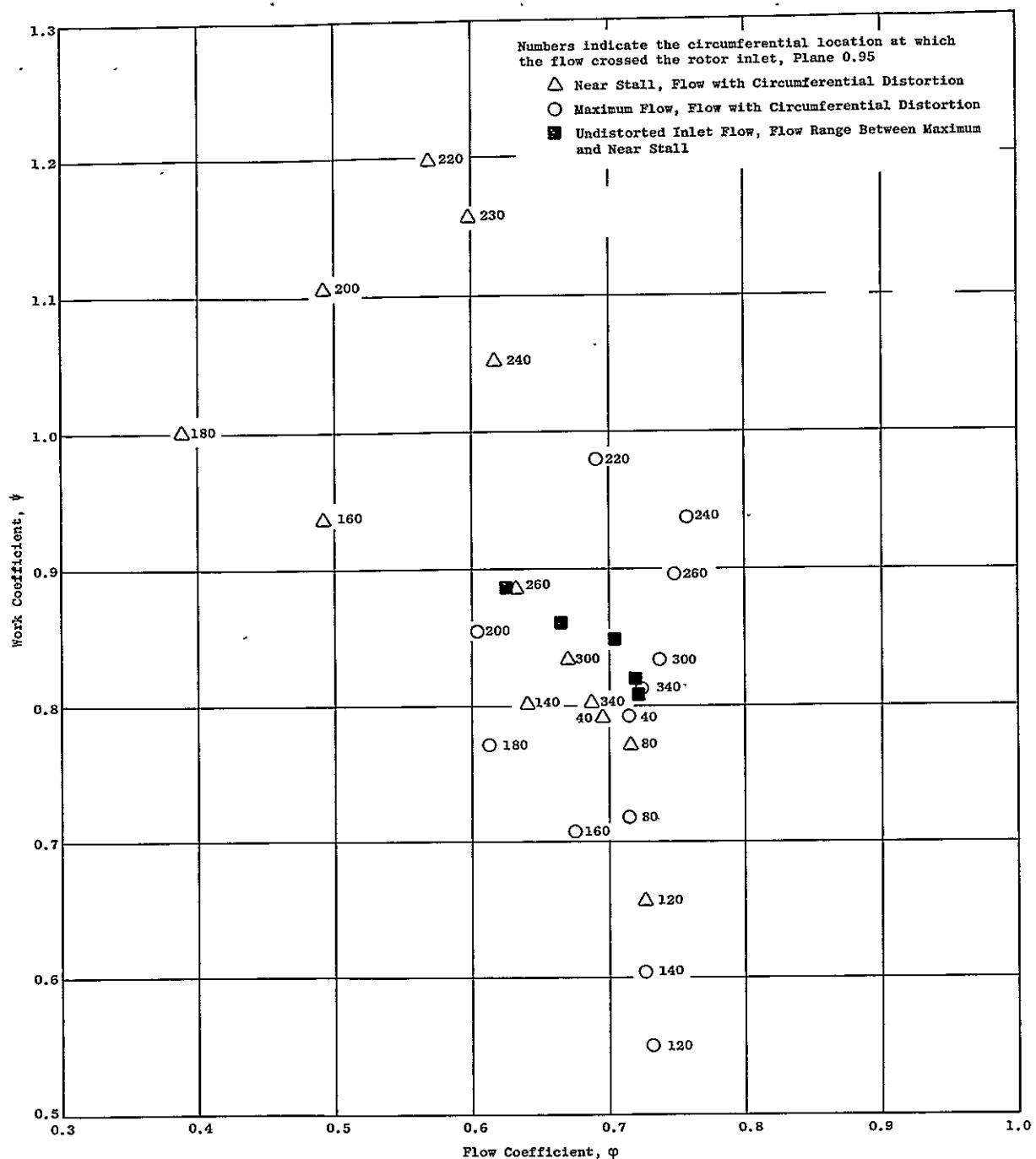


Figure 43 (a). Rotor Blade Element Work Coefficient - Flow Coefficient Characteristics, Uncorrected for Inlet Swirl and Axial Velocity Change at 100% Speed; 90% Immersion from Tip.

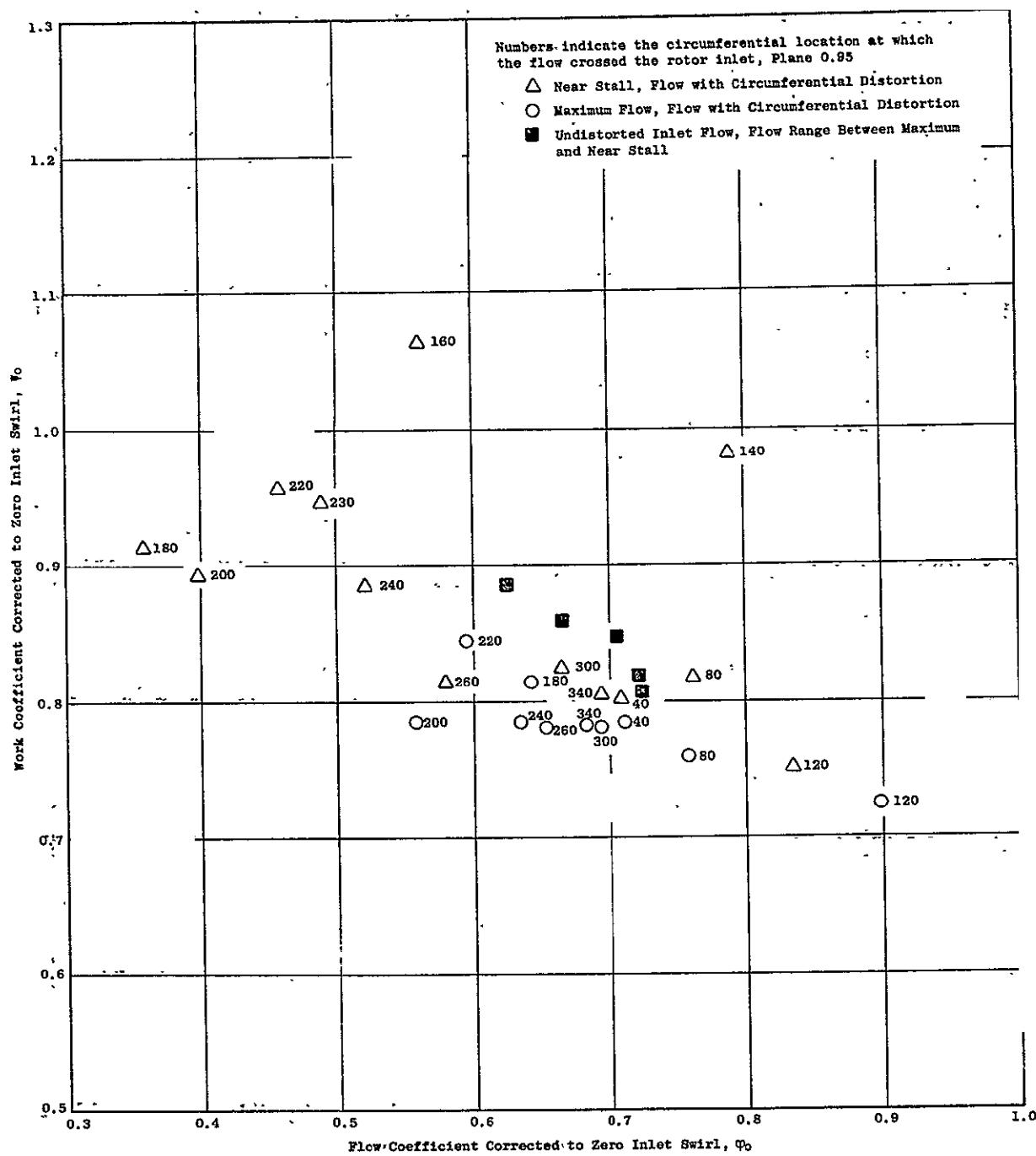


Figure 43 (b). Rotor Blade Element Work Coefficient - Flow Coefficient Characteristics, Corrected for Inlet Swirl at 100% Speed; 90% Immersion from Tip.

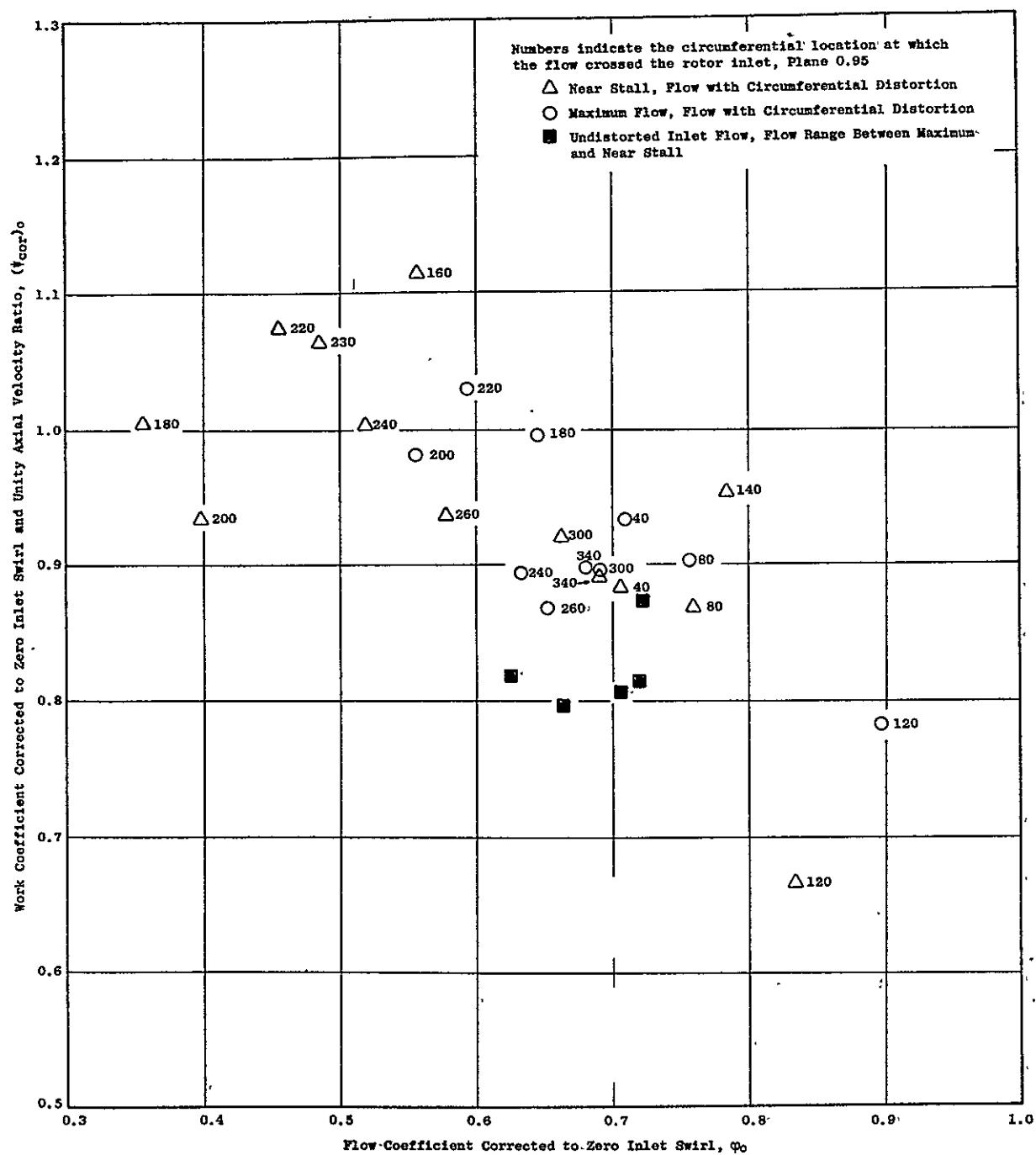


Figure 43 (c). Rotor Blade Element Work Coefficient - Flow Coefficient Characteristics, Corrected for Inlet Swirl and Axial Velocity Change at 100% Speed; 90% Immersion from Tip.